Searching for Vector-like Quarks Using 36.1 fb^{-1}of Proton-Proton Collisions Decaying to Same-Charge Dileptons and Trileptons + b-Jets at $\sqrt{s}$ = 13 TeV with the ATLAS Detector

by

Sarah Louise Jones

Copyright © Sarah Louise Jones 2017

A Dissertation Submitted to the Faculty of the

DEPARTMENT OF PHYSICS

In Partial Fulfillment of the Requirements
For the Degree of

DOCTOR OF PHILOSOPHY

In the Graduate College

THE UNIVERSITY OF ARIZONA

2017

THE UNIVERSITY OF ARIZONA
GRADUATE COLLEGE

As members of the Dissertation Committee, we certify that we have read the dissertation prepared by *Sarah Louise Jones* entitled *Searching for Vector-like Quarks Using 36.1 fb^{-1} of Proton-Proton Collisions Decaying to Same-Charge Dileptons and Trileptons + b-Jets at $\sqrt{s}$ = 13 TeV with the ATLAS Detector* and recommend that it be accepted as fulfilling the dissertation requirement for the Degree of Doctor of Philosophy.

Date: November 7, 2017

Kenneth Johns

Date: November 7, 2017

Erich Varnes

Date: November 7, 2017

Elliott Cheu

Date: November 7, 2017

Ina Sarcevic

Date: November 7, 2017

Doug Toussaint

Final approval and acceptance of this dissertation is contingent upon the candidate's submission of the final copies of the dissertation to the Graduate College.
I hereby certify that I have read this dissertation prepared under my direction and recommend that it be accepted as fulfilling the dissertation requirement.

Date: November 7, 2017

Dissertation Chair: Kenneth Johns

STATEMENT BY AUTHOR

This dissertation has been submitted in partial fulfillment of requirements for an advanced degree at the University of Arizona and is deposited in the University Library to be made available to borrowers under rules of the Library.

Brief quotations from this dissertation are allowable without special permission, provided that accurate acknowledgment of the source is made. Requests for permission for extended quotation from or reproduction of this manuscript in whole or in part may be granted by the copyright holder.

SIGNED: Sarah Louise Jones

ACKNOWLEDGEMENTS

There are so many people I must thank for supporting me throughout this process. A Ph.D. may seem like an individual's achievement, but it cannot come to fruition in a vacuum.

First, I want to thank my advisor, Kenneth Johns, whose steadfast support and research guidance throughout these last few years has been crucial to my success. Also, thank you to my secondary advisor (in all but official title) Erich Varnes, who has always been an endless source of knowledge from statistics to analysis techniques. To the rest of my committee Elliott Cheu, Ina Sarcevic, and Doug Toussaint: thank you so much for being on my committee and for being a knowledgeable resource throughout the years.

I would also like to thank Jason Veatch, Fionnbarr O'Grady, and Matt Leone for being great labmates during my first few years and always being willing to answer my naïve questions. To UA post-docs and former post-docs: to Xiaowen Lei, thank you for always being a source of information, your guidance in the beginning with respect to the fake background techniques was extremely helpful; to Ruchika Nayyar, thank you for being such a friendly person to chat with, especially about basic analysis tools as I was learning the ropes early on; to Matt LeBlanc for all your help with the limit setting tools.

Acknowledgements go to Mike Eklund and Matt Jones for always being willing to help out when our computer clusters went down or when Condor was not cooperating. I also want to issue a posthumous thank you to Roger Haar, who was a wonderful friend, mentor for teaching physics, and who was loved by many in the UA Physics Department.

I have so much gratitude for my wonderful friends Sophia Chen, Sirandon Johnson, Dheeraj Golla, Abhay Shastry, Adarsh Pyarelal, Alex Brasington, Hannah Carson, Alex Plunkett, and Matt Yankowitz for being such good company and limitless sources of good humor and intellectual conversations throughout the years. To Rebekah Cross, who became my closest friend: I have so much gratitude for all those nights and days you were willing to spend with me geeking out about literally anything, from Star Trek to String Theory.

Ample thanks are due to the broader group at CERN and other institutions on my analysis team. To Romain Madar, for your analysis tools and help debugging things; Cécile Deterre, Zhi Zheng, Simon Berlendis, Thibault Chevalérias, and Sergey Senkin for always being willing to chat about issues in the analysis via skype or email. And to the rest of the analysis team as well as the HQT conveners and the Vector-like Quark combination team: thank you all so much for providing such a fun and collaborative experience.

The hard work on the Micromegas front-end electronics also merits thanks to the whole Micromegas team at Brookhaven National Lab, Harvard, University of Michigan, Weizmann Institute, and the rest of the institutions and CERN. I must personally acknowledge Givi Sekhniaidze, Vinnie Polychronakos, Theodoros Argyropoulos, George Iakovidis, Paris Moschovakos, Panos Gkountoumis, and Christos Bakalis for being such fun people to test the electronics with and learn from during my multiple visits to CERN. Also, thanks to

Lorne Levinson and Stephanie Zimmermann for all your hard work managing the craziness of this upgrade work. Thank you to Gianluigi de Geronimo for your work on the VMM ASIC designs and answering all our (many) questions as we tested them.

Thank you to my magnanimous parents, Betty and Sheldon Jones, and the rest of my family, without whom this process would have seemed insurmountable. Your unwavering support of me pursuing physics throughout the years has meant more to me than words can describe. To my wonderful love in life, Daniel MacDougall: your amazing patience and encouragement throughout this process has driven me to succeed and instilled a deeper sense of grit and determination in my life. It is a pleasure to continue to grow and learn with you by my side. And thank you to the rest of the MacDougall clan for being another supportive family to me.

Lastly, I gratefully acknowledge the United States Department of Energy (DOE) for funding the work presented in this dissertation (supported by DOE grant number DE-SC0009913). DOE also supported the funding and the construction of the LHC. I also acknowledge my kind scholarship donor, Mark Jennings, whose generous contributions to the ARCS Foundation scholarship provided funding for this work as well.

DEDICATION

For my parents.

Science and everyday life cannot and should not be separated.
- Rosalind Franklin

TABLE OF CONTENTS

TABLE OF CONTENTS – *Continued*

TABLE OF CONTENTS – *Continued*

LIST OF FIGURES

LIST OF FIGURES – *Continued*

LIST OF FIGURES – *Continued*

LIST OF FIGURES – *Continued*

LIST OF FIGURES – *Continued*

LIST OF FIGURES – *Continued*

LIST OF FIGURES – *Continued*

LIST OF FIGURES – *Continued*

LIST OF FIGURES – *Continued*

LIST OF FIGURES – *Continued*

LIST OF FIGURES – *Continued*

LIST OF FIGURES – *Continued*

LIST OF FIGURES – *Continued*

LIST OF FIGURES – *Continued*

LIST OF FIGURES – *Continued*

LIST OF FIGURES – *Continued*

LIST OF TABLES

LIST OF TABLES – *Continued*

LIST OF TABLES – *Continued*

LIST OF TABLES – *Continued*

LIST OF TABLES – *Continued*

ABSTRACT

Since the discovery of the Higgs boson in 2012, the search for new physics beyond the Standard Model has been greatly intensified. At the CERN Large Hadron Collider (LHC), ATLAS searches for new physics entail looking for new particles by colliding protons together. Presented here is a search for a new form of quark matter called Vector-like Quarks (VLQ), which are hypothetical particles that are expected to have mass around a few TeV. VLQ can come in a variety of forms and can couple to their Standard Model (SM) quark counterparts, particularly to the third generation. They are necessary in several beyond the SM theories in order to solve the hierarchy problem. This search uses 36.1 $\text{fb}^{-1}$of proton-proton collision data collected with the ATLAS detector at the LHC from August 2015 to October 2016. Only events with two leptons of the same charge, or three leptons, plus b-jets and high missing transverse energy are considered in the main analysis. This signature is rarely produced in the SM, which means the backgrounds in this analysis are relatively low. This analysis is sensitive to specific predicted decay modes from pair production of an up-type VLQ with a charge of $+2/3$, T, an up-type VLQ with a charge of $+5/3$, $T_{5/3}$, and a down-type quark with a charge of $-1/3$, B, as well as single production of $T_{5/3}$. There is another theorized VLQ that this analysis is not sensitive to: $B_{-4/3}$, due to its primary decay mode, which is unable to produce the final-state signature of interest. The results from this analysis suggest only a slight deviation of data from SM backgrounds reaching as high as 1.89σ, which does not indicate evidence for VLQ. A mostly frequentist statistical technique, called the CL_S Method, is used to interpret the data and set limits on the T, B, and $T_{5/3}$ signal models. Using this method, exclusion limits are set at the 95% confidence level, effectively excluding T mass below 0.98 TeV, $T_{5/3}$ mass below 1.2 TeV, and B mass below 1.0 TeV, assuming singlet branching ratios. Also, branching ratio independent limits are set on the T and B VLQ.

CHAPTER 1
INTRODUCTION

Particle physics is a field primarily concerned with understanding matter interactions on the subatomic scale. These interactions happen between the fundamental particles in nature.[1] The predominant goal of particle physics is to describe the observable universe in terms of a theoretical framework, which is testable through experiments. If fundamental particle interactions observed through experiments can be accurately described by the mathematical framework, then it is reasonable to assume that nature can be interpreted as consisting of these fundamental particles.

Presented in this dissertation is a search for new types of particles that may offer an extension to the underlying theoretical framework used to describe the universe, called the Standard Model of particle physics, hereafter referred to as just the Standard Model. This model is a well-tested framework for the universe, but it remains incomplete. Searching for new types of particles can reveal information about what extensions to the Standard Model are needed to complete our fundamental picture of nature.

Since the late 19^{th} century a myriad of particles, both fundamental and composite, have been discovered through various experiments. It was not until the 1960's and 1970's that protons and neutrons, which form the nuclei of atomic matter, were discovered to be composed of the smaller elementary particles quarks and gluons [2]. Gradually throughout the latter half of the 20^{th} century, physicists realized that electrons, which orbit the nuclei in atoms, along with quarks and gluons are not the only fundamental particles in nature. Current evidence suggests there are three generations of fermionic matter (spin $\frac{1}{2}$), four force-mediating gauge bosons (spin 1), and one scalar boson called the Higgs (spin 0). The most recent fundamental particle to be discovered, as of this writing, is the Higgs boson, discovered in 2012 using data taken at the Large Hadron Collider [3, 4]. The mass of the fundamental particles in the Standard Model arises from their interactions with the Higgs boson.

[1] *Fundamental* means these particles cannot be subdivided into smaller particles (in contrast to *composite* particles, which consist of more fundamental particles).

Recently, subatomic particles and their interactions have been probed by accelerating certain particles to higher and higher energies before colliding them with either fixed targets or other accelerated particles. Increasing the energy is necessary because in order to produce more massive particles, a large amount of initial energy is required. More massive particles are typically unstable, so observing them is done indirectly through their decay products. Nowadays, particle physics is concerned with probing these interactions using some of the largest physics experiments ever built. The ATLAS (A Toroidal LHC ApparatuS) experiment at the LHC is one of the largest experiments used to probe particle interactions using proton-proton collisions. ATLAS is the apparatus used to collect the data for the search presented in this dissertation.

The fundamental particles in nature have been formulated by physicists into a framework known as the Standard Model (SM). All interactions between the different particles are governed by force mediating particles called gauge bosons. These interactions are described in the mathematical formalism of the SM: relativistic quantum field theory. This formalism is discussed in more detail in Chapter 2.

Since its inception, the SM has been intensely scrutinized by experimentalists and theorists for any possible deviation that could hint at where to look for new physics. As it is, the SM provides one of the most tested and well understood theoretical frameworks for understanding and predicting the particles of nature and their interactions. For example, in 1995 the top quark was discovered at the Tevatron [5, 6] at Fermilab (Batavia, Illinois, USA), what was then the world's leading particle accelerator. The top quark was predicted to exist prior to its discovery based on the physics in the SM. The Higgs boson was predicted prior to its discovery as well. Some things in the SM are open parameters, however. For example, the masses of the elementary particles were discovered at their respective values by performing many experiments. In general, the mass values themselves cannot be derived from first principles in the SM, and are left as parameters to be measured by experiments.

The discovery of the the Higgs in 2012 essentially completed the SM as we know it now. However, there still exist many unanswered questions about certain phenomena in nature. For example, what is the nature of dark matter and dark energy? Why are there three generations of matter in the SM? Why is there more matter than anti-matter in the Universe? What was the nature of the early universe immediately following the Big Bang? Why is the Higgs mass situated around roughly 125 GeV? These questions are just a few of the myriad mysteries occupying particle physicists' time, and they are what drive continued efforts to build larger and more sophisticated experiments.

It is inaccurate to say that the lack of a discovery so far of new physics *beyond* the SM at colliders such as the LHC is a failure of modern science. On the contrary, particle physics has thrived in an environment where so-called *null* results are ubiquitous and *discoveries* are few in number. While it is always the intention of physicists to try to discover hints of new physics, the understanding that comes from repeated and intense scrutiny of physics previously discovered is vital. This pushes the current understanding of the SM to higher precision, where subtler effects from new physics might manifest themselves.

Searching for new physics requires a theoretical framework that typically includes parameters that can be probed using experiments. This framework describes the interactions and parameters required to produce the new particles. Experiments set constraints on the properties of these theoretical models. In other words, with predictions from theory, experimental measurements can be improved; and with more precise measurements from experiments, the theories themselves may be further refined. This cycle continues until a theoretical model of interest is excluded fully (or in some cases no longer of interest) or verified through a discovery. Figure 1.1 depicts the exchange of information between the theoretical models and experiments in particle physics.

The search presented here uses theoretical models that extend the Standard Model to include additional particles in the form of Vector-like quarks. Vector-like quarks are theoretical particles that are predicted to have higher mass than their SM counterparts. They also interact with the weak force in a slightly different way than their SM counterparts. They arise in models that provide a solution to the hierarchy problem, which is essentially a problem of reconciling the Higgs mass at its observed value of 125 GeV (which is relatively low) and extending the SM to higher energy scales. Previous searches for Vector-like quarks have been performed using data taken at the LHC, and the theoretical models and search parameters have been refined as a result. A list of previous searches for Vector-like quarks is discussed in Chapter 2.

1.1 Note on Units and Notation

In experimental particle physics, it is customary to use natural units. This means $c = \hbar = 1$, where c is the speed of light, and $\hbar$ is the Planck constant in quantum mechanics divided by 2π. In natural units, length and time have the same units and both the mass and momentum of particles are quoted in orders of magnitude of electronvolts (just like the energy of the particle). For example, MeV means 10^6 electronvolts and mass (momentum) is denoted MeV (MeV) instead of MeV/c^2 (MeV/c). Commonly used units in this analysis

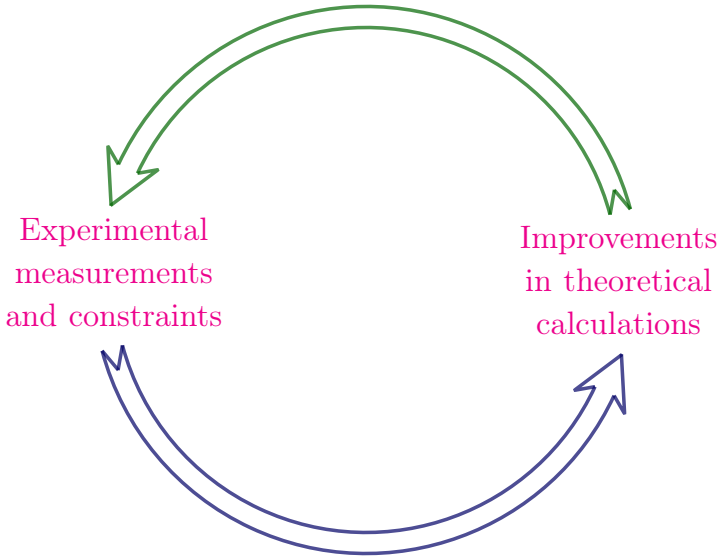

Figure 1.1: Theory and experiment provide a flow of knowledge given experimental measurements and constraints, and eventually, improvements on the theoretical calculations.

are GeV, which is 10^9 electronvolts, and TeV, which is 10^{12} electronvolts. One electronvolt is approximately 1.6×10^{-19} J of energy and 1.78×10^{-36} kg of mass in natural units.

Due to the small length scales of subatomic interactions, the typical SI unit of length measured in meters is far too large for this scale. Typically, femtometers (fm) is used instead, where the prefix *femto* means 10^{-15}. Cross sections are a unit of area measuring the probability of two particles interacting in a scattering process. In the context of proton bunches colliding at the LHC, discussed more in Chapter 3, the cross sections are typically denoted in picobarns (pb), where *pico* means 10^{-12}, or femtobarns (fb). One *barn* is equal to about 10^{-24} cm^2 or 100 fm^2.

There are also a couple subtle differences between experimentalist and theorist language in terms of referencing particle types in the SM. For example, with the exception of Chapter 2, when referring to 'leptons' in the data taken with ATLAS, only electrons and muons are included. Neutrinos will be referred to as neutrinos (as opposed to grouped with other leptons) and, in the context of reconstructing objects in the detector, these are included in the reconstruction of missing transverse energy ($E_{\mathrm{T}}^{\mathrm{miss}}$) because they are invisible to the detector (transverse means perpendicular to the beamline). Massive leptons of the third generation, or τ-leptons, are also separated from the discussion of leptons with ATLAS data. This is because, experimentally, their signature within the ATLAS detector is relatively

different from electrons and muons, so they are treated separately during reconstruction.

1.2 Overview of Exotic Search for Vector-like Quarks

In this analysis, massive particles referred to as Vector-like quarks (VLQ) are searched for as evidence of new, beyond the SM physics. They are included in models as a fourth generation of quarks to ameliorate the issues with the relatively small value of the Higgs boson mass (discussed more in Chapter 2). VLQ are more exotic forms of the SM quarks. If VLQ exist, they would exhibit the same quantum numbers as SM quarks but they would have masses on the TeV scale, and in some cases more exotic electric charges. The theoretical models predicting VLQ assume couplings to the SM quarks, mostly to the top and bottom quarks. There are several varieties of VLQ considered: Vector-like Top (simply denoted T), Vector-like Bottom (simply denoted B), and Vector-like Top with an exotic charge of $+5/3$ (denoted $T_{5/3}$) and Vector-like Bottom with exotic charge $-4/3$ (denoted $B_{-4/3}$). The models used for this search predict only three decay modes, or decay channels, for the T and B, and only one decay mode for each of the exotically charged VLQ.

Other theoretical models can predict more decay channels depending on the parameters of the model. For example, some models invoking Supersymmetry include VLQ with different decay channels from the "normal" modes considered in non-Supersymmetric models [7, 8]. In the context of this analysis, however, only the three decay modes present in most non-Supersymmetric models are considered.

Signature-based Searches Searching for VLQ typically means looking for certain types of events[2] that have a unique signature in the detector. The layers of the detector and which particles are detected are discussed more in Chapter 3.

Several searches are currently underway to look for VLQ with data from the LHC. Each search focuses on a unique signature obtained from one or more of the VLQ decay channels. This analysis searches for enhanced production of events containing two leptons (denoted *dileptons*) of the same charge (or events with three leptons: denoted *trileptons*) with corresponding b-jets and missing transverse energy ($E_{\mathrm{T}}^{\mathrm{miss}}$) as a unique signature to search for

[2]As will be discussed later, an *event* is essentially what ATLAS 'captures' in a brief window of time following a proton-proton collision. Events contain only information from stable particles that deposit their energy or are detected as particle tracks inside the detector.

VLQ without focusing on a specific decay channel.[3] VLQ can potentially produce multiple leptons from their decay patterns in greater numbers than what is predicted from the SM. Not all production modes and decay channels of the VLQ varieties can produce same-charge dileptons, however. As a result this analysis is only focused on searching for T, B, and $T_{5/3}$. Also, the T and B varieties of VLQ have different branching ratios to their decay modes depending on whether they are singlet or belong to a doublet or triplet. The analysis presented here focuses on T and B assuming they are singlets.

Beyond VLQ, this analysis also considers different exotic signals decaying to same-charge dileptons. These signals include exotic production modes of 4-tops ($t\bar{t}t\bar{t}$) as well as Standard Model production of 4-tops. The latter production is included because it has yet to be observed with high significance. Positively charged pairs of top quarks (t^+t^+) are also searched for, normally being suppressed by Standard Model physics. A pair of same-charge tops can be produced from some dark matter mediator models. For the most part, the object and event selection in data and simulation is treated exactly the same for these signal models as for the VLQ signal model search. The primary focus of this dissertation is on the VLQ search, so these other signal models will not be covered in detail. However, discussions of the other signal models will be included when necessary to enhance the discussion on the VLQ search.

Once the events are filtered into only those relevant for searching for particular signals, like VLQ, data and background events can be compared to search for any excess of data beyond what is predicted from the Standard Model production cross section of the same type of signature. If no data excess is observed or an excess is observed but is not significant enough to claim discovery, limits are set on the mass and production cross sections of the VLQ; this is discussed more in Chapter 9.

The rest of this dissertation is organized as follows. Chapter 2 describes the theoretical framework for particle physics and where the search presented here fits into that framework. Chapter 3 outlines the LHC and ATLAS experimental apparatus used to collect data. Chapter 4 discusses the reconstruction of objects from the datasets. The specific objects important to this analysis are discussed in detail. Next, in Chapter 5, the event selection is presented, where events that are identified as containing at least two leptons of the same charge, or three leptons, with associated jets are saved. The general analysis strategy as well as a discussion of the control regions and validation regions for the backgrounds are also

[3]When referring to leptons, quarks, or other particles with anti-particles, it is implied that the corresponding anti-particle is included in the discussion unless stated otherwise. For example, this search can look for both same charge leptons both with a positive charge and both with a negative charge.

presented. Chapter 6 presents the data and Monte Carlo simulation samples used in this analysis. A discussion on the simulation of the signal samples is also presented. Chapter 7 discusses a set of major backgrounds in this analysis: the data-driven backgrounds, which consist of charge mis-identification of electrons, and fake or non-prompt leptons. These backgrounds are difficult to estimate and cannot be accurately simulated with Monte Carlo. An overview of the methods used to estimate the two main backgrounds included in the data-driven background estimations is presented, along with a comparison of two methods for the fake/non-prompt lepton background estimation. The major systematics uncertainties are discussed in Chapter 8. The statistical interpretation of the results along with the final event yields for all backgrounds and data in the signal regions are presented in Chapter 9. Finally, conclusions and the future implications for this search as well as the VLQ combination search are discussed in Chapter 10.

CHAPTER 2
Theoretical Interpretation

Developing the current understanding of the fundamental particles in nature required theoretical predictions and experimental observation working in tandem. Over the course of the last half of the 20$^{\text{th}}$ century, the formalism for the Standard Model was constructed and provided experimentalists with the chance to search for specific particles that would complete the Standard Model framework. The last fundamental particles to be discovered, after being predicted by the SM in the 1960's-70's, were the top quark and the Higgs boson. The top quark was discovered at the Tevatron in 1995 [9, 10] and the Higgs boson was discovered at the LHC in 2012 [3, 4]. Since the discovery of the Higgs boson, and the subsequent confirmation that it is a scalar boson as predicted in the SM, the field of experimental particle physics has turned to searching for extensions of the SM.

To understand the theoretical framework for the analysis presented in this dissertation, an overview of the Standard Model (SM) is provided in this chapter. The SM has been tested with experiments over and over again and has shown remarkable resiliency. However, there are still several unresolved issues remaining that would require extensions to the theory. Some examples of these unresolved issues include the nature of dark matter, why the SM Higgs mass is around 125 GeV, at what point does gravity fit in to the SM, etc. Therefore, the SM is considered an incomplete theory for describing nature. Many beyond the Standard Model (BSM) theories are proposed and are continually updated with input from experiments, in order to provide possible answers for these unresolved aspects of nature.

This chapter is divided into two main sections; the first covers the Standard Model and its relevant features pertaining to the search presented later. The second section covers the BSM theories that invoke Vector-like quarks (VLQ) as a way of resolving the hierarchy problem in the current SM framework. The focus here is theoretical models that include VLQ and that are relevant to this analysis, since a broad overview of the multitude of BSM theories is beyond the scope of this dissertation. The VLQ models and properties are

discussed, especially VLQ decay modes sensitive to same-sign[1] leptons, which is the final state of interest for this analysis.

2.1 The Standard Model Quantum Field Theory

The current consensus is that the Universe is comprised of the following fundamental particles: twelve fermions (six leptons and six quarks), four gauge bosons, and a scalar Higgs boson, and all their associated anti-particles. Anti-particles are particles with the same mass, but with opposite charge. Note that some particles are their own anti-particle: notably, the photon (γ), Z^0, H, and gluons (g), which are each charge neutral. Each fermion has spin-$\frac{1}{2}$, obeys Fermi-Dirac statistics and consequently, the Pauli exclusion principle. There are six flavors and three generations each for quarks and leptons. Each generation forms a more massive version of the particle in the previous generation. The top quark is the heaviest of the known SM particles. Quarks with electric charge $\frac{2}{3}$ are classified as *up*-type quarks, while quarks with charge $-\frac{1}{3}$ are *down*-type. The four gauge bosons are all spin-1 and obey Bose-Einstein statistics.[2] The only scalar boson in the SM is the Higgs boson, which has spin-0. These particles constitute the Standard Model (SM) of particle physics and are summarized in Figure 2.1.

Ordinary everyday matter is made up of protons, neutrons, and electrons. Protons and neutrons are baryons, which means they are composite particles made up of quarks and gluons. Protons are formed from two u-quarks and one d-quark, whereas neutrons are comprised of two d-quarks and one u-quark. These baryons form the nuclei in every atom in the periodic table of the elements and electrons orbit in clouds around the nuclei of the atoms. The other two generations of quarks and leptons in the SM are forms of more massive fundamental matter, which typically have finite lifetimes leading to their decaying to less massive particles. The quarks inside protons and neutrons do not exist by themselves, and are in fact surrounded by a *sea* of quark and anti-quark pairs and gluons. Each of these constituents is called a *parton*. A discussion on the relevance of partons to the collisions of protons at the LHC is discussed in §2.1.3.

The gauge bosons mediate the three fundamental interaction forces in the SM: the strong force, also known as the color force, is mediated by gluons; the electromagnetic force is

[1] The terms 'same charge' and 'same-sign' refer to the electric charge of the two leptons being identical, and both terms are used interchangeably throughout this dissertation.

[2] Bosons with a spin equal to 1 are also called "vector bosons" and so the gauge bosons of the SM will sometimes be referred to as such in this dissertation.

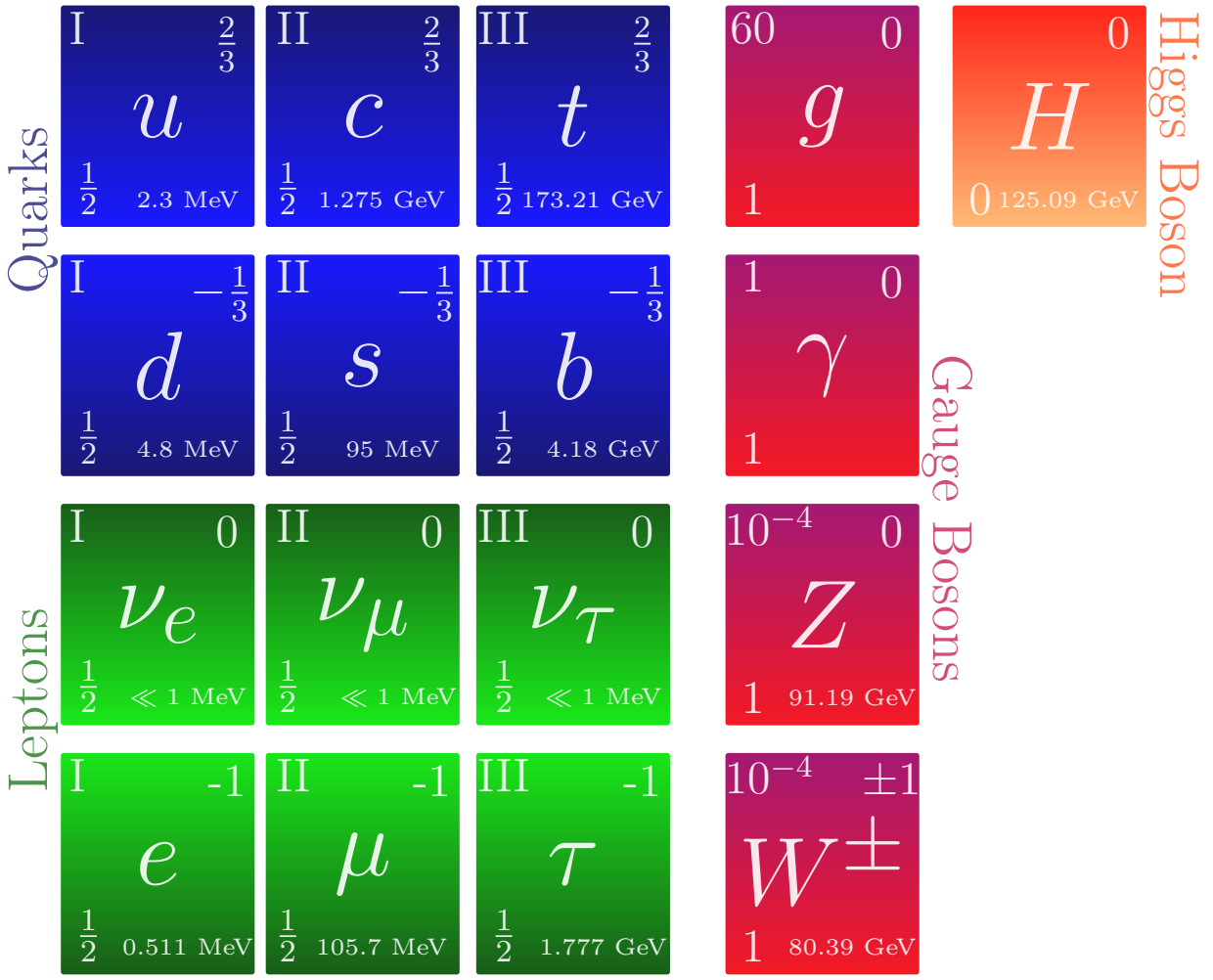

Figure 2.1: A visual representation of the Standard Model particles and their properties. The middle symbol represents the typical notation used for the particle (anti-particles are represented by the same symbol, but with a bar over the symbol: $\overline{u}$, for example, or in the case of the W, by the charge sign). The approximate mass (given in GeV), spin, and charge are shown for each particle. All mass values are from the Particle Data Group (PDG) reference [11] where the statistical and systematic uncertainties for measurements of the masses can be found. The Higgs boson nominal mass value has been updated to include the combined results from CMS and ATLAS as of 2015 [12]. The electric charge of the particles is represented by q/e (upper right corner), where e is the electron charge. For fermions, the generation is in the upper left corner of each box, while for the gauge bosons that spot is reserved for the magnitude of the force strength relative to the EM force between two u quarks at a distance of 3×10^{-17}m. Compared to these relative strengths, gravity is predicted to be weaker than the Electromagnetic force by roughly 10^{-41}. *Note, the individual masses of the neutrinos is still under experimental investigation, but data from cosmological observations suggest that the sum of the masses of the three flavors of neutrinos has an upper limit of about 1-2 eV [13].

mediated by photons; and the weak force is mediated by the Z^0 and $W^{\pm}$ vector bosons.[3] There is a fourth force, the gravitational interaction, which has not yet been reconciled with the other three fundamental interactions in the theoretical framework of the SM. Some searches with LHC data are looking for evidence of the production of gravitons, which are theorized to be spin-2 gauge bosons mediating the gravitational field. No evidence for gravitons has yet been found.

Quantum Field Theory For a theoretical model to be considered a quantum field theory (QFT) it must mathematically describe particles as continuous fields in space and time and provide a framework for particle dynamics and interactions based on symmetries within the theory. The Standard Model is one such quantum field theory. Particles are described as excitations of the underlying field. For example, the photon is an excitation of the electromagnetic (EM) field. Interactions between particles are governed by couplings between fields.

The SM is mathematically described by the Standard Model Lagrangian ($\mathscr{L}_{\text{SM}}$), which describes the physically allowed interactions between all the fields. For each allowed interaction, an explicit term in the Lagrangian is included. Figure 2.2 shows a few examples of allowable weak interactions and gluon interactions with top quarks in the SM. Each vertex in a Feynman diagram is a representation of a term in the Lagrangian. Feynman diagrams can become quite complex depending on the interaction and level to which one wishes to calculate the scattering amplitude. However, in this treatment, *tree level* (lowest order) diagrams are typically shown for most interactions. For processes that require a more accurate calculation, next-to-leading order (NLO) or next-to-next-to-leading order (NNLO) are used. NLO and NNLO processes include loop corrections to the underlying process.[4] Most of the time a solution to the scattering amplitudes requires numerical computation, which are included in MC simulators, discussed in Chapter 6.

Symmetries in a quantum field theory arise from conservation laws, as originally postulated for any physical system with action, $\int \mathscr{L} \mathrm{d}t$ (where $\mathscr{L}$ is the Lagrangian for the system), in Noether's theorem [14]. An important symmetry of the SM Lagrangian is that it is locally gauge invariant. Local gauge invariance refers to the transformation of a field in space or time. For example, a simple transformation of a field by an arbitrary phase shift:

[3] The Z-boson has a neutral charge, represented by the 0 superscript. Henceforth, when referring to Z^0, the superscript is dropped. The same can be said about the Higgs.

[4] In principle, one can numerically calculate diagrams to higher orders than this (e.g. N^{3}LO and beyond), however the computation gets quite complex past the third leading order.

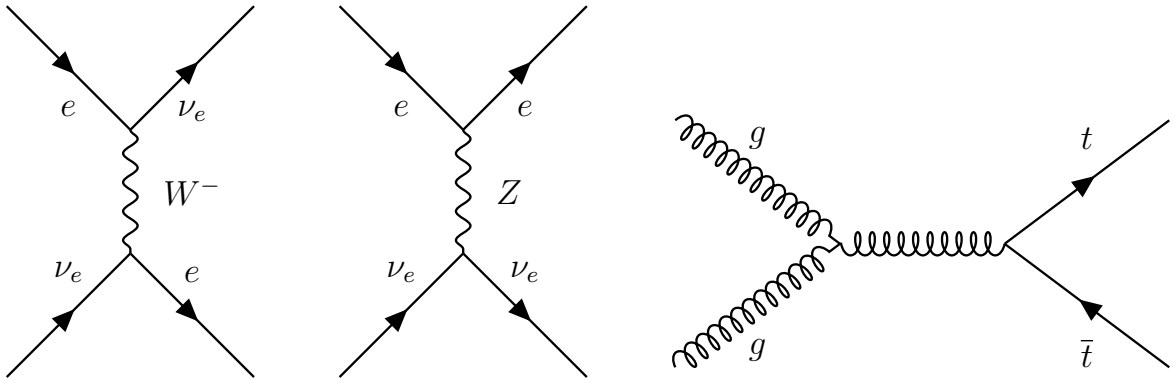

Figure 2.2: Example tree level diagrams for *charged* (left) and *neutral* (middle) current weak processes involving electron-neutrino scattering. On the right is a tree level diagram for $t\bar{t}$ production via gluon-gluon fusion.

$\psi(\mathbf{x},t) \to e^{i\phi(\mathbf{x},t)}\psi(\mathbf{x},t)$ or $A_\mu(\mathbf{x}) \to A_\mu(\mathbf{x}) - \frac{1}{e}\partial_\mu\phi(\mathbf{x})$. Requiring local gauge invariance in the SM Lagrangian imposes a symmetry requirement on the fields. The gauge boson fields arise as a direct result of this requirement.

The SM combines the field theories for Quantum Electrodynamics (QED), the charged and neutral current Weak interactions, the Yukawa coupling between the Higgs and the SM fermions, and the interactions governed by Quantum Chromodynamics (QCD) all under the $SU(3)_C \times SU(2)_L \times U(1)_Y$ gauge symmetry.[5] The first three field theories (QED, Weak, Yukawa) are unified under $SU(2)_L \times U(1)_Y$. The Yukawa coupling is what gives rise to the fermion masses from their interactions with the Higgs field after *spontaneous electroweak symmetry breaking*, which is discussed in §2.1.1. $SU(3)_C$ governs all of the QCD interactions discussed in §2.1.2.

2.1.1 Electroweak Theory

Electroweak (EW) field theory, also known as Glashow-Weinberg-Salam (GWS) theory, is described by requiring gauge invariance in $SU(2)_L \times U(1)_Y$. The subscript L indicates coupling of the Weak force to the left-handed fermions. The subscript Y indicates the generator of the $U(1)$ group and is the weak hypercharge related to the electric charge q and weak isospin I_3 by $Y = 2(q - I_3)$. This quantity is conserved in the GWS theory. *Up*-type fermions have $I_3 = +1/2$, while *down*-type fermions have $I_3 = -1/2$.

Four massless gauge fields arise from requiring gauge invariance in $SU(2)_L \times U(1)_Y$. The

[5] $SU(N)$ refers to a 'special unitary' symmetry group of dimension N.

four fields are denoted A^i, where $i = \{1, 2, 3\}$, and B^0.[6] The SM force mediating bosons γ, Z, and $W^{\pm}$ are derived from mixing these four fields as shown in equation 2.1.

$$\begin{aligned} W^{\pm} &= \frac{1}{\sqrt{2}}(A^1 \mp iA^2) \\ Z^0 &= \cos(\theta_w)A^3 - \sin(\theta_w)B^0 \\ \gamma &= \sin(\theta_w)A^3 + \cos(\theta_w)B^0 \end{aligned} \tag{2.1}$$

where θ_w is a parameter called the *weak mixing angle*. Upon interaction between the A^i and B^0 boson fields with a complex Higgs doublet composed of two scalar Higgs fields, three of the four fields have their symmetry broken to produce massive particles Z and $W^{\pm}$, while one remains massless, producing the photon (γ). The mass of the Z and $W^{\pm}$ bosons (and, consequently, the γ having no mass) comes from *spontaneous electroweak symmetry breaking* after the Higgs field attains a non-zero vacuum expectation value. A remaining degree of freedom from the Higgs doublet transformation yields the massive, scalar Higgs boson in the SM. This process of spontaneously breaking the symmetry of the gauge fields in $SU(2)_L \times U(1)_Y$ in order for the Z and $W^{\pm}$ to attain mass from the Higgs field is also known as the Brout-Englert-Higgs Mechanism (BEH) after three physicists who first proposed it in 1964 [15, 16].

Interactions Quarks and leptons both interact with the EW fields via their left-handed *chiral* states. Under charge-parity (CP) transformation, the associated anti-fermions interact with the electroweak fields with their right-handed *chiral* states. Each generation of left-handed fermions forms an SU(2) weak-isospin doublet as shown in Table 2.1; so the left-handed up quark (u_L) and down quark (d_L) form a doublet that interacts under the weak force. Likewise, the left-handed electron-neutrino ($\nu_{e,L}$) and electron (e_L) form a doublet under the SU(2) group, and each subsequent generation follows suit. The right-handed chiral states for each fermion are SU(2) singlets and do not interact with the weak force.

Chirality has to do with the spin vector and momentum vector of the particle, and whether or not they are in the same direction. For massive particles, forced to travel below the speed of light, the chirality of a particle could flip if an observer is traveling faster than the particle. Anti-particles can be interpreted as particles traveling backwards through time. Right-handed anti-fermions forming doublets interact with the Weak force via the

[6] Note here that the A^i is chosen as the label for the fields, but they are commonly labeled W^i in the literature on this topic. This choice is made so as not to confuse with the $W^{\pm}$ bosons, arising after mixing.

same mechanism that left-handed fermions do. This chiral nature of massive fermions in the SM means that a direct mass term inserted into the SM Lagrangian would violate Lorentz invariance. Instead, the fermions in the SM get their mass from the Higgs mechanism.

generation	I	II	III
quarks	$\begin{pmatrix} u_L \\ d_L \end{pmatrix}$	$\begin{pmatrix} c_L \\ s_L \end{pmatrix}$	$\begin{pmatrix} t_L \\ b_L \end{pmatrix}$
leptons	$\begin{pmatrix} \nu_{e,L} \\ e_L \end{pmatrix}$	$\begin{pmatrix} \nu_{\mu,L} \\ \mu_L \end{pmatrix}$	$\begin{pmatrix} \nu_{\tau,L} \\ \tau_L \end{pmatrix}$

Table 2.1: Summary of the left-handed doublets for quarks and leptons that interact with the electroweak gauge fields. The generations of fermions in the SM are represented by I, II, III.

In the SM, the mass of neutrinos is predicted to be zero. However, experimental evidence of neutrino oscillations between flavor states implies that neutrinos are shown to have non-negligible, though small, mass [13, 17]. Due to the nature of neutrino interactions with matter being extremely rare, neutrinos are generally thought of as 'invisible' to most detectors, like those in ATLAS. In this analysis, neutrinos are treated as missing transverse energy. The multiple lepton final states searched for in this analysis do require neutrinos due to the fact that the Weak interaction (mostly via W exchanges) produces most of the leptons, and thus a certain amount of missing transverse energy is required by the search parameters in this analysis.

2.1.2 Quantum Chromodynamics

The strong force is governed by interactions between quarks and gluons in a quantum field theory called Quantum Chromodynamics (QCD). There are eight independent gauge fields (i.e. gluons) arising from the requirement of gauge symmetry on the $SU(3)_C$ gauge group. The subscript C indicated the *color* charge and is the generator of this gauge group. Of the fermions in the SM, only quarks interact with gluons under the $SU(3)_C$ gauge group because only quarks and gluons have a *color* charge. Color charge is simply another quantum number with three values, arbitrarily denoted as red, green, or blue. Both quarks and gluons possess color charge, though gluons possess one color and one anti-color charge. Anti-quarks possess one of the conjugates of each of the three colors: anti-red, anti-green, or anti-blue.

Gluons can self-interact due to possessing color charge as well, giving QCD a unique

property that, as two colored particles, say a $q\bar{q}$ pair, are pulled farther apart a constant force acts to keep them together. Beyond a certain distance, it becomes energetically favorable to create a $q\bar{q}$ pair from vacuum, which then ensures the original quarks are still bound in a colorless state. This phenomenon is called *color confinement*, which means colored particles cannot exist on their own, they must be bound in a colorless state (i.e. free particles are colorless). Baryons and mesons, collectively called hadrons, are such bound states. Baryons consist of three quarks, each of a different color, and mesons consist of two quarks, one with a color and another with anti-color, resulting in a colorless combination. Hadrons with more than three quarks have been observed in nature, for example, in the recent discovery of pentaquarks at LHCb, one of the experiments at the LHC [18]. Studying bound quark states could potentially reveal why the constituents of matter (protons and neutrons) have their observed structure.

The result of colliding hadrons together, as is done at the LHC, tends to produce a mess of quark and gluon byproducts. The resulting quarks and gluons recombine into baryons and mesons through a process known as *hadronization*, which is a consequence of *color confinement* as mentioned previously. Hadronization involves quarks combining with other quarks and gluons produced from a collision into hadrons. Quarks can also radiate gluons during an interaction producing more quarks or gluons to combine with others into hadrons. Hadrons with finite lifetimes decay further or interact with other particles and produce more quarks and gluons in a spray transverse to the collision point. Figure 2.3 shows a depiction from a simulated scatter event of what this could look like. The *hadronization* process from a particular quark or gluon originating from the hard scatter process inside the ATLAS detector produces a collimated spray of particles that results in an object called a *jet*. Jet identification and reconstruction in the detector are discussed more in §4.2.1.

Due to the complicated nature of QCD calculations, especially in the lower energy regime where the Strong interactions are intensely coupled, exact analytical calculations are untenable [19]. Perturbation theory is not valid in this regime since the coupling constants get very large. Non-perturbative techniques are needed to calculate the dynamics of these QCD interactions. Monte Carlo methods are often employed to solve the calculations numerically.

2.1.3 Parton Distribution Functions

A very important part of understanding proton-proton collisions at the LHC is understanding the dynamics of parton interactions. When a proton collides with another proton, the quantum field interactions taking place are between quarks and gluons inside the proton.

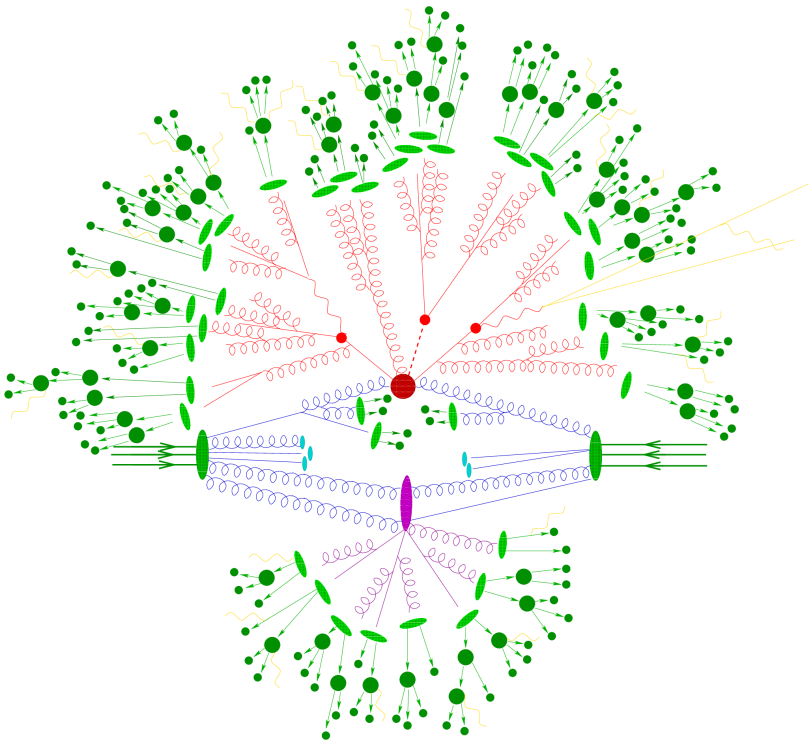

Figure 2.3: Visualization of hadronization process in a simulated event from a Monte Carlo generator [20]. The outer green blobs indicate hadrons, formed from partons (quarks and gluons). The constituents of the event that would be observable inside the detector would be hadronic decay products.

As already mentioned, protons are baryons made up of not only a trio of quarks (uud), called *valence* quarks, but also a *sea* of $q\overline{q}$ pairs and gluons, collectively called *sea* partons.

It is impossible to know *a priori* from QCD calculations what the fractional distribution of momentum allotted to each parton is with respect to the total momentum of the proton. In order to probe this structure, parton distribution functions (PDF) are derived through experimental measurements of deep inelastic scattering (DIS) between leptons and nucleons [21]. Figure 2.4 shows a depiction of DIS, where a lepton, typically an electron in experiments, probes the parton structure of a nucleon (a proton) with four-momentum $\mathbf{p}$. A parton with momentum fraction $x \cdot \mathbf{p}$, where x is the fraction of the total momentum $\mathbf{p}$ of the nucleon, interacts with the electron probe via electroweak interactions (this means the boson exchange particle in the diagram can be either γ, Z, or $W^{\pm}$). Thus, the nucleon structure depends on the energy scale of the probe.

Parton distribution functions are measured for different hard interaction energy scales

(Q^2)[7] using several collider experiments including ATLAS, CMS, and LHCb at the LHC. Some colliders have dedicated DIS experiments to measure PDF through fixed target experiments. The phase space coverage of these experiments can cover a large range in Q^2 and x. As the LHC continues to make precision measurements of electroweak gauge boson properties and QCD jet production, the PDF distributions are expected to become more refined for a wider kinematic range [23]. Figure 2.5 shows a couple examples of PDF for different values of Q^2. The *valence* quarks have the largest fraction of momentum. For *sea* partons the number density increases for smaller values of momentum fraction, x.

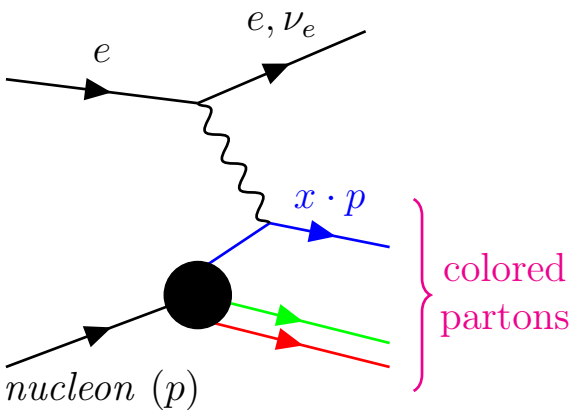

Figure 2.4: Diagram of deep inelastic scattering (DIS). Measurements of structure functions (*a.k.a.* parton distribution functions) are made by probing the nucleus with another particle, typically an electron. The colored lines represent the fact that the partons are colored particles.

2.2 Exotic Models Beyond the Standard Model

As mentioned previously, the SM does not give a complete picture of the interactions in nature. The gravitational force is not included in the SM, for example, nor is the nature of dark matter or dark energy. Instead the SM is considered to be an effective field theory valid for a lower energy regime (also, lower temperature regime). Low energy, in this context, simply means the highest energies capable of being probed with the collider experiments in

[7]The definition of the square of the energy scale of the hard interaction is $Q^2 \equiv -q^2$, where q is the momentum of the exchanged photon (or Z, $W^{\pm}$) in the interaction [22]. Q can also be related to the center of mass energy of the collision, $\sqrt{s}$, by the following: $Q^2 = x \cdot y \cdot s$, where the fraction of energy lost by the electron probe is given by y.

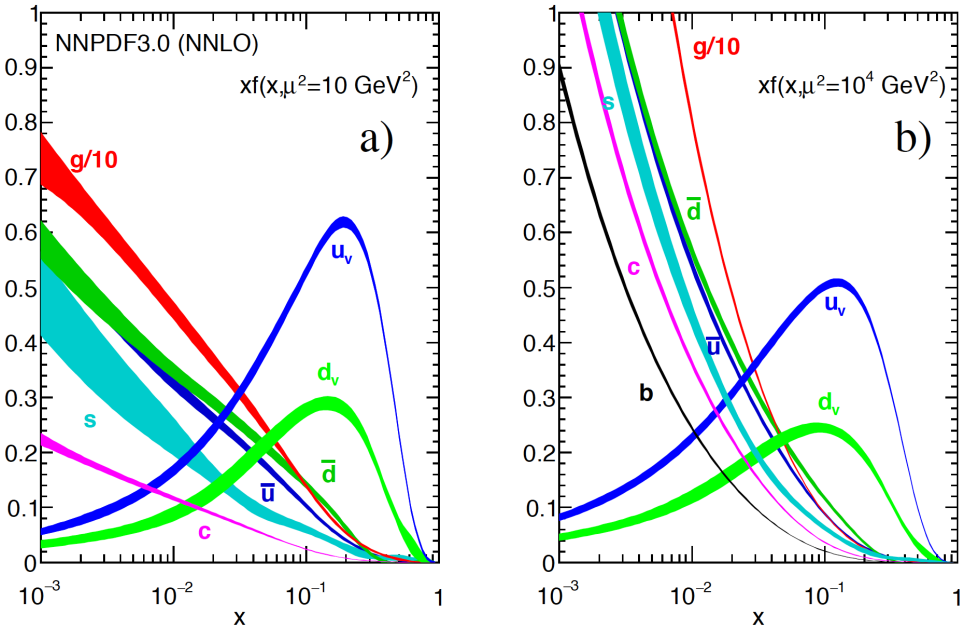

Figure 2.5: Example parton distribution functions as a function of x (fraction of energy) for two values of Q^2 [23]. The thickness of the bands represents the uncertainties on the distributions.

use today (i.e. TeV scale). Then the question is, does the SM hold up when extended to higher energy regimes?

Due to couplings with higher mass particles, like the top quark, the Higgs mass suffers from divergences arising from radiative corrections, which would tend to force the Higgs mass to be much larger than it is observed. Subsequently, the mass of the Higgs would require couplings to other massive particles in order to cancel out the apparent amount of fine-tuning needed at higher energy scales. Equation 2.2 shows the problem of fine-tuning for different SM energy scales, where Λ and μ represent the high and low order energy scales, respectively, and δm is a parameter dependent on these energy scales and on the couplings of the Higgs to other particles. The amount of fine-tuning necessary would depend on how high the energy scale is at which one expects to start finding new physics beyond the SM (i.e. where is Λ set). For example, *Grand Unification* theories, where gravity is unified with the other three forces, assume Λ is near the order of the Planck scale, $\sim 10^{19}$ GeV, which would imply enormous corrections in δm to get $m^2(\mu)$ anywhere close to $m^2(\Lambda)$ [19]. Fine-tuning on this scale presents a problem to the underlying theory and is often referred to as the

naturalness problem, or the hierarchy problem [24, 25].

$$m^2(\Lambda) = m^2(\mu) + \delta m^2 \tag{2.2}$$

Higher mass particles induce larger corrections to the Higgs mass because their coupling to the Higgs field is stronger. The top quark is the most massive particle in the SM and therefore demands the largest correction to account for the Higgs mass $m^2(\mu) = 125$ GeV and $m^2(\Lambda) \sim 10^{19}$ GeV. The SM by itself suffers from the hierarchy problem and therefore several physics models beyond the SM (BSM) have been proposed to solve the mass divergence issue. Theoretical and phenomenological proposals for addressing the hierarchy problem in a *natural* way invoke heavier particles at the TeV scale that partner with their SM counterparts to correct for the divergences.[8] Experiments at the LHC have been leading the search for evidence of these exotic models in the energy frontier.

Supersymmetry (SUSY) is an elegant model that proposes a solution for the hierarchy problem. SUSY proposes a *symmetrization* between the SM particles and heavier supersymmetric particles, such that each SM boson has a supersymmetric partner fermion, and vice versa. Each of these supersymmetric partners must share similar quantum numbers to their SM counterparts. SUSY particles are predicted to have larger masses in order to cancel out the divergent loop corrections to the Higgs mass.

SUSY extensions to the SM are not the only way of providing massive partners to the particles that contribute most to the Higgs mass divergences, however. Also, there has been no evidence of SUSY from data taken at the LHC so far, so other theories could still have merit. Other theories, most of which do not invoke SUSY,[9] derive the existence of heavy top and bottom partners, called Vector-like quarks (denoted in Feynman diagrams with Q). Typically, theories that include VLQ as a mechanism for solving the hierarchy problem are Little Higgs [29, 30] and composite Higgs [31, 32] models, which include a Higgs emerging as a pseudo–Nambu–Goldstone boson [33]. VLQ in these models generally couple to the SM 3$^{\text{rd}}$ generation quarks. This is because the SM 3$^{\text{rd}}$ generation quarks are the more massive quarks in the SM and couplings would follow an extended CKM matrix [34].

[8] The mass of the these partner particles must still be small enough, typically order 2-10 TeV, in order for the corrections to remain *natural*. Otherwise, other mechanisms may be needed to explain their large mass. *Naturalness* just means no further fine-tuning to account for.

[9] There are some SUSY models that do include heavy quarks, as reported in Ref [7, 26–28]. However, the description in this section is generalized and will not explicitly consider these models. Some of these models predict other branching decay modes, discussed in the next section, that are not explicitly considered in this analysis.

2.2.1 Vector-like Quarks

As discussed in 2.1.1, the SM quarks are chiral and they attain their mass through Yukawa couplings with the Higgs field. This coupling results in a measurable production cross section of the Higgs boson at the LHC. One method to solve the hierarchy problem is by introducing another generation of chiral quarks to the SM, which would mean an additional generation of quarks that attain their mass via Yukawa coupling. An additional generation of chiral quarks would increase the Higgs production cross section by roughly 9 times its observed value, however. Therefore, extensions to the SM with a fourth generation of chiral quarks have been ruled out because there has been no obvious observed enhancement to the Higgs production at this level.

Extensions to the SM that do not require this drastic of an enhanced to Higgs production often invoke non-chiral, spin-$\frac{1}{2}$ quarks called Vector-like Quarks [34]. "Vector-like" in the name refers to the fact that they do not have an axial weak interaction term in the Lagrangian (due to cancellation), only a vector term, unlike their SM counterparts. For chiral quarks (SM quarks), the Lagrangian contains projection operator terms that look like $(1 \pm \gamma^5)$, where the $+$ (right-handed) or $-$ (left-handed) depends on the chirality of the quark and the γ^5 is formed from the Dirac γ-matrices.[10] The vector and axial vector terms in the Lagrangian basically regulate how the weak force – specifically the W boson – interacts with the particle fields. VLQ left-handed and right-handed chiralities transform identically under the $SU(2)$ gauge group, and therefore interact weakly in the same way, so their axial vector term cancels.

The non-chiral symmetry for VLQ allows for an explicit mass term, of the form $M\overline{Q}Q$, to be inserted into the Lagrangian that does not violate the gauge symmetry of the theory. This implies VLQ do not receive their mass from the BEH mechanism like SM quarks. However, they can still couple to the Higgs and potentially provide a slight increase in Higgs production at the LHC. This coupling would happen through a term of the form in equation 2.3 [34, 36]. Here, Y_{QQ} is the Yukawa coupling between the VLQ (Q) and the Higgs boson.[11] This coupling depends on the mass of the Higgs and VLQ and the mixing angles between the VLQ and the SM third generation quarks. These mixing angles are constrained by precision

[10] For more on these terms and the Dirac matrices, see [35].

[11] Note that in ref. [34], Y_{QQ} depends only on the $\sin(\theta_{\mathrm{L/R}})$ mixing angles, and the mass ratio and coupling constant g are multiplied by Y_{QQ}. Here, Y_{QQ} encompasses all the coupling components: g, masses, and mixing angles.

electroweak tests to be small, on the order of 0.1.

$$\mathcal{L}_H = Y_{QQ}\overline{Q}QH \tag{2.3}$$

The dominant production mode of the Higgs at the LHC is $gg \to H$ via a quark loop, with the top quark occupying the loop as the primary mechanism for production. This quark loop also contributes to the decay width of $H \to \gamma\gamma$. VLQ can affect this cross section and decay width via replacing the top quark in the loop with VLQ via the term in equation 2.3. However, VLQ enhancements to Higgs production and decay in this manner are typically suppressed in minimal extension models because of the small mixing angles and because the coupling decreases with increasing mass of VLQ. An increase in the Higgs production via $gg \to H$ due to VLQ would be on the order of a few % (driven mostly by couplings with B), which is currently below the precision of the measurements at the LHC.

The VLQ masses are not predicted by the theories and remain open parameters, which are currently being constrained by data collected with ATLAS and CMS. In order for VLQ to provide a solution to the hierarchy problem, in most models their masses would need to be around the TeV scale. Because VLQ would be heavier than their SM counterparts, they are also generically referred to as *heavy quarks*.[12]

The VLQ considered in most searches can come in different varieties: two *up*-type heavy quarks, T and $T_{5/3}$, and two *down*-type heavy quarks, B and $B_{-4/3}$. The T and B have the same charges as t and b SM quarks, $\frac{2}{3}$ and $-\frac{1}{3}$, respectively. Two other varieties of VLQ have exotic charges: $T_{5/3}$, sometimes referred to as X, and $B_{-4/3}$, sometimes referred to as Y, where the subscript is the charge. VLQ models with couplings to SM quarks predict seven multiplets in the form of singlets, doublets, or triplets with these VLQ varieties under $SU(2)$, as shown in Table 2.2 [37]. Only the singlets are considered in this search. The practical difference between the multiplets is the branching fractions to their decay modes, discussed shortly.

Couplings of VLQ to SM particles have been shown to favor certain processes based on the stronger Yukawa couplings of the 3$^{\text{rd}}$ generation SM quarks [38]. Technically, the VLQ could mix with 1$^{\text{st}}$ or 2$^{\text{nd}}$ generation quarks through an extension of the CKM matrix, however, this is highly disfavored [39]. For the purposes of this analysis, VLQ are considered to couple preferentially to the 3$^{\text{rd}}$ generation quarks. VLQ couple to the SM bosons Z, H,

[12]Throughout this dissertation, the term 'heavy quark' is used to refer to VLQ. Quarks comprising the three generations in the Standard Model will be referred to by their generation (e.g. third generation quarks (t and b) are sometimes referred to heavy quarks in the literature, but are 3$^{\text{rd}}$ here).

	singlets		doublets			triplets	
Q_q	$T_{2/3}$	$B_{-1/3}$	$\begin{pmatrix} T_{5/3} \\ T_{2/3} \end{pmatrix}$	$\begin{pmatrix} T_{2/3} \\ B_{-1/3} \end{pmatrix}$	$\begin{pmatrix} B_{-1/3} \\ B_{-4/3} \end{pmatrix}$	$\begin{pmatrix} T_{5/3} \\ T_{2/3} \\ B_{-1/3} \end{pmatrix}$	$\begin{pmatrix} T_{2/3} \\ B_{-1/3} \\ B_{-4/3} \end{pmatrix}$

Table 2.2: Summary of the multiplets for VLQ with electric charge q. As noted in the text both left-handed and right-handed multiplets are valid here, since VLQ are non-chiral.

or W in these decay modes as well, such that a VLQ will decay to one of these bosons and a 3$^{\text{rd}}$ generation quark. Figure 2.6 shows a schematic of the possible decay modes. There are theoretical extensions to the SM predicting VLQ that include other interactions between VLQ and SM particles than the aforementioned ones. Such models could include VLQ decaying to other particles than the three modes shown in figure 2.6 [8]. These models are not assumed for the analysis presented here, however. The decay modes in figure 2.6 are well established in the context of the models assumed for this analysis and only three possible decay modes are assumed for T and B, while only one decay mode each is assumed for $T_{5/3}$ and $B_{-4/3}$. In general, if the VLQ exist as different multiplets they could have different branching ratios to their decay modes. In this analysis, the singlet form of VLQ is searched for with the branching ratios described in reference [40]. Branching ratios are also dependent on the mass of the VLQ, though with a mass above about 1 TeV the ratios vary little. Figure 2.7 shows the branching ratios for the singlet T and B decay modes. For $T_{5/3}$ ($B_{-4/3}$), the branching ratio is 100% to Wt (Wb), so is not shown in figure 2.7.

A primary production mechanism at the LHC for VLQ would be through QCD interactions, which is advantageous since the LHC is a hadron collider and QCD interactions are produced in abundance. VLQ can also be produced via electroweak interactions, though less frequently. If VLQ exist, they can produce an enhancement to the production cross sections of QCD and electroweak production at the LHC. Figure 2.8 shows a few diagrams for pair production modes of VLQ. Pair production of VLQ is primarily achieved through QCD interactions. Figure 2.9 shows a few diagrams for single production modes of VLQ.

Figure 2.10 shows the cross section versus mass curves for different multiplet models of VLQ. Single production becomes the dominant mode for higher VLQ masses, whereas pair production is dominant for lower masses. Pair production cross sections for VLQ are independent of the multiplet model assumption for the VLQ (so there is only one curve shown for pair production). The production modes this analysis is sensitive to are pair

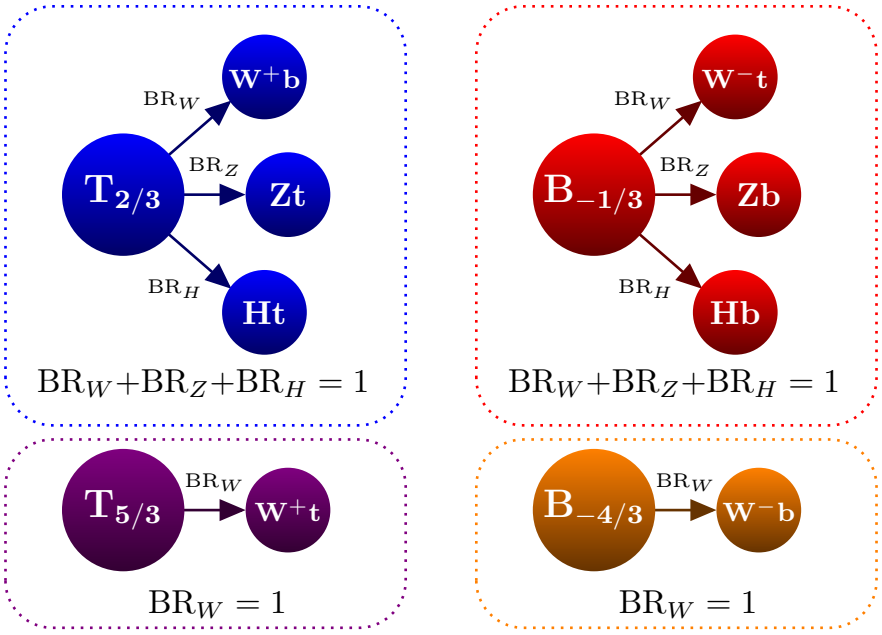

Figure 2.6: Representation of the decay modes for the various VLQ assuming only coupling to 3$^{\text{rd}}$ generation SM quarks. The same processes, but with charge conjugation where necessary, are assumed for the anti-particles of T, B, $T_{5/3}$, and $B_{-4/3}$.

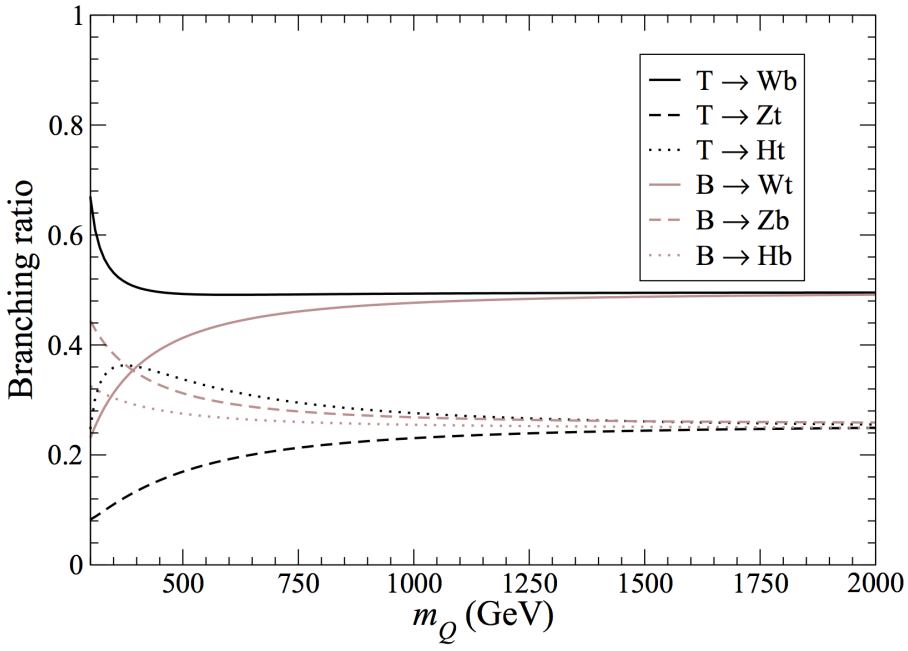

Figure 2.7: Branching ratios of VLQ varieties singlet T and B for the mass range $300-2000$ GeV [40]. Only singlet T and B VLQ are shown here.

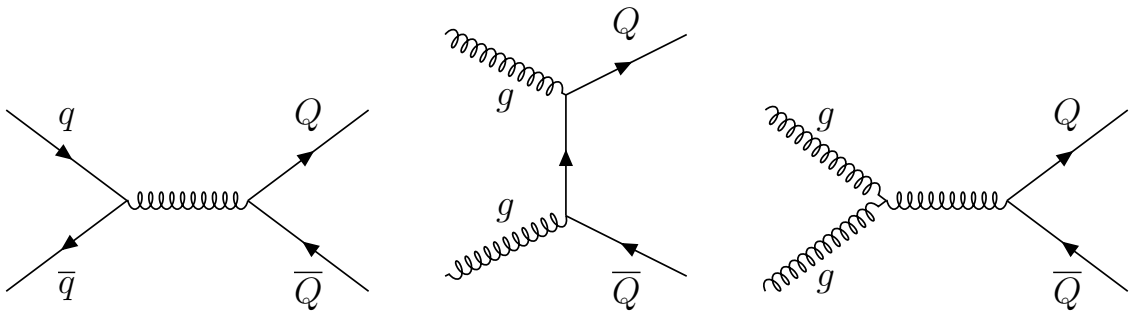

Figure 2.8: Dominant modes of pair production of VLQ from QCD processes. It should be noted that production from electroweak or scalar modes (exchange of a W, Z, or even H) could be possible, but these modes would depend on the model of the VLQ and would be suppressed by the QCD modes.

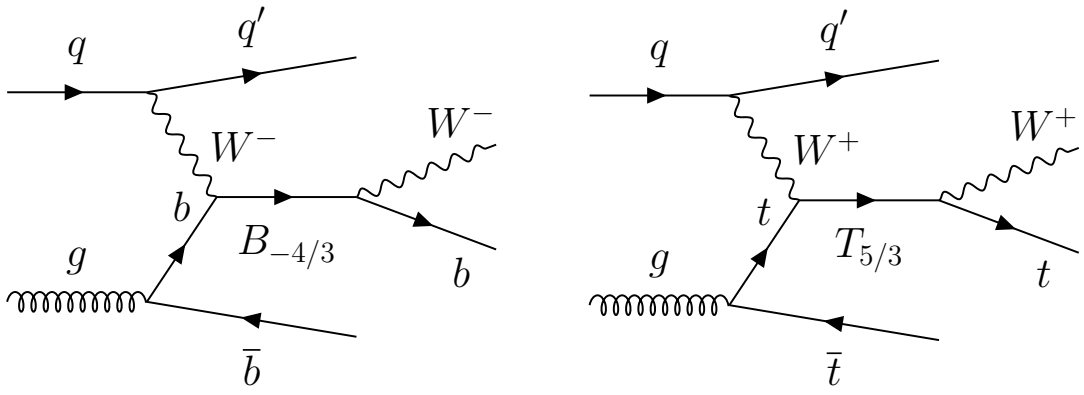

Figure 2.9: Single production of $B_{-4/3}$ (left) and $T_{5/3}$ (right). The primary decay modes for these quarks are 100% to the following: $B_{-4/3} \to W^-b$ and $T_{5/3} \to W^+t$. The same processes, but with charge conjugation where necessary, are assumed for the anti-particles of $B_{-4/3}$ and $T_{5/3}$.

production of T and B, and pair and single production of $T_{5/3}$ because only these modes can result in two leptons of the same charge (e.g. $T\overline{T} \to W^+bZt(\to W^+b) \to \ell^+\nu_\ell bq\overline{q}\ell^+\nu_\ell b$). Single production of T and B is unlikely to produce a pair of same-charge leptons in the final state, so those modes are not included in this analysis. Also, $B_{-4/3}$ cannot produce a pair of same charge leptons via pair or single production modes.

In the majority of cases, the same-charge leptons in the final state topology for this analysis come from multiple W boson decays, where at least two W must have the same charge and decay leptonically. In the case of $T_{5/3}$, there are always two same charge W from the decay, assuming 100% branching fraction $T_{5/3} \to Wt$. Both W must decay leptonically to have two same-charge leptons in the final state. For pair production of T and B, the

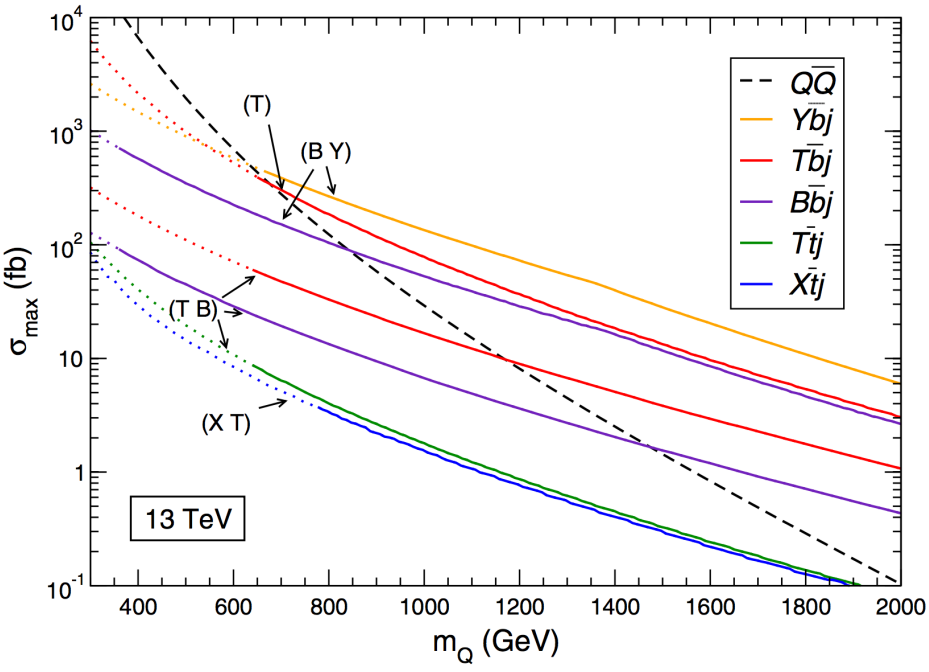

Figure 2.10: Production cross sections at $\sqrt{s} = 13$ TeV for different VLQ multiplets [34]. Pair production only has one line (dashed) because the only mechanism for pair production of VLQ is QCD, so only one cross section is calculated for each mass point. At higher VLQ masses the single production modes become dominant. In this plot X refers to $T_{5/3}$ and Y refers to $B_{-4/3}$. Different multiplet models for single production have different cross sections as shown in the colored curves.

final states can include many topologies with leptons coming mostly from W, Z, decaying leptonically, or H, decaying to τ leptons, which subsequently decay to electrons or muons.

LHC Searches for VLQ Previous searches with LHC pp collision data have so far not found significant evidence for the VLQ mentioned here. There have been a variety of searches looking for VLQ in different decay channels and with different final state signatures. Multi-lepton final state searches are generally favorable channels to look for VLQ since their multiple decay modes through charged and neutral currents can readily produce more than one lepton in the final state. Since the mass of the VLQ is not predicted by the theories, these searches set lower bounds on the mass of the VLQ to the 95% Confidence Level (CL). Previous lower limits from CMS and ATLAS searches on the mass of VLQ are summarized in Table 2.3. Upper limits on the cross sections are also set at the 95% CL, which can be found in the accompanying references. The early $\sqrt{s} = 13$ TeV dataset results for the search presented in this analysis can be found in reference [41]. Setting the limits on the mass and

cross sections for VLQ is discussed in more detail in Chapter 9.

$\sqrt{s}$ **[TeV]**	$\int \mathcal{L}dt$ **[fb^{-1}]**	**Observed limit (95%CL) [GeV]**	**Channel**	**Reference**
ATLAS limits				
7	1.04	$m_Q > 350$	$pp \to Q\overline{Q} + X \to qW^+\overline{q}W^-$, 2ℓ	[42]
7	4.7	$m_{t'} > 656$	$pp \to t'\overline{t'} + X \to bW^+\overline{b}W^-$, $1\ell + > 0b$	[43]
8	20.3	$m_{b'} > 720$	$pp \to b'\overline{b'} + X \to tW^-\overline{t}W^+$, $SS\ell\ell + > 0b$	[44]
8	20.3	$m_T > 655$, $m_B > 685$	$pp \to T\overline{T}(B\overline{B}) + X \to \ell^-\ell^+t(b) + X$, Z channel	[45]
13	3.2	$m_{T_{5/3}} > 990$, $m_{T_{\text{singlet}}} > 780$, $m_{B_{\text{singlet}}} > 830$	$pp \to \ell^\pm\ell^\pm$(or 3ℓ) $+ > 0b$	[41]
13	3.2	$m_{T_{\text{singlet}}} > 750$, $m_{T_{\text{doublet}}} > 800$	$pp \to T\overline{T}$ (singlet), ℓ+jets (boosted), $pp \to T\overline{T}$ (doublet), ℓ+jets (boosted)	[46]
13	36.1	$m_{T_{\text{singlet}}} > 1170$, $m_{B_{\text{singlet}}} > 1080$, $m_{T_{\text{doublet}}} > 1350$, $m_{B_{\text{doublet}}} > 1250$	$pp \to \ell$+jets (Wb and Wt channels)	[47]
13	36.1	$m_{T_{\text{singlet}}} > 870$, $m_{T_{\text{doublet}}} > 1050$	$pp \to \ell$, ≥ 4 jets (Zt channel)	[48]
CMS limits				
7	5.0	$m_{t'} > 557$	$pp \to t'\overline{t'} + X \to bW^+\overline{b}W^-$, $2\ell + 2b$	[49]
7	5.0	$m_{b'} > 675$	$pp \to b'\overline{b'} + X \to \ell$+jets, $\ell+$ jets	[50]
7	5.0	$m_{b',t'} > 685$	$pp \to \ell$+jets, combined	[51]
8	19.5	$m_T > 687 - 782$	$pp \to \geq 1\ell$	[52]
8	19.7	$m_T > 745$	$pp \to T\overline{T} \to Ht + X$, all had (boosted t)	[53]
13	2.3	$m_T > 750$	$pp \to T\overline{T}$, ℓ+jets	[54]
13	2.3	$m_T > 1000 - 1800$	$pp \to T$ (single production, Ht channel)	[55]
13	2.3	$m_{T_{5/3}} > 1400$	$pp \to T$ or $T_{5/3}$, ℓ+jets (single production)	[56]
13	2.6	$m_{T_{\text{singlet}}} > 860$, $m_{T_{\text{doublet}}} > 830$, $m_{B_{\text{singlet}}} > 730$	$pp \to T\overline{T}(B\overline{B}) \to \ell+$ jets (W or H channel)	[57]

Table 2.3: Summary of the various VLQ mass limits to date from CMS and ATLAS. Limit setting is described in more detail in Chapter 9. The accompanying references are public results for each analysis.

CHAPTER 3
Experimental Apparatus

In 2008, the Large Hadron Collider (LHC) superseded what was then the world's foremost particle accelerator in terms of energy, the Tevatron in Batavia, Illinois, United States. Located at the CERN research complex near Geneva, Switzerland, the LHC currently claims the mantle as the world's largest and most energetic particle accelerator. The design energy for each of the LHC's proton beams is 7 TeV, 7 times that of the beams used in the Tevatron, meaning the design center-of-mass energy is $\sqrt{s} = 14$ TeV. The LHC is based on synchrotron technology; it is designed to bring into collision two opposing beams of either protons or lead (Pb) ions,[1] accelerated in opposite directions, inside a closed-loop beam-line. The collisions occur between the constituents inside the protons, which are called quarks and gluons (collectively referred to as *partons*).

The spray of particles resulting from the collisions is collected by several large detectors located at specific points on the circumference of the LHC ring. The detectors are generally designed in a cylindrical manner surrounding the beam-pipe. In the case of ATLAS and CMS, the two general purpose physics detectors at the LHC, and ALICE, a dedicated physics experiment studying lead ion collisions, the collisions happen at the center of the detectors and the spray of particles is not biased in any one direction. In the case of LHCb, which is designed to study b-quark physics, the collisions are biased in one direction to better measure the production of B-hadrons, which are identified by a distinct displacement from the collision point.

In this chapter, the properties and operational structure of the LHC are briefly outlined followed by an explanation of the experimental apparatus, ATLAS, which is used to collect data for this analysis. Since there is more than one experiment at the LHC, section 3.1 briefly describes all the experiments and their primary scientific priorities. Section 3.2 discusses the properties of ATLAS and its detector subsystems.

[1] For the search presented here, only proton-proton collision data are used.

3.1 The Large Hadron Collider

The LHC ring sits about 100 m under the France-Swiss border where its main synchrotron ring, about 27 km in circumference, is positioned to collide particles. Part of the tunnel and facilities left over from the Large Electron Positron (LEP) collider, which collided electrons and positrons from 1989−2000 in an effort to better understand electroweak interactions is used for the LHC tunnel. Two beams of protons are accelerated through multiple smaller booster synchrotrons before being injected into the main LHC ring and brought into collision at four points along the circumference of the ring. Hereafter, the collisions of these beams are referred to as 'pp collisions' or 'pp interactions.' Figure 3.1 shows an overview schematic of the LHC, its various experiments, the interaction points, and the booster rings. There are four primary experiments located at four interaction points (IP) along the circumference of the large ring. The experiments are called ATLAS, CMS, LHCb, and ALICE. Each carries out independent and complementary physics research using the data collected from the colliding beams. There are also three smaller experiments, TOTEM, LHCf, and MoEDAL, which share the IPs with CMS, ATLAS, and LHCb, respectively.

3.1.1 The Experiments

There are two general purpose physics experiments at the LHC: CMS (Compact Muon Solenoid) located at IP 5 and ATLAS (A Toroidal LHC ApparatuS) located at IP 1. Both have unique designs for detecting the different types of Standard Model particles and their decay products as well as measuring particles' energies and momenta. Since the discovery of the Higgs Boson in 2012 [3], there are two main goals for these experiments:

(1) Searching for new physics beyond the Standard Model

(2) Making precision measurements of processes from known Standard Model physics

Goal (2) facilitates goal (1) by providing precise measurements of decay widths, lifetimes, cross sections, and other properties of particles known to exist already. For example, precision measurements of the cross section of pp interactions producing a Higgs boson are needed so that a comparison of expected production rates can be made to check if there is new physics providing an enhancement to Higgs production. The work presented in this dissertation is one of many searches under the broad umbrella of goal (1).

The other two main physics experiments are ALICE (A Large Ion Collider Experiment) and LHCb (LHC Beauty). IP 2 is where ALICE is located. Its primary purpose is to study

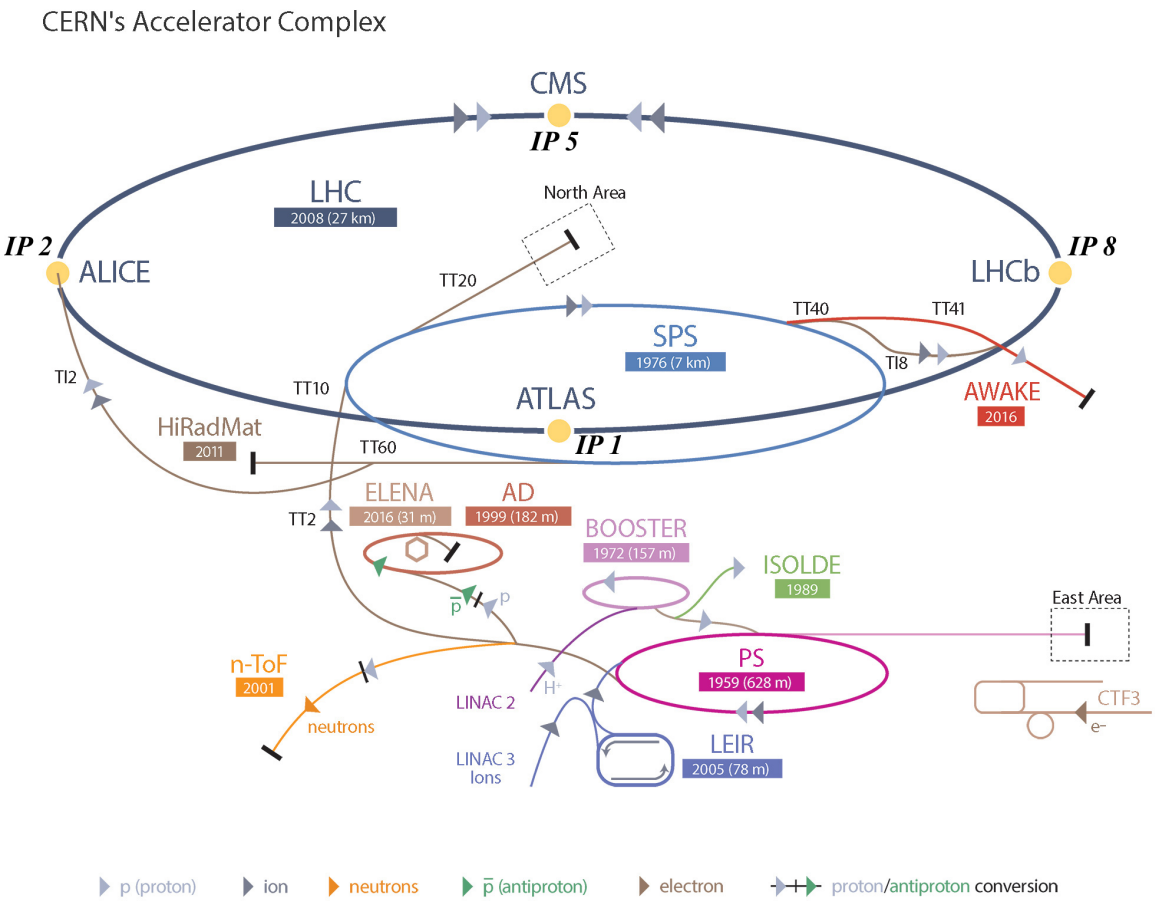

Figure 3.1: The CERN accelerator complex and the main physics experiments and different levels of the synchrotron booster rings used to accelerate or remove protons [58].

quark confinement and hot, dense quark-gluon plasma using Pb ion collisions [59]. Quark-gluon plasma is theorized to be the state of quarks and gluons in the very early universe. IP 8 is where LHCb is located. This experiment aims to study the physics resulting from b-quark and $\bar{b}$-quark decays in an effort to understand why the universe is dominated by matter rather than anti-matter [60].

Lastly, there are three smaller experiments at the LHC. The TOTEM experiment is located in the forward regions of CMS and its main goal is to measure the total pp collision cross section accurately [61]. This is an extremely important measurement for reconstructing the physics in a collision. TOTEM also aims to study events in the very forward region of CMS (close to the beam-line) to better understand the production of high energy cosmic rays. Similarly, in the forward region of ATLAS, the LHCf experiment makes measurements of neutral pions in an effort to better understand ultra-high energy cosmic rays [62]. LHCf

also provides information about photon (γ) and neutral pion (π^0) forward production and leading particle spectra.

MoEDAL is a newer LHC experiment designed to search for exotic physics in a complementary way to ATLAS and CMS searches by utilizing a unique detector design tailored for slower, massive exotic particles [63]. It is located at IP 8 along with LHCb. The existence of a magnetic monopole and other ionizing stable massive particles has been suggested in many BSM theories, and the MoEDAL experiment aims to detect them by using a passive technique, where the massive particle leaves a physical deformation in the plastic detectors of MoEDAL. This allows for the detection of particles that move much slower ($\frac{v}{c} \ll 1$) than the typical particle resulting from *pp* collisions, without the need for the fast trigger systems, discussed in § 3.2.4, of the main experiments.

3.1.2 LHC Magnets

The LHC is designed to maintain two proton beams in precise circular orbits while they are accelerated to their final energy of 7 TeV each, and then focused down to collide with each other at the four main IPs. These two steps are achieved with powerful superconducting magnets wound with Niobium-Titanium (Nb-Ti) cables. There are 1232 dipole magnets for bending the beams into their orbits, 392 quadrupole magnets for focusing the beams, and several higher-order magnets. The higher-order magnets (e.g. sextupole, octupole, decapole) are used at certain points along the ring for orbital corrections of the beams where the dipole fields deviate. These higher order magnets are also used for diverting the beams to safely "dump" where the beams disperse and their energy is absorbed by concrete and graphite composite after each data-taking run or when a magnet is undergoing a quench.[2] The magnets are cooled to ∼1.9 K using super-fluid helium, which allows for the production of very high magnetic fields (between 8 and 9 T, or about 10^5 times that of Earth's magnetic field).

The LHC would have to be physically much larger, to get the same design beam energy, were the magnets not superconducting magnets. This is illustrated in equation 3.1, which shows the radius of curvature of a particle with charge q, momentum p_{T} (where the subscript T here means the particle's velocity is transverse to the magnetic field), inside a magnetic

[2] In 2008, the LHC suffered from a magnet quench incident that resulted in several magnets being severely damaged and shut down the accelerator for a year while the magnets were repaired. As a result of this, the LHC has not yet achieved its design $\sqrt{s}$ = 14 TeV. By 2010, the LHC was successfully taking data at $\sqrt{s}$ = 7 TeV, and then in 2012, at $\sqrt{s}$ = 8 TeV. The data presented in this analysis were collected during LHC runs from 2015 to 2016 at $\sqrt{s}$ = 13 TeV (each proton beam therefore had 6.5 TeV of energy).

field of strength B. For a non-superconducting magnet, the B-field would have a smaller upper limit and therefore, to achieve the same beam energy, R would need to be higher (not to mention the issues with needing many more higher-order magnets along the beam-line to ensure the beam stays in its correct path).

$$R = \frac{p_{\mathrm{T}}}{qB} \tag{3.1}$$

3.1.3 LHC Injection Chain

Figure 3.1 shows the main boosters and injection chain of the LHC [64]. Protons come from stripping hydrogen gas (H_2) atoms of their electrons. This process involves injecting the gas into a Duoplasmatron cylinder surrounded by an electric field. Electrons from a cathode filament in the Duoplasmatron strip the electrons off the atoms in the gas. The resulting hydrogen ions (protons) are then accelerated to 90 keV before entering the radio frequency (RF) quadrupole. From there, they are accelerated further and injected into the LINAC2 (linear accelerator). The LINAC2 feeds the protons into a 4-ring synchrotron called the Proton Synchrotron Booster (PSB) and, after accelerating even further, the protons enter the Proton Synchrotron (PS) where they are bunched into 25 ns spacings using RF cavities. There are RF cavities in the synchrotrons as well as at point 4 of the LHC, between CMS and ALICE. They operate at a very low temperature of 4.5 K and high frequency of 400 MHz. They are designed so a proton at the center of the bunch will feel no acceleration after being brought up to its final energy, and the protons around the central one oscillate back and forth, accelerating and decelerating, staying in a close bunch to the central proton. Upon injection into the main LHC ring, the protons have 450 MeV of energy and the bunches consist of approximately 10^{11} protons. There are 2808 bunches per beam at full design luminosity. Bunches circumnavigate the ring several times, accelerated by the RF cavities, to reach their peak energy before being collided. Each bunch measures approximately 7.5 cm in length and 1 mm in diameter before they are focused down by the quadrupole magnets to a diameter of 16µm at the interaction points. During normal data-taking conditions, the beams circulate for several hours after they reach their maximum energy.

3.2 ATLAS

This section describes the ATLAS detector [65–67] as it operates in the current run (Run II, data collection from 2015−2018). Appendix A describes the changes to ATLAS due to

the upgrade work in the post-Run II operation of the LHC, when the luminosity will be at least twice design luminosity and the center-of-mass energy may be increased to 14 TeV.

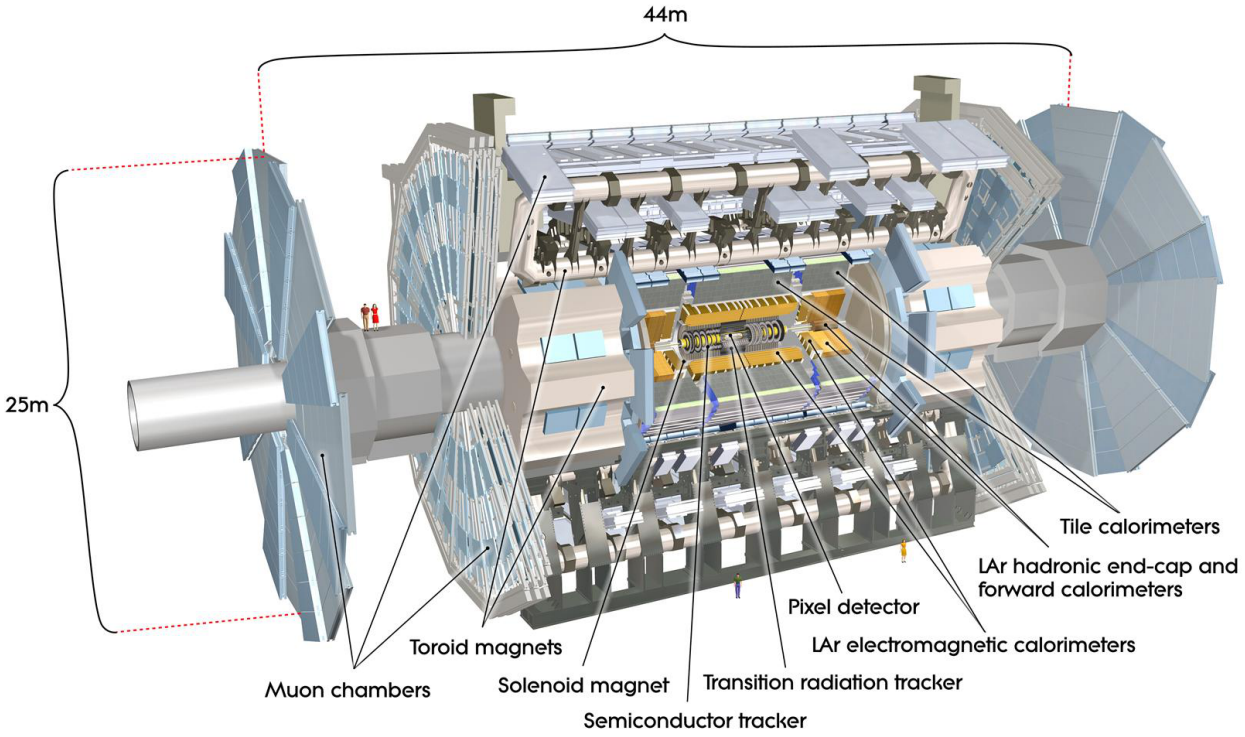

Figure 3.2: ATLAS experiment with key detector systems and magnet systems labeled [58]. The outer layers colored in shades of blue and gray constitute the Muon Spectrometer. The inner regions colored in gold and gray constitute the calorimeter systems. Inside the calorimeters lies the inner tracking detectors. The toroidal and solenoidal magnet systems are also labeled.

Figure 3.2 shows ATLAS and some of its main systems. ATLAS is physically the largest of the LHC experiments at approximately 44 m in length and 25 m in diameter. It weighs approximately 7 thousand metric tons. There are several cylindrical layers of detector systems and magnets surrounding the beam-pipe, which is the experiment's axis of symmetry. Each detector is designed for a specific purpose, whether to track charged particles, to measure particle energy, or to trigger on specific particles. A section of ATLAS is removed in figure 3.2 to reveal the inner detector and calorimeter layers. The barrel region consists of the parts of ATLAS parallel to the beam-pipe, while the end-cap regions enclose the barrel region on either side perpendicular to the beam axis. Together, these regions cover the majority of the solid angle surrounding the proton IP at the center of ATLAS, with as few gaps between detectors as possible. There is a region where the transition between the barrel calorimeters

and the end-cap detectors creates a small crack where, for electrons in this region especially, reconstruction is very inefficient. Particle reconstruction is discussed more in Chapter 4

The coordinate system for locating particles in ATLAS is right-handed with the origin at the IP. The z-axis points along the beam-pipe towards IP 8, the x-axis points towards the center of the LHC ring, and the y-axis points towards the ground surface (upward). The half of ATLAS on the $+z$ side of the IP is called side A and the half on the $-z$ side is called side C.

Of course, due to the cylindrical nature of the apparatus, cartesian coordinates (x, y, z) are typically not used to identify particle tracks. Instead, a particle's trajectory is determined by using the azimuthal angle, ϕ, pseudorapidity, η, and a transverse measure of either its momentum (p_{T}) or energy (E_{T}), depending on the particle. The quantity η is related to the polar angle between the particle's trajectory and the beam axis, θ, by equation 3.2. The closer a particle is to the beam-pipe, on either side of the IP, the larger value of $|\eta|$, diverging to infinity along the beam axis. The *forward* region of ATLAS is typically classified as $|\eta| > 2.5$. The *central* region of ATLAS is typically classified as $|\eta| \leq 2.5$.

$$\eta = -\ln\left[\tan\left(\frac{\theta}{2}\right)\right] \tag{3.2}$$

If two particles producing tracks in the detectors have angular coordinates (η_1, ϕ_1) and (η_2, ϕ_2), then the angular separation between the two tracks is $\Delta R \equiv \sqrt{(\eta_2 - \eta_1)^2 + (\phi_2 - \phi_1)^2}$. These coordinates are used because the differences, $\Delta\eta \equiv \eta_2 - \eta_1$ and $\Delta\phi \equiv \phi_2 - \phi_1$, are invariant under Lorentz transformation from a boost along the beam axis. A plot of particle occupancy vs η will be relatively flat, so pseudorapidity is convenient for visualizing the angular distribution of particles in an event, as opposed to using the polar angle θ. In the limit of ultra-high relativistic speeds or when the mass of the particle is negligible, $\eta \approx y$, where y is the rapidity and given by Equation 3.3

$$y = \frac{1}{2}\ln\left(\frac{\mathrm{E} + p_{\mathrm{z}}}{\mathrm{E} - p_{\mathrm{z}}}\right) \tag{3.3}$$

Here, E is the particle's energy and p_{z} is the particle's momentum component along the beam axis. Typically, y is more difficult to use for practical purposes in collider experiments since measurements of both E and p_{z} are required. Equation 3.2, however, clearly shows the pseudorapidity only relies on the measure of the polar angle, θ.

ATLAS is comprised of three major subsystems: the Inner Detector (ID), two calorimeters, and the Muon Spectrometer (MS). The ID surrounds the interaction point and provides the primary tracking capability of charged particles. It covers the central region. The two

calorimeters, electromagnetic and hadronic, are used to measure energy of particle showers and occupy the concentric layers just outside the ID, covering $|\eta| < 4.9$. The MS occupies the outermost regions of ATLAS in the barrel and in the end-caps. This space is shared by the toroidal magnet system, which facilitates the measurement of muon transverse momentum (p_{T}). The ATLAS magnet system consists of two main superconducting magnet parts [68]. The barrel toroid and end-cap toroids each provide a 4 T magnetic field tangent to the beam axis. The central solenoid, outside the Inner Detector (ID), provides a magnetic field of about 2 T that points along the beam axis in the central tracking region.

3.2.1 The Inner Detector

There are three main components to the inner tracking system: Silicon Pixel Tracker, Semiconductor Tracker (SCT), and Transition Radiation Tracker (TRT). Each are layered in concentric barrel layers or identical end-cap discs layered in the $\pm z$ direction. Figure 3.3 shows a cut-away of the Inner Detector (ID) system of ATLAS.

Located at the innermost detection region of the ID is the Pixel Tracker. There are over 80 million active silicon pixel channels in the Pixel Tracker, with a nominal pixel size of 50 µm × 400 µm [69]. The square surface area coverage for both barrel and end-caps is roughly 1.7 m^2. This pixel density is needed for extremely high precision tracking of charged particles in the highest particle density area of ATLAS, around the interaction point. Precision impact parameter measurements and vertex reconstruction of charged particle tracks are among the most important factors during reconstruction, and rely heavily on the Pixel Tracker's design.

As of 2014, after Run I data collection, the closest layer of the Pixel Tracker to the IP was augmented with a new, higher precision Insertable B-Layer (IBL) sitting between the first B-layer and a new smaller-diameter beam-pipe [70]. The primary purpose of the IBL is to provide better tracking resolution for charged particles in the highest radiation environment inside ATLAS, preparing ATLAS for the HL-LHC after the Phase-I upgrade in 2019−2020, where the luminosity is expected to increase to at least 5 times design luminosity. The B-layer prior to the installation of the IBL was expected to be efficient only up to about double the design luminosity ($\mathcal{L} = 10^{34}\ \mathrm{cm}^{-2}\,\mathrm{s}^{-1}$). Improvements to vertex reconstruction, impact parameter measurements, and b-tagging (discussed in § 4.2) are provided by the IBL. The IBL includes approximately 6.02 million pixels. It uses FE-14 130 nm CMOS readout chips for faster signal processing and CO_2 cooling staves to cool the electronics in the high radiation environment.

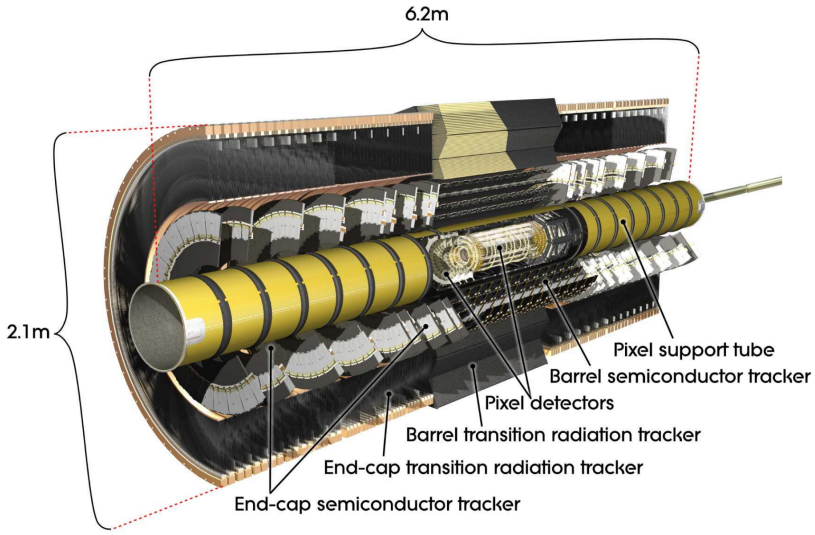

(a) ATLAS Inner Detector

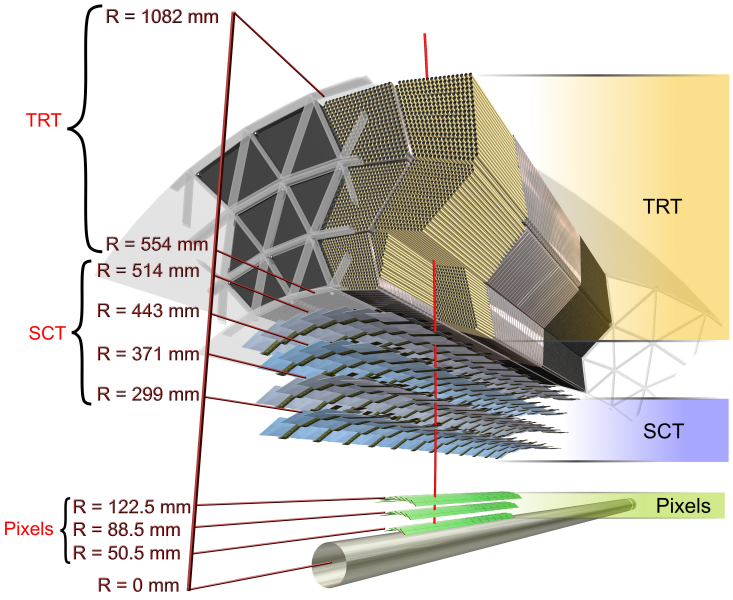

(b) Inner Detector layers

Figure 3.3: Innermost regions of ATLAS responsible for tracking of charged particles [58].

The SCT is the next set of concentric layers outside the pixel detector layers [71]. In total there are 4088 silicon-strip modules in the SCT, including barrel and end-cap detectors, covering an area of roughly 61 m^2. The SCT has about 6.3 million readout channels of

electronics capable of measuring a particle's track with a resolution of about 17 µm in the direction transverse to the strips. The strips have a pitch of 80 µm. Over 99% of the channels have remained operational since commissioning the SCT with about 99.9% data acquisition efficiency [72].

Outside the SCT is the TRT, where a different kind of detector is used instead of silicon pixels or strips. The TRT consists of 52,544 densely packed gaseous drift tube detectors in the barrel and 245,760 tubes in the end-cap regions [73]. Each tube is equipped with 31 µm diameter gold-plated tungsten wire. Surrounding the wire is a region of Xe-CO_2-O_2 gaseous mixture. The TRT is designed to track particles via ionization in the gas, with tracking resolution of ∼170 µm, and provides coverage up to the solenoid layer located just outside the ID. It is designed to differentiate between electrons and pions by distinguishing the gas ionization signature from the anode wires and by using the region between the tubes, filled with polymer fibers or foils, to create transition radiation sensitive to electrons [74]. Lastly, a fast level-2 trigger is also provided by this layer of the ID, as well. The level-2 trigger is discussed more in § 3.2.4.

The Central Solenoid The central solenoid of ATLAS is a superconducting magnet that provides a 2 T magnetic field in the ID region for spectrometry of charged particles. A particles' momentum and charge can be measured by knowing the magnetic field and measuring the radius of curvature, as shown in equation 3.1. Typically, particles do not encircle the magnetic field lines completely, rather small but measurable deviations from a particle's linear trajectory from the interaction point can be determined from multiple hits in the layers of the ID and its curvature in the magnetic field. The solenoid is cylindrical and measures roughly 5.3 m in length with an inner diameter of about 2.4 m. It is made of high-strength aluminum stabilizing NbTi/Cu superconducting cables. To generate the 2 T magnetic field, the current through the solenoid is roughly 7,600 A during normal operation [75].

3.2.2 ATLAS Calorimeters

The ATLAS calorimeter system is designed to collect the energy deposited by particles as they pass through several layers of material. Most particles (e.g. hadrons, photons, electrons) deposit the majority or all of their energy in the calorimeter systems. Precision energy measurements, enabled by the unique calorimeter designs, are important elements in the reconstruction of the collisions. Notable exceptions are muons and neutrinos. Muons typically pass unimpeded through the calorimeters and are detected in the Muon Spectrometer (MS),

discussed in the next section. Neutrinos rarely interact with any of the detector systems and are only revealed in aggregate as "missing energy," after reconstruction. The physical size of the calorimeters is balanced not only with the monetary cost of adding more dense material, but with the reconstruction cost of high energy 'punch-through' events, which tends to reduce the efficacy of missing energy and jet reconstruction. Particle identification and reconstruction is discussed more in § 4.2. The total ATLAS calorimeter coverage extends to $|\eta| \sim 4.9$.

Calorimeter Shower Development Shower shape and structure, resulting from particle interactions with matter, depend on the type and energy of the incoming particle and the material with which the incoming particle is interacting. There are two main types of showers in ATLAS: electromagnetic showers and hadronic showers. The first is typically reconstructed in the electromagnetic (EM) calorimeter, which is the layer just outside of the inner tracking detector and the central solenoid. Hadronic showers, on the other hand, typically develop inside the hadronic TileCal calorimeter, situated just outside the EM calorimeter. Notably, hadronic showers are more complex and can contain their own EM shower components, since electrons and photons can radiate from the particles typically involved in a hadronic shower.

EM showers are initiated by an electron or photon and develop through *bremsstrahlung* radiation and electron-positron pair production. The development of the shower and how many *radiation lengths* it lasts depends on how much initial energy the particle has. A *radiation length* is the mean distance over which a high-energy particle, like an electron, will lose $1/e$, or ∼37%, of its energy due to *bremsstrahlung* in a material. It depends on the material atomic number and mass number. Once the initial energy is reduced in the shower to below a critical level, the number of particles produced in the shower drops drastically and eventually all energy from the incoming particle is absorbed into the material. EM showers are typically compact and well-collimated, leaving a unique signature very distinct from hadronic showers.

Hadronic showers, in contrast to the relatively simple structure of EM showers, can have multiple components due to inelastic hadronic interactions. Typically, EM showers are a component of hadronic showers, especially when π^0 mesons form and decay into two photons. Photons from de-excitation of atomic nuclei can also initiate EM showers if the energy is high enough. An incoming particle initiating a hadronic shower in the hadronic calorimeter will lose energy by exciting the atoms inside the material or breaking up atomic nuclei, causing a cascade of multiple hadron collisions. Some hadrons created in the shower break apart other nuclei, if the energy is high enough, or decay into other particles, some of

which may be neutrinos. Neutrinos are invisible to the detector, so the energy from these particles essentially leaves the detector and remains undetected. Analogous to the radiation length used in EM showers, the *nuclear interaction length* is a measure of the mean free path of a hadron. The *nuclear interaction length* also depends on the atomic number and density of the material, and is typically much larger than the radiation length for a given material. This is because, in general, more material is needed to stop a high-energy hadron than for an electron or photon at the same energy. This is also why, in ATLAS, the hadronic calorimeter is larger than the EM calorimeter.

Two types of calorimeters are used in the ATLAS calorimetry system: (1) liquid argon (LAr) interleaved with a dense absorber material and (2) the Hadronic Tile Calorimeter (TileCal) with scintillators instead of LAr as the active region. Each is designed to differentiate between electromagnetic showers, which are initiated by electrons and photons, and hadronic showers, which are initiated by protons, pions, neutrons, and other massive or composite particles.

LAr Calorimeters Liquid argon, cooled to ∼90 K, is used as the active region to sample the incoming particle's shower at various points through ionization of the liquid. It is also radiation hard, so primarily used in the forward regions and the barrel regions of the EM calorimeters, where the particle flux is highest. Electrical signals are generated on the roughly 180,000 readout channels and registered by the calorimeter front-end electronics. LAr regions are sandwiched between absorber regions composed of copper or tungsten for the forward (FCAL), or lead or stainless steel for the electromagnetic end-cap (EMEC), barrel (EMB), and hadronic end-cap (HEC) calorimeters. The absorber regions are used to absorb the energy of the incoming particle, inducing showering. FCAL, EMEC, EMB, and HEC are shown in Figure 3.4. Identical calorimeters exist for end-cap subsystems on both sides (A and C) of the IP of ATLAS.

The FCAL subsystem provides coverage from $3.1 < |\eta| < 4.9$, as close to the beam-pipe as possible to provide near hermetic coverage to the calorimeter region [76]. There are three cylindrical layers to the FCAL: FCAL1, FCAL2, and FCAL3. FCAL1 consists of a copper matrix module encasing 24,520 electrodes (total for both sides) oriented parallel to the beam-pipe. Each electrode consists of a central anode rod that is set to high voltage running along the axis of each electrode, surrounded by a tube casing set to ground. The casing and rod are separated by a 269 µm LAr gap with electric field around 1 kV/mm. FCAL1 is closest to the IP and is primarily designed for detecting EM showers. FCAL2 and FCAL3 layers are stationed further from the IP and primarily focused on hadronic shower

detection. FCAL2 and FCAL3 both consist of matrix modules of tungsten housing 20,400 and 16,448 electrodes, respectively. The LAr gaps in these layers are 376 µm for FCAL2, and 508 µm for FCAL3. The FCAL unique design is optimized, using the very thin LAr gaps for fast signal readout, for sampling particles in the very high particle rate environment of the forward region of ATLAS.

The EMB and EMEC subsystems consist of an accordion-like structural design with multiple layers of LAr gap regions, around 2 mm in width, interleaved with lead or stainless steel absorber regions [77, 78]. The accordion structure is used to ensure gap-free uniformity in ϕ. The EMB extends to $|\eta| < 1.475$ and is about 22 radiation lengths thick, while the EMEC extends the coverage with a wheel on each end-cap of ATLAS, covering $1.375 < |\eta| < 3.2$. Several layers to the EMB and EMEC of different granularities exist to ensure EM showers deposit a majority of their energy in the middle layer, reserving the terminal layers for collecting the shower tails. Fine granularity in each layer gives the calorimeter discrimination power between shower shapes, especially for photon (γ) detection since the inner tracker is unable to detect photons.

The HEC consists of two wheels with 5632 readout channels, located concentrically just outside the FCAL layers and covers the region $1.5 < |\eta| < 4.9$. For particle detection, the HEC consists of parallel-plate modules of copper absorber material and LAr gaps of approximately 2 mm as the active regions. The modules are oriented orthogonal to the beam-pipe and cover the full ϕ range. Primarily, the HEC assists the TileCal, discussed next, in reconstruction of hadronic showers and is physically deeper than the EM calorimeters, about 11 nuclear interaction lengths, to account for the difference in hadronic and EM shower characteristics.

Hadronic Tile Calorimeters Also shown in the barrel region in figure 3.4, located radially outside the inner LAr calorimeters, is the hadronic TileCal subsystem [79, 80]. The coverage for the TileCal is $|\eta| < 1.7$. This calorimeter consists of a central barrel layer and extended barrel layers on either side of the central layer, with plastic scintillating material interleaved with iron absorber material in the form of tiles. Scintillating tiles act as the active regions by emitting light when a particle passes through the material. The photons from the scintillation events travel to photomultiplier tubes and are read out via optical fibers. Compared to the EM calorimeters, the TileCal is physically much larger, about 7.4 nuclear interaction lengths (at $\eta = 0$). The depth allows for measurement of energy from hadronic showers, which tend to be longer in length and produce different shower shapes and characteristics than EM showers. The granularity of this calorimeter is coarser than that of

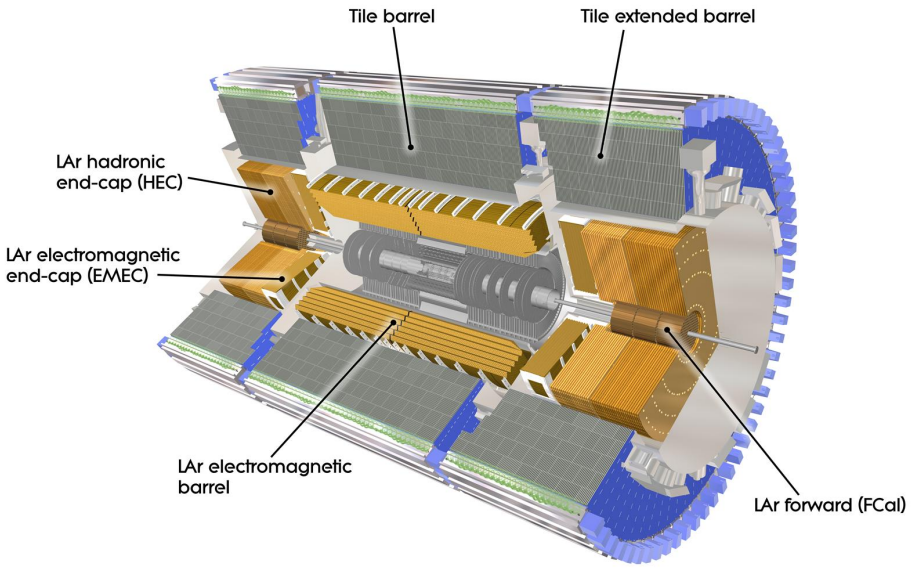

Figure 3.4: Calorimeter regions of ATLAS responsible for measurements of the energy of particles. The barrel region consists of both the LAr regions and TileCal regions [58].

the EM calorimeters, with $\Delta\eta \times \Delta\phi = 0.1 \times 0.1$ to $\Delta\eta \times \Delta\phi = 0.2 \times 0.1$ depending on the layer, but still fine enough to meet physics requirements for jet and $E_{\mathrm{T}}^{\mathrm{miss}}$ reconstruction, which is discussed in § 4.2.1. In total there are about 10,000 readout channels of electronics in the TileCal.

3.2.3 The Muon System

Muons typically lose very little energy traversing the distance from the interaction point to the outer layers of ATLAS and therefore go mostly undetected by the calorimeters. ATLAS is designed such that its outer layers can sample muon trajectories as they pass through most of the detector space. The Muon Spectrometer (MS) of ATLAS [81] consists of several gaseous drift detector systems layered in the barrel region and the end-caps to optimize the measurement of a muon's momentum. Its inner radius measures approximately 4.25 m from the axis, and its outer radius is the full radius of ATLAS at 12.5 m.

The MS is shown in Figure 3.5, with the ID and calorimeter systems removed to show the inner wheels. There are two end-cap detectors: Small Wheels and Big Wheels with Cathode Strip Chambers (CSC) and Monitored Drift Tubes (MDT) for precision tracking and Thin Gap Chambers (TGC) for Level-1 triggering in the Big Wheel end-caps. These detectors are layered in several trapezoidal wedge modules in ϕ to provide several tracking points along

the trajectory of a muon. In the barrel region of the MS, MDT detectors provide precision tracking in three concentric layers. Resistive Plate Chambers (RPC) provide the Level-1 triggering capability in the barrel MS. Level-1 triggering is discussed more in § 3.2.4. A toroidal magnetic field permeates the Muon Spectrometer's barrel region, which is vital for distinguishing muons and anti-muons by their curvature. In each end-cap, a toroidal end-cap magnet sits between the the Small Wheel region and the Big Wheel to measure muons in the forward region. The coverage of the wheels is $|\eta| < 2.7$. The MS barrel region covers $|\eta| < 1$.

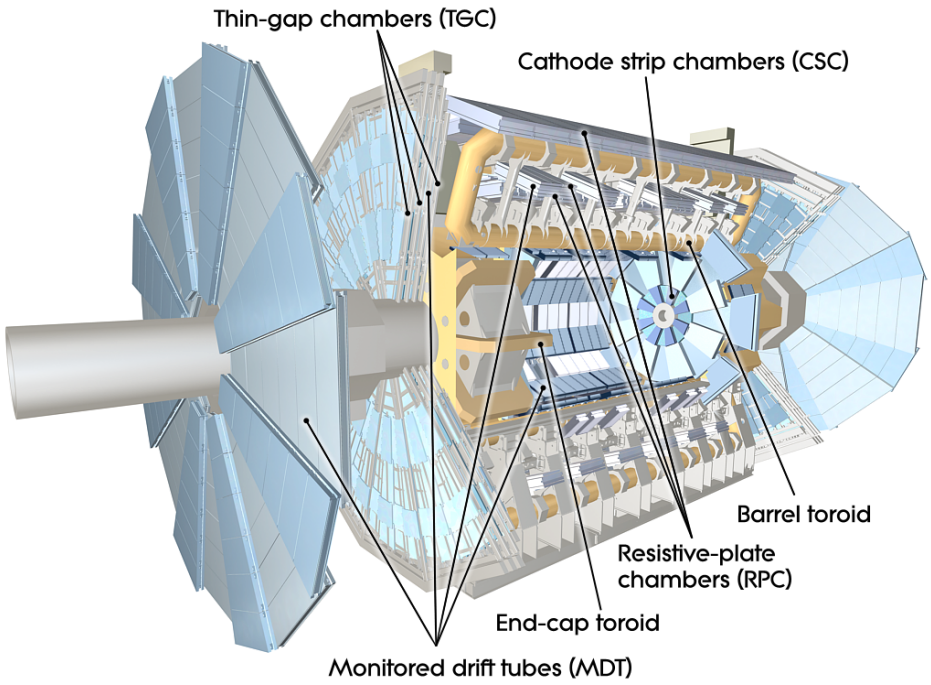

Figure 3.5: The Muon Spectrometer of ATLAS with key detector systems labeled. The inner trackers and calorimeter systems have been removed to show detail.

Small Wheels The Small Wheels (SW) of ATLAS lie at the innermost end-cap region of the Muon Spectrometer. The inner region of the SW, where the CSC are located, are oriented as a slight angle of approximately 11.6° from perpendicular relative to the beam axis. This design is used to optimize the detection of muons in the forward region.

In the current operation of ATLAS, the SW have three gaseous detector systems designed to detect muons. These are CSC, MDT, and TGC. The CSC detectors provide precision tracking in the Small Wheels in the $2.0 < |\eta| < 2.7$ region. CSC are multiwire proportional chambers with 48 readout strips in ϕ per wedge layer and 196 readout strips in η per wedge

layer. There are 16 chambers, 8 large and 8 small, with 4 layers per chamber for separate measurements in η and ϕ, per side of ATLAS. In the rest of the SW, there is a layer of TGC detectors and several layers of MDT detectors. The TGC primary function in the SW is to augment the azimuthal tracking of muons by the MDT. In the Big Wheels, TGC are used primarily for triggering, but the Level-1 triggering capability in the end-caps is restricted to the Big Wheel TGC chambers in the current run. In the upgrade to the SW taking place between Run II and Run III of the LHC, this trigger functionality will be included in the SW. The MDT detectors in the SW are primarily used for precision tracking, in addition to the CSC chambers, and provide $1.3 < |\eta| < 2.4$ coverage.

Part of the work presented in this dissertation is focused on the Phase-I upgrade of the Small Wheels of ATLAS during the 2019−2020 Long Shutdown 2. This upgrade is proposed to mitigate the limitations of the current detector systems due to increasing the luminosity, as well as to provide a secondary point in the Level-1 trigger capability for the end-cap Muon Spectrometers. The end-cap regions see a large particle flux and it is therefore very important to have detector systems in this region capable of handling high particle hit rates. As the operational luminosity is increased for the LHC, the particle rates in these regions will greatly increase. The CSC chambers can handle a particle hit rate of up to around 1 kHz/cm^2 for a luminosity of $\mathcal{L} = 1 \times 10^{34}$ cm^{-2} s^{-1}. The expected maximum hit rate for the post-Phase-I luminosity is expected to increase to about 15 kHz/cm^2, with luminosity expected to reach at least $2 - 3 \times 10^{34}$ cm^{-2} s^{-1}. Technical details on the NSW upgrade can be found in reference [82]. Testing for a demonstrator version of the front-end electronics for the new detector system to replace the CSC chambers is discussed in more detail in Appendix A. Several phases of testing, and iterations of the front-end electronics design, are expected before the final production design is built and tested for use with the full system.

3.2.4 ATLAS Trigger and Data Acquisition (TDAQ)

Given the design instantaneous luminosity of the LHC and the design bunch crossing rate of 25 ns, the average number of collisions per bunch crossing is about 25 in Run II. The initial interaction rate is around 1 GHz. ATLAS and all its computing resources do not have the capability to save every single event at this rate. Therefore, a sophisticated Trigger and Data Acquisition (TDAQ) system is used to collect and save the interactions that are interesting for the physics analyses.

The layered structure of the detectors in ATLAS is designed to optimize identification of particles based on their interactions with the materials in the detectors. Several detectors in

ATLAS are specifically designed to operate in the triggering system; for example, the TGC detectors in the MS end-cap regions. Once a particle's position and energy (or momentum) are registered by the detector readout channels, an electrical response is sent to the on-chamber electronics. These boards then shape the signals, digitize the hit information, and send the particle identifiers (e.g. charge, time of hit, location, etc.) from a large number of readout channels through electronics to the first level of the trigger system. Minimum thresholds for p_{T} or E_{T} of the particle must be met in order for the trigger rate to be kept at a usable level during data acquisition. For Run II, this trigger rate is on the order of 1 kHz.

Figure 3.6 shows an overview of the TDAQ system of ATLAS. There are two levels to the trigger system: Level-1 (L1) and the Event Filter (EF). The L1 trigger uses minimal information from the calorimeters, muon detectors, and the tracking system in order to quickly identify interesting events. L1 consists of the L1 calorimeter system (L1Calo), L1 muon system (L1Muon), L1 topological trigger modules (L1Topo), and the Central Trigger Processor (CTP) [83]. The CTP is responsible for the final trigger decision in the L1 system. It handles the inputs from the other L1 trigger modules.

The bunch crossing rate constrains the L1 trigger response and processing rate, so it is largely based on custom hardware logic installed in the front-end electronics of the detector systems. Events are processed within 100 bunch crossings due to the electronic latency of 2.5 µs. The L1 trigger typically picks out events based on jet or b-jet activity, lepton (electron or muon) activity, or $E_{\mathrm{T}}^{\mathrm{miss}}$ by requiring a minimum threshold in transverse energy (E_{T}) or momentum (p_{T}). Lepton triggers are especially important for this analysis, and other exotic or BSM physics analyses, because leptons tend to appear in events less frequently than quark and gluon related activity (QCD). Events with leptons are also easier to reconstruct than QCD events because they result in a cleaner signal. The muon triggers require multiple hits from dedicated trigger detectors in the Muon Spectrometer, while the electron triggers require calorimeter energy deposit information. In order to pass L1, the trigger must consist of a large Region of Interest (RoI) identified with (η, ϕ) coordinates and potential object candidates with p_{T} greater than a specified threshold (more on this in § 4.2).

The Run II L1 triggering scheme was improved from the ATLAS trigger system in Run I in order to streamline the processing time and allow for an increase in the trigger acceptance rate to 100 kHz [84]. L1Calo was improved in Run II by adding better filtering and improved signal processing to the front-end electronics. L1Topo was added to the L1 scheme for Run II to accept events based on topological cluster information and to augment the L1 trigger system from the calorimeter by suppressing backgrounds. L1Muon was also improved

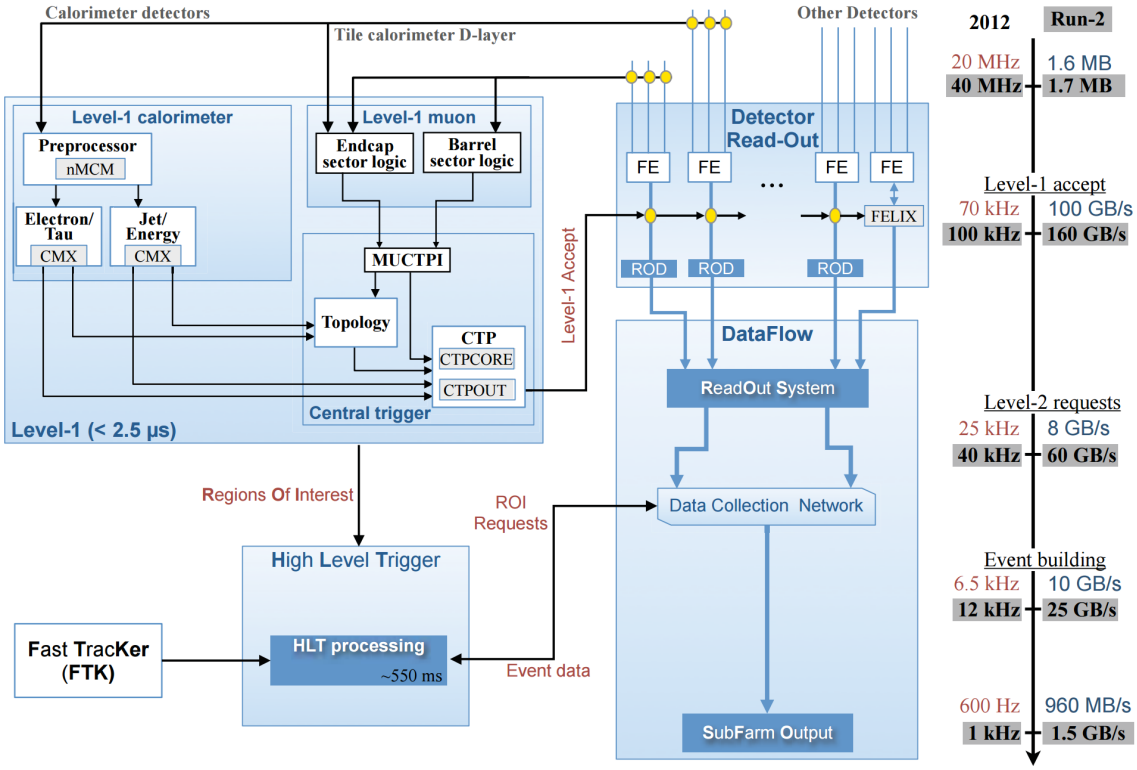

Figure 3.6: Data flow and event building in the ATLAS Trigger and Data Acquisition System [84].

upon by adding coincidence in front of the toroids in the end-caps and in the barrel. This was mainly included to help alleviate the high rate of fake muon triggers at L1. Further improvements to the muon triggering system are expected after the Phase-I upgrade when triggering capability will be added to the new Small Wheels to further reduce the fake muon incidences. More on the Phase-I upgrade effort is covered in Appendix A.

After the event rate has been reduced from 1 GHz to below 100 kHz at the L1 trigger, the events are transmitted to the Central Trigger Processor where the information awaits a decision based on multiple trigger selections. Events passing L1 are sent to the Readout Drivers (RODs) and Readout Buffers (ROBs) to await processing in the software-based EF trigger system.

The Run II High Level Trigger (HLT) is comprised of the Event Filter and Event Builder and is purely software based. Events passing the L1 conditions move on to the Event Builder, where the full event information is combined so the objects can be built using different parts of the detector (e.g. matching calorimeter candidates with tracks from the inner tracker for electrons). Several algorithms are used to make the final selection of events from the

information in the EF trigger step. The EF in Run II can handle a total output rate of $1 - 1.5$ kHz with a latency of a few seconds, which improves upon the several hundred Hz output from Run I. This improvement was made possible by streamlining and improving the HLT algorithms. Once the final decision for an event is made, it moves to ATLAS event storage. More information on the specific triggers and identification criteria for this analysis is discussed in the next chapter.

CHAPTER 4
Identifying Objects and Event Reconstruction

This chapter explains the identification and reconstruction of the objects produced from pp collision events. An object's characteristic signature is recorded as an digital response in the detectors' electronics and is combined with signals from other parts of ATLAS to identify the object. Event reconstruction is the process by which the objects resulting from a collision are identified from the electronic information and processed through algorithms to determine the energy and location of the particle. Objects with charge are matched to vertices and tracks in the Inner Detector (ID) with calorimeter clusters and other tracks in the barrel and end-cap detectors. Objects without charge (e.g. photons) do not have tracks in the ID, but can have a characteristic signature inside the calorimeters. The primary elements of an event are the following physics objects: singly identifiable particles (e.g. a muon), calorimeter clusters, groups of particles identified as single objects (e.g. a jet), missing energy ($E_{\mathrm{T}}^{\mathrm{miss}}$), and vertices (collision points). Due to running the LHC at higher luminosities, the increase in pile-up creates complications in the physics reconstruction since more vertices need to be reconstructed.

Each physics analysis, in general, uses certain working points determined from the Combined Performance (CP) groups in ATLAS for each physics object's definition and reconstruction p_{T} threshold. An analysis can choose a different working point if it is deemed more effective for that analysis in terms of optimizing significance, background rejection, or other reason. For the analysis presented here, the most important physics objects are jets, b-jets, leptons (i.e. electrons and muons), and missing transverse energy ($E_{\mathrm{T}}^{\mathrm{miss}}$). The working points used for these objects are discussed in the relevant sections for each object.

This chapter is organized as follows. Section 4.1 covers the reconstruction framework software, *Athena* and *AnalysisTop*. This section includes a brief discussion on the production of datasets from raw data to xAOD derivations, which are smaller datasets for offline data analysis. Section 4.2 provides an outline of the identification and reconstruction criteria of each object important to this analysis as well as the specific triggers used.

4.1 Reconstruction Framework

Event reconstruction is software-based within ATLAS. The framework is called *Athena* [85, 86], and the software release version used to reconstruct 2016 data is 20.7. This was updated from the 2015 analysis using version 20.1, and has been used to reprocess the 2015 data and Monte Carlo (MC) simulations (the set of all samples used is under the MC15c run of simulations). The specific data and Monte Carlo samples themselves are discussed in Chapter 6. *Athena* is a `C++` or `Python` based collection of code providing common tools and algorithms to be used in the analysis of ATLAS data.

Within the *Athena* framework several analysis framework packages exist, operating with the CP group recommendations. The framework packages include software tools to expedite particle reconstruction and identification. The package used in this analysis is called *AnalysisTop* [87]. The *Top Reconstruction* Group is responsible for the recommended working points in *AnalysisTop*, collectively referred to as *Top Common Objects*, as well as maintaining the base analysis software.

Figure 4.1 shows the data flow for reconstruction and the output data formats. The file size decreases with each step in order to optimize processing time. The size per raw event is about 1.6 MB. After processing through the TDAQ system, the size per event is about 100 kB in the primary event data model [88, 89]. The raw ByteStream data is processed through the Trigger and then converted to C++ objects in Raw Data Object (RDO) format to be processed by the reconstruction software. The output from reconstruction is Event Summary Data (ESD), Performance Ntuples (NTUP), and Analysis Object Data (xAOD). ESD and NTUP are used for re-reconstruction and reprocessing for calibration and detector performance studies. The xAOD is the Run II primary event data model used for physics analyses and is readable by both *Athena* and `ROOT` [90]. The xAOD samples are processed further through the Derivation Framework, producing *derivation xAOD* files (DxAOD) to reduce the file size and processing time by specifying only the objects and events of interest for an analysis framework, such as *AnalysisTop*. Table 4.1 shows the specific derivations used in the *Top Reconstruction* group. This analysis uses TOPQ1 derivations for both the data-driven background samples and the main analysis datasets and MC samples, discussed in Chapter 6. Finally, the derivations are run through a package of code with specific object and event criteria for the analysis. In this analysis, this package is called *SSbjetsTools*. The package outputs flat ntuples to be used in event processing with analysis specific `ROOT` scripts and plotting macros.

4.2 Object Identification

The objects reconstructed in an event represent the best estimate of the final state of the underlying collision process. Precision measurements of transverse energy and momentum of

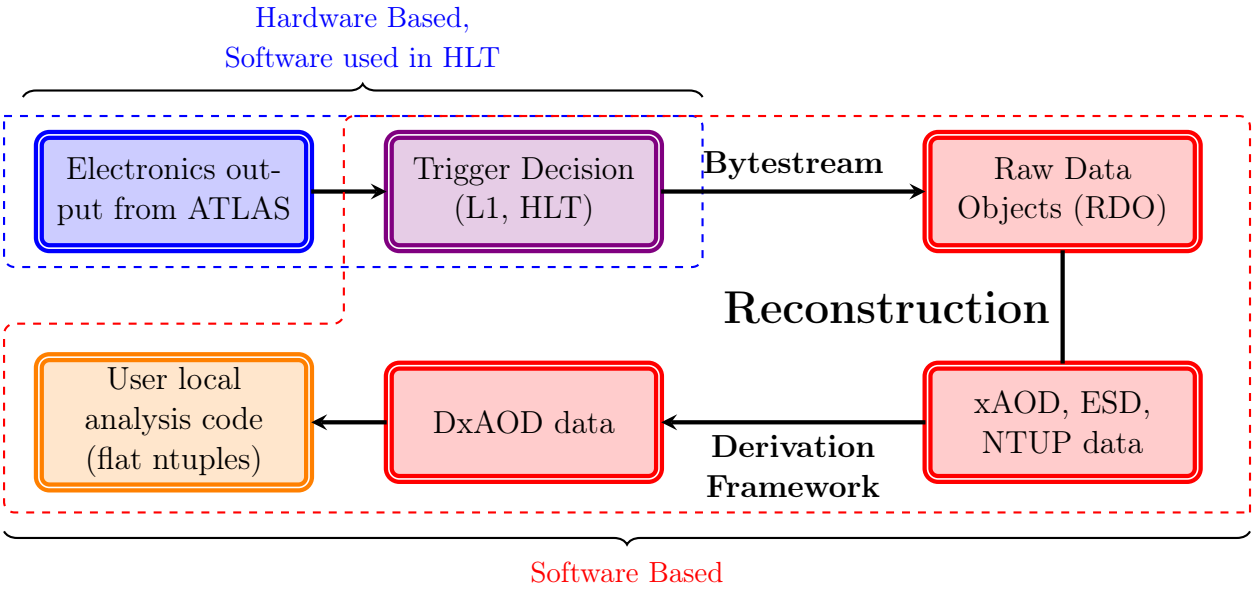

Figure 4.1: Data flow chart depicting the reconstruction process and resulting data formats. The dashed lines separate the hardware based readout from the software-based code. The software-based code is written in the *Athena* framework. The user local analysis code is the last step, which is written in basic `ROOT` and `Python` scripts, and uses the xAOD derivations of the samples as input.

Top Derivation	Event Selection
TOPQ1	$\geq$1 muon, $p_{\mathrm{T}} > 20$ GeV OR $\geq$1 electron, $p_{\mathrm{T}} > 20$ GeV
TOPQ2	$\geq$2 leptons, $p_{\mathrm{T}} > 15$ GeV OR $\geq$2 leptons, $p_{\mathrm{T}} > 10$ GeV AND $\geq$1 lepton with $p_{\mathrm{T}} > 20$ GeV
TOPQ3	$\geq$1 muon, $p_{\mathrm{T}} > 20$ GeV OR $\geq$1 electron, $p_{\mathrm{T}} > 20$ GeV AND $\geq$4 antiKt4 jets (or $\geq$1 largeR jet), $p_{\mathrm{T}} > 15$ GeV($p_{\mathrm{T}} > 200$ GeV)
TOPQ4	$\geq$5 antiKt4 jets, $p_{\mathrm{T}} > 20$ GeV AND at least on b-tag OR $\geq$1 largeR jet, $p_{\mathrm{T}} > 200$ GeV
TOPQ5	$\geq$1 muon, $p_{\mathrm{T}} > 20$ GeV OR $\geq$1 electron, $p_{\mathrm{T}} > 20$ GeV OR 2 additional muons, $2 < \mathrm{M}_{\mu\mu} < 4$ GeV

Table 4.1: Derivation definitions for *TopReconstruction* DxAODs. All leptons and jets in the above also have the additional criteria of $|\eta| < 2.5$. More on these derivations can be found on the twiki page in reference [91]

the objects in each event are made so they can be reconstructed back to the collision point. Objects are identified using track candidates, calorimeter clusters, and muon candidates. The parameters calculated from this process include primary and secondary vertices, transverse momentum (p_{T}), or transverse energy (E_{T}) from clusters in the case of calorimeter objects like electrons and photons, and the position coordinates (η, ϕ) for each object.

Tracks are reconstructed in two stages using several algorithms [92, 93]. The first stage uses seeds from the ID silicon pixel detectors and then extends into the TRT to identify tracks from the inner-most regions of the trackers to the outer regions. The second stage reverses this process and identifies TRT tracks before attempting to identify corresponding tracks in the silicon pixel detectors. Charged particles reconstructed from the main event must be matched to a full track with both silicon pixel and TRT hits. As recommended by the *Tracking Performance* group, quality track candidates must consist of at least 7 hits in the Silicon Pixel Detector, with no more than two holes in the silicon layers or no more than one hole in the pixel layers (a hole is simply a missing hit in the specified layer).

Vertices are reconstructed using at least two reconstructed tracks as seeds [92]. Using a χ^2 iterative fit method, tracks are matched to vertices. Tracks that are displaced by more than 7σ from a vertex are used to seed another vertex. The primary vertex in the event is identified as the vertex with the highest sum of squared transverse momenta of the tracks. In other words, the primary vertex represents the underlying hard-scatter process from which the majority of the transverse energy originates. For this analysis, events must contain a primary vertex with at least two tracks with $p_{\mathrm{T}} > 0.4$ GeVreconstructed to that vertex.

During pp collisions, several protons may interact simultaneously producing secondary vertices in roughly the same 25 ns (bunch crossing) time frame that the primary vertex is identified. This is known as in-time pile-up. Additionally, since collisions happen every 25 ns, pile-up events from preceding or subsequent bunch crossings can create secondary events that clutter the current event being reconstructed. The detector response does not have an instantaneous response time during reconstruction, and is thus sensitive to events immediately before and after the current event being reconstructed. This is out-of-time pile-up.

The amount of in-time pile-up is given by μ, a measure of the number of interactions per bunch crossing, and is dependent on the instantaneous luminosity $\mathcal{L}$, as shown in Equation 4.1 [94]. The value of μ is given by

$$\mu = \frac{\mathcal{L}\sigma_{\mathrm{in}}}{n_c f_{\mathrm{rev}}}, \tag{4.1}$$

where f_{rev} is the revolution frequency of the LHC, about 11.3 kHz [95]. The number of colliding bunch pairs in the LHC is given by n_c and σ_{in} is the inelastic cross section of the pp interactions. As the instantaneous luminosity increases, so too does the pile-up, which creates significant challenges for the event reconstruction process.

Objects that are eventually matched to tracks are identified with transverse (d_0) and longitudinal (z_0) track position parameters as shown in Figure 4.2. A Track-to-Vertex Association (TTVA) tool is used to formulate these variables and provide selection of tracks with respect to a vertex position. For use in this analysis, the relevant TTVA cuts for particles are covered in the next sections.

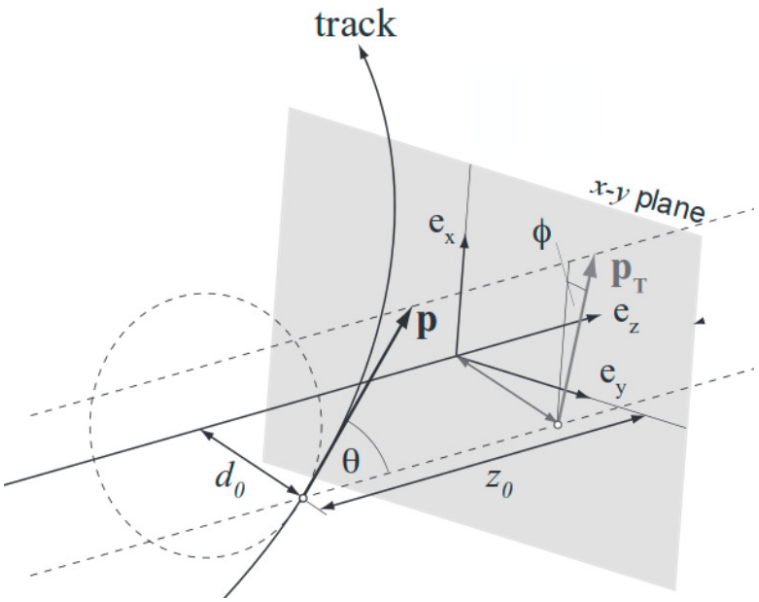

Figure 4.2: Track position parameters, d_0 and z_0, depicted with respect to the primary vertex [96]. The momentum of the particle is represented with $\mathbf{p}$.

4.2.1 Jet Identification and Reconstruction

Topological calorimeter clusters ('topo-clusters') in the ATLAS calorimeters are used for identifying and reconstructing jets [97, 98]. Jets are defined as cone-like objects consisting of multiple tracks and energy depositions, which are combined to form the clusters, resulting from hadron fragmentation of quark or gluon production in the original collision event. Calorimeter clusters are combined according to a particular algorithm resulting in an axis defining the jet's direction, and a cone around the axis defining jet's size. The cone encompasses the majority of the energy from the quark or gluon fragmentation and hadron formation process, which is known as hadronization [99]. Typically, the unique particles

and hadrons forming a jet are too close together to be reconstructed individually due to the limited resolution of the detectors. Thus, jets are generally treated as single objects.[1]

Jet *anti*-k_{T} Algorithm There are several algorithms that have been used historically to reconstruct jets at hadron colliders. The one used to reconstruct jets in this analysis is the anti-k_{T} algorithm [100, 101].[2] Other algorithms, like Cambridge-Aachen and k_{T} algorithms, may also be used in order to identify jets [102, 103]. All of these algorithms are classified as cluster or sequential recombination algorithms, which means they begin by clustering particles or groups of particles sequentially based on distance parameters. Equations 4.2 and 4.3 define the parameters for these algorithms. Parameter d_{ij} is the distance between particle i and particle j in the list of particles to be clustered, while d_i indicates the distance between particle i and the beam-line. If d_{ij} is the smaller of the two parameters, particle i is combined with particle j, sequentially, until d_i is the smallest parameter. Once d_i is smallest, i is defined as a jet and removed from the clustering list. The process continues until all remaining particles belong to a jet.

$$d_{ij} = \min(k_{\mathrm{T,i}}^{2\mathrm{n}}, k_{\mathrm{T,j}}^{2\mathrm{n}}) \frac{\Delta_{ij}^2}{R^2} \tag{4.2}$$

$$d_i = k_{\mathrm{T,i}}^{2\mathrm{n}} \tag{4.3}$$

The geometric distance is defined: $\Delta_{ij} \equiv \sqrt{(y_i - y_j)^2 + (\phi_i - \phi_j)^2}$, where y and ϕ are the rapidity and azimuthal angle of the particle, respectively. The parameter R defines the radius of the cone size for the jet, effectively determining the resolution with which two jets can be resolved. Typically, $R = 0.4$ in this analysis and in most analyses using so-called 'small radius' jets. The transverse momentum of particle i is represented by $k_{T,i}$. The parameter n defines the behavior of the algorithm with respect to the energy scale of the particles. For $n > 0$, the normal k_{T} algorithm behavior is observed,[3], which preferentially combines softer clusters together first.

[1] In some cases, such as larger radius ('large-R') jets, enough information can be gleaned to understand the 'substructure' of a jet and several variables can be defined to identify certain parts inside a jet. This can be useful in events with highly boosted jets, where two jets' cones can become collimated themselves. Large-R jets are not used in this analysis except for comparison studies.

[2] Note, it is convention in jet algorithms to use k_{T} for the transverse momentum of the jets (as opposed to p_{T}, used for other objects). This convention is adopted in this discussion of jet algorithms.

[3] As described in reference [100] behavior of the algorithms can be generalized for $n < 0$ ($n > 0$), however, the simplest case of $n = -1$ ($n = 1$) is typically used in the literature to describe anti-k_{T} (k_{T}) algorithm behavior. This analysis uses $n = -1$.

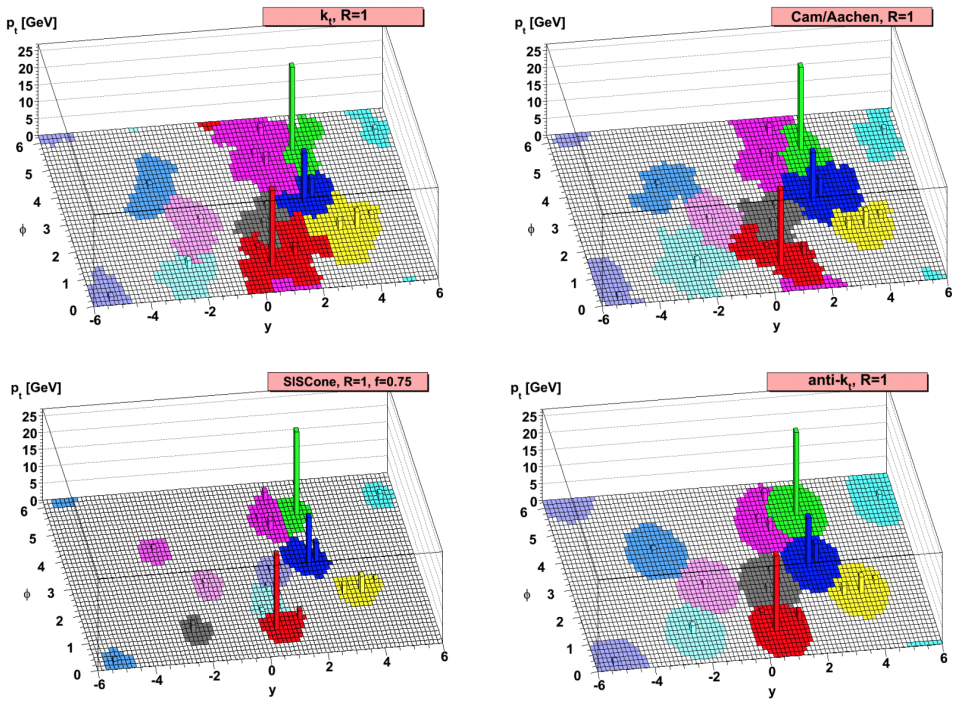

Figure 4.3: Results from simulated jet reconstruction with a large influence of soft terms using four different jet algorithms [100]. This same clusters are used for all four algorithms. The anti-k_T algorithm produces roughly circular jets in y-ϕ space due to clustering soft radiation around the hard radiation. The irregular shapes resulting from the other algorithms indicates a reconstruction process that is more sensitive to soft radiation particles. However, it should be noted that irregularly shaped jets are not necessarily wrong, just more difficult to calibrate. The SISCone plot is showing the resulting jets from a cone algorithm that is not classified as a sequential recombination algorithm. This algorithm is not used often so is not discussed here.

For $n = 0$, the special case of the Cambridge-Aachen algorithm is recovered and clustering effectively only depends on the geometric distance between particles. For $n < 0$, the anti-k_T algorithm behavior is observed, which has the effect of clustering harder radiation (high k_T) particles first and subsequently adding softer radiation particles. Anti-k_T clustering is therefore not as sensitive to fluctuations in the softer radiation, allowing the algorithm to build the jet around the axis defined by the high k_T clusters. An algorithm that produces jets that are not significantly altered in terms of composition or direction due to soft radiation in the calorimeter is called infrared (IR) safe. This is an ideal feature of algorithms like the anti-k_T algorithm. In the end, this tends to produce nicely shaped cone jets with well defined boundaries, which is beneficial for jet calibration and cleaning. Figure 4.3 shows an example of the difference in jet shape from a simulated jet reconstruction process using different jet algorithms.

Jet Quality Several factors can cause a jet to be mis-identified or faked. Tile and Liquid Argon calorimeter noise, beam induced background, and cosmic ray showers are all examples of backgrounds in the detector that can lead to fake jets. In order to select jets that are from the hard-scatter event, as opposed to these backgrounds, several jet quality selection criteria are defined [104]. For example, in order to discriminate good quality jets from fake jets due to calorimeter noise, a measure of the ionization signal shape quality (Q) can be quantified. Then, f_Q^{LAr} can be defined as the fraction of energy of a jet that has poor signal shape quality in the LAr calorimeter. f_Q^{HEC} is similarly defined for the hadronic calorimeter. Typically, good jets will have f_Q^{LAr} and f_Q^{HEC} close to 0. Values that deviate from 0 are jets which have a signal shape quality influenced by pile-up and calorimeter noise.

Another set of variables that can discriminate jet quality is the fraction of energy of a jet deposited inside the electromagnetic (f_{EM}) or hadronic (f_{HEC}) calorimeters, as well as the maximum energy fraction deposited in any single layer of the calorimeters. To discriminate good quality jets using track-based techniques, by making sure charged hadrons inside the jet can be traced back to tracks in the ID, the variable f_{Ch} is defined as the fraction of the scalar sum of the p_{T} of the tracks in the jet associated with the primary vertex in the event, to the total jet p_{T}. Figure 4.4 shows some of these discriminating variables. Fake jets tend to have f_{EM} clustered around 1 or around 0 for all ranges of f_Q^{LAr}. Fake jets also tend to have close to 0 or close to 1 values of f_{EM} with f_{Ch} close to 0. The quality of fake or real jets can be defined using these variables into the following categories: *BadLoose*, *BadTight*, *Loose*, and *Tight*.

Calibration A calibration process is performed on jets in order to ensure clusters are calibrated to the hadronic energy scale and to account for pile-up, leakage, dead material, and any other calorimeter inefficiencies [105]. This is important because jets make up a large fraction of the energy reconstructed in events and typically influence how well the underlying kinematics and uncertainties are understood. Several parameters influence the jet energy calibration procedure and are used to derive scale factors for Jet Energy Scale (JES) and Jet Energy Resolution (JER):

1. Pile-up subtraction using average transverse energy density, ρ, and the area of the jet, A, in the η - ϕ plane

2. Jet energy scale corrections via matching truth jets to reconstructed jets (simulation)

3. Detector biases in the η direction of the jet

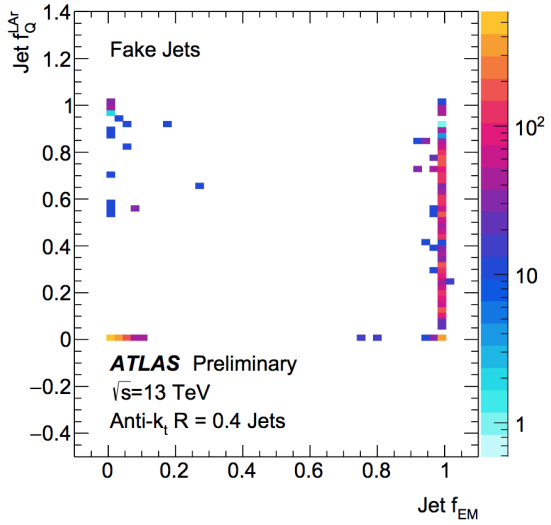

(a) f_Q^{LAr} vs. EM energy fraction for fake jets.

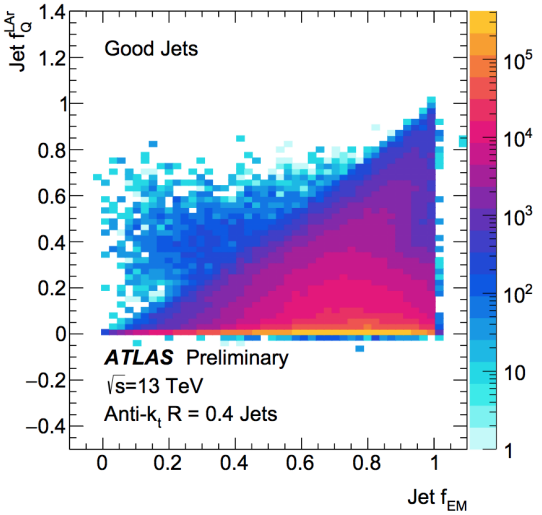

(b) f_Q^{LAr} vs. EM energy fraction for good jets.

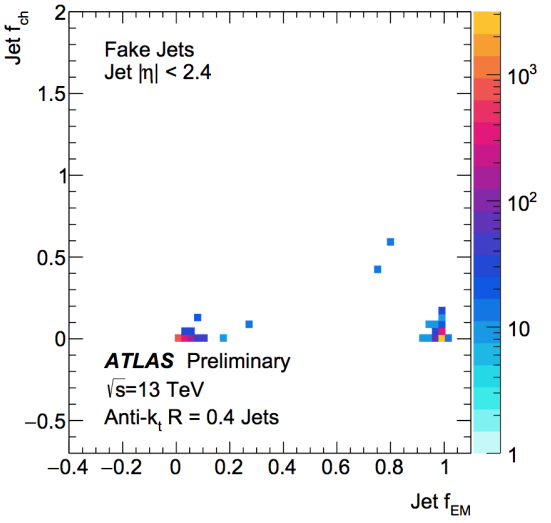

(c) f_{Ch} vs. EM energy fraction for fake jets.

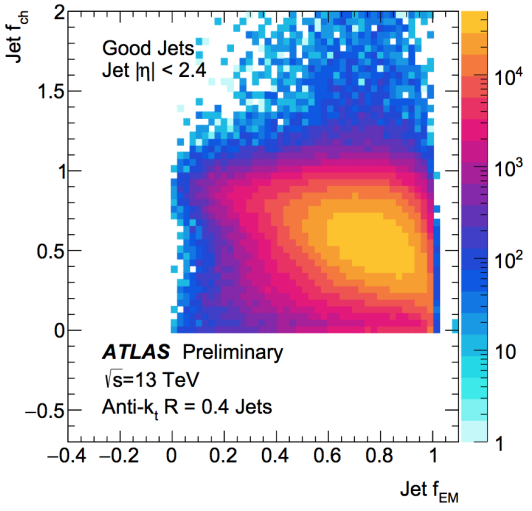

(d) f_{Ch} vs. EM energy fraction for good jets.

Figure 4.4: Distributions for fake and good quality jets using f_Q^{LAr}, f_{Ch}, and jet electromagnetic energy fraction f_{EM} [104]. The fake jets populate very specific regions in these plots (see text for details).

4. Reductions in the dependence of jet energy on transverse and longitudinal structure of the jet as well as on leakage, or jets that are not fully contained in the calorimeters

5. *In-situ* studies that provide corrections based on differences between data and MC simulations

Rejection of jets from pile-up effects involves combining a set of track-based factors from a

multivariate analysis into a final discriminant variable called Jet Vertex Tagger (JVT) [106]. The nominal recommendation is JVT > 0.59 for jets below 50 GeV and located in the region $|\eta| < 2.4$. This leads to an efficiency of 92% for hard-scattering jets, with 2% contamination from pile-up jets. Jets with $p_{\mathrm{T}} > 50$ GeVand $|\eta| > 2.4$ are accepted regardless of JVT. Figure 4.5 shows the JVT values for p_{T} range between 20 and 30 GeVused to distinguish pile-up (PU) jets from hard-scattering (HS) jets.

The correction factors resulting from the jet calibration procedure are applied as systematic uncertainties. The specific systematic uncertainties for jets in this analysis are discussed in Chapter 8. The jet collection used in this analysis is called `AntiKt4EMTopoJets` [107]. 'AntiKt' refers to the jet algorithm used, while the '4' refers to using $R = 0.4$ as the cone radius size of the reconstructed jets. 'EMTopo' refers to using topological clusters seeded from cells with high signal-to-noise energy deposits at the EM energy scale.

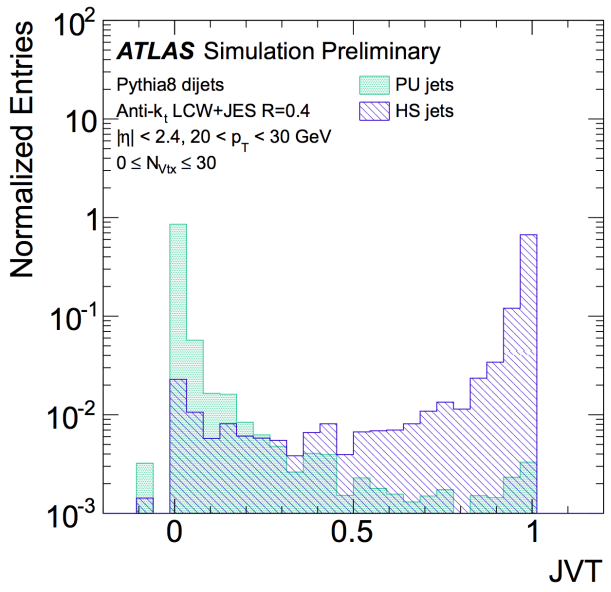

Figure 4.5: Distribution of JVT values for pile-up (PU) and hard-scattering (HS) jets for $20 <$ jet $p_{\mathrm{T}} < 30$ GeV [106].

4.2.2 *b*-Jets Identification and Reconstruction

Reconstructed jets can be further categorized by their flavor, or the original source of the jet: light-flavored jets (u, d, s, or gluon) or heavy-flavored jets (c and b).[4] A subset of jets important to this analysis is categorized as b-tagged jets (or simply, 'b-jets'), which are

[4]Hadronically decaying τ leptons also produce jets and can be identified or tagged as such.

jets that are identified as originating from B-hadrons (which contain b-quarks). Typically, a displaced vertex from the primary vertex can be measured, as shown in Figure 4.6. A secondary vertex results from the relatively longer lifetime of b-hadrons, which is on the order of 1.5 ps ($\approx$ 450 µm) [108]. Several other factors aid in the identification of b-jets, including relatively large jet mass (due to higher mass of the hadrons that contain b quarks) and the possibility of soft leptons within the jet cone due to occasional semi-leptonic decay of the B-hadron.

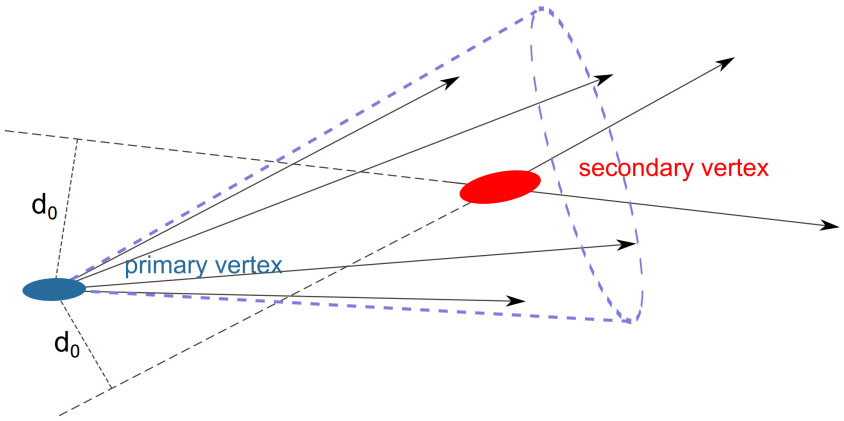

Figure 4.6: Diagram of the secondary vertex used to identify a b-Jet [109].

Since the installation of the Insertable B-layer in the ID of ATLAS (see §3.2.1), the b-tagging algorithms for Run II have been substantially improved due to enhanced track and impact parameter resolution [110]. Simulated events are used to train the multivariate algorithms used to identify b-jets and to perform studies on b-tagging efficiency. In simulated $t\bar{t}$ events, jets are matched to their corresponding flavor based on ΔR between the jet and the hadron. If no B-hadron is found within $\Delta R < 0.3$ of the jet axis, the algorithm looks for C-hadrons; if still no match is found, then it looks for hadronically decaying τ leptons. If the jet does not match up to these sources, it is labeled a light-flavored jet.

Several different algorithms employ varying techniques to identify b-jets. The algorithms primarily rely on impact parameters and secondary vertex metrics to define a likelihood that the jet belongs to a B-hadron. The results from these algorithms are combined into a multivariate Boosted Decision Tree (BDT) to define a single discriminant variable used to identify b-jets. The output of the BDT is a variable called MV2. Several working points are defined as different cuts on MV2 each with different mixtures of b-jets, c-jets, and light-flavored jets. The *Flavor Tagging* group in ATLAS defines the working points for a specified

b-jet identification efficiency to be utilized by physics analyses [111, 112]. Analysis teams are free to choose different b-tagging working points, depending on the sensitivity of their analysis on b-jet reconstruction; however, a b-tagging efficiency of 77% is generally employed, and used in this analysis, as the default working point.

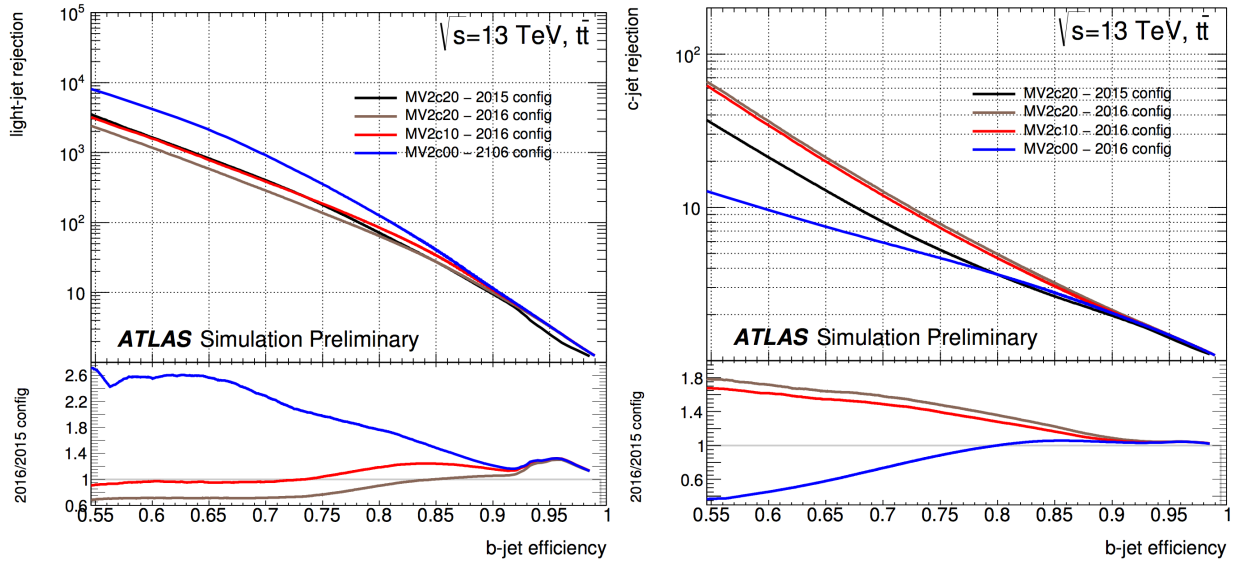

(a) (b)

Figure 4.7: Performance of `MV2cxx` output variables with different c-jet fractions using MC simulated $t\bar{t}$ samples. Fig. 4.7a shows the rejection of light-flavored jets vs. the b-tagging efficiency, while Fig. 4.7b shows the same for c-jet rejection. Comparisons between 2015 (20% of c-jets for `MV2c20`, 10% of c-jets for `MV2c10`) and 2016 (15% of c-jets for `MV2c20`, 7% of c-jets for `MV2c10`) MV2 algorithms are shown to indicate the performance enhancements from the lower c-jet fraction in the 2016 sample [113].

The multivariate discriminant (BDT output) used in this analysis is `MV2c10`, where 'c10' indicates the percentage of c-tagged jets in the simulated training sample, which, in an earlier version of the BDT algorithm, was set at 10% (the other 90% being classified as light-flavored jets). However, in the updated '2016 configuration' version of the BDT, the c-jet fraction was reduced to 7% in order to improve the performance of the algorithm with respect to light-jet vs. c-jet rejection [113]. Figure 4.7 shows the performance of the 2015 vs. 2016 MV2 variable and its working points. `MV2c20` was originally used as the discriminant variable in an earlier version of this analysis [41]. However, due to the relatively poor light-jet rejection performance at the 77% working point with the updated BDT, as shown in figure 4.7a, `MV2c10` was adopted as the standard discriminant. `MV2c10` clearly shows almost the same improvement as `MV2c20` in c-jet rejection as shown in Fig. 4.7b, while still maintaining an

improvement in light-jet rejection, at the working point of 77%.

4.2.3 Lepton Identification and Reconstruction

Of the leptons in the SM, only electrons and muons (and their antiparticles) are collectively referred to as leptons, as used in ATLAS. Neutrinos are invisible to the detector and are therefore accounted for in $E_{\mathrm{T}}^{\mathrm{miss}}$. In addition, τ-leptons can have signatures similar to those from hadronic jets due to their higher mass and relatively rapid decay within the detector. Therefore, identifying τ-leptons is generally more difficult than identifying electrons or muons. In this analysis, τ-leptons are not directly relevant except in so far as they decay leptonically, to electrons or muons, in the final state.

Electrons Reconstruction of electrons consists of identifying cluster seeds as a first step. The cluster seeds are located in the EM calorimeter, in $\eta \times \phi$ space, with cluster energy > 2.5 GeV. Next, a cluster candidate is identified based on EM shower shape and size criteria, and matched to an ID track candidate loosely identified as oriented in the same direction as the cluster. Photons are identified and reconstructed in a similar way but distinguished from electrons in that they do not have associated tracks in the innermost layers of the pixel detector. In Run II, EM particles are reconstructed with a cluster size of $\Delta\eta \times \Delta\phi = 0.075 \times 0.175$, if located in the barrel, or a cluster size of $\Delta\eta \times \Delta\phi = 0.125 \times 0.125$, if located in the end-caps [114].

The *EGamma* group [115, 116] is responsible for the reconstruction and calibration of electron objects and provides recommendations for the physics analysis groups. The identification of a quality electron candidate requires algorithms dependent on several factors including track quality, cluster size and shape, and several variables identified to distinguish signal electron candidates from background sources. Table 4.2 lists the variables important for electron identification.

To calibrate the energy of particles in the EM calorimeter, a multivariate regression algorithm is used to apply correction factors to account for variations in the energy response. The calibration process is MC based, and applied to both data and simulated events. Improvements were added to the Run I calibration for Run II to render the calibration in the barrel-endcap transition region more reliable [114, 117]. However, for this analysis electrons that fall in the transition region, or 'crack region' ($1.37 < |\eta_{cl}| < 1.52$), are not included due to energy measurement inefficiencies and poor instrumentation coverage. Additional calibrations for the electron energy scale and resolutions are added from *in-situ* studies using

$Z \to ee$ events at $\sqrt{s} = 13$ TeV. Several systematic uncertainty scale factors are determined from these calibrations and applied for electron trigger, energy resolution, identification, and isolation. These are discussed further in Chapter 8.

In contrast to Run I, the Run II algorithms for electron identification and distinction from hadronic clusters operate using a multivariate likelihood (LH) based method [118].[5] A combined discriminant variable $d_{\mathcal{L}}$ is defined using the signal ($\mathcal{P}_{s,i}(x_i)$) and background ($\mathcal{P}_{b,i}(x_i)$) probability density functions of the ith variable, as shown in equation 4.4, where $\vec{x}$ is the set of discriminating variable values, which are described in table 4.2.

$$d_{\mathcal{L}} = \frac{\mathcal{L}_S}{\mathcal{L}_S + \mathcal{L}_B}, \quad \text{where } \mathcal{L}_{S(B)} = \prod_{i=1}^{N} \mathcal{P}_{s(b),i}(x_i) \tag{4.4}$$

Three sets of LH based working points are defined and optimized in E_{T} and η for the quality of electrons: *LooseLH*, *MediumLH*, and *TightLH* (where the selection results in: *TightLH* $\subset$ *MediumLH* $\subset$ *LooseLH*). Figure 4.8 shows the efficiencies, using MC events, for these three working points of the LH identification algorithm to choose signal electrons from real $Z \to ee$ events, and to distinguish these electrons from background events from dijets. In this analysis, the working point[6] for election identification quality is *TightLH* with the additional requirements of $p_{\mathrm{T}} > 28$ GeV and $|\eta_{cl}| < 2.47$. The track position parameters (TTVA parameters), depicted in figure 4.2, help to define certain identification working points for quality electron tracks as well. The following recommendations from the *EGamma* group are used for the TTVA cuts for electrons in this analysis: $|d_0^{\mathrm{sig}}| < 5$, where $|d_0^{\mathrm{sig}}|$ is the d_0 significance and is defined as $|d_0/\sigma_{d_0}|$, where σ_{d_0} is the standard deviation on d_0, and $\Delta z_0 \sin(\theta) < 0.5$ mm. Additionally, isolation criteria are further applied for electrons in this analysis to distinguish quality real (signal) electrons from background electrons.

Two types of isolation criteria are applied to the analysis electrons: calorimeter isolation and track cluster isolation. For the calorimeter isolation, a cone of radius $\Delta R = 0.2$ is defined around the candidate electron topological clusters [97], and the variable `topoetcone20` is taken as a sum of the E_{T} of all the topological clusters energy not associated with the candidate. The 'cone20' refers to the cone size of $\Delta R = 0.2$. Several correction factors are applied based on E_{T} and η to account for any leakage outside the cluster. For the track isolation, a similar cone is defined around the candidate electron track of radius $\Delta R = \Delta R_{\mathrm{max}}$, where ΔR_{max} is defined in equation 4.5. The variable `ptvarcone20` is defined as the sum of

[5] The Run I electron ID quality implemented square cut-based algorithms.

[6] Except as described in the data driven fake/non-prompt lepton background estimation, described in § 7.1, where a looser definition of electrons is needed when computing the efficiencies for the Matrix Method.

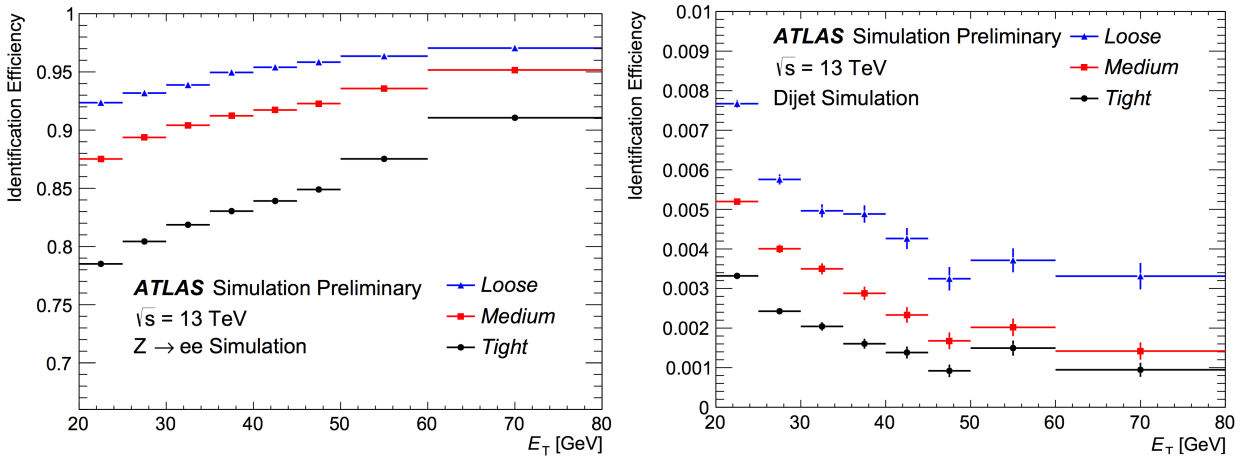

(a) (b)

Figure 4.8: Identification efficiency (see text) for signal electrons from $Z \to ee$ simulated events (4.8a) and to misidentify hadrons as electrons from simulated dijet events (4.8b) [118].

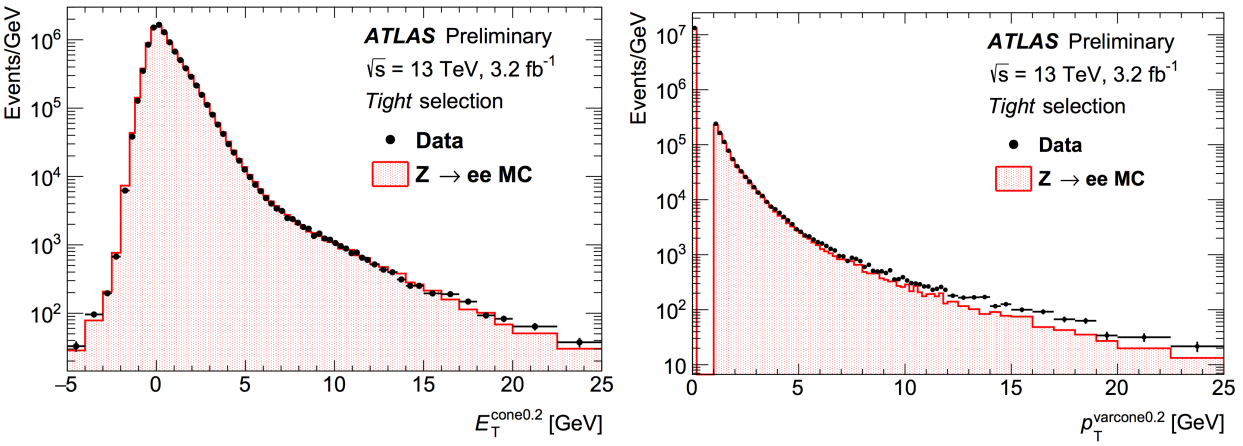

(a) (b)

Figure 4.9: Distributions of isolation variables `topoetcone20` and `ptvarcone20` using $Z \to ee$ simulated events compared to data events. Selection for electrons includes $E_{\mathrm{T}} > 27$ GeV and the *TightLH* identification quality requirements. The background is not subtracted here, as evident by the slight discrepancy at larger values of ${E_{\mathrm{T}}}^{\mathrm{cone0.2}}$ and ${p_{\mathrm{T}}}^{\mathrm{varcone0.2}}$ [118].

the p_{T} of the tracks within ΔR_{max} of the candidate electron track, excluding the candidate's track or associated tracks (e.g. from additional *bremsstrahlung* tracks). The advantage of the p_{T} dependence of ΔR_{max} is that at higher transverse momentum, closer tracks are considered isolated. Figure 4.9 shows the isolation distributions for `topoetcone20` (4.9a)

and `ptvarcone20` (4.9b) using MC events.

$$\begin{aligned} \texttt{topoetcone20} &= \sum_{\Delta R<0.2} {E_{\mathrm{T}}}^{\mathrm{topo}}, \\ \texttt{ptvarcone20} &= \sum_{\Delta R<\Delta R_{\mathrm{max}}} {p_{\mathrm{T}}}^{\mathrm{trk}}, \\ \text{where } \Delta R_{\mathrm{max}} &= \min\Big(\frac{10 \text{ GeV}}{p_{\mathrm{T}}}, 0.2\Big) \end{aligned} \tag{4.5}$$

Several working points are defined using the `topoetcone20` and `ptvarcone20` variables depending on whether a specific isolation efficiency or isolation cut value is required [119]. For this analysis, the following working points are used (targeting fixed isolated cut): `topoetcone20` / $E_{\mathrm{T}} < 0.06$ and `ptvarcone20` / $E_{\mathrm{T}} < 0.06$. This set of cuts is referred to as *FixedCutTight* and is the nominal isolation working point for electrons in this analysis.

Muons Information from both the inner detector layers and the Muon Spectrometer (MS) system are used in the identification and reconstruction of muons. Calorimeter clusters supplement the information used in the reconstruction, however muons lose very little of their energy to showering in the calorimeter systems. The MS detects muons for $|\eta| < 2.7$ using the subdetector systems described in § 3.2.3. The reconstruction of muon tracks in the ID is similar to electron track reconstruction. Muon track reconstruction in the MS proceeds independently of the ID track reconstruction. The MS is designed to measure the transverse momentum of a muon with 3% resolution for muons up to about 1 TeV. Above roughly 1 TeV, muon momentum measurements have a resolution closer to 10% [120].

Track candidates in the MS are constructed using seeds from hits in the middle layers of the detectors. A combinatorial search algorithm then fits hits to track segments in the outer and inner layers of the detector and a muon track candidate is formed using a global χ^2 fit. Tracks from the MS are then combined with the candidates from the ID in an 'outside-in' manner. For cross-checks, the opposite 'inside-out' approach is used for matching tracks.

Muon transverse momentum is calibrated to ensure a corrected momentum scale and resolution by calculating scale factors in $Z \to \mu\mu$ events from simulation and data samples. The momentum scale is dependent on the energy loss in the MS detectors and any radial distortions of the magnetic field integral in the MS region. For the momentum resolution, energy loss fluctuations in the material traversed by the muon are corrected for. Also, corrections to the momentum resolution are calculated for multiple scatterings, local magnetic field and radial distortions, intrinsic resolution affects, and detector misalignments, which

Type	Description	Name
Hadronic Leakage	Ratio of E_{T} in the first layer of the hadronic calorimeter to E_{T} of the EM cluster (used over range $\|\eta\| < 0.8$ and $\|\eta\| > 1.37$).	R_{had1}
	Ratio of E_{T} in the hadronic calorimeter to E_{T} of the EM cluster (used over range $0.8 < \|\eta\| < 1.37$).	R_{had}
Back layer of EM Calorimeter	Ratio of the energy in the back layer to the total energy in the EM accordion calorimeter. This variable is only used below 100 GeVbecause it is known to be inefficient at high energies.	f_3
Middle layer of EM Calorimeter	Lateral shower width, $\sqrt{(\sum E_i\eta_i^2)/(\sum E_i) - ((\sum E_i\eta_i)/(\sum E_i))^2}$, where E_i is the energy and η_i is the pseudorapidity of cell i and the sum is calculated within a window of 3×5 cells.	$w_{\eta 2}$
	Ratio of the energy in 3×3 cells over the energy in 3×7 cells centered at the electron cluster position.	R_ϕ
	Ratio of the energy in 3×7 cells over the energy in 7×7 cells centered at the electron cluster position.	R_η
Strip layer of EM Calorimeter	Shower width, $\sqrt{(\sum E_i(i - i_{max})^2)/(\sum E_i)}$, where i runs over all strips in a window of $\Delta\eta \times \Delta\phi \approx 0.0625 \times 0.2$ corresponding typically to 20 strips in η, and i_{max} is the index of the highest-energy strip.	w_{stot}
	Ratio of the energy difference between the largest and second largest energy deposits in the cluster over the sum of these energies.	E_{ratio}
	Ratio of the energy in the strip layer to the total energy in the EM accordion calorimeter.	f_1
Track Conditions	Number of hits in the innermost pixel layer; discriminates against photon conversions.	n_{Blayer}
	Number of hits in pixel detector.	n_{pixel}
	Number of total hits in the pixel and SCT detectors.	n_{Si}
	Transverse impact parameter with respect to the beam-line.	d_0
	Significance of transverse impact parameter defined as the ratio of d_0 and its uncertainty.	d_0/σ_{d_0}
	Momentum lost by the track between the perigee and the last measurement point divided by the original momentum.	$\Delta p/p$
TRT	Likelihood probability based on transition radiation in the TRT.	eProbabilityHT
Track-cluster matching	$\Delta\eta$ between the cluster position in the strip layer and the extrapolated track.	$\Delta\eta_1$
	$\Delta\phi$ between the cluster position in the middle layer and the track extrapolated from the perigee.	$\Delta\phi_2$
	Defined as $\Delta\phi_2$, but the track momentum is rescaled to the cluster energy before extrapolating the track from the perigee to the middle layer of the calorimeter.	$\Delta\phi_{\mathrm{res}}$
	Ratio of the cluster energy to the track momentum.	E/p

Table 4.2: List of discriminating variables for electron identification quality [118].

are all modeled with simulations. Simulations in the ID and MS for these residual corrections are modeled independently and applied as a linear combination to both simulation and data. Uncertainties on the parameters that result from these corrections provide systematic uncertainties on muon reconstruction and identification. Systematic uncertainties for muons and other objects in this analysis are discussed in detail in Chapter 8.

As with electrons, the identification of quality muon candidates is studied in simulated events to distinguish real, prompt muons from background muons (e.g. from the decay of heavy flavor hadrons). Muons originating from the decay of heavy flavor hadrons tend to have a 'kink' in their track topology, which would result in a poor fit to the tracks. The following variables are used to distinguish quality muon candidates from background muons because they provide good discriminating power in the topology of the tracks of muons.

- q/p significance: ratio of charge to momentum of the muons measured in both the ID and the MS, divided by the sum in quadrature of the respective uncertainties
- ρ': the absolute value of the difference between the p_{T} measured in the ID and the MS, divided by the p_{T} of the combined track
- Normalized χ^2 of the combined track fit

Four categories of identification quality are defined: *Loose*, *Medium*, *Tight*, and *High-*p_{T} (with the selection resulting in: *Tight* $\subset$ *Medium* $\subset$ *Loose*, and *High-*p_{T} are typically a subset of *Medium* but with $p_{\mathrm{T}} > 100$ GeV). The *Medium* quality is characterized by a real muon reconstruction efficiency of 95.5% for $4 < p_{\mathrm{T}} < 20$ GeV muons and 96.1% for $20 < p_{\mathrm{T}} < 100$ GeV, and the fraction of muons from heavy flavor decays misidentified as prompt muons is 0.38% and 0.17% for the same p_{T} ranges, respectively. The *Medium* working point provides a good balance of high reconstruction efficiency while minimizing the reconstruction and calibration uncertainties for muons. Therefore, this is the default identification quality used in ATLAS and is used in this analysis. Figure 4.10 shows the efficiencies for *Medium* muons using $Z \to \mu\mu$ simulated events. In addition to the *Medium* identification quality for muons in this analysis, the following requirements are used: $p_{\mathrm{T}} > 28$ GeV, $|\eta| < 2.5$, and TTVA cuts: $|d_0^{\mathrm{sig}}| < 3$ and $\Delta z_0 \sin(\theta) < 0.5$ mm.

Another distinguishing factor for muons is their isolation from other activity in the event. Unlike electrons, muons used in this analysis only have track based isolation, defined in a similar manner to `ptvarcone20`.

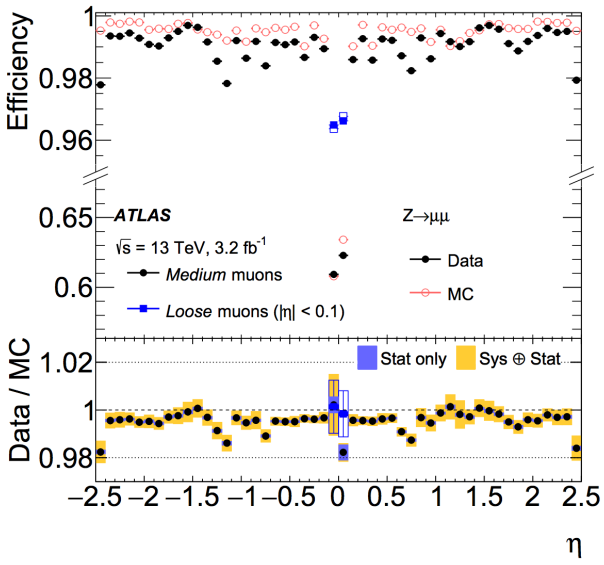

Figure 4.10: Identification efficiencies (see text) for signal muons from $Z \to \mu\mu$ simulated events [120].

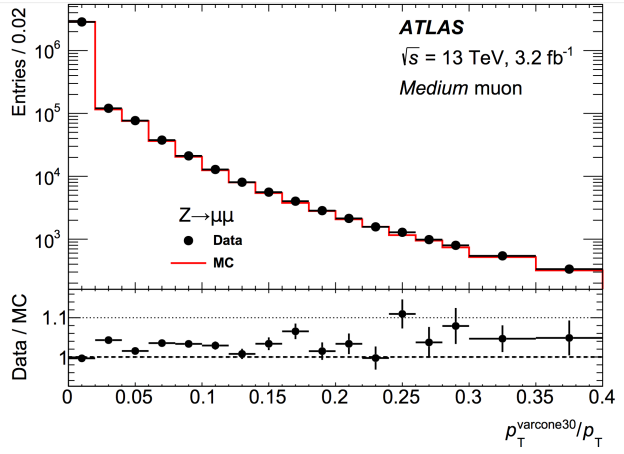

Figure 4.11: Distribution of isolation variable `ptvarcone30` divided by the p_{T} of the muon using $Z \to \mu\mu$ simulated events compared with data events. Muons included satisfy the *Medium* identification quality criteria [120].

$$\texttt{ptvarcone30} = \sum_{\Delta R < \Delta R_{\mathrm{max}}} {p_{\mathrm{T}}}^{\mathrm{trk}}, \quad \text{where } \Delta R_{\mathrm{max}} = \min\left(\frac{10 \text{ GeV}}{p_{\mathrm{T}}}, 0.3\right) \tag{4.6}$$

The tracks included in the p_{T} sum in equation 4.6 are tracks coming from the primary vertex with transverse momentum above 1 GeV surrounding the muon track in a cone radius

of 0.3. The sum excludes the muon candidate track. This is a measure of how much activity is in the vicinity of the muon candidate track. Figure 4.11 shows the distribution of isolation values for `ptvarcone30` / p_{T}. The working point used in this analysis for isolated muons is `ptvarcone30` / $p_{\mathrm{T}} < 0.06$, which is referred to as *FixedCutTightTrackOnly*.[7]

Overlap Removal An important step for reconstruction is the removal of any object defined by a set of calorimeter energy deposits which happens to be reconstructed as more than one physical object. This is called Overlap Removal (OVR). For example, an electron can be reconstructed as both an electron and a jet. The quality of the reconstruction helps to determine which physics identification the object belongs to. The *Top Reconstruction* group recommends OVR be performed on the loosest definitions of the objects, which is adopted in this analysis. The following procedure is applied, in the specified order, for the OVR in this analysis. In the following, ΔR uses the rapidity (y) of the object instead of pseudorapidity (η), e means electron, and μ means muon.

1. If an electron and muon share a track, the electron is removed
2. If $\Delta R(\mathrm{jet}, e) < 0.2$, the jet is removed
3. If $\Delta R(e, \mathrm{jet}) < 0.2$, the electron is removed
4. If $\Delta R(\mu, \mathrm{jet}) <$ (0.04 + 10 GeV/ p_{T}), the muon is removed

4.2.4 Missing Transverse Energy ($E_{\mathrm{T}}^{\mathrm{miss}}$)

$E_{\mathrm{T}}^{\mathrm{miss}}$ is an important variable, especially for exotic searches, since it is a measure of the transverse momentum, or energy, not directly detectable by the detectors in ATLAS. It is reconstructed as the negative sum of the calibrated, reconstructed transverse momentum, or energy, of all the detectable particles, like jets and leptons, in an event as well as any left-over energy from the reconstruction process. The net momentum transverse to the beam-line must be conserved, so any detectable net momentum in one direction in the detector must result in a net missing transverse momentum sum in the opposite direction. Equation 4.7 includes two terms for the reconstructed missing transverse energy. The first term, $\sum_{\mathrm{obj}} E_{\mathrm{x,y}}^{\mathrm{obj}}$, is the transverse energy of all the reconstructed and calibrated objects (*hard objects*) in the

[7] This is a standard Run II recommended working point from the *Muon Combined Performance* group. Other working points for isolation can be used, but in the *Top Common Objects* definitions, this is the default so is used here.

event: jets, μ, τ, γ, and electrons. The sum is performed in x and y coordinates separately. $E_{\mathrm{x,y}}^{\mathrm{miss,\ soft}}$ is the missing transverse energy from soft tracks, which is not matched to any hard objects and tracks from the underlying event activity (pile-up). Equation 4.8 shows the magnitude $E_{\mathrm{T}}^{\mathrm{miss}}$ and ϕ^{miss}, which is calculated from the x and y components and measures the azimuthal direction of the reconstructed $E_{\mathrm{T}}^{\mathrm{miss}}$.

$$E_{\mathrm{x,y}}^{\mathrm{miss}} = -\Big(\sum_{\mathrm{obj}} E_{\mathrm{x,y}}^{\mathrm{obj}}\Big) + E_{\mathrm{x,y}}^{\mathrm{miss,\ soft}} \tag{4.7}$$

$$\begin{aligned} E_{\mathrm{T}}^{\mathrm{miss}} &= \sqrt{(E_{\mathrm{x}}^{\mathrm{miss}})^2 + (E_{\mathrm{y}}^{\mathrm{miss}})^2} \\ \phi^{\mathrm{miss}} &= \arctan\Big(\frac{E_{\mathrm{y}}^{\mathrm{miss}}}{E_{\mathrm{x}}^{\mathrm{miss}}}\Big) \end{aligned} \tag{4.8}$$

$E_{\mathrm{T}}^{\mathrm{miss}}$ includes, or could potentially include, the following:

1. Particles like Standard Model (SM) neutrinos
2. Stable, exotic beyond the SM particles weakly interacting with the detector, like dark matter candidates, gravitons, etc.
3. Observable particles that were not reconstructed properly or went through cracks in the detector

Several algorithms for reconstructing $E_{\mathrm{T}}^{\mathrm{miss}}$ exist, each with their own benefits [121]. The first type of algorithm is track-based, using primarily tracks from reconstructed particles in the ID to reconstruct $E_{\mathrm{T}}^{\mathrm{miss}}$. This has the advantage of being resilient to pile-up tracks (both in-time and out-of-time pile-up). However, its disadvantage is that neutral particles (e.g. neutrons, photons) are not included. The second type of algorithm is calorimeter-based, which primarily uses calorimeter energy deposits from the calorimeter objects, as well as a soft term, which includes deposits not associated with reconstructed particles. The main drawback from just using calorimeter-based algorithms is that the soft term is highly sensitive to pile-up interactions. A combination of track-based and calorimeter-based algorithms is provided by $E_{\mathrm{T}}^{\mathrm{miss}}$ called TST $E_{\mathrm{T}}^{\mathrm{miss}}$, where the TST refers to track-based soft term. Hard object calorimeter measurements are included in the calculation of $E_{\mathrm{T}}^{\mathrm{miss}}$ in this case. TST $E_{\mathrm{T}}^{\mathrm{miss}}$ is the primary Run II method of $E_{\mathrm{T}}^{\mathrm{miss}}$ reconstruction. In this analysis, the TST $E_{\mathrm{T}}^{\mathrm{miss}}$ term collection in the datasets is called `MET_Reference_AntiKt4EMTopo` (using anti-k_{T} jets).

The calibration of $E_{\mathrm{T}}^{\mathrm{miss}}$ is treated similar to other objects, by defining corrections from simulated events, in this case $t\bar{t}$ events, and applying the corrections to simulation and

data. The calorimeter term is sensitive to pile-up effects, while the purely track-based soft term is more sensitive to effects from large numbers of high p_{T} jets but low in-time pile-up. Systematic uncertainties for $E_{\mathrm{T}}^{\mathrm{miss}}$ are calculated using the systematic uncertainties for each object propagated to the hard term in equation 4.7. Systematic uncertainties on the soft term $E_{\mathrm{T}}^{\mathrm{miss}}$ are discussed further in Chapter 8.

CHAPTER 5
Event Selection

Each event selected for this analysis must pass additional criteria applied to the objects described in the reconstruction process in Chapter 4. Event criteria are chosen in order to take advantage of final states favorable to VLQ and other exotic signal decay patterns, while reducing the backgrounds as much as possible.

Once final state objects have been identified, events are subjected to a series of square cuts designed to reduce background events and increase signal selection efficiency as much as possible. A 'square cut' generally refers to a conditional statement applied to a kinematic variable or object in an event such that the event is rejected if it does not pass. A simple example is a cut of $E_{\mathrm{T}}^{\mathrm{miss}} < 40$ GeV applied to all events. Events with $E_{\mathrm{T}}^{\mathrm{miss}}$ below 40 GeV are accepted, while events with $E_{\mathrm{T}}^{\mathrm{miss}}$ above 40 GeV are rejected. Cut-based analyses typically operate with more complex cuts than this, applied in the event selection, sometimes including several variables.[1] Events are selected from the full dataset and from MC using the same *cutflow*. The *cutflow* is simply the series of sequential cuts applied on the data and MC samples, which contain events passing each step of the selection criteria. Different regions are defined with different selection cuts in order to either validate the background estimation or search for the signal.

This chapter begins by describing the cut-and-count strategy, in section 5.1, which is the primary strategy adopted in this analysis. Next, the object selection of post-reconstructed objects used in this analysis: muons, electrons, jets and b-jets, and $E_{\mathrm{T}}^{\mathrm{miss}}$ are discussed in section 5.2. The preselection and final event selection are described in section 5.3. The signal regions and background validation regions are described in sections 5.3.3 and 5.3.4. Finally, the expected yields for the major backgrounds, VLQ signals (using MC simulation) at different mass points, and data in the different regions are presented.

[1] Note: the term 'cut' may also include simple Boolean variables.

5.1 The Cut-and-Count Strategy

The basic cut-and-count analysis is used frequently in ATLAS searches. It is the simplest strategy for event selection. A *cutflow* is used to keep track of the number of events passing each sequential cut. Due to the nature of same charge lepton final states being extremely rare (see §2.2), the cut-and-count strategy is the natural choice for this analysis. However, a multivariate boosted decision tree strategy has been implemented in prior instances of this search to study any differences with the cut-and-count strategy [44]. Only a slight increase on the order of 5% was seen in the observed mass limits for VLQ T and B varieties using this strategy compared with a simpler cut-and-count strategy.

In the cut-and-count method the following three steps are applied:

1. Regions are defined by a set of square cuts, which are kinematically favorable to yield a significant number of signal events[2]

2. Event selection cuts are applied on data and MC background to select only events that are within this region

3. Count the number of events from data and total expected background in the region, and compare

A calculation of the significance of data vs. total expected background allows for a determination of how statistically significant an excess of data above the total background is, if there is one. The significance calculation used in this analysis is discussed in §9.1. In the absence of any statistically significant excess, exclusion limits are set on the various signal models. The statistical interpretation of the results in the signal regions and the limit setting for this analysis is discussed more in Chapter 9. Of course, any statistical and systematic uncertainties must be accounted for in the comparison of data to total background. Systematic uncertainties are covered in detail in Chapter 8.

5.2 Object Selection

The object definitions used in this analysis are derived from the various *Combined Performance (CP)* groups and refined by the *Top Working Group*. *Top Common Objects* is

[2]Typically, these regions undergo an optimization procedure to identify the selection that maximizes the significance of a particular signal. The optimization used for this analysis is discussed in §5.3.3.

the set of physics objects in common to analyses using standard top working points for reconstruction and background rejection efficiencies. Object recommendations for ID quality, isolation, overlap removal with other objects, and jet identification are included in this set of working points. This analysis uses the *Top Common Objects* definitions except where explicitly stated. In addition to the fact that calibrations and uncertainties are derived for these common objects, searches that are looking for the same signal using different final states may wish to combine their search effort after the individual searches produce results. The common objects ensure any correlation or overlap between analyses can be handled correctly. A combination can potentially increase the sensitivity of a search by combining events that would otherwise be excluded in an individual search. For more on the VLQ combination effort see §10.1 and [122].

Due to the presence of fake leptons in this analysis, additional criteria are necessary to define a *looser* set of leptons. The *tight* definition is chosen as the lepton definition used in the main analysis and form a subset of the *loose* set. Any deviations from the *Top Common Objects* definitions are explained in §4.2. Table 5.1 summarizes the object definitions for this analysis.

	Electrons		Muons		Jets	*b*-jets
	MM-loose	MM-tight	MM-loose	MM-tight		
p_{T} lower limit (GeV)	28	28	28	28	25	25
$\lvert\eta\rvert$ upper limit	2.47(1.37)	2.47(1.37)	2.5	2.5	2.5	2.5
Crack region veto	yes	yes	no	no	no	no
ID quality	mediumLH	tightLH	medium	medium		MV2c10, 77%
Isolation (after OVR)	no	calo, track	no	track		
Track cut (after OVR):						
– $\lvert d_0^{\mathrm{sig}}\rvert$	< 5	< 5	< 3	< 3		
– $\lvert\Delta z_0 \times \sin\theta\rvert$ (mm)	< 0.5	< 0.5	< 0.5	< 0.5		

Table 5.1: Summary of the object definitions used in this analysis. The major reconstructed objects are electrons, muons, jets, and *b*-jets, along with $E_{\mathrm{T}}^{\mathrm{miss}}$, which is not shown in this table because once reconstructed in the normal way (see §4.2.4), the selection simply requires cuts on $E_{\mathrm{T}}^{\mathrm{miss}}$. The (1.37) cut on electron $|\eta|$ is only applied for the SSee and SSeμ channels to reduce the charge mis-identification background (see §7.2).

5.3 Event Selection

Event selection proceeds in two phases: preselection and final event selection. The preselection is typically a set of criteria for which all events included in the analysis must pass,

such as requiring every event to be on the Good Runs List (GRL) and to pass one of the main analysis triggers. Most preselection criteria are often similar among most physics analyses. For example, a common GRL is used by most analyses for a given luminosity period to indicate quality runs with normal operations for most detector systems. Therefore, the event level cut `passGRL` is common to most analysis preselections.

The final event selection consists of multiple square cuts, after the preselection, which limit events to subregions of phase space expected to be kinematically favorable for observing the signal(s). In this analysis, several regions are defined where the event selection is optimized to provide the best available signal significance for VLQ and the other signals. These subregions of phase space are called *signal regions*.

5.3.1 Preselection

The ntuples used for event selection already have the objects and preselection included. This is done by the *SSbjetsTools* package, which is the collection of code specifically for this analysis, in order to reduce the size of the ntuples. Every event included in these ntuples passes the following requirements for preselection:

- Must contain at least one primary vertex with at least five tracks with $p_{\mathrm{T}} > 0.4$ GeV
- Must pass at least one single lepton or dilepton trigger, defined in Table 5.2
- Must be on Good Runs List, and have no LAr noise burst or corrupted data and no TileCal corrupted events
- Must contain ≥ 1 jet defined by `AntiKt4EMTopoJets` criteria

In addition to this preselection, events are required to have two or more leptons (electrons or muons) and are further categorized by lepton flavor and charge into channels. Dilepton events constitute the majority of the events ($\sim$80% of preselected events) from data. In order to deterministically separate events into dilepton and trilepton channels, events with three leptons in the leading three p_{T} leptons are categorized as trilepton events if the three leptons all meet the isolation and quality definitions defined for *tight* leptons (see §4.2.3 for definitions of *tight*). Events with only two *tight* leptons in the leading two or three leptons, where both *tight* leptons have the same charge, are categorized as dilepton events. Table 5.3 summarizes the event selection based on the flavor of the leptons, dividing events into three dilepton channels (SSee, SSeμ, SS$\mu\mu$) and four trilepton channels (eee, eeμ, e$\mu\mu$, $\mu\mu\mu$).

Final event selection requires additional kinematic cuts applied to the events in the dilepton or trilepton channels. Figure 5.1 shows some H_{T} distributions with all backgrounds vs. a couple signal models passing the preselection and split by dilepton and trilepton channels. The variable H_{T} is the scalar sum of the transverse momenta or energies of all jets and leptons in the event. Additional cuts are placed on the number of b-jets. The data-driven backgrounds in these plots are estimated with MC simulations because they were created prior to the final data-driven background estimation.

Trigger type	**Triggers Applied**
Periods: 2015 data (D-J)	
Dilepton	`HLT_2e12_lhloose_L12EM10VH`, `HLT_e17_lhloose_mu14`, `HLT_e7_lhmedium_mu24`, `HLT_2mu10`, `HLT_mu18_mu8noL1`
Single electron	`HLT_e24_lhmedium_L1EM20VH`, `HLT_e60_lhmedium`, `HLT_e120_lhloose`
Single muon	`HLT_mu50`
Periods: 2016 data (A-L)	
Dilepton	`HLT_2e17_lhvloose_nod0`, `HLT_e17_lhloose_nod0_mu14`, `HLT_e7_lhmedium_nod0_mu24`, `HLT_2mu14`, `HLT_mu22_mu8noL1`
Single electron	`HLT_e60_lhmedium_nod0`, `HLT_e140_lhloose_nod0`
Single muon	`HLT_mu50`

Table 5.2: HLT single lepton and dilepton triggers used to select events. Since no trigger relies on isolation of the leptons at the HLT stage, a logical OR is used between all triggers during preselection. Events within specified data period must be triggered by a lepton matched to at least one of these triggers. For details on data periods, see Table 6.1.

The data-driven backgrounds are estimated using the same preselection criteria as described above (with the exception of the triggers, described in Chapter 7) and in the same control, validation, and signal regions described in the next sections. The charge misidentification of electrons is only estimated for SSee and SSeμ.[3] The fake/non-prompt lepton background is estimated separately for the dilepton and trilepton channels. This is because the Matrix Method requires a 4×4 matrix for the dilepton channels and a 8×8 matrix for

[3]The reason is the same as previously mentioned, muon charge misidentification is typically negligible.

the trilepton channels. The Matrix Method and data-driven background calculations are described in detail in Chapter 7.

Triggers The triggers used in this analysis are single lepton, where the events saved are triggered by at least one relatively high p_{T} lepton, and dilepton triggers, where the events have two recorded leptons. The p_{T} threshold at which leptons trigger the TDAQ system varies by trigger. This threshold is set in order to keep the event acceptance rate manageable for data acquisition, while still maintaining a relatively high efficiency of the trigger. The presence of more than one lepton in the event can result in one of several dilepton triggers being fired. The dilepton triggers can have lower p_{T} thresholds for the electron or the muon due to the requirement of two leptons per event, which keeps the output rate below the maximum threshold. Some single lepton triggers have a low enough p_{T} that their normal firing rate may be too much for the ATLAS readout data rate to handle (∼1 kHz in Run II) [123]. In this case, the trigger only fires a fraction of the time or is disabled during data taking, and a prescale factor must be applied to scale up the the number of fired events

Channel Name	**Conditions**
Dilepton Selection	
SSee	Two *tight*, same charge electrons of the three leading p_{T} leptons; additional quarkonia/Z veto: $m_{\mathrm{ee}} > 15$ GeVand $\lvert m_{\mathrm{ee}} - 91\rvert > 10$ GeV
SSeμ	One *tight* muon and one *tight* electron with the same charge, of the three leading p_{T} leptons
SSμμ	Two *tight*, same-charge muons of the three leading p_{T} leptons
Trilepton Selection	
eee	Three *tight* electrons of the leading p_{T} leptons
eeμ	One *tight* muon and two *tight* electrons of the leading p_{T} leptons
eμμ	Two *tight* muons and one *tight* electron of the leading p_{T} leptons
μμμ	Three *tight* muons of the leading p_{T} leptons

Table 5.3: Criteria for defining the same charge (±) dilepton and trilepton channels. If there is a third lepton present in the event and it is *anti-tight*, the event can be counted with the dilepton channels. *Anti-tight* refers to a lepton that is *loose* but not *tight*. Additionally, each event must contain at least one lepton that matches at least one of the analysis triggers. The quarkonia/Z veto is applied to the SSee channel because charge-flipped electrons from quarkonia or Z bosons (for example, $Z \to e^{\pm}e^{\mp}$) would be a large background in this channel and is best cut. The reason why this channel is singled out for this cut is two-fold: (1) $Z \to \mu^{\pm}\mu^{\mp}$ charge-flip rates are negligible due to the long lever-arm of muons and having two measurements of charge, from the inner detector and from the Muon Spectrometer, and (2) Z decay to $e^{\pm}\mu^{\mp}$ is not possible.

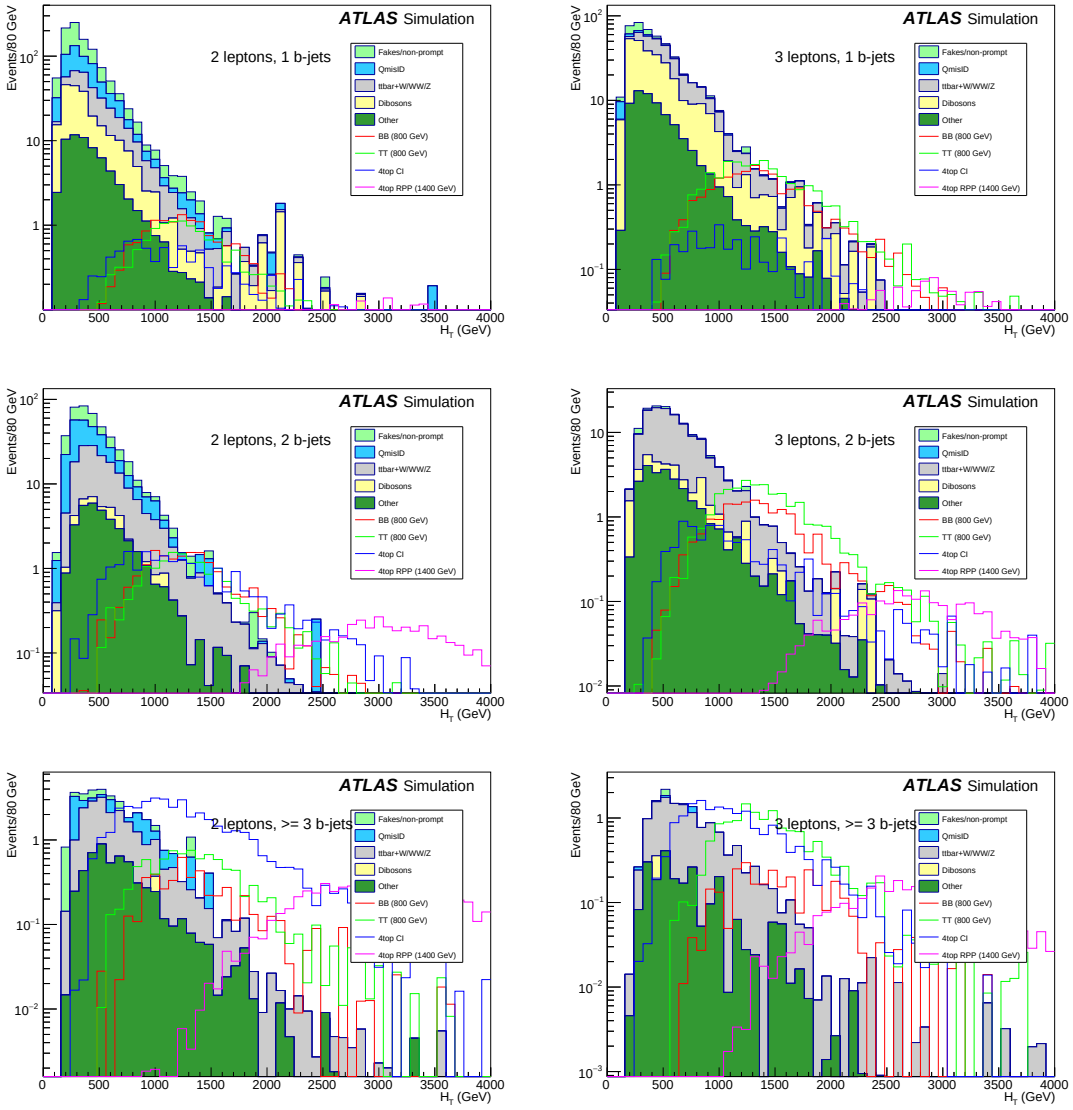

Figure 5.1: H_{T} distributions for dilepton (left column) and trilepton (right column) for 1 b-jet (top), 2 b-jets (middle), and $\geq$3 b-jets (bottom) at preselection. The fake/non-prompt lepton and charge mis-id backgrounds are estimated with MC simulations. All simulations are normalized to 36.1 fb^{-1}.

to the proper number based on the run's total luminosity. The prescale need not be the same factor for each run and in some cases can be quite large depending on the trigger used. Single lepton prescaled triggers are used only in the fake and non-prompt lepton background estimation, discussed in Chapter 7.

This analysis uses the HLT triggers shown in table 5.2 to identify events in the main analysis. If an event only has two electrons (muons), only dilepton triggers with two electrons

(muons) are used in the dilepton and trilepton channels with at least two electrons (muons). For the channels that have mixed lepton flavor, the triggers with both an electron and a muon p_{T} threshold are used (e.g. `HLT_e17_lhloose_nod0_mu14`, where the p_{T} threshold on electrons is 17 GeV and for muons is 14 GeV). The single lepton triggers are included in the trigger decision for the channels with at least one of the corresponding leptons. The trigger decision is a logical OR between all the triggers for each channel, so each event must pass at least one of the triggers.

A few of the triggers mentioned above have a requirement on the identification quality of the lepton (e.g. *MediumLH* for `HLT_e60_lhmedium_nod0`). This means there is a requirement on the ID quality for the electrons firing that trigger, and the electrons in the main analysis should not have a looser cut than this, but it can have a more tight cut. The 'nod0' in the name of the trigger refers to the d_0 transverse track parameter, see figure 4.2, not being used as a parameter for the trigger. In one of the dimuon triggers, 'mu8noL1' means the second muon triggered in the event is identified in the HLT instead of at the Level-1 (L1) trigger. The first muon in the trigger name with the higher p_{T} threshold triggers the event at L1. Lastly, the 'L1yEMxxVH' in a trigger name means the L1 event is triggered by y number of electrons (y is left out if only one electron), each passing the LH ID requirement for the trigger with p_{T} threshold of xx GeV.

5.3.2 Event Selection Optimization

Since there are multiple signals for this analysis, the optimization of the signal regions takes into account the best cuts for whichever signals have the highest significance. However, it would be unwieldy to have too many signal regions optimized for each signal individually, so a compromise is made to provide the best signal significance while maintaining a reasonable number of signal regions. Since no evidence for VLQ has been observed with mass below roughly 800 GeV (see Table 2.3), the cuts have been re-optimized from the early iterations of this analysis to search for VLQ signals with mass $>$ 800 GeV. However, the early version of this analysis with Run II data did recheck the old signal region definitions for any excess with the Run II data, and the optimization took place only after it was confirmed that no excess was found with the previous definitions.

The optimization of the signal region cuts includes several caveats and constraints. First, a set of signals are used to optimize the signal significance in the final regions and the number of these regions was constrained to eight for practical purposes. For VLQ, the signals used in the optimization include $m_Q = 800$ and 1200 GeV, where $Q = B$, T, assuming singlet

branching ratios to the three VLQ decay modes.

Equation 9.2 shows how the significance is estimated in the optimization process. This method of calculating significance was chosen to explore the effect of the expected total systematic uncertainty on the background estimation in the optimization. Note that the total systematic uncertainty on the background in the signal regions was not known at the time of the optimization. This is because the analysis is blinded until the control and validation regions on the background show good agreement. The majority of the systematic uncertainties arise from the data-driven backgrounds, which cannot be unblinded in the signal regions until validated in the control and validation regions. In order to avoid using data or data-driven estimations in the optimization process, the data-driven backgrounds (discussed in detail in Chapter 7) were estimated using MC samples. In particular, $t\bar{t}$ and V+jets were used in the optimization to represent these backgrounds. Values of $\delta\mathrm{B}/\mathrm{B} = 0.1$ (i.e. 10% total background uncertainty) through $\delta\mathrm{B}/\mathrm{B} = 1.0$ are explored, where B is the expected number of background events (S is the expected yield of signal events). A conservative estimate of $\delta\mathrm{B}/\mathrm{B} = 0.25$ being used as a baseline. The expected yield on the various signals was computed using an integrated luminosity of 30 fb^{-1}, which is the same order of magnitude as the final dataset used in this analysis.

A similar optimization procedure was performed on the validation regions in order to understand the backgrounds in kinematically similar regions to the signal regions. For this optimization, the significance test used the background hypothesis and was optimized with respect to $\mathrm{B}/\sqrt{\mathrm{S}+\mathrm{B}}$.

5.3.3 Signal Regions

Signal regions are optimized in the procedure outlined in §5.3 in order to enhance potential signal events over background events. In previous instances of this analysis (i.e. with Run I data at $\sqrt{\mathrm{s}} = 8$ TeV), the signal regions were determined for the VLQ signals, with a subset of the regions optimized to give higher significances for other exotic signals in this search (e.g. $t\bar{t}t\bar{t}$) [44]. The Run I data showed a slight excess in two signal regions where more data events were seen than expected from background. The significance of the discrepancy[4] between data and background reached 2.5σ in the regions with the highest cuts on H_{T}, $E_{\mathrm{T}}^{\mathrm{miss}}$, and N_{bjets} assuming the $t\bar{t}t\bar{t}$ signal. The first instance of this analysis using 2015 Run II data ($\sqrt{\mathrm{s}} = 13$ TeV) checked this excess using the same signal region definitions. No excess was found [124], so the signal regions were re-optimized for the higher energy Run II dataset.

[4]For a discussion on significance, see §9.1.

Table 5.4 summarizes the signal region definitions used for Run II with the full 2015 - 2016 dataset. In Chapter 9, the final results in the signal regions are defined, with the total statistical and systematic uncertainties. Figure 5.2 shows the expected fraction for each major background source in the signal regions. The data-driven background fractions are estimated using MC.

No. of Leptons	**No. of b-jets**	**No. of jets**	**Kinematic cuts [GeV]**	**Signal Region Name**
2	1	≥ 1	$H_{\mathrm{T}} > 1000$ and $E_{\mathrm{T}}^{\mathrm{miss}} > 180$	*SR1b2l*
2	2	≥ 2	$H_{\mathrm{T}} > 1200$ and $E_{\mathrm{T}}^{\mathrm{miss}} > 40$	*SR2b2l*
2	≥ 3	≥ 7	$500 < H_{\mathrm{T}} < 1200$ and $E_{\mathrm{T}}^{\mathrm{miss}} > 40$	*SR3b2l_L*
2	≥ 3	≥ 3	$H_{\mathrm{T}} > 1200$ and $E_{\mathrm{T}}^{\mathrm{miss}} > 100$	*SR3b2l*
3	1	≥ 1	$H_{\mathrm{T}} > 1000$ and $E_{\mathrm{T}}^{\mathrm{miss}} > 140$	*SR1b3l*
3	2	≥ 2	$H_{\mathrm{T}} > 1200$ and $E_{\mathrm{T}}^{\mathrm{miss}} > 100$	*SR2b3l*
3	≥ 3	≥ 5	$500 < H_{\mathrm{T}} < 1000$ and $E_{\mathrm{T}}^{\mathrm{miss}} > 40$	*SR3b3l_L*
3	≥ 3	≥ 3	$H_{\mathrm{T}} > 1000$ and $E_{\mathrm{T}}^{\mathrm{miss}} > 40$	*SR3b3l*

Table 5.4: Signal regions for dilepton and trilepton channels, split by number of leptons, jets, b-jets and kinematic cuts in H_{T} and $E_{\mathrm{T}}^{\mathrm{miss}}$.

5.3.4 Background Validation

In order to validate the background estimations of the data-driven backgrounds, as well as the MC simulations for the irreducible backgrounds, one main control region and several validation regions are defined. Events are selected according to the cuts described in table 5.5, after preselection. The control region is used to understand the background modeling without looking in regions favorable to the signals. The cut $H_{\mathrm{T}} < 400$ GeV was chosen to ensure this since the exotic signals searched for are typically expected to deliver final states with much higher total transverse energy. The validation regions are optimized for background significance ($\mathrm{B}/\sqrt{\mathrm{S}+\mathrm{B}}$) and select events in a region of phase space that is kinematically similar to the signal regions. These regions include a strict veto on the signal regions (and on the control region) to ensure orthogonality and to maintain signal region blinding.

Figure 5.3 shows the expected fraction for each major background source in the validation regions. The data-driven background fractions are estimated using MC. Figure 5.4 shows a visual representation of the various subregions of $E_{\mathrm{T}}^{\mathrm{miss}}$ and H_{T} space. The validation regions have a veto on the control region ($H_{\mathrm{T}} < 400$ GeV). Note that this cartoon is a generalization of the orthogonality between the background validation regions and the signal regions. There

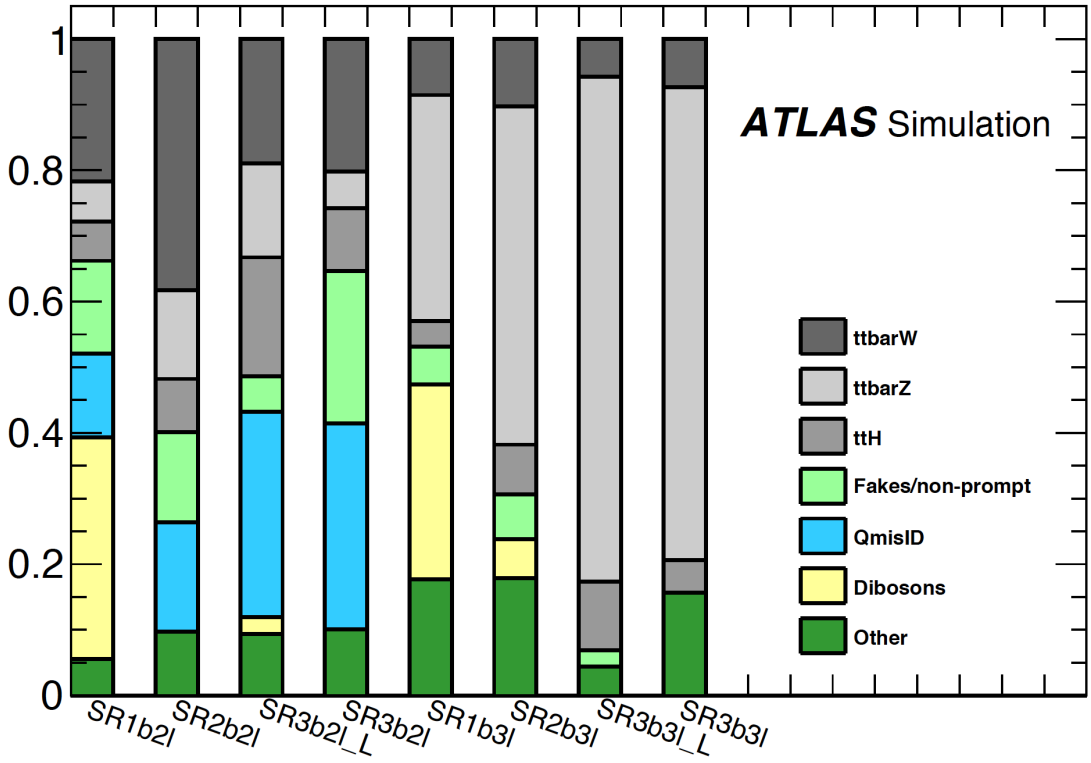

Figure 5.2: Expected fractions of major background sources in the signal regions. MC simulations are used for the instrumental backgrounds.

No. of Leptons	**No. of b-jets**	**No. of jets**	**Kinematic cuts [GeV]**	**Region Name**
2 or 3	$\geq$0	$\geq$ 1	$H_{\mathrm{T}} < 400$	*Control Region*
2	1	$\geq$ 1	$H_{\mathrm{T}} > 400$ and ($H_{\mathrm{T}} < 2400$ OR $E_{\mathrm{T}}^{\mathrm{miss}} < 40$) and !(*SR1b2l*)	*VR1b2l*
2	2	$\geq$ 2	$H_{\mathrm{T}} > 400$ and !(*SR2b2l*)	*VR2b2l*
2	$\geq$3	$\geq$ 3	$H_{\mathrm{T}} > 400$ and ($H_{\mathrm{T}} < 1400$ OR $E_{\mathrm{T}}^{\mathrm{miss}} < 40$) and !(*SR3b2l*)	*VR3b2l*
3	1	$\geq$ 1	$H_{\mathrm{T}} > 400$ and ($H_{\mathrm{T}} < 2000$ OR $E_{\mathrm{T}}^{\mathrm{miss}} < 40$) and !(*SR1b3l*)	*VR1b3l*
3	2	$\geq$ 2	$H_{\mathrm{T}} > 400$ and ($H_{\mathrm{T}} < 2400$ OR $E_{\mathrm{T}}^{\mathrm{miss}} < 40$) and !(*SR2b3l*)	*VR2b3l*
3	$\geq$3	$\geq$ 3	$H_{\mathrm{T}} > 400$ and !(*SR3b3l*)	*VR3b3l*

Table 5.5: Control and validation regions for determining if the backgrounds are estimated and modeled correctly. The expression: !(*region name*) means a veto on that region.

may exist only partial or full gaps in the region between the validation and signal regions, represented by the space between the dotted green line and the signal region, because the

selections are broken up by number of leptons and number of b-jets as well as $E_{\mathrm{T}}^{\mathrm{miss}}$ and H_{T}. The main consideration for the validation regions is to understand the backgrounds in kinematically similar regions to the signal regions.

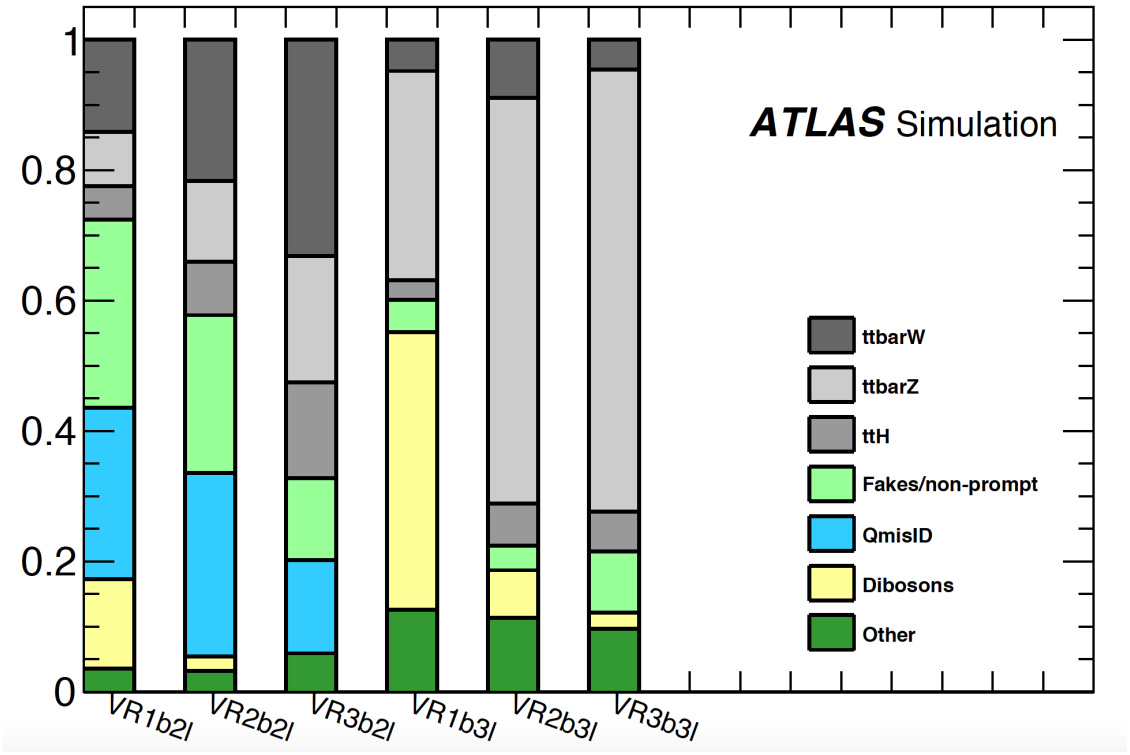

Figure 5.3: Expected fractions of major background sources in the validation regions. MC simulations are used for the instrumental backgrounds.

Figures 5.5 show the control plots depicting data and background comparison in the control region for the dilepton channels. Figures 5.6 show the control plots depicting data and background comparison in the control region for the trilepton channels. The control plots are separated by dilepton and trilepton flavor channel in order to understand any background mis-modeling affecting one lepton channel that may not affect other channels. Figure 5.7 shows the control region plots for all channels combined for a final assessment of the validation in this region.

Figures 5.8 through 5.13 show the validation plots depicting the comparison of data and background in the different validation regions. Tables 5.6 through 5.7 show the yields with statistical and systematic errors in the validation regions. Statistics can be limited in some region (e.g. 3 b-jets) so some fluctuations seem larger. However, overall the agreement is good.

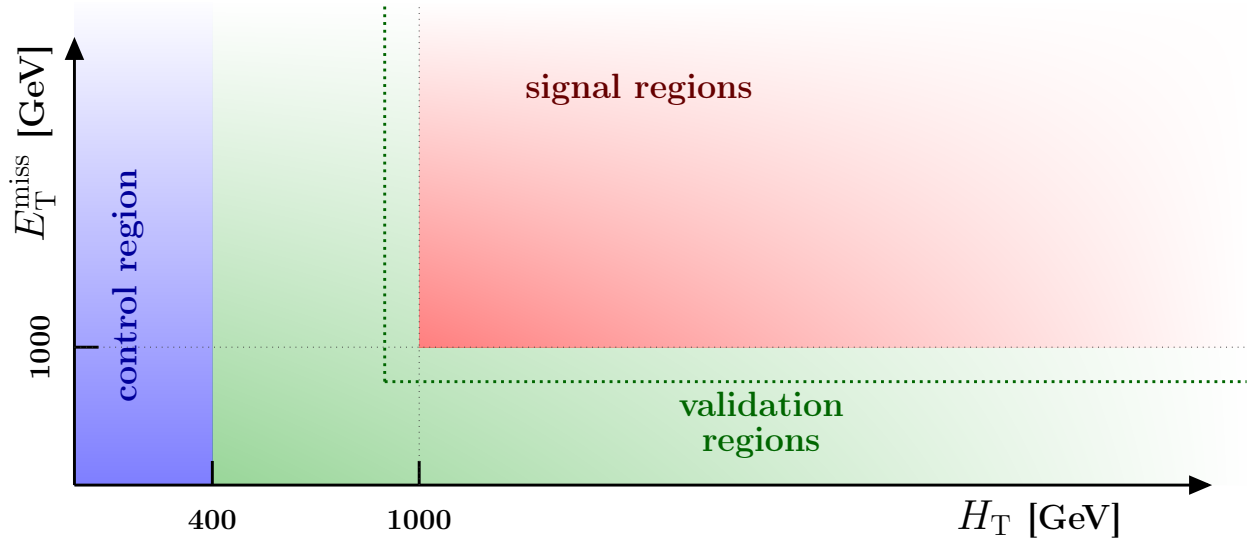

Figure 5.4: Cartoon of the control, validation, and signal regions defined in $E_{\mathrm{T}}^{\mathrm{miss}}$ vs. H_{T} space. The validation regions are orthogonal to the control region. The dotted line between the validation and signal regions is left to signify that in some cases, the validation regions do not reach to the signal regions in either $E_{\mathrm{T}}^{\mathrm{miss}}$ or H_{T}.

Process	*VR1b2l*	*VR2b2l*	*VR3b2l*
Fake/Non-prompt	$169.63 \pm 7.85 \pm 88.21$	$53.35 \pm 4.53 \pm 28.28$	$7.76 \pm 1.55 \pm 3.88$
Charge mis-ID	$70.62 \pm 0.73 \pm 11.56$	$54.81 \pm 0.60 \pm 9.30$	$4.46 \pm 0.16 \pm 0.79$
$t\bar{t}Z$	$28.73 \pm 0.45 \pm 2.40$	$27.62 \pm 0.44 \pm 2.15$	$3.41 \pm 0.20 \pm 0.28$
$t\bar{t}H$	$17.67 \pm 0.39 \pm 1.48$	$18.35 \pm 0.40 \pm 1.52$	$2.58 \pm 0.17 \pm 0.22$
$t\bar{t}W$	$48.73 \pm 0.67 \pm 6.84$	$48.41 \pm 0.67 \pm 6.38$	$5.82 \pm 0.28 \pm 0.81$
Dibosons	$47.50 \pm 3.46 \pm 5.84$	$4.91 \pm 1.34 \pm 0.87$	0.00 ± 0.46
Other bkg	$12.27 \pm 0.46 \pm 3.49$	$7.26 \pm 0.34 \pm 2.01$	$1.05 \pm 0.22 \pm 0.27$
Total bkg.	$395.15 \pm 8.67 \pm 89.53$	$214.72 \pm 4.86 \pm 30.64$	$25.08 \pm 1.68 \pm 4.07$
Data	407	269	27

Table 5.6: Dilepton validation region yields for all background processes and data. Yields are displayed as nominal ± stat. error ± syst. error.

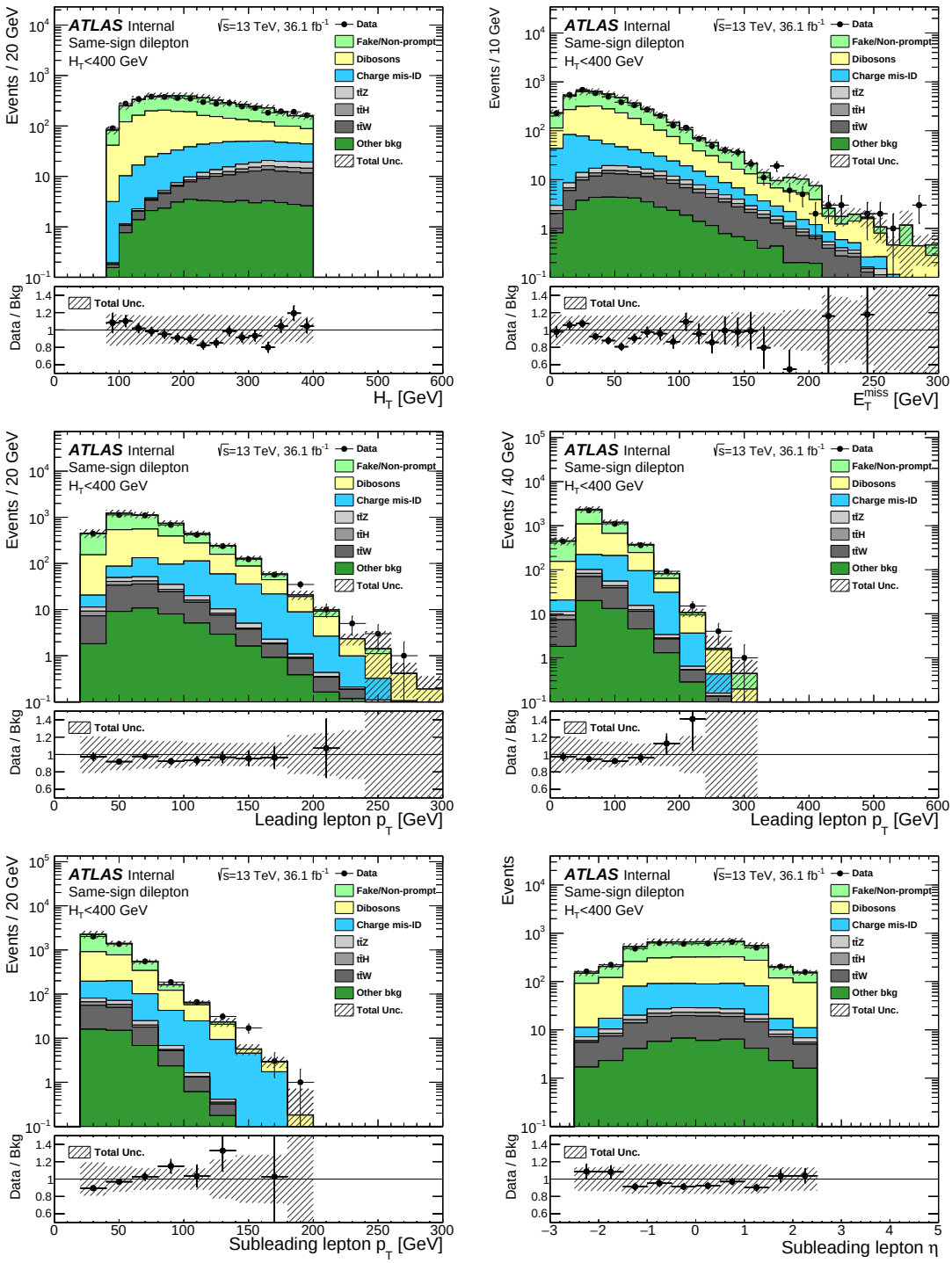

Figure 5.5: Control plots showing different variables for the dilepton (SSee, SSeμ, SSμμ) channels. The top row shows H_{T} (left) and $E_{\mathrm{T}}^{\mathrm{miss}}$ (right); the middle leading lepton p_{T} (left) and leading lepton η (right); the bottom row subleading lepton p_{T} (left) and subleading lepton η (right).

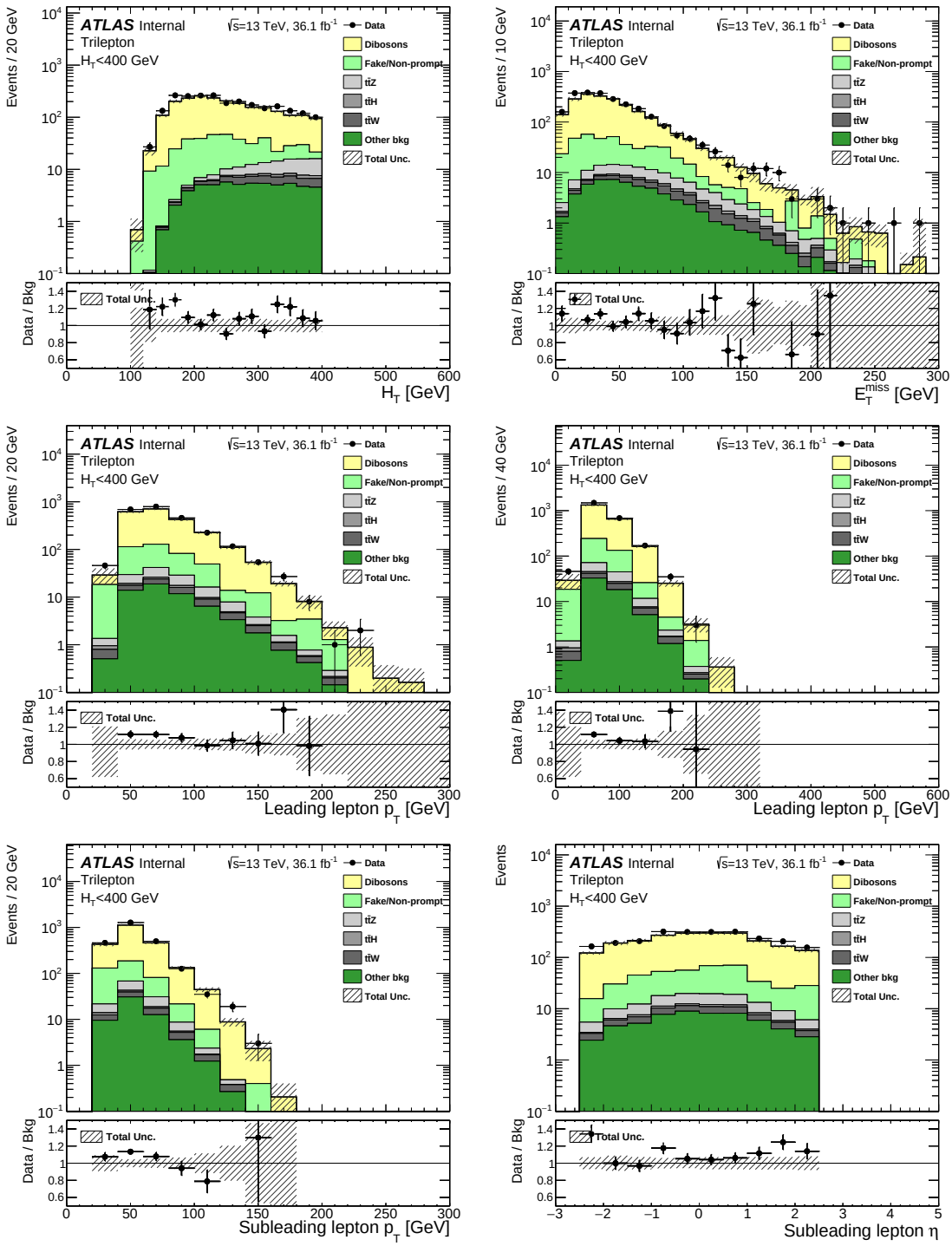

Figure 5.6: Control plots showing different variables for the trilepton (eee, eeμ, e$\mu\mu$, $\mu\mu\mu$) channels. The top row shows H_{T} (left) and $E_{\mathrm{T}}^{\mathrm{miss}}$ (right); the middle leading lepton p_{T} (left) and leading lepton η (right); the bottom row subleading lepton p_{T} (left) and subleading lepton η (right).

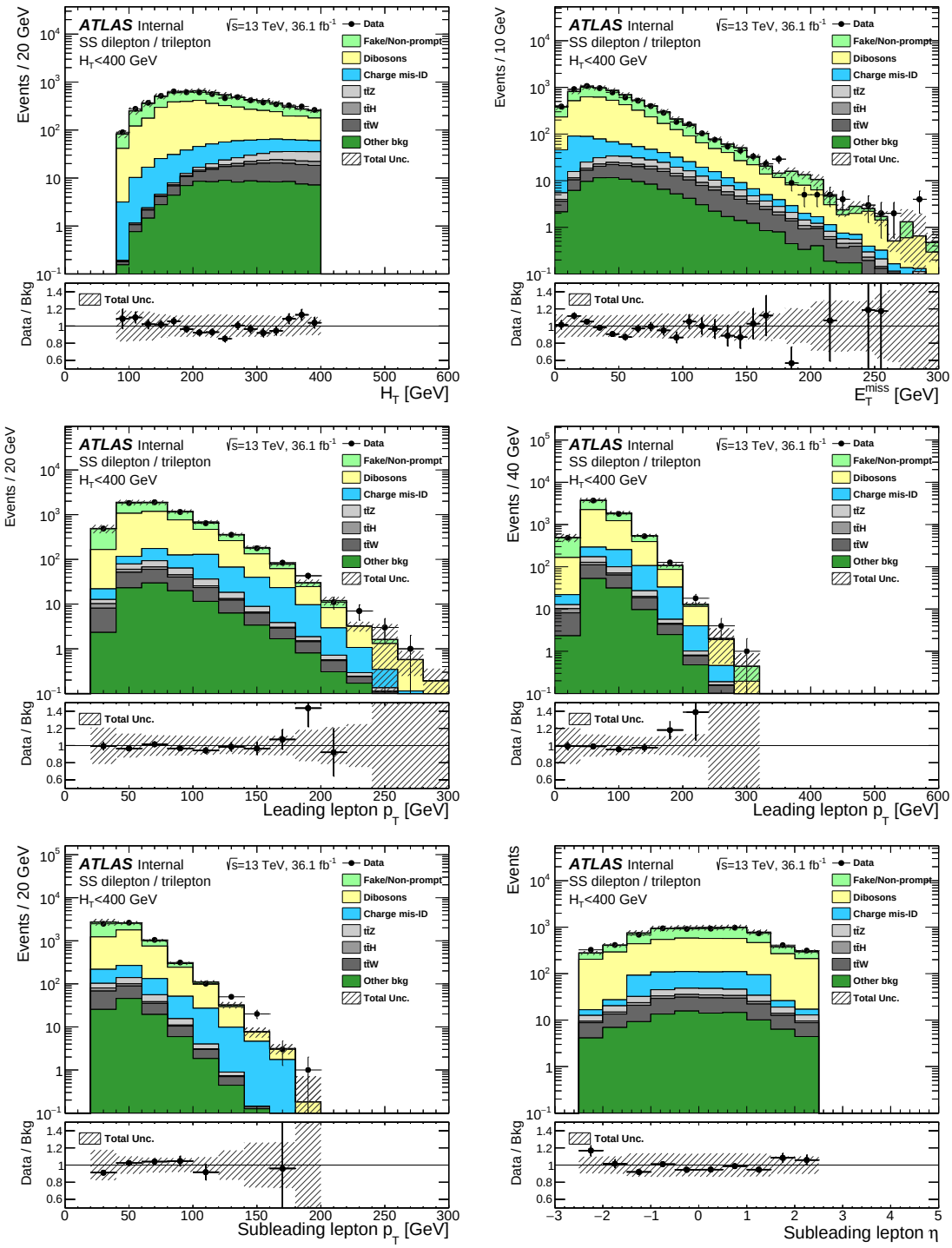

Figure 5.7: Control plots showing different variables for the dilepton and trilepton channels. The top row shows H_{T} (left) and $E_{\mathrm{T}}^{\mathrm{miss}}$ (right); the middle leading lepton p_{T} (left) and leading lepton η (right); the bottom row subleading lepton p_{T} (left) and subleading lepton η (right).

Process	*VR1b3l*	*VR2b3l*	*VR3b3l*
$t\bar{t}Z$	$69.87 \pm 0.65 \pm 6.01$	$65.62 \pm 0.65 \pm 5.84$	$4.56 \pm 0.20 \pm 0.49$
$t\bar{t}H$	$6.50 \pm 0.18 \pm 0.47$	$6.81 \pm 0.20 \pm 0.49$	$0.41 \pm 0.05 \pm 0.03$
$t\bar{t}W$	$10.44 \pm 0.30 \pm 1.37$	$9.37 \pm 0.29 \pm 1.27$	$0.31 \pm 0.09 \pm 0.05$
Dibosons	$92.80 \pm 6.65 \pm 12.01$	$7.71 \pm 2.07 \pm 1.17$	$0.17 \pm 0.46 \pm 0.05$
Fake/Non-prompt	$21.86 \pm 3.91 \pm 12.90$	$2.70 \pm 1.48 \pm 2.18$	$0.21 \pm 0.31 \pm 0.11$
Other bkg	$27.38 \pm 0.67 \pm 8.98$	$11.98 \pm 0.49 \pm 3.93$	$0.65 \pm 0.24 \pm 0.21$
Total bkg.	$228.84 \pm 7.78 \pm 20.72$	$104.19 \pm 2.69 \pm 7.58$	$6.31 \pm 0.65 \pm 0.55$
Data	248	126	5

Table 5.7: Trilepton validation region yields for all background processes and data. Yields are displayed as nominal ± stat. error ± syst. error.

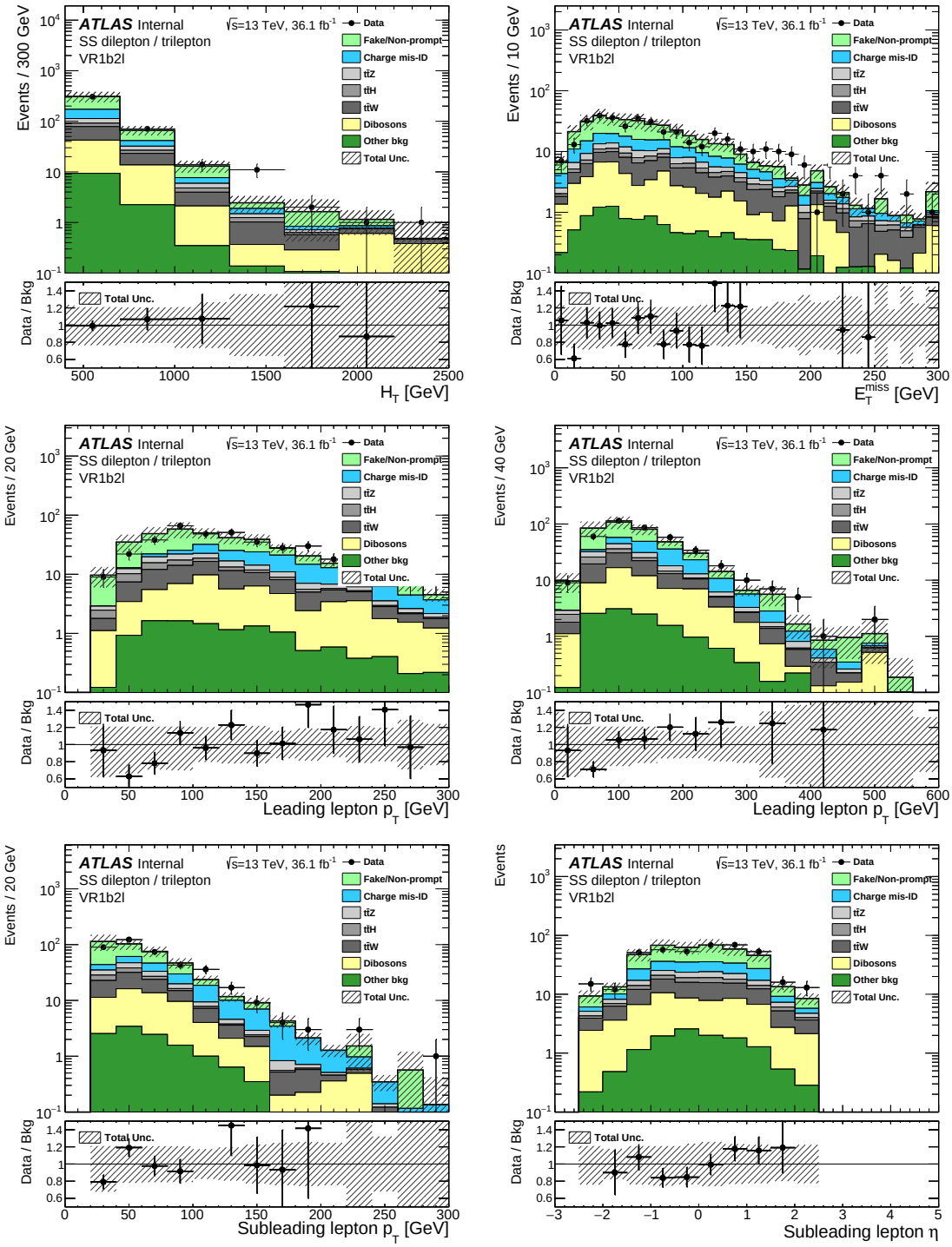

Figure 5.8: Validation plots showing different variables for VR1b2l (validation regions are defined in table 5.5.). The top row shows H_{T} (left) and $E_{\mathrm{T}}^{\mathrm{miss}}$ (right); the middle leading lepton p_{T} (left) and leading lepton η (right); the bottom row subleading lepton p_{T} (left) and subleading lepton η (right).

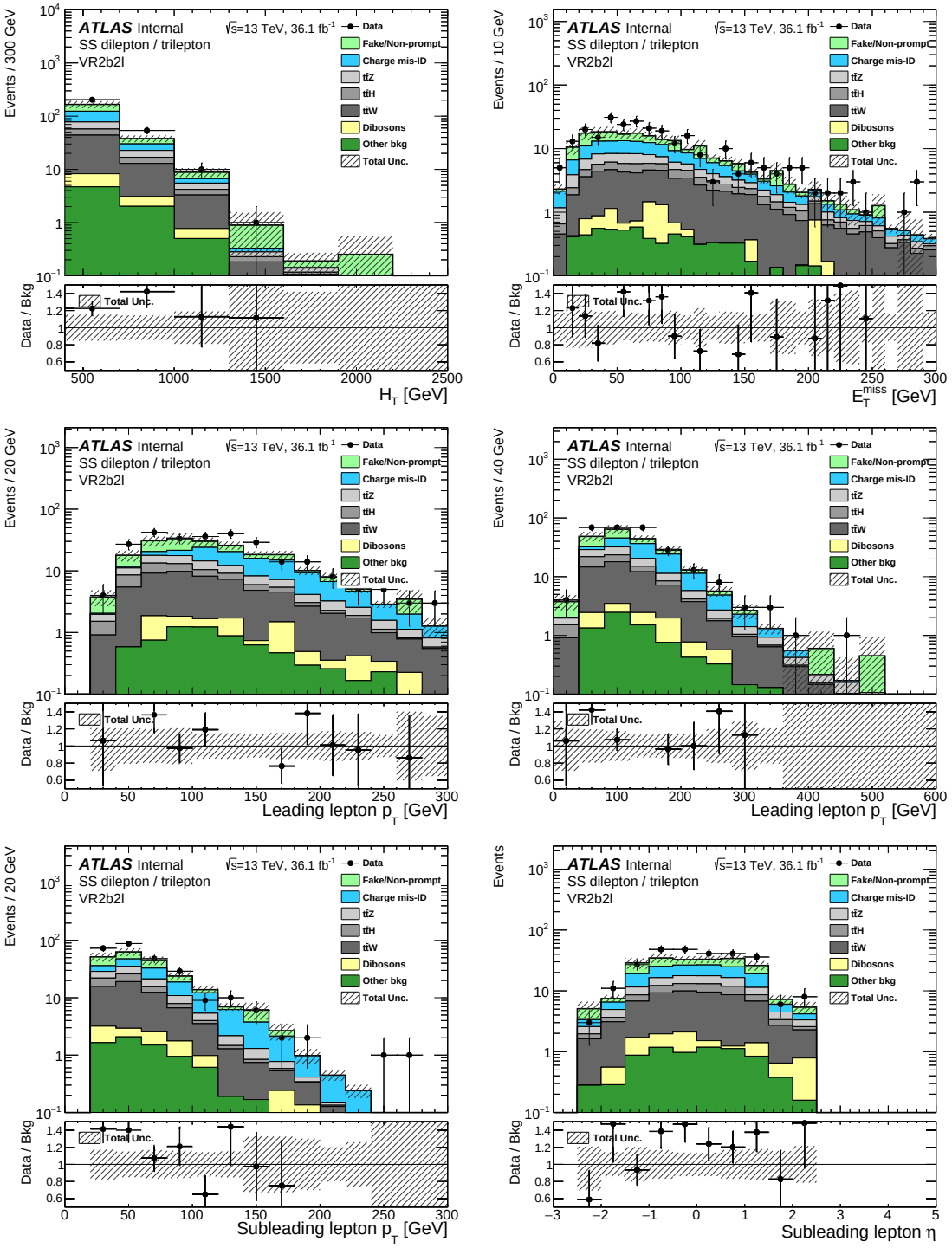

Figure 5.9: Validation plots showing different variables for VR2b2l (validation regions are defined in table 5.5.). The top row shows H_{T} (left) and $E_{\mathrm{T}}^{\mathrm{miss}}$ (right); the middle leading lepton p_{T} (left) and leading lepton η (right); the bottom row subleading lepton p_{T} (left) and subleading lepton η (right).

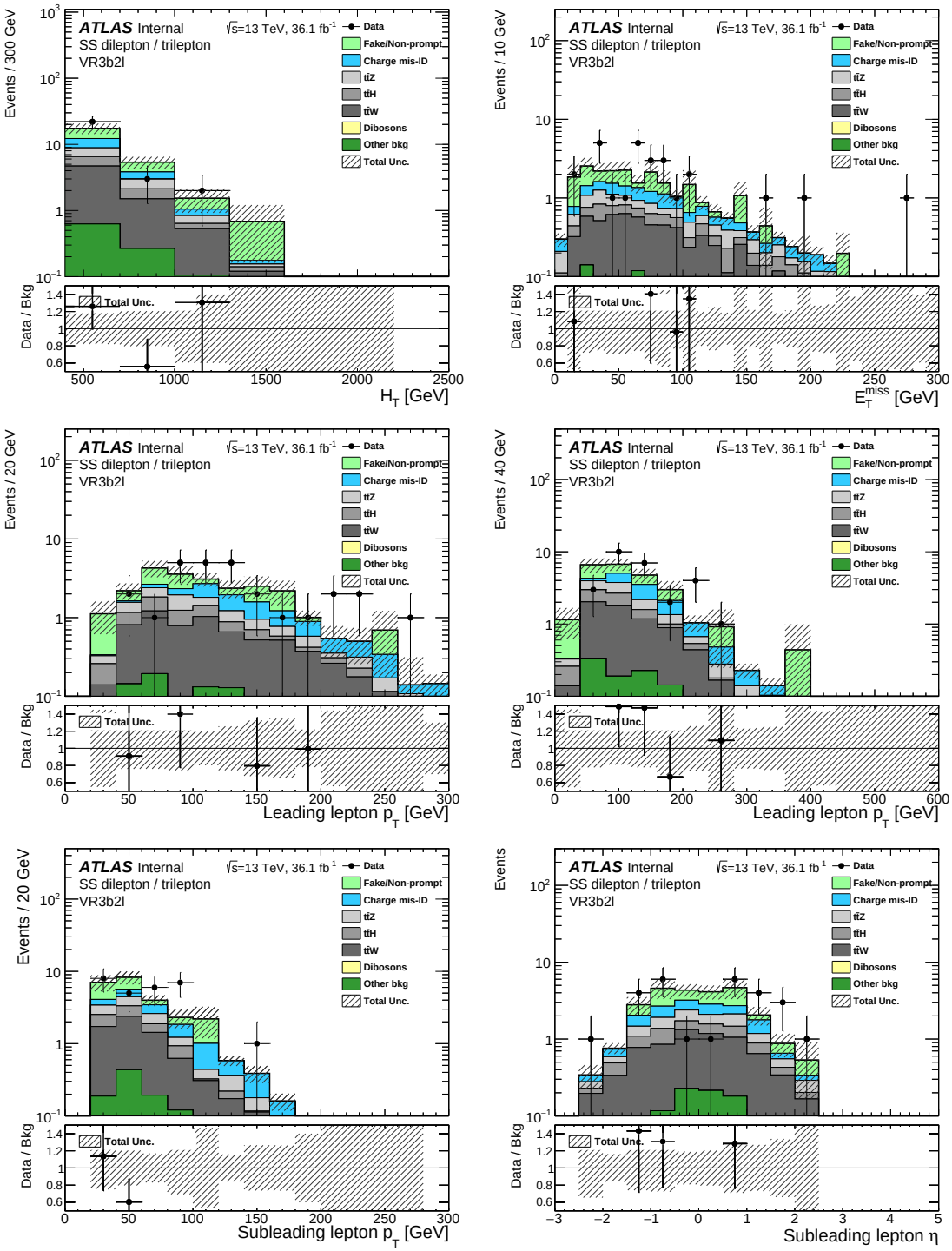

Figure 5.10: Validation plots showing different variables for VR3b2l (validation regions are defined in table 5.5.). The top row shows H_{T} (left) and $E_{\mathrm{T}}^{\mathrm{miss}}$ (right); the middle leading lepton p_{T} (left) and leading lepton η (right); the bottom row subleading lepton p_{T} (left) and subleading lepton η (right).

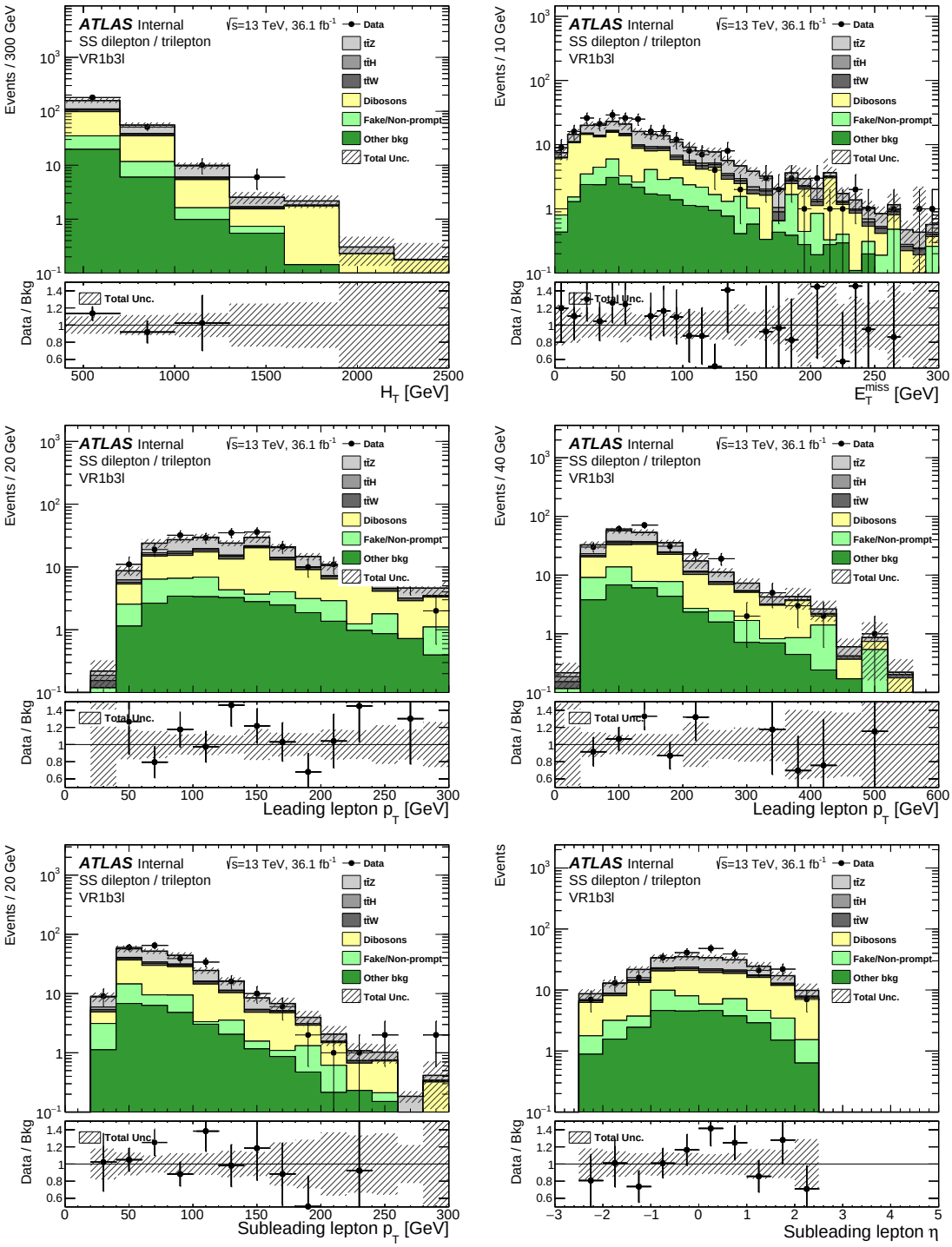

Figure 5.11: Validation plots showing different variables for VR1b3l (validation regions are defined in table 5.5.). The top row shows H_{T} (left) and $E_{\mathrm{T}}^{\mathrm{miss}}$ (right); the middle leading lepton p_{T} (left) and leading lepton η (right); the bottom row subleading lepton p_{T} (left) and subleading lepton η (right).

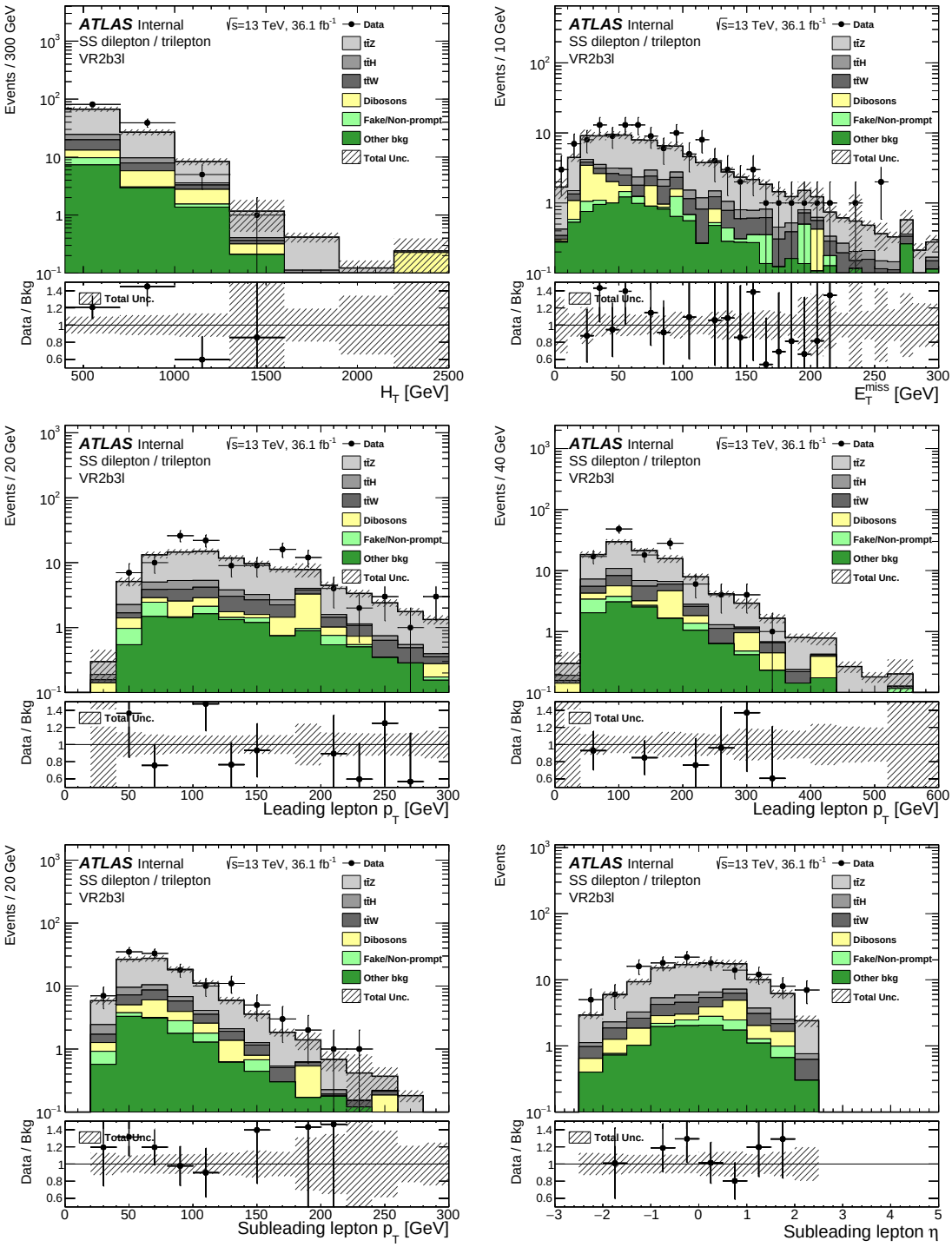

Figure 5.12: Validation plots showing different variables for VR2b3l (validation regions are defined in table 5.5.). The top row shows H_{T} (left) and $E_{\mathrm{T}}^{\mathrm{miss}}$ (right); the middle leading lepton p_{T} (left) and leading lepton η (right); the bottom row subleading lepton p_{T} (left) and subleading lepton η (right).

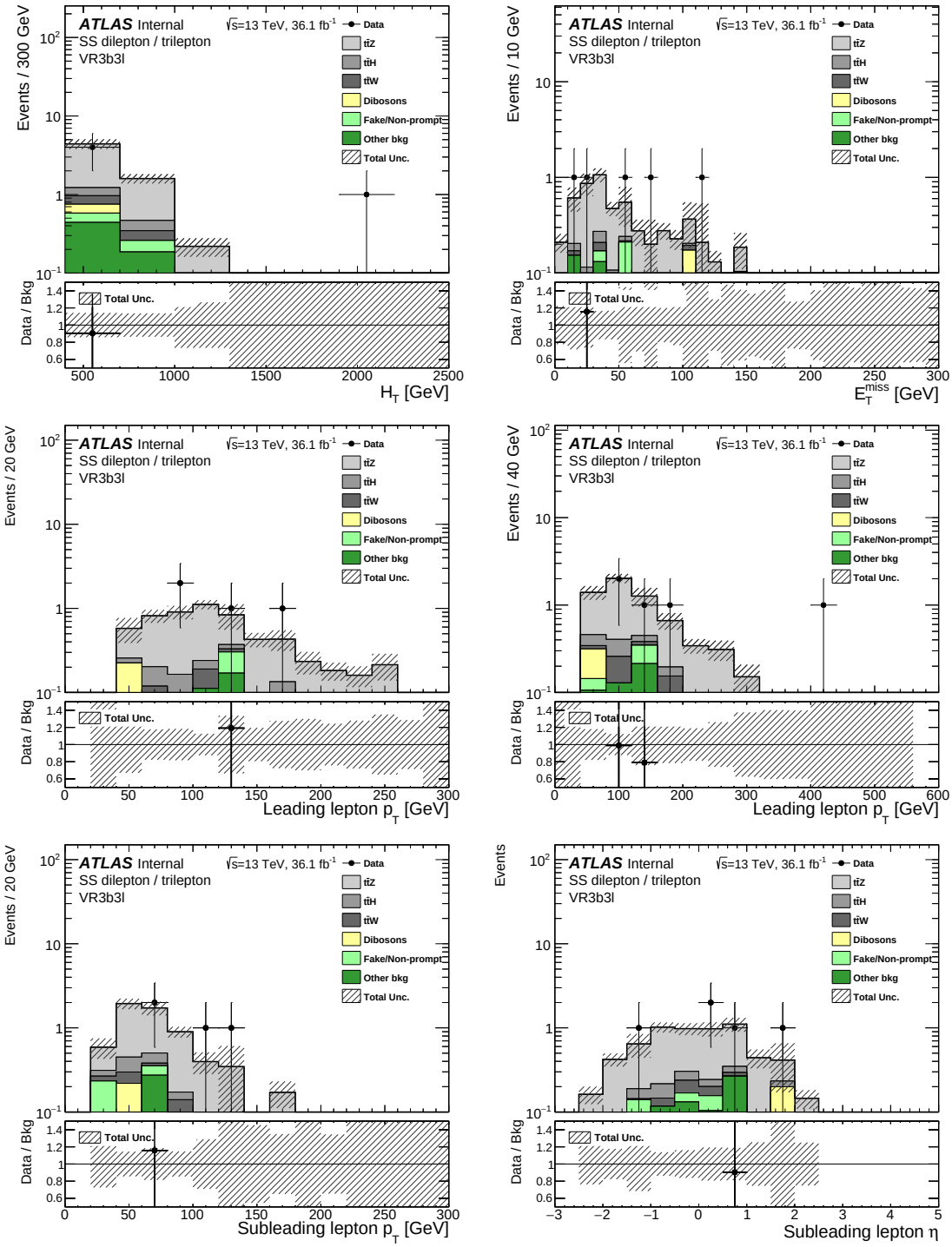

Figure 5.13: Validation plots showing different variables for VR3b3l (validation regions are defined in table 5.5.). The top row shows H_{T} (left) and $E_{\mathrm{T}}^{\mathrm{miss}}$ (right); the middle leading lepton p_{T} (left) and leading lepton η (right); the bottom row subleading lepton p_{T} (left) and subleading lepton η (right).

CHAPTER 6
Data Samples and Monte Carlo Backgrounds

Data accumulated over the course of the first ATLAS experimental runs of Run II during the years 2015−2016 is used for this analysis. The cumulative dataset totals 36.1 $\text{fb}^{-1}$of pp collisions at $\sqrt{s} = 13$ TeV. It is convention to use the term 'data' when referring to experimental data actually collected with the ATLAS detector. Simulated data are classified as Monte Carlo (MC) events or simulations. In order to glean information from ATLAS data, especially with respect to discovering new physics, comparisons to processes already understood via the Standard Model (SM) must be made. Therefore, this analysis uses MC to simulate SM processes that produce the same final state topology of interest: same-sign pairs of leptons, or trilepton events, with associated b-jets and relatively large total missing transverse energy. MC simulations constitute the irreducible backgrounds. MC simulations are also used to estimate the VLQ signal contribution given certain input variables, such as theoretical cross sections, mass, decay branching ratios, etc.

Aside from the irreducible MC backgrounds, another set of backgrounds arise from detector reconstruction inefficiencies, which are poorly modeled with MC simulations and need to be estimated using data samples. These constitute the data-driven backgrounds for this analysis, and are discussed in detail in Chapter 7. MC is also used to study data-driven backgrounds in more, limited detail, but the final estimate for the data-driven backgrounds is done using data.

This chapter is organized as follows. Section 6.1 describes the data stream sample production as well as data quality and luminosity determination. Section 6.2 describes the production of MC samples as well as the various MC generators used to simulate SM and signal processes. A brief discussion of the detector simulation is also presented.

6.1 Data Samples

Collision data at $\sqrt{s} = 13$ TeV taken during the latter half of 2015, continuing through the end of October 2016 are used for this analysis. The total integrated luminosity for this

period is 36.1 fb$^{-1}\pm$ 2.1%, where the uncertainty is derived using a method called van der Meer (vdM) $x-y$ beam separation scans performed in August 2015 and May 2016 [125]. The peak luminosity for the full dataset occurred in 2016 and was 1.38×10^{34} cm^{-2} s^{-1} [126]. The data runs for the dataset from 2015 through 2016 are listed in table 6.1. Periods are defined as blocks of data containing multiple runs, running alphabetically throughout the year. Each run can last for a few hours to a few days and contains multiple *LumiBlocks*. A *LumiBlock* is a time block used to delineate sequential frames in a data run with a particular trigger configuration [127]. The time frame is variable, but usually on the order of $1-2$ minutes.

Period	**Run Number**	**Date Range (YY-Month-DD)**
Data 2015: 3.21 fb^{-1}		
D	276262–276954	15-Aug-16 to 15-Aug-23
E	278880–279928	15-Sep-08 to 15-Sep-20
F	279932–280368	15-Sep-20 to 15-Sep-26
G	280423–281075	15-Sep-26 to 15-Oct-06
H	281317–281411	15-Oct-09 to 15-Oct-11
J	282625–284484	15-Oct-20 to 15-Nov-02
Data 2016: 32.9 fb^{-1}		
A	297730–300279	16-Apr-28 to 16-May-26
B	300345–300908	16-May-27 to 16-Jun-05
C	301912–302393	16-Jun-11 to 16-Jun-20
D	302737–303560	16-Jun-24 to 16-Jul-09
E	303638–303892	16-Jul-10 to 16-Jul-15
F	303943–304494	16-Jul-16 to 16-Jul-25
G	305380–306448	16-Aug-01 to 16-Aug-16
I	307126–308084	16-Aug-25 to 16-Sep-09
K	309375–309759	16-Sep-26 to 16-Oct-02
L	310015–311481	16-Oct-06 to 16-Oct-26

Table 6.1: Periods and run numbers for the 2015–2016 dataset accessed via the COMA database. The date of the each run is given as well.

The ATLAS TDAQ system, described in §3.2.4, is responsible for providing the data stream format used by the physics analyses. Different data streams correspond to data selected with different triggers. Each data event used in this analysis is triggered by at least one high p_{T} single lepton trigger or one dilepton trigger, which are provided by the electron and muon data streams. The triggers have different thresholds for lepton p_{T} and some have specific requirements on the ID quality of the lepton. The triggers used are discussed in detail in §4.2.3.

Figure 6.1 shows the total integrated luminosity over the $2015-2016$ data taking period, separated by year. The 2015 dataset totaled 3.2 fb^{-1} of quality data for physics analyses, and the 2016 dataset totaled 32.9 fb^{-1}. The difference in the green (LHC delivered) and yellow (ATLAS recorded) bands is mostly due to the TDAQ filtering of events. The difference in the blue (good for physics) bands is due to extra filtering of events if certain detector subsystems were off or not functioning within normal parameters.

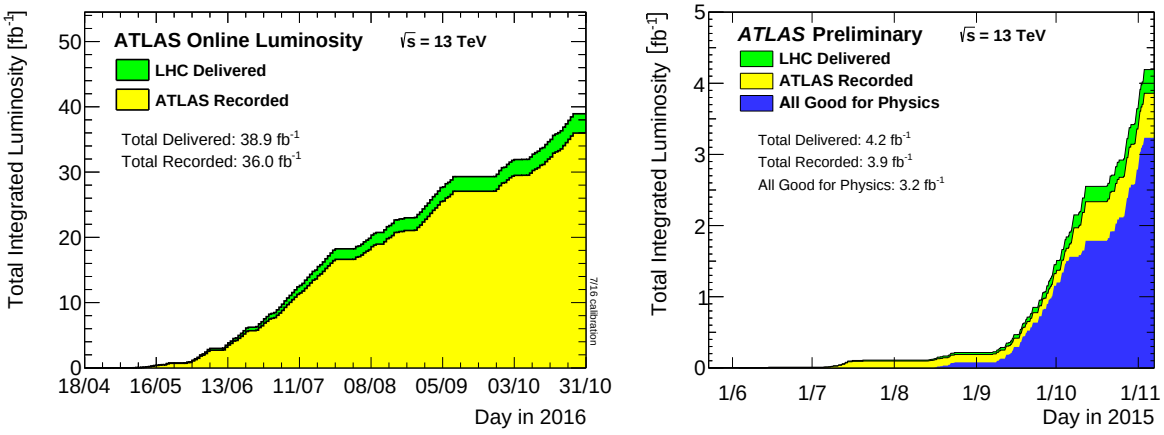

Figure 6.1: Integrated luminosity over the course of 2016 (left) and 2015 (right) recorded by ATLAS. The run number indicated good runs for physics only.

The *Data Quality* group provides an XML file, called a Good Runs List (GRL), for use by physics analyses, which have quality monitoring for the various runs of data with ATLAS. Due to potential complications with detector performance, calibration, electronics, noise, toroid or solenoid magnet issues, etc, some runs are not included in the final GRL used by the analyses [127]. This is why the total recorded and "good for physics" integrated luminosity is not necessarily the same. Most of these issues are transient and do not require the cessation of data acquisition during the particular run. Also, depending on which part of the detector to which an analysis is most sensitive, the runs with other detector components turned off or malfunctioning may not pose an issue for that analysis. In this case, the data from that run can still be safely used. The data runs in table 6.1 are chronological and constitute runs for which the majority of ATLAS subsystems were functioning within normal parameters.

6.2 Monte Carlo Samples

Simulated data, often referred to as Monte Carlo (MC), provide an important aspect to most physics analyses because simulations allow comparisons of the expectations from SM processes. MC simulations give an estimate of what to expect from known physics, and a comparison with data can potentially reveal new physics. MC events are treated the same way as data with respect to event filtering based on trigger p_{T} thresholds, $E_{\mathrm{T}}^{\mathrm{miss}}$ thresholds, etc as well as reconstruction, as discussed in §4.2. A flow chart of the simulated event process for ATLAS is shown in figure 6.2, beginning with the generators and ending with the reconstruction. The four major steps are *generation*, *simulation*, *digitization*, and *reconstruction*. *Generation* is done using at least one of several MC generators, described in more detail below, which focus on the fundamental interaction at the parton level and the resulting fast decay chain. The hard scatter differential cross section is calculated at this level using the matrix elements. This requires a set of Parton Distribution Functions (PDF) as input to the generator. *Simulation* is the next step that replicates the final state particles' interactions with the detector and other decays from the initial interaction. The output of the simulations is processed through the *digitization* stage, which emulates the digital electronics of the detectors to produce the Raw Data Objects (RDO). Finally, *reconstruction* of the RDO proceeds similarly to the way physics objects are produced from data.

Typically, an analysis will choose simulated events of a particular background or signal process rather than a generalized simulation of all data.MC simulations of particular processes are separated into different samples, sometimes using different generators and simulators due to the potential complexity of certain processes. *MC Truth* is also included in the early simulation process in order to save the information about a particle's properties, origin, parent, and daughter particles. It is often beneficial to use the *MC Truth* to study in more detail the behavior of certain particles given particle location within the detector and the event kinematics. For example, appendix B discusses additional studies using *MC Truth* on the data-driven backgrounds for this analysis.

6.3 Irreducible Backgrounds

Each background process has its own MC sample simulated using a particular generator, PDF set, and detector simulation. The dominant SM processes producing same-sign leptons are $t\bar{t}$ production plus a vector boson ($t\bar{t}$+$W/Z/WW$) and diboson production (WW/ZZ). Tree level diagrams for these processes are shown in Figures 6.3 and 6.4. Several other sources

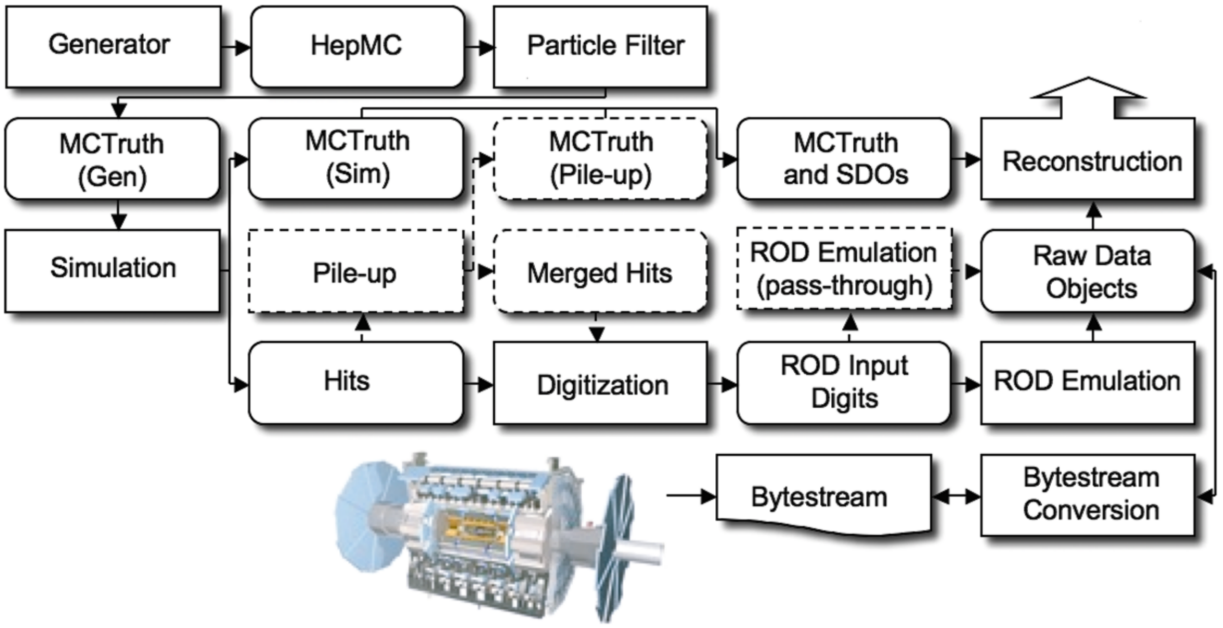

Figure 6.2: Flowchart of simulated data in ATLAS. Algorithms are in squared boxes, persistent data objects are in rounded boxes, and pile-up options for overlaying events are in dashed boxes [128].

produce same-sign leptons in the final state, although the cross sections are relatively small: tribosons (WWW/ZZZ), Higgs decay ($WH/ZH/t\bar{t}+H$), and multi-top (3-top and 4-top production). Table 6.2 summarizes the samples used for MC production of the irreducible backgrounds.

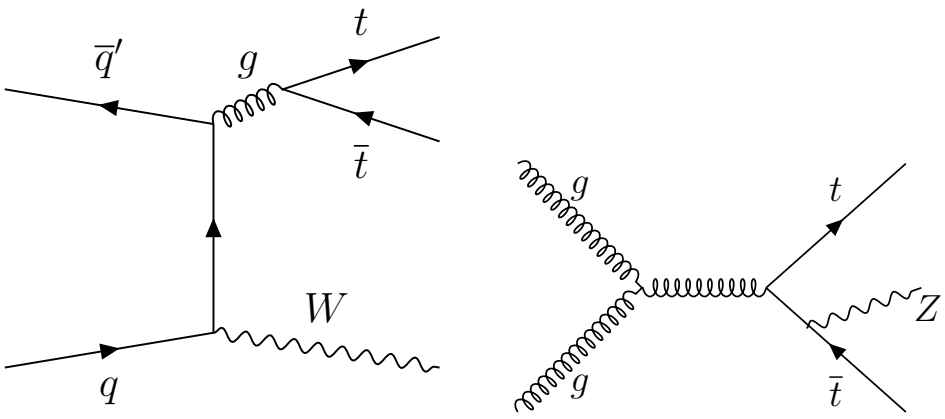

(a) $t\bar{t}+W$ (b) $t\bar{t}+Z$

Figure 6.3: Important LO Feynman diagrams for $t\bar{t}$ + V processes.

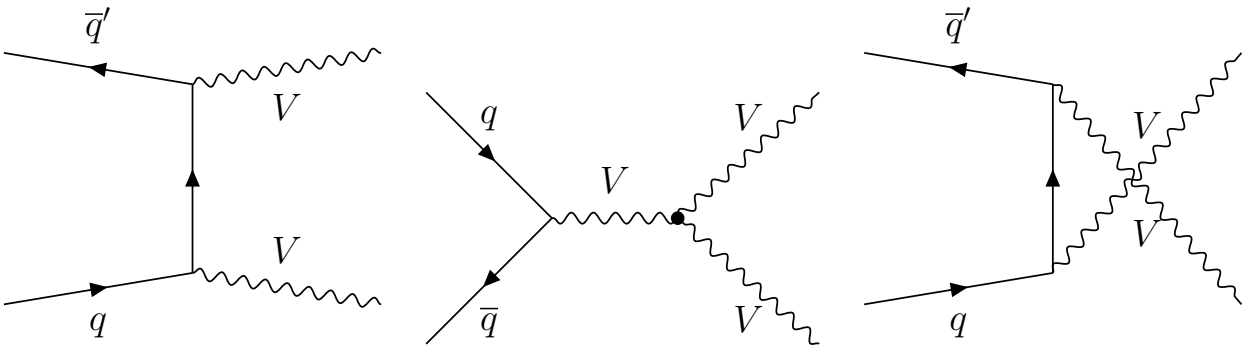

Figure 6.4: Important LO Feynman diagrams for diboson processes. The s-channel contains the TGC vertex.

Corrections to MC When comparing MC to data, each MC sample must be normalized and corrected to the specified integrated luminosity using the formula is equation 6.1. N_{corr} is the corrected number of events given by,

$$\begin{aligned} N_{\text{corr}} &= N_{\text{norm}} \times w_{\text{evt}} \\ \text{where } N_{\text{norm}} &= \frac{\sigma_{pp\to X} \times \text{BR} \times k \times \int \mathcal{L}\text{dt}}{N_{\text{MC}}} \end{aligned} \tag{6.1}$$

$$w_{\text{evt}} = \prod_i w_i \tag{6.2}$$

The number of simulated events in the MC sample is N_{MC}, $\int \mathcal{L}\text{dt}$ is the total integrated luminosity, $\sigma_{pp\to X}$ is the cross section of the process being simulated, calculated to LO or NLO as necessary, BR is the branching ratio of the process if the MC sample is for a particular final state (e.g. dilepton events only), and k is the k-factor, which is given by $k = \sigma_{\text{NLO}}/\sigma_{\text{LO}}$. Additionally, there is the event weight (w_{evt}) in equation 6.1 that must be applied to account for any correction factors in order to reliably model the MC with respect to the data. Equation 6.2 shows the product of all weights, and includes corrections for pileup and other event level disagreements with data as well as scale factors for jets, like the b-tagging working point (77%) and JVT calculation. Corrections for lepton reconstruction, identification, and isolation efficiencies are applied as scale factors as well. The scale factors are derived by using a specific data samples to calibrate the simulated events and calculated as the ratio of data to MC for whatever observable for which the scale factor is being derived.

Sample DSID	**Simulated Process**	**Generator**	**PDF set**	**Cross section [pb]**	**k-factor**	**Detector Simulation**
		$t\bar{t}+V$				
410155	$t\bar{t}+W$	MG5+aMC@NLO + Pythia 8	NNPDF3.0NLO	0.54830	1.10	FullSim
410218	$t\bar{t}+Z \to t\bar{t}ee$	MG5+aMC@NLO + Pythia 8	NNPDF3.0NLO	0.036888	1.12	FullSim
410219	$t\bar{t}+Z \to t\bar{t}\mu\mu$	MG5+aMC@NLO + Pythia 8	NNPDF3.0NLO	0.036895	1.12	FullSim
410220	$t\bar{t}+Z \to t\bar{t}\tau\tau$	MG5+aMC@NLO + Pythia 8	NNPDF3.0NLO	0.036599	1.12	FullSim
		$t\bar{t}+H$				
343365	$t\bar{t}+H$ dilepton	aMC@NLO + Pythia 8	NNPDF3.0NLO	0.05343	1.00	FullSim
343366	$t\bar{t}+H$ semileptonic	MG5+aMC@NLO + Pythia 8	NNPDF3.0NLO	0.22276	1.00	FullSim
343367	$t\bar{t}+H$ all hadronic	MG5+aMC@NLO + Pythia 8	NNPDF3.0NLO	0.23082	1.00	FullSim
		VH				
342284	$WH, W \to$ any, $H \to$ incl.	Pythia 8	NNPDF2.3LO	1.1021	1.00	FullSim
342285	$ZH, Z \to$ any, $H \to$ incl.	Pythia 8	NNPDF2.3LO	0.60072	1.00	FullSim
		Diboson VV				
361063	$ZZ \to llll$	Sherpa 2.2.1	CTEQ10	12.805	0.91	FullSim
361064	$ZW^- \to lll\nu$ SF Minus	Sherpa 2.2.1	CTEQ10	1.8446	0.91	FullSim
361065	$ZW^- \to lll\nu$ OF Minus	Sherpa 2.2.1	CTEQ10	3.6235	0.91	FullSim
361066	$ZW^+ \to lll\nu$ SF Plus	Sherpa 2.2.1	CTEQ10	2.5656	0.91	FullSim
361067	$ZW^+ \to lll\nu$ OF Plus	Sherpa 2.2.1	CTEQ10	5.0169	0.91	FullSim
361069	$WW \to ll\nu\nu + jj$ (EW4)	Sherpa 2.2.1	CTEQ10	0.025797	0.91	FullSim
361070	$WW \to ll\nu\nu + jj$ (EW6)	Sherpa 2.2.1	CTEQ10	0.043004	0.91	FullSim
361071	$ZW \to lll\nu + jj$ (EW6)	Sherpa 2.2.1	CTEQ10	0.042017	0.91	FullSim
361072	$ZZ \to llll + jj$ (EW6)	Sherpa 2.2.1	CTEQ10	0.031496	0.91	FullSim
361073	$gg \to llll$	Sherpa 2.2.1	CTEQ10	0.020931	0.91	FullSim
		Triboson VVV				
361620	$WWW \to l\nu l\nu l\nu$	Sherpa 2.2	CTEQ10	0.008343	1.00	FullSim
361621	$WWZ \to l\nu l\nu ll$	Sherpa 2.2	CTEQ10	0.001734	1.00	FullSim
361622	$WWZ \to l\nu l\nu\nu\nu$	Sherpa 2.2	CTEQ10	0.0034299	1.00	FullSim
361623	$WZZ \to l\nu llll$	Sherpa 2.2	CTEQ10	0.00021783	1.00	FullSim
361624	$WZZ \to l\nu ll\nu\nu$	Sherpa 2.2	CTEQ10	0.0019248	1.00	FullSim
361625	$ZZZ \to llllll$	Sherpa 2.2	CTEQ10	1.7059e-05	1.00	FullSim
361626	$ZZZ \to lllll\nu\nu$	Sherpa 2.2	CTEQ10	0.00044125	1.00	FullSim
		Other top-quark				
304014	ttt	MG5+aMC@NLO + Pythia 8	NNPDF2.3LO	0.0016398	1.00	AFII
410080	$t\bar{t}t\bar{t}$	MG5+aMC@NLO + Pythia 8	NNPDF2.3LO	0.0091622	1.0042	FullSim
410081	$t\bar{t}+WW$	MG5+aMC@NLO + Pythia 8	NNPDF2.3LO	0.0081	1.22	FullSim
410050	$t+Z$	MG5+aMC@NLO + Pythia 8	CTEQ6L1	0.24013	1.00	FullSim
410215	$t+WZ$	MG5+aMC@NLO + Pythia 8	NNPDF2.3LO	0.015558	1.00	FullSim

Table 6.2: MC Samples produced for the irreducible backgrounds in this analysis. The lepton label (l) means an electron or muon. The DSID number refers to the unique sample identification number in the ATLAS MC production. The generators, PDF, *k-factor*, and detector simulators are described in the text.

6.3.1 Generators

Several event generators are used to produce the MC simulations. These are, in general, used by not just ATLAS, but a variety of high energy physics experiments and phenomenology studies. The generators produce final state particles from simulating parton level interactions and their decay chains [128, 129]. They are capable of simulating the physics on very small distance scales, using perturbation theory, as well as larger scales up to and including hadron formation and their decay products [130].

Generators typically begin by calculating the leading order (LO) differential cross section for the hard scatter process. Next-to-leading order (NLO) calculations are more difficult to evaluate, especially when QCD is involved (as is the case with hadron collisions). Therefore, in order to calculate the NLO cross sections, a *k-factor* is typically calculated which multiplies the LO calculation with a NLO correction factor.

An important input to the generators is the set of parton distribution functions (PDF set). A PDF set is used to specify the fraction of momentum attributed to each parton in the simulation of the hard scatter collision. As discussed in more detail in §2.1.3, PDFs are not directly calculable from perturbative QCD. Instead, data from measurements of deep inelastic scattering experiments are used to quantify the internal structure of the protons (and other hadrons) in a collision. Data from these measurements are input into PDF wrapper codes. An example is the Les Houches Accord PDF sets (LHAPDF) [131, 132], which combine data into PDF sets common to a type of PDF with predicted uncertainties on the PDF. Each generator is typically used in conjunction with a particular PDF set. The main ones used for MC samples for this analysis are CTEQ [133, 134] and NNPDF v2.3 or NNPDF v3.0 (either at LO or NLO as necessary) [135, 136], with additional tunes provided by Perugia 2012 (P2012) [137] and A14 [136].

The main generators used for simulation samples in this analysis are summarized below. In some cases, more than one generator is used to produce the samples. This is because some generators are designed to handle the matrix element calculations and others the parton hadronization process (that produces the jets in an event).

MadGraph_aMC@NLO MadGraph is a `Python`-based generator capable of evaluating any Leading Order (LO) SM and BSM process. Next-to-Leading Order (NLO) corrections can be applied as well. aMC@NLO, as its name implies, is capable of evaluating matrix elements at NLO. The generator used for some of the major backgrounds in this analysis ($t\bar{t}+V$, $t\bar{t}+H$) is a combination of MadGraph5 and aMC@NLO. The combi-

nation software integrates together and supersedes the previous versions of the individual generators MadGraph and aMC@NLO [138]. This generator is capable of handling the matrix element calculations for tree level and NLO amplitudes of most major processes. It is usually combined with another generator to produce the parton showering simulations.

Pythia Two versions of Pythia are used: Pythia 6 [139] and Pythia 8 [140]. Pythia 6 is an older conglomeration of code used extensively by many particle physics experiments for generating MC events. The newer, standalone successor to Pythia 6 is Pythia 8. The Pythia generator can simulate hundreds of $2 \to n$ parton showering processes and is capable of handling hard scattering of pp collisions, in addition to $p\bar{p}$, pion scattering, and same generation lepton scattering. Parton showering for initial and final state evolution is ordered in p_{T}. Also included internally is the underlying event calculation. Typically, Pythia is combined with another generator for the matrix element calculations. PDF sets can be input to Pythia from the LHAPDF and Les Houches Event Files (LHEF) libraries.

A combination of MadGraph v5 aMC@NLO v2.2.2 interfaced with Pythia v8.186 is used for modeling Next-to-Leading-Order (NLO) or Leading Order (LO) simulations of $t\bar{t}+W/Z$, $t\bar{t}+H$, and the multi-top ($t\bar{t}t\bar{t}$, ttt, etc.) samples.

Powheg Powheg [141] is similar to aMC@NLO and calculates the hard scatter matrix elements at LO, with additional NLO corrections available. The resulting events are fed to a parton showering MC generator (e.g. Sherpa). Powheg is used to generate the dijet, $t\bar{t}$, and single top (t) samples for the fake/non-prompt lepton background in this analysis.

Sherpa Another general purpose parton showering generator is Sherpa [129]. Parton showering for initial and final state evolution is ordered in p_{T}. Sherpa v2.2.1 is used in this analysis to simulate the $V+$ jets, diboson (VV), and triboson (VVV) background samples.[1]

Protos An event generator often used for simulating several SM and BSM processes at LO involving the top quark is called Protos [142]. Typically, it is combined with other generators like Pythia for parton showering. Protos is used to simulate some of the signal samples in this analysis, particularly, the pair production of the different VLQ models (T, B, $T_{5/3}$).

[1] Here, V stands for W or Z bosons.

EvtGen Events with many jets are inherently more complicated to simulate, so a dedicated generator is often used to model the decay of bottom and charm flavored hadron decays. The generator used is called EvtGen [143]. In this analysis, the EvtGen v1.2.0 program is employed specifically to model bottom and charm hadron decays in several of the $t\bar{t}$ + boson backgrounds.

6.3.2 Detector Simulation

After calculating the matrix elements and parton showering for the simulated events, the next step is simulating the detector response. Geant4 [144] is a general purpose, object-oriented simulation toolkit used to emulate the ATLAS detector's response with information about how particles interact with matter. It is designed to employ the latest upgrades to the detector geometry, including active and inactive layers, and response rates. As such, Geant4 provides a highly reliable simulation of the full detector, but at a cost of relatively high CPU time. Due to the complexity of all the calculations involved in simulating the particle interactions in all parts of the detector, it takes roughly $15-20$ minutes per event to simulate full events (this is called *FullSim* for full simulation). Faster simulation procedures are available in Geant4 as well, but at reduced accuracy. These are called: *FastG4*, which uses pre-simulated calorimeter showers to speed up simulation, *AltFastII* simulation (also, *AFII*), which uses a parametrized calorimeter simulation, and *AltFastIIF*, which uses both parametrized calorimeter and fast track simulations.

The full simulation creates hits that emulate the tracker and calorimeter responses and reconstructs the particle's p_{T} through a process of transporting the particle step-by-step through the detectors. The fast simulation speeds up the momentum calculation by smearing p_{T} through the tracker. The digitization of the hits emulates the actual data digitization from the detector electronics. Reconstruction of simulation events in the Raw Data Object (RDO) format then follows the same procedure as is done using data.

6.4 Signal Samples

Monte Carlo samples are also used to simulate the different signal models in this analysis. Simulations of these signals are done with standard MC generators. For VLQ, the generators most often used combine Protos 2.2 with Pythia 8. Simulations of the signals used to predict expected yields in the control, validation, and signal regions as well as for optimization purposes, as described in §5.3. One MC sample with a unique DSID number is produced

per mass point for most of the signal model. Multiple mass points over a large range for the VLQ signals are used to set limits, since the mass of the different varieties of VLQ are unknown. Simulated events are generated for the mass points shown in table 6.3. Each signal includes a range of mass points for the VLQ models. Even though masses below roughly 750−800 GeV are excluded due to previous searches using 8 and 13 TeV data, signal mass points are generated for VLQ mass above 500 GeV. Mass intervals of 50 or 100 GeV are used to give relatively smooth interpolation in the limit setting, discussed more in §9.4. VLQ next-to-next-to-leading order (NNLO) cross sections are calculated for 13 TeV, found in reference [145]. Note that all VLQ produced in pairs have the same cross sections (see figure 2.10).

Sample DSID (TTS)	**Sample DSID** (BBS)	**Sample DSID** ($T_{5/3}$)	**VLQ Mass (GeV)**	**Events simulated**	**Cross section [pb]**
Pair Produced Vector-Like Quarks					
302468	302486	302504	500	250,000	3.38
302469	302487		600	250,000	1.16
302470	302488	302505	700	500,000	0.455
302471	302489		750	500,000	0.295
302472	302490	302506	800	500,000	0.195
302473	302491		850	500,000	0.132
302474	302492	302507	900	500,000	0.0900
302475	302493		950	500,000	0.0624
302476	302494	302508	1000	500,000	0.0438
302477	302495		1050	500,000	0.0311
302478	302496	302509	1100	500,000	0.0223
302479	302497		1150	500,000	0.0161
302480	302498	302510	1200	500,000	0.0117
302481	302499		1300	250,000	0.00634
302482	302500	302511	1400	250,000	0.00350

Table 6.3: Vector-Like Quark production MC signal samples for 15 mass points of T and B and 8 mass points of VLQ $T_{5/3}$ pair production. All pair produced samples were simulated using PROTOS 2.2 + PYTHIA8 event generator, the PDF calculation was done using the NNPDF2.3LO PDF set, and the detector full simulation was GEANT4.

CHAPTER 7
Data-Driven Background Estimation

As described in §6.3, same-sign lepton pairs resulting from W, Z, or τ decays that originate from well understood SM processes can be simulated using Monte Carlo (MC). These processes are classified in this analysis as irreducible background. Another category of backgrounds must be modeled with *data* instead of MC due to difficulties in modeling detector-related effects. Included in this category are the following:

- Objects that are sometimes reconstructed and identified as real leptons but are not, in fact, real leptons. This can happen, for example, when a jet is mistakenly identified as a lepton due to similar calorimeter features or significant overlap in the object reconstruction.
- Leptons that are real, but that originate from SM quark decays (typically c or b quarks), rather than the hard scatter process, are classified as non-prompt.
- Leptons that are mis-characterized in terms of their charge – called charge mis-identified leptons.

Leptons belonging to the first two categories are classified as *fake/non-prompt* leptons. Leptons belonging to the third category are classified as charge mis-identified (*charge mis-id*) leptons. It should be noted that there can be some overlap between these two backgrounds, and how this is dealt with is discussed in §7.3. Since these leptons originate mostly from detector irregularities or reconstruction effects, these backgrounds together are also sometimes called instrumental backgrounds. Instrumental backgrounds are typically estimated using data, instead of MC, since detector effects and the statistical nature of the physics processes which lead to these mis-measurements are difficult to accurately model with simulations. Thus, the estimate of these backgrounds use a *data-driven* approach, and therefore these

backgrounds are also sometimes referred to as *data-driven* backgrounds.[1]

This chapter describes the data-driven estimation methods of the instrumental backgrounds. Section 7.1 discusses the *fake/non-prompt* lepton background and the likelihood Matrix Method used for the estimation. Section 7.2 discusses the *charge mis-id* background estimation using a likelihood minimization charge flip-rate method. Section 7.3 discusses the overlap removal between the two instrumental backgrounds.

7.1 Fake and Non-prompt Lepton Background

One of the major instrumental backgrounds in this analysis is the fake and non-prompt lepton background. Both fake and non-prompt sources of leptons are included in this background because they can be estimated using the same method, described below. This is an important background to estimate given its large contribution for both electrons and muons in the control and validation regions defined in §5.3.4.

Fake lepton sources include heavy flavor charged hadrons being mis-identified as leptons, most often if the hadronic signature in the detector is overlapping with a photon or neutral pion. For example, an electron signature may look similar to a photon signature coupled with a charged hadronic signature that leaves behind a track in the inner detector could lead to identifying and reconstructing the combined object as a fake lepton, if both point in roughly the same direction. Non-prompt leptons can come from a variety of sources including semi-leptonic decay of SM b and c quarks, photon conversions, etc.

7.1.1 Samples

Single lepton data samples are produced to estimate this background using a looser lepton requirement than the ID quality and isolation definitions used for leptons in the main analysis. The looser definition is used to calculate the efficiencies for the Matrix Method, which is described in the next section. The data samples contain single lepton events, where each event contains either one electron or one muon. Selection criteria similar to what is described in §5.2 are used to select objects and events, except the selection for real and fake control regions for this background is separate from the main analysis selection. MC samples

[1]For the purposes of this dissertation, the use of the term 'data-driven' is typically applied in reference to the estimation of the background, whereas 'instrumental' is in reference to the backgrounds or when specifically talking about the detectors. However, sometimes 'data-driven backgrounds' is used and therefore should be interpreted as interchangeable with 'instrumental backgrounds.'

are also used to estimate the prompt contamination in the fake control region, described next, and that contamination is subtracted from the fake sample measured from data.

Sample DSID	Simulated Process	Generator	PDF	Cross section [pb]	k-factor	Detector Simulation
			$t\bar{t}$			
410501	$t\bar{t}$	Powheg+Pythia 8	P2012	377.9932	1.195	FastSim
			W+jets			
364156 - 364169	$W \to \mu\nu$ + jets	Sherpa 2.2.1	NNPDF3.0NNLO	15770.00 - 1.23	0.9702	FastSim
364170 - 364183	$W \to e\nu$ + jets	Sherpa 2.2.1	NNPDF3.0NNLO	15769.64 - 1.23	0.9702	FastSim
364184 - 364197	$W \to \tau\nu$ + jets	Sherpa 2.2.1	NNPDF3.0NNLO	15799.44 - 1.23	0.9702	FastSim
			Z+jets			
364100 - 364113	$Z \to \mu\mu$ + jets	Sherpa 2.2.1	NNPDF3.0NNLO	1630.22 - 0.15	0.9751	FastSim
364114 - 364127	$Z \to ee$ + jets	Sherpa 2.2.1	NNPDF3.0NNLO	1627.18 - 0.15	0.9751	FastSim
364128 - 364141	$Z \to \tau\tau$ + jets	Sherpa 2.2.1	NNPDF3.0NNLO	1627.73 - 0.15	0.9751	FastSim
			Diboson $WW/WZ/ZZ$			
361063	$ZZ \to llll$	Sherpa 2.2.1	CTEQ10	12.805	0.91	FullSim
361064	$ZW^- \to lll\nu$ SF Minus	Sherpa 2.2.1	CTEQ10	1.8446	0.91	FullSim
361065	$ZW^- \to lll\nu$ OF Minus	Sherpa 2.2.1	CTEQ10	3.6235	0.91	FullSim
361066	$ZW^+ \to lll\nu$ SF Plus	Sherpa 2.2.1	CTEQ10	2.5656	0.91	FullSim
361067	$ZW^+ \to lll\nu$ OF Plus	Sherpa 2.2.1	CTEQ10	5.0169	0.91	FullSim
361069	$WW \to ll\nu\nu + jj$ (EW4)	Sherpa 2.2.1	CTEQ10	0.025797	0.91	FullSim
361070	$WW \to ll\nu\nu + jj$ (EW6)	Sherpa 2.2.1	CTEQ10	0.043004	0.91	FullSim
361071	$ZW \to lll\nu + jj$ (EW6)	Sherpa 2.2.1	CTEQ10	0.042017	0.91	FullSim
361072	$ZZ \to llll + jj$ (EW6)	Sherpa 2.2.1	CTEQ10	0.031496	0.91	FullSim
361073	$gg \to llll$	Sherpa 2.2.1	CTEQ10	0.020931	0.91	FullSim
			Single top (t)			
410011	$t \to bl\nu$ t-channel	Powheg+Pythia 6	P2012	43.739	1.0094	FullSim
410012	$\bar{t} \to \bar{b}l\nu$ t-channel	Powheg+Pythia 6	P2012	25.778	1.0193	FullSim
410013	$W + t$	Powheg+Pythia 6	P2012	34.009	1.054	FullSim
410014	$W + \bar{t}$	Powheg+Pythia 6	P2012	33.989	1.054	FullSim
410025	$t \to bl\nu$ s-channel	Powheg+Pythia 6	P2012	2.0517	1.005	FullSim
410026	$\bar{t} \to \bar{b}l\nu$ s-channel	Powheg+Pythia 6	P2012	1.2615	1.022	FullSim

Table 7.1: Instrumental background samples used for estimation fake and non-prompt background estimation. The cross section values for W/Z+jets are rounded to two decimal places and only a range is given because the cross sections vary based on which sample is used. To find more precise values of the cross sections see [146].

Table 7.1 shows the MC samples used to estimate the prompt contribution in the fake/non-prompt lepton background. The primary processes that most often contribute to the prompt contribution are $t\bar{t}$ and V+jets because the prompt contamination includes leptons from vector bosons (W/Z), τ, and/or top decays. Also included are diboson ($WW/WZ/ZZ$) and single top processes, where the top decays semi-leptonically.

Several studies are also performed using these MC samples (mostly the $t\bar{t}$ sample) to better understand the physics processes that lead to fake and non-prompt leptons. These

studies are described in more detail in appendix B.3.

7.1.2 Matrix Method

The Matrix Method (MM) is an algorithm used to calculate the number of fake/non-prompt leptons in a sample, and is commonly used in analyses sensitive to such backgrounds [147–149]. It is designed to take advantage of the differences between fake lepton and real lepton behavior with respect to the lepton definitions and certain kinematic variables. A set of *loose* leptons is identified (this definition is called *MM-loose*), which has a relaxed definition of the lepton ID quality and isolation criteria from the set of *tight* leptons (this definition is called *MM-tight*). *MM-tight* is the definition used for leptons in the main analysis. In order to preserve the logic of the MM, *MM-tight* $\subset$ *MM-loose*. Table 7.3 summarizes the definitions for each set of leptons as well as the triggers used in the efficiency calculations. Table 5.1 gives an overview of the selection criteria for the electron and muon lepton definitions for *MM-loose* and *MM-tight*.

The MM can be defined for single lepton, dilepton, and trilepton events, as shown below. The MM is extendible to higher numbers of leptons, but the mathematics of inverting the matrix gets complicated quickly since the matrix dimensions become $2^n \times 2^n$, where n is the number of leptons per event. In this analysis, the dilepton and trilepton MM are used because the event selection requires at least two *tight* or three *tight* leptons in the final state. Equation 7.1 shows the system of equations used to extract the number of fakes from a given sample with two leptons in each event.

$$\begin{pmatrix} N_{tt} \\ N_{t\bar{t}} \\ N_{\bar{t}t} \\ N_{\bar{t}\bar{t}} \end{pmatrix} = \mathbf{M}_{4\times4} \begin{pmatrix} N_{rr} \\ N_{fr} \\ N_{rf} \\ N_{ff} \end{pmatrix}, \text{ where } \mathbf{M}_{4\times4} = \begin{pmatrix} r_1 r_2 & r_1 f_2 & f_1 r_2 & f_1 f_2 \\ r_1 \overline{r_2} & r_1 \overline{f_2} & f_1 \overline{r_2} & f_1 \overline{f_2} \\ \overline{r_1} r_2 & \overline{r_1} f_2 & \overline{f_1} r_2 & \overline{f_1} f_2 \\ \overline{r_1}\,\overline{r_2} & \overline{r_1}\,\overline{f_2} & \overline{f_1}\,\overline{r_2} & \overline{f_1}\,\overline{f_2} \end{pmatrix} \tag{7.1}$$

The quantity N_{tt} and the rest of the quantities on the left in equation 7.1 are measured in data. The subscripts on the number of events are p_{T} ordered such that, for example, the number with the leading lepton passing the *tight* criteria and the sub-leading lepton passing the *anti-tight* criteria (i.e. *loose* but not *tight*) is $N_{t\bar{t}}$. The same idea applies to N_{tt}, $N_{\bar{t}t}$, $N_{\bar{t}\bar{t}}$, N_{rr}, N_{rf}, N_{fr}, and N_{ff}. The quantity N_{rr} is related to the number of *tight* leptons in the sample by $N_{rr} = N_{tt}^{rr}/(r_1 r_2)$, where r_1 and r_2 are the real efficiencies for the first and second p_{T}-ordered leptons, respectively, and N_{tt}^{rr} is the number of events with two tight real leptons. The same relationship holds for the quantities N_{rf}, N_{fr}, and N_{ff}. The matrix $\mathbf{M}_{4\times4}$ contains

the efficiencies r (where $\overline{r} \equiv 1 - r$) and f (where $\overline{f} \equiv 1 - f$) measured in the real or fake enriched control regions, defined in the next section. The indices on the efficiencies indicate the first lepton (1) or second lepton (2) in the event. Likewise, the matrix for trilepton events is a straight forward extension of the matrix in the dilepton case, except it is an 8×8 matrix, as shown in equation 7.2.

The matrix must be inverted to calculate the total number of events where events with two (or three) *tight* leptons are fake. The standard MM was used in previous versions of this analysis, but the current version uses the Likelihood MM. The differences between these two methods are described in §7.1.4.

$$\begin{pmatrix} N_{ttt} \\ N_{tt\bar{t}} \\ N_{t\bar{t}t} \\ N_{t\bar{t}\bar{t}} \\ N_{\bar{t}tt} \\ N_{\bar{t}t\bar{t}} \\ N_{\bar{t}\bar{t}t} \\ N_{\bar{t}\bar{t}\bar{t}} \end{pmatrix} = \mathbf{M}_{8\times 8} \begin{pmatrix} N_{rrr} \\ N_{rrf} \\ N_{rfr} \\ N_{rff} \\ N_{frr} \\ N_{frf} \\ N_{ffr} \\ N_{fff} \end{pmatrix} \tag{7.2}$$

$$\text{where } \mathbf{M}_{8\times 8} = \begin{pmatrix} r_1 r_2 r_3 & r_1 r_2 f_3 & r_1 f_2 r_3 & r_1 f_2 f_3 & f_1 r_2 r_3 & f_1 r_2 f_3 & f_1 f_2 r_3 & f_1 f_2 f_3 \\ r_1 r_2 \overline{r_3} & r_1 r_2 \overline{f_3} & r_1 f_2 \overline{r_3} & r_1 f_2 \overline{f_3} & f_1 r_2 \overline{r_3} & f_1 r_2 \overline{f_3} & f_1 f_2 \overline{r_3} & f_1 f_2 \overline{f_3} \\ r_1 \overline{r_2} r_3 & r_1 \overline{r_2} f_3 & r_1 \overline{f_2} r_3 & r_1 \overline{f_2} f_3 & f_1 \overline{r_2} r_3 & f_1 \overline{r_2} f_3 & f_1 \overline{f_2} r_3 & f_1 \overline{f_2} f_3 \\ r_1 \overline{r_2 r_3} & r_1 \overline{r_2 f_3} & r_1 \overline{f_2 r_3} & r_1 \overline{f_2 f_3} & f_1 \overline{r_2 r_3} & f_1 \overline{r_2 f_3} & f_1 \overline{f_2 r_3} & f_1 \overline{f_2 f_3} \\ \overline{r_1} r_2 r_3 & \overline{r_1} r_2 f_3 & \overline{r_1} f_2 r_3 & \overline{r_1} f_2 f_3 & \overline{f_1} r_2 r_3 & \overline{f_1} r_2 f_3 & \overline{f_1} f_2 r_3 & \overline{f_1} f_2 f_3 \\ \overline{r_1} r_2 \overline{r_3} & \overline{r_1} r_2 \overline{f_3} & \overline{r_1} f_2 \overline{r_3} & \overline{r_1} f_2 \overline{f_3} & \overline{f_1} r_2 \overline{r_3} & \overline{f_1} r_2 \overline{f_3} & \overline{f_1} f_2 \overline{r_3} & \overline{f_1} f_2 \overline{f_3} \\ \overline{r_1} \overline{r_2} r_3 & \overline{r_1} \overline{r_2} f_3 & \overline{r_1} \overline{f_2} r_3 & \overline{r_1} \overline{f_2} f_3 & \overline{f_1} \overline{r_2} r_3 & \overline{f_1} \overline{r_2} f_3 & \overline{f_1} \overline{f_2} r_3 & \overline{f_1} \overline{f_2} f_3 \\ \overline{r_1 r_2 r_3} & \overline{r_1 r_2} \overline{f_3} & \overline{r_1} \overline{f_2 r_3} & \overline{r_1} \overline{f_2 f_3} & \overline{f_1 r_2 r_3} & \overline{f_1 r_2} \overline{f_3} & \overline{f_1 f_2 r_3} & \overline{f_1 f_2 f_3} \end{pmatrix}$$

7.1.3 Efficiencies

Using data, two nominal control regions are defined where the efficiencies, r and f, are measured. The efficiency f (r) is the probability that a fake (real) *loose* lepton in the event passes the *tight* criteria in the fake (real) control region. Equivalently, $f\,(r) \equiv N_t^{fCR\,(rCR)}/N_l^{fCR\,(rCR)}$, where fCR (rCR) indicates the fake (real) control region

Lepton channel	Selection	Jets selection	Efficiency extraction
Nominal Control Regions			
μ+jets	$M_{\mathrm{T}}^{\mathrm{W}} > 100$ GeV	$\{1\mathrm{j}, \geq 2\mathrm{j}\} \times \{0\mathrm{b}, \geq 1\mathrm{b}\}$	*real*
μ+jets	$\lvert d_0^{\mathrm{sig}} \rvert > 5$	$\{1\mathrm{j}, \geq 2\mathrm{j}\} \times \{0\mathrm{b}, \geq 1\mathrm{b}\}$	*fake*
e+jets	$E_{\mathrm{T}}^{\mathrm{miss}} > 150$ GeV	$\{1\mathrm{j}, \geq 2\mathrm{j}\} \times \{0\mathrm{b}, \geq 1\mathrm{b}\}$	*real*
e+jets	$M_{\mathrm{T}}^{\mathrm{W}} < 20$ GeV, $(E_{\mathrm{T}}^{\mathrm{miss}} + M_{\mathrm{T}}^{\mathrm{W}}) < 60$ GeV	$\{1\mathrm{j}, \geq 2\mathrm{j}\} \times \{0\mathrm{b}, \geq 1\mathrm{b}\}$	*fake*
Systematic Control Regions			
μ+jets	$M_{\mathrm{T}}^{\mathrm{W}} > 110$ GeV	$\{1\mathrm{j}, \geq 2\mathrm{j}\} \times \{0\mathrm{b}, \geq 1\mathrm{b}\}$	*real*
μ+jets	$M_{\mathrm{T}}^{\mathrm{W}} < 20$ GeV, $(E_{\mathrm{T}}^{\mathrm{miss}} + M_{\mathrm{T}}^{\mathrm{W}}) < 60$ GeV	$\{1\mathrm{j}, \geq 2\mathrm{j}\} \times \{0\mathrm{b}, \geq 1\mathrm{b}\}$	*fake*
e+jets	$E_{\mathrm{T}}^{\mathrm{miss}} > 175$ GeV	$\{1\mathrm{j}, \geq 2\mathrm{j}\} \times \{0\mathrm{b}, \geq 1\mathrm{b}\}$	*real*
e+jets	$E_{\mathrm{T}}^{\mathrm{miss}} < 20$ GeV	$\{1\mathrm{j}, \geq 2\mathrm{j}\} \times \{0\mathrm{b}, \geq 1\mathrm{b}\}$	*fake*

Table 7.2: Selection for the real and fake enriched control regions used to calculate the efficiencies in the MM. Additional selection on the events comes from the jet selection: $\{1j, \geq 2j\} \times \{0b, \geq 1b\}$ means all combinations of the four conditions are calculated. Efficiencies are also calculated separately for the triggers defined in Table 7.3.

Leptons	ID Quality		Lepton Isolation		Triggers
	MM-Loose	*MM-Tight*	*MM-Loose*	*MM-Tight*	
Muons (2016)	*Medium*	*Medium*	none	*FixedCutTight-TrackOnly*	`HLT_mu24`, `HLT_mu50`
Electrons (2016)	*LHMedium*	*LHTight*	none	*FixedCutTight*	`HLT_e24_lhmedium_nod0_L1EM18VH`, `HLT_e60_lhmedium_nod0`, `HLT_e140_lhloose_nod0`
Muons (2015)	*Medium*	*Medium*	none	*FixedCutTight-TrackOnly*	`HLT_mu20`, `HLT_mu50`
Electrons (2015)	*LHMedium*	*LHTight*	none	*FixedCutTight*	`HLT_e24_lhmedium_L1EM20VH`, `HLT_e60_lhmedium`, `HLT_e120_lhloose`

Table 7.3: Summary of the working points used for selecting *loose* and *tight* leptons used in the fake/non-prompt background estimation. The lepton isolation working points are separate from the isolation in the low p_{T} isolated trigger requirement (discussed in §4.2.3).

where the lepton is measured. In this analysis, the *tight* criteria means the isolation requirement is applied to the lepton, with the exception that for electrons an additional tighter requirement on the ID quality is added to the *tight* definition. Table 7.3 shows these definitions. The control regions are defined as regions enriched in either real leptons or fake leptons using kinematic variables such as $E_{\mathrm{T}}^{\mathrm{miss}}$ or $M_{\mathrm{T}}^{\mathrm{W}}$. The regions are the same for both the *loose* and *tight* lepton definitions since the *tight* sample must remain a strict subset of the *loose* sample. Table 7.2 summarizes the control region definitions with additional cuts for computing the efficiencies. The triggers shown in table 7.3 each have a set of efficien-

cies calculated separately due to the fact that the triggers are expected to differ somewhat kinematically.

Of course, the ratio between the number of *tight* events and the number of *loose* events in the control region is only an average of the efficiency for that region. The efficiencies must take into account variations from kinematic variables that can influence how many leptons pass the *tight* criteria. For the main analysis, the variables used typically depend on the lepton kinematics, not on event level kinematics that would be unique to single lepton events, such as $E_{\mathrm{T}}^{\mathrm{miss}}$. The *tight* selection criteria for the leptons depends on how much activity exists in proximity to the lepton and the p_{T} of the lepton and event level kinematics like $E_{\mathrm{T}}^{\mathrm{miss}}$ may be different between single lepton and dilepton/trilepton events. The dependence of the efficiencies on the lepton's kinematics is accounted for by binning the efficiencies with respect to the lepton's own kinematics, such as p_{T}, η, and the distance between the lepton and the closest jet in the event, $\Delta R(\ell, \mathrm{jet})$. Additionally, the efficiencies are calculated for different numbers of jets (N_{jet}) and b-jets (N_{b}) because some dependence is observed (especially on number of b-jets, see appendix B.5 for more details).

For electrons, a correlation was shown to exist between the p_{T} and η_{cl} of the electron. Therefore, a 2-dimensional efficiency calculation is implemented where the efficiencies are binned in $|\eta_{\mathrm{cl}}|$ vs. p_{T}. The third variable for the electron efficiencies, $\Delta R(e, \mathrm{jet})$, is kept as a 1-dimensional calculation.[2] Muons, on the other hand, have 1-dimensional binned efficiencies for all three variables. The efficiencies for any correlations between two variable pairs were studied for muons and those are discussed more in appendix B.2. The 1-dimensional binned efficiencies are used as the nominal case for muons.

Figures 7.1 - 7.2, show the efficiencies calculated for electrons using the 2016 datasets. Figures 7.3 - 7.4, show the efficiencies calculated for electrons using the 2015 datasets. Figures 7.5 - 7.6 show the efficiencies for muons using the 2016 datasets. Figures 7.7 - 7.8 show the efficiencies for muons using the 2015 datasets. The reason there are separate efficiencies for 2015 and 2016 is because there are separate triggers used during the data collection in 2015 and 2016.

When calculating the number of fake or non-prompt leptons in a samples using the Matrix Method, the real or fake efficiency assigned to a lepton must take into account the efficiencies

[2]Note, 1-dimensional here means that the variable used to bin efficiencies in is assumed to be uncorrelated with the other variables, while 2-dimensional efficiencies mean two variables are correlated and the efficiency calculation is done in the 2D plane formed by the two variables. Also, when referring to 1-dimension and 2-dimension efficiency dependence, it is implied that the dependence on N_{jet}, N_{b}, and trigger are not included in this discussion of dimensionality, even though, strictly speaking this adds to the parametrization.

from the binned variables using the following formulas. Equation 7.3 is used for electrons due to the 2-dimensional correlation.

$$r = \frac{r_{ij}(p_{\mathrm{T}}, |\eta|) \times r_k(\Delta R)}{\langle r \rangle} \tag{7.3}$$

$$r = \frac{r_i(p_{\mathrm{T}}) \times r_j(|\eta|) \times r_k(\Delta R)}{\langle r \rangle^2} \tag{7.4}$$

where the average real efficiency is given by $\langle r \rangle$. Indices i, j, and k represent the bin numbers in the efficiencies for the p_{T}, η, and ΔR values of the lepton in the event. Equation 7.4 is calculated for muons, using only the 1-dimensional variables. Similar formulae to equations 7.3 and 7.4 apply to the calculation of the fake efficiencies for both electrons and muons, but replacing r with f.

MC Subtraction As already mentioned, in the calculation of the fake efficiencies, there exists a non-negligible contamination from real leptons in the fake enriched control region. This contamination depends mostly on the lepton flavor and which trigger fired the event as well as the number of b-tagged jets in the event. Table 7.4 shows the approximate contamination from different sources in the MC. The $V+$ jets processes contribute the most to the contamination in the electron fake enriched control region, rising to about 64% in the most extreme case for the high p_{T} triggers. For muons, the $t\bar{t}$ or $V+$ jets sources contributes the most depending on how many b-jets are in the event. However, the fake enriched region is still primarily dominated by fakes so the contamination from MC is less than ∼10% in all cases.

To purify the sample as best as possible with respect to fake leptons, the real lepton contamination is subtracted using the MC samples. To do this, the MC samples undergo the same selection defined for the fake enriched control region and the resulting number of events from all MC sources ($t\bar{t}$, $V+$ jets, single t, diboson) is subtracted from the number of data events in the fake control region. For events that pass the low p_{T} prescaled trigger (e.g. for data16 electrons `HLT_e24_lhmedium_nod0_L1EM18VH` and data16 muons `HLT_mu24`), the MC subtraction is done after applying the prescale[3] to the number of data events.

[3]Too many events may fire the low p_{T} trigger due to a lower p_{T} threshold. Only a fraction of these events are saved to reduce the data collection stream to a manageable level. A scaling factor, called the prescale, is applied to scale up the data saved from this trigger to the appropriate value. The prescale value is dependent on the run number of the data set and the luminosity during that run number.

Trigger Strategy The trigger strategy in this analysis has undergone different iterations since the Run I version of the analysis. Appendix B.4 explains more about testing different strategies. The efficiencies calculation is not split by the triggers in table 7.3 since all listed triggers are unbiased by isolation. In an earlier version of the analysis, isolated triggers were used and the efficiencies were split by trigger because the isolated trigger provides very high trigger efficiency for identifying electrons and muons. However, the trigger strategy for calculating and applying the Matrix Method efficiencies with isolated triggers is much more complicated. To simplify, one set of real and fake efficiencies is calculated using a

Selection: fake CR1	$\mathbf{N_j \geq 2, N_b = 0}$			
Loose	**low p_T trigger**	**high p_T trigger**	**low p_T trigger**	**high p_T trigger**
other sources	0.1	0.4	0.2	1
V+jets sources	1	6	12	40
Tight				
other sources	0.1	0.6	0.5	2
V+jets sources	3	10	36	58
Selection: fake CR1	$\mathbf{N_j \geq 2, N_b \geq 1}$			
Loose	**low p_T trigger**	**high p_T trigger**	**low p_T trigger**	**high p_T trigger**
other sources	0.5	2	3	25
V+jets sources	0.3	1	4	20
Tight				
other sources	2	7	13	36
V+jets sources	1	4	17	29
Selection: fake CR1	$\mathbf{N_j = 1, N_b = 0}$			
Loose	**low p_T trigger**	**high p_T trigger**	**low p_T trigger**	**high p_T trigger**
other sources	0.0	0.08	0.02	0.2
V+jets sources	0.8	4.1	14	28
Tight				
other sources	0.02	0.1	0.06	0.3
V+jets sources	2	6.4	34	42
Selection: fake CR1	$\mathbf{N_j = 1, N_b \geq 1}$			
Loose	**low p_T trigger**	**high p_T trigger**	**low p_T trigger**	**high p_T trigger**
other sources	0.02	0.3	0.2	2.6
V+jets sources	0.2	1	2.2	16
Tight				
other sources	0.08	0.5	0.9	4.5
V+jets sources	0.9	2	11	28

Table 7.4: Approximate *percentage* of prompt lepton contamination, for both the *loose* sample and *tight* sample, in the fake enriched control region from V+jets sources and 'other' sources, which include $t\bar{t}$, diboson, and single top sources. Percentages here are estimated with the MC samples shown in Table 7.1. The percentage is broken up by lepton flavor, trigger, and number of b-tagged jets to show the differences in contamination.

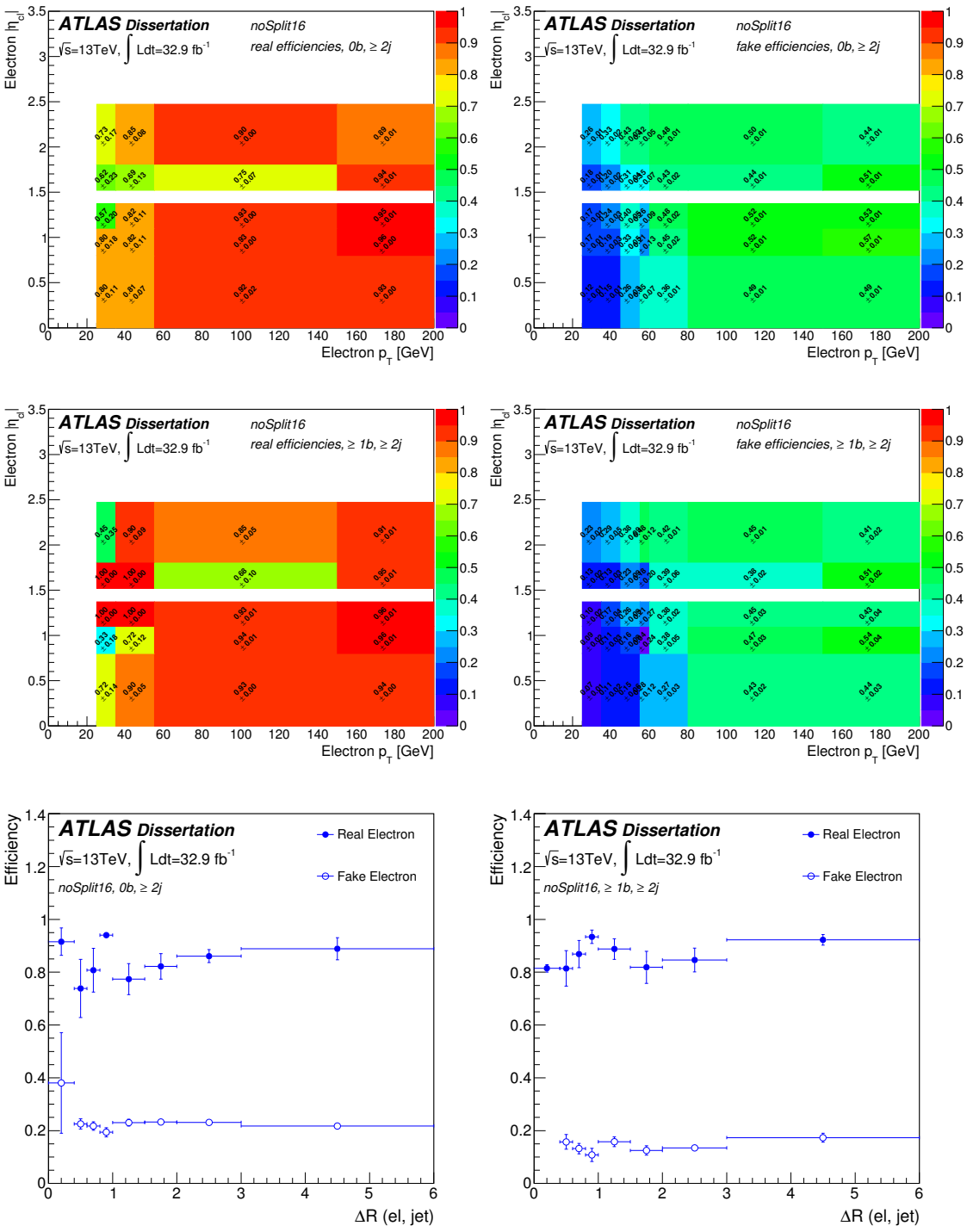

Figure 7.1: Real and fake efficiencies for electrons using the 2-dimensional parametrization of electron p_{T} and $|\eta_{\mathrm{cl}}|$. The bottom row is the 1-dimensional parametrization $\Delta R(e, \mathrm{jet})$. These efficiencies are for events from the 2016 dataset and using MC normalized to the data16 luminosity, with $N_{\mathrm{jet}} \geq 2$ and separated by b-tagged jets: $N_{\mathrm{b}} = 0$ (top and bottom left), $N_{\mathrm{b}} \geq 1$ (middle and bottom right). The 'noSplit16' label refers to logical OR being used between all the triggers in Table 7.3.

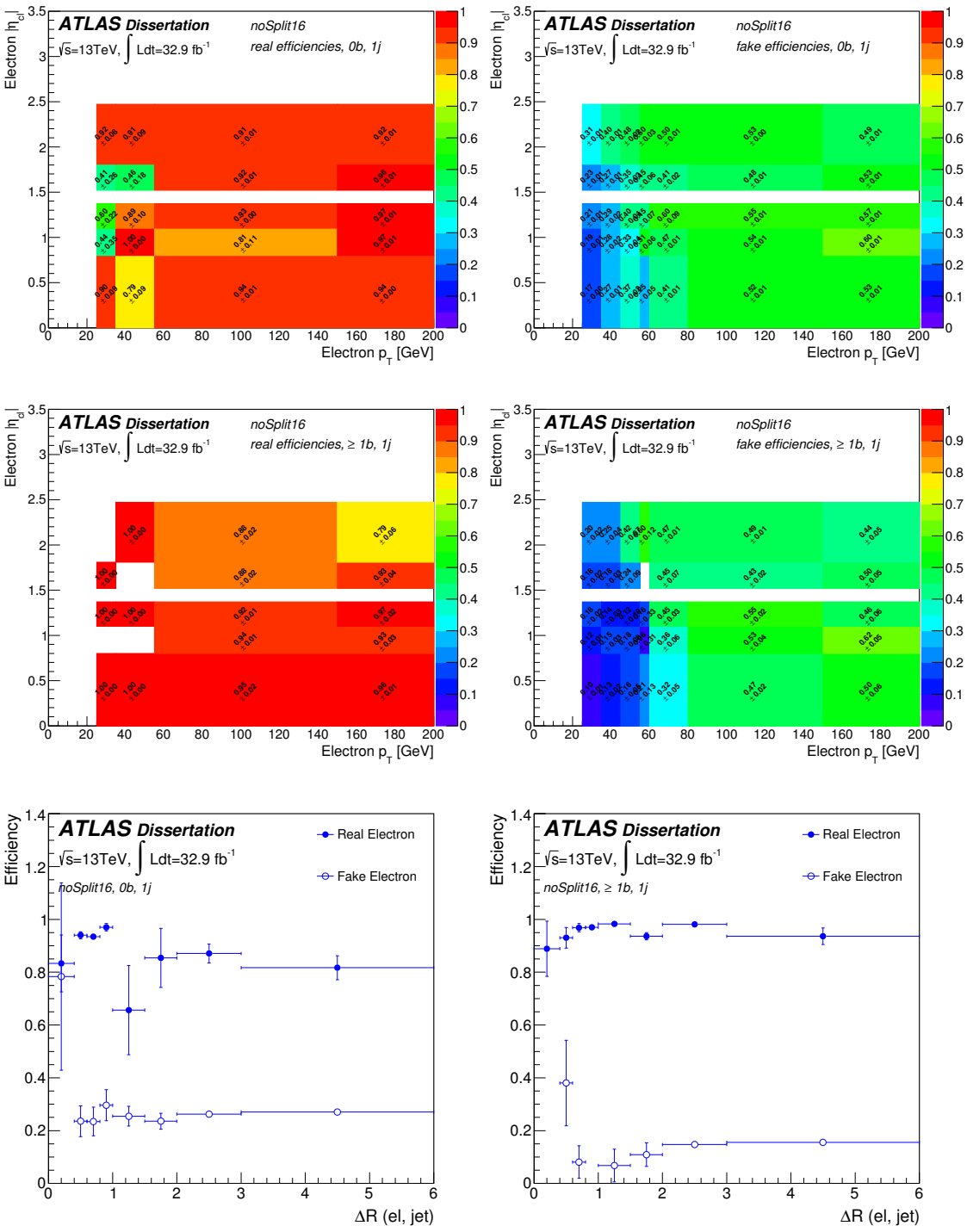

Figure 7.2: Real and fake efficiencies for electrons using the 2-dimensional parametrization of electron p_{T} and $|\eta_{\mathrm{cl}}|$. The bottom row is the 1-dimensional parametrization $\Delta R(e, \mathrm{jet})$. These efficiencies are for events from the 2016 dataset and using MC normalized to the data16 luminosity, with $N_{\mathrm{jet}} = 1$ and separated by b-tagged jets: $N_{\mathrm{b}} = 0$ (top and bottom left), $N_{\mathrm{b}} \geq 1$ (middle and bottom right). The 'noSplit16' label refers to logical OR being used between all the triggers in Table 7.3.

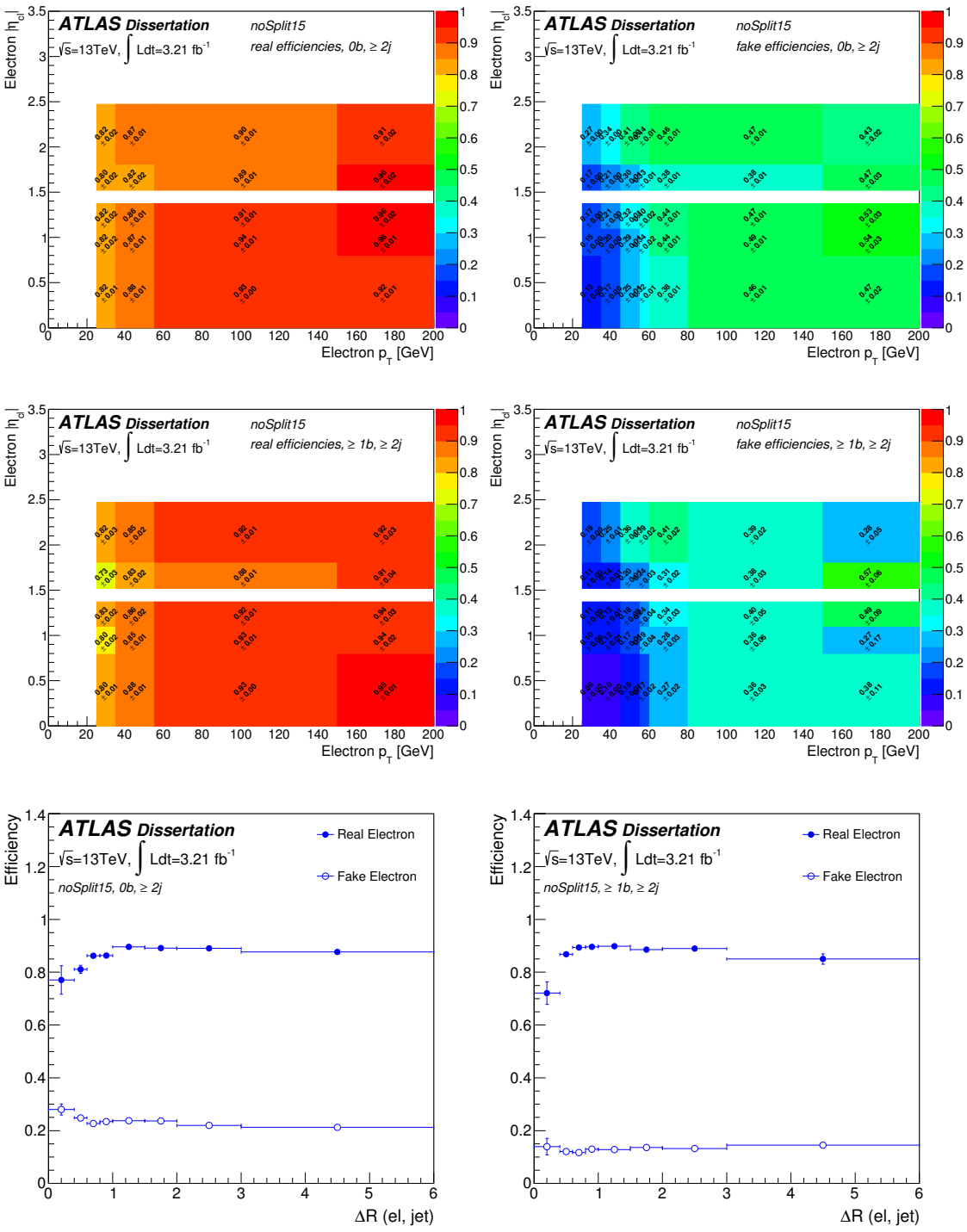

Figure 7.3: Real and fake efficiencies for electrons using the 2-dimensional parametrization of electron p_{T} and $|\eta_{\mathrm{cl}}|$. The bottom row is the 1-dimensional parametrization $\Delta R(e, \mathrm{jet})$. These efficiencies are for events from the 2015 dataset and using MC normalized to the data15 luminosity, with $N_{\mathrm{jet}} \geq 2$ and separated by b-tagged jets: $N_{\mathrm{b}} = 0$ (top and bottom left), $N_{\mathrm{b}} \geq 1$ (middle and bottom right). The 'noSplit15' label refers to logical OR being used between all the triggers in Table 7.3.

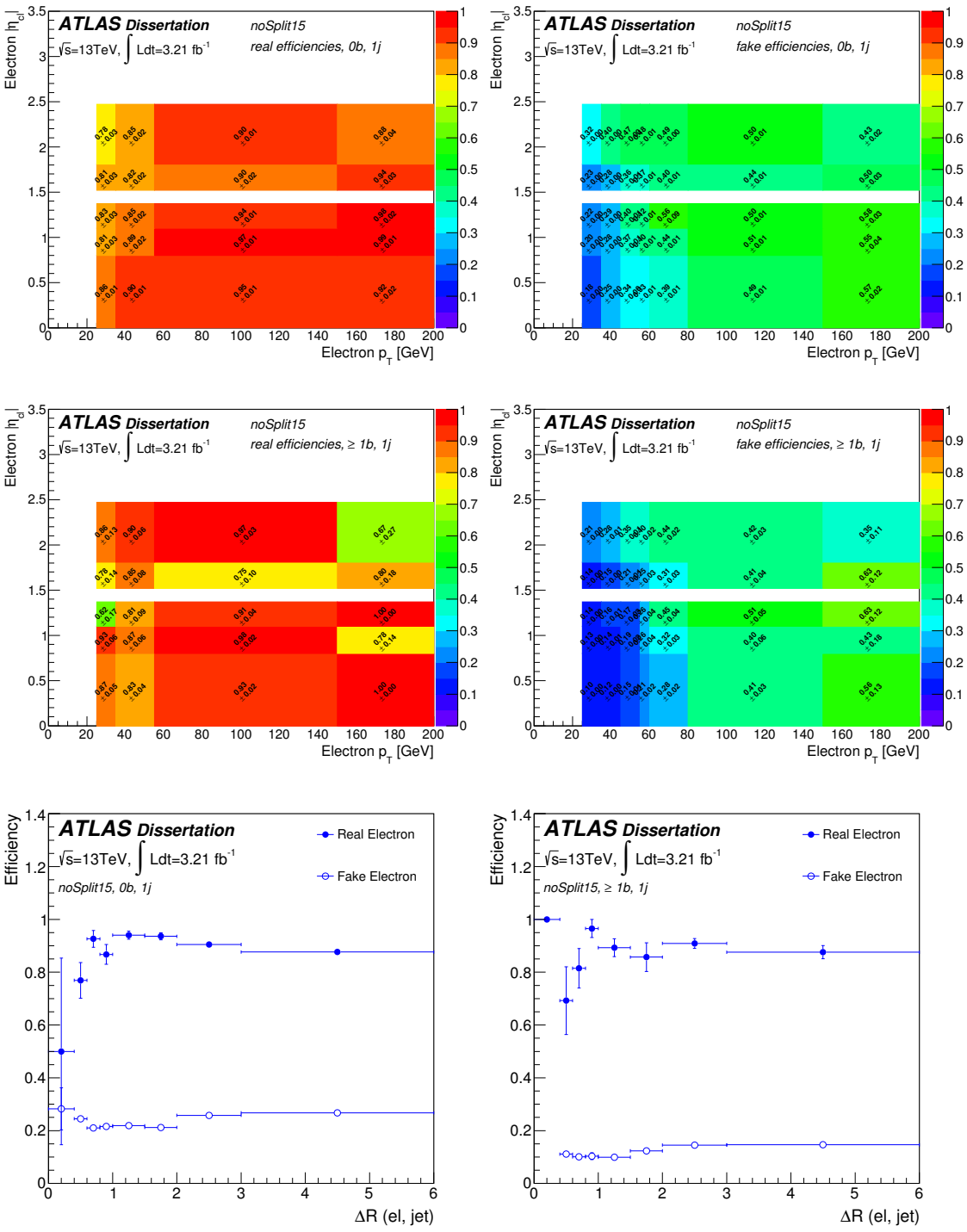

Figure 7.4: Real and fake efficiencies for electrons using the 2-dimensional parametrization of electron p_{T} and $|\eta_{\mathrm{cl}}|$. The bottom row is the 1-dimensional parametrization $\Delta R(e, \mathrm{jet})$. These efficiencies are for events from the 2015 dataset and using MC normalized to the data15 luminosity, with $N_{\mathrm{jet}} = 1$ and separated by b-tagged jets: $N_{\mathrm{b}} = 0$ (top and bottom left), $N_{\mathrm{b}} \geq 1$ (middle and bottom right). The 'noSplit15' label refers to logical OR being used between all the triggers in Table 7.3.

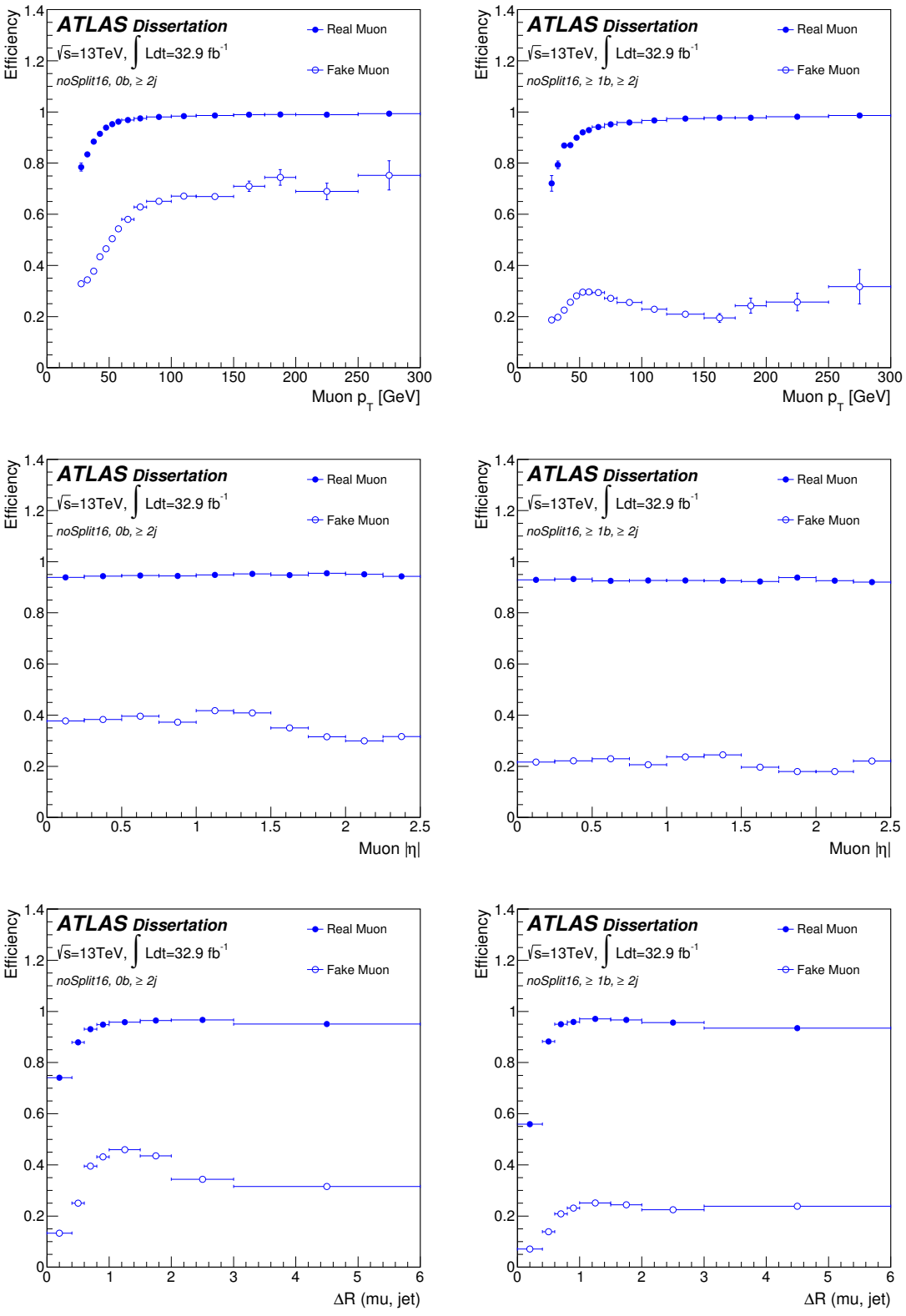

Figure 7.5: Efficiencies for muons parametrized in 1-dimension for p_{T} (top), $|\eta|$ (middle), and $\Delta R(e, \mathrm{jet})$ (bottom). These efficiencies are for events from the 2016 dataset and using MC normalized to the data16 luminosity, with $N_{\mathrm{jet}} \geq 2$ and separated by b-tagged jets: $N_{\mathrm{b}} = 0$ (left), $N_{\mathrm{b}} \geq 1$ (right). The 'noSplit16' label refers to logical OR being used between all the triggers in Table 7.3.

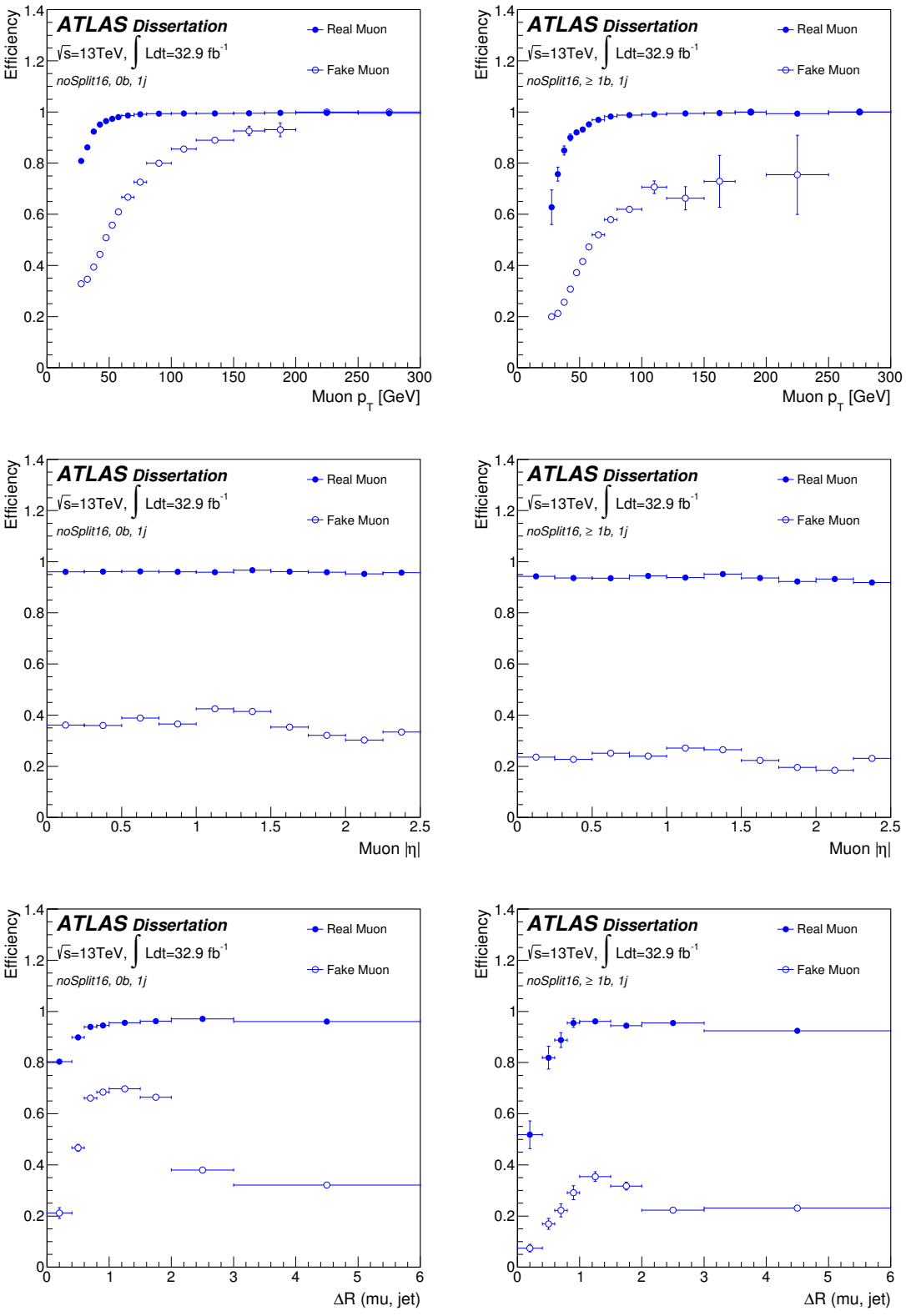

Figure 7.6: Efficiencies for muons parametrized in 1-dimension for p_{T} (top), $|\eta|$ (middle), and $\Delta R(e, \mathrm{jet})$ (bottom). These efficiencies are for events from the 2016 dataset and using MC normalized to the data16 luminosity, with $N_{\mathrm{jet}} = 1$ and separated by b-tagged jets: $N_{\mathrm{b}} = 0$ (left), $N_{\mathrm{b}} \geq 1$ (right). The 'noSplit16' label refers to logical OR being used between all the triggers in Table 7.3.

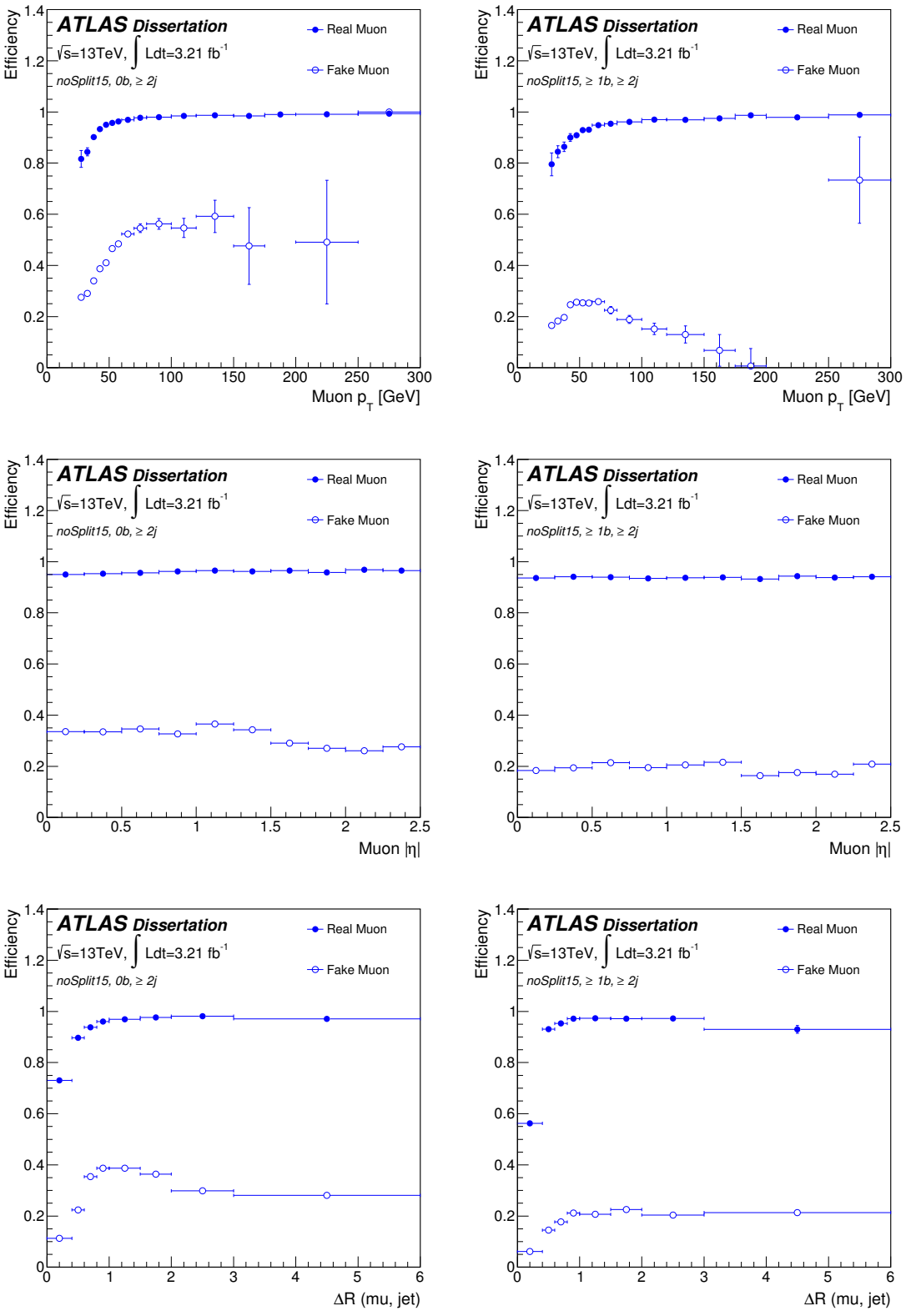

Figure 7.7: Efficiencies for muons parametrized in 1-dimension for p_{T} (top), $|\eta|$ (middle), and $\Delta R(e, \mathrm{jet})$ (bottom). These efficiencies are for events from the 2015 dataset and using MC normalized to the data15 luminosity, with $N_{\mathrm{jet}} \geq 2$ and separated by b-tagged jets: $N_{\mathrm{b}} = 0$ (left), $N_{\mathrm{b}} \geq 1$ (right). The 'noSplit15' label refers to logical OR being used between all the triggers in Table 7.3.

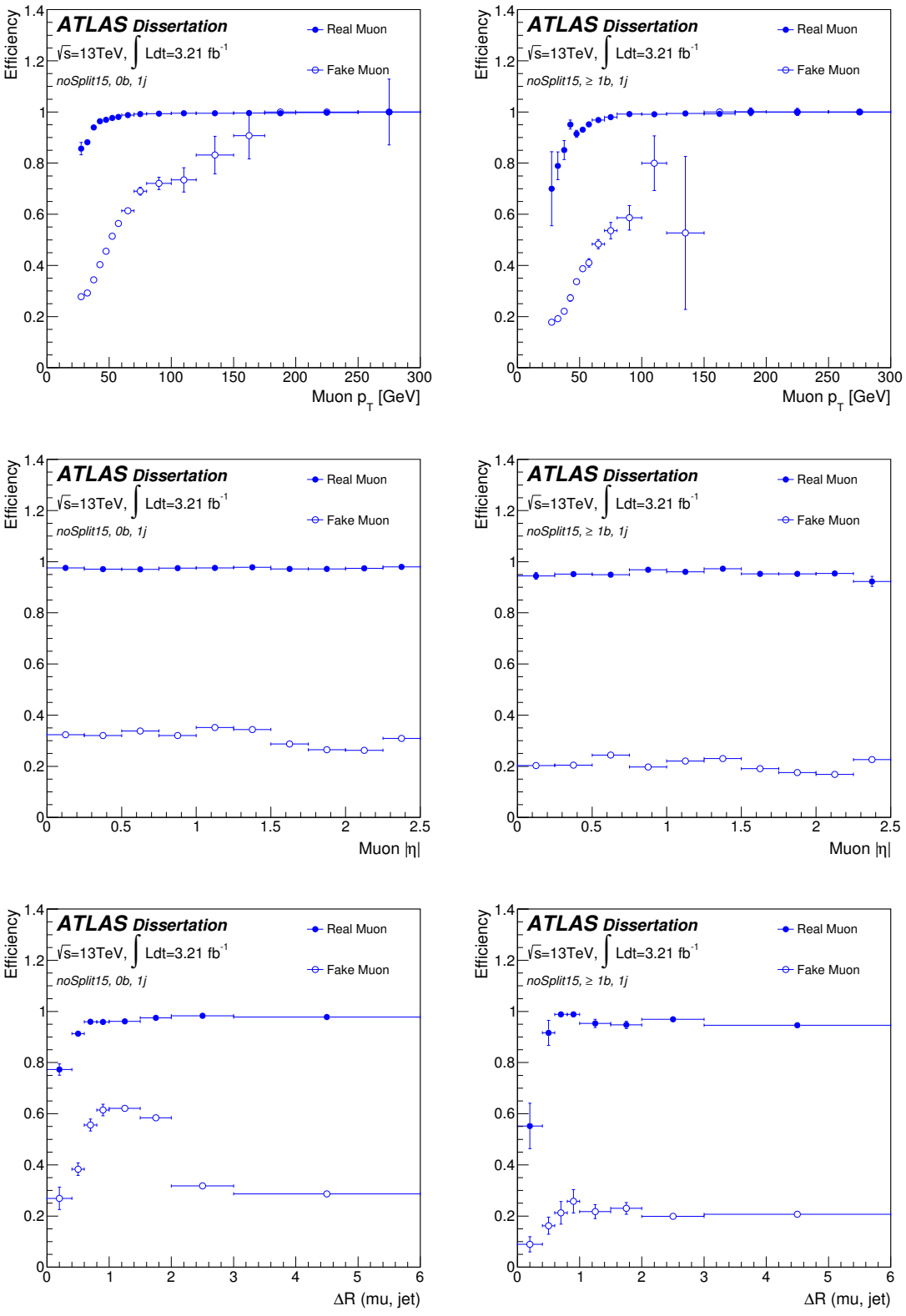

Figure 7.8: Efficiencies for muons parametrized in 1-dimension for p_{T} (top), $|\eta|$ (middle), and $\Delta R(e, \mathrm{jet})$ (bottom). These efficiencies are for events from the 2015 dataset and using MC normalized to the data15 luminosity, with $N_{\mathrm{jet}} = 1$ and separated by b-tagged jets: $N_{\mathrm{b}} = 0$ (left), $N_{\mathrm{b}} \geq 1$ (right). The 'noSplit15' label refers to logical OR being used between all the triggers in Table 7.3.

logical OR between the non-isolated triggers and each lepton in the event is applied the appropriate efficiency based on the number of b-jets and number of jets in the event. The main analysis uses dilepton triggers in addition to the high p_{T} single lepton (non-isolated) triggers and therefore does not use the low p_{T} prescaled trigger to collect low p_{T} leptons. The non-trigger-split (*noSplit16* or *noSplit15*) efficiencies are applied to any lepton that pass any one of the dilepton or high p_{T} triggers in the main event.

No trigger splitting for the efficiencies is advantageous because some of the low p_{T} triggers are prescaled, which means only a fraction of the events satisfying the trigger are saved. Any fluctuations in the efficiencies from low statistics in one trigger are smoothed out by not splitting the efficiencies by trigger. However, for some events the statistical error on the efficiency is influenced by how many leptons pass the tight criteria for each of the triggers and in some cases, the low p_{T} trigger can contribute a smaller statistical error.

7.1.4 Comparison of Standard vs Likelihood Matrix Method

Many algorithms exist to estimate the fake/non-prompt lepton background [148, 150–152]. The two main algorithms historically used in this analysis are the so-called standard Matrix Method (SMM), and the Likelihood Matrix Method (LHMM). In general, the SMM is the preferred method by the *TopFakes* physics analysis subgroup within ATLAS (whose code is typically used by all *Top* group analyses sensitive to faked leptons). This is because the framework to calculate fakes based on the SMM is in place already and has dedicated developers who standardize the algorithms for use by many analyses. Also, the SMM is a well-studied method that estimates the fake/non-prompt lepton background with fairly high fidelity in most cases. The two methods are described and compared here briefly.

Standard Matrix Method To illustrate the standard Matrix Method (SMM) implementation, the case of only one lepton per event will be used here for simplicity. Similar to equations 7.1 and 7.2, a 2×2 matrix is constructed as shown in equation 7.5 with the same notation for the p_{T} ordered number of leptons as defined previously, except there is only one lepton per event. The matrix is inverted to solve for the number of tight fake leptons, $N_t^{\mathrm{fake}} \equiv f N_f$, given in equation 7.6.

$$\begin{pmatrix} N_t \\ N_{\bar{t}} \end{pmatrix} = \begin{pmatrix} r & f \\ \overline{r} & \overline{f} \end{pmatrix} \begin{pmatrix} N_r \\ N_f \end{pmatrix} \tag{7.5}$$

$$N_t^{\mathrm{fake}} = \frac{f}{r - f}(r N_l - N_t) \tag{7.6}$$

The number of fake leptons passing the *tight* criteria can be re-cast as a weight, w_i, to be applied on an event by event basis (i.e. for event i). Equation 7.6 can be rewritten using the weight w_i as in equation 7.7, where $\delta_i = 1$ only if the lepton in the event passes the tight criteria; otherwise, $\delta_i = 0$. The total number of fake leptons in the sample is then a simple sum of N_t^{fake} over all events and the statistical uncertainty on N_t^{fake} is $\pm\sqrt{\sum_i (N_{t,i}^{\text{fake}})^2}$.

$$w_i = \frac{f_i}{r_i - f_i}(r_i - \delta_i) \tag{7.7}$$

Note that f_i and r_i are given subscripts here to explicitly point out that r and f can vary from lepton to lepton given the parameterization of the lepton p_{T}, $|\eta|$, and $\Delta R(\ell, \text{jet})$. In practice, the data sample containing the loose lepton sample has this weight added as a variable that can then be applied with the selection in whichever region one wishes to calculate the number of fake/non-prompt leptons. If there is more than one lepton in each event, the weight is calculated as a sum of the real and fake contributions for the *tight* and *anti-tight* multi-lepton events (i.e. resulting from the inverted matrix). Due to the relative simplicity of applying this weight with a given selection, the overall calculation using this method is easier. As discussed next, the LHMM is a bit more complicated in its application to the data. However, the LHMM is typically more stable in its estimation.

Likelihood Matrix Method The formalism behind the matrix calculation in the Likelihood Matrix Method (LHMM) is essentially the same as in the SMM. In other words, equations 7.5, 7.1, and 7.2 are still utilized for single lepton, dilepton, and trilepton events, respectively. However, when computing the total number of tight, fake leptons in a sample with the LHMM, a Poisson likelihood approach is used [152]. In the dilepton event case, instead of the number of fakes being calculated from the fakes weight applied to each event, the number of events for N_{tt}^{rr}, N_{tt}^{fr}, N_{tt}^{rf}, and N_{tt}^{ff}[4] are treated as parameters, constrained by Poisson statistics, which are to be optimized using the set of real and fake efficiencies calculated from the single lepton samples. In practice, the parameters are estimated on a bin-by-bin basis for a given kinematic variable. The variables are binned into a histogram for different kinematic variables (as shown in figures 5.5 through 5.7), and the number of fakes is derived for each bin. For the signal region summary plot (as shown in figure 9.3), the bins represent the total number of events in each signal region, so the number of fakes is derived for each signal region. Note that estimating the fit by bins is always going to give larger statistical errors for the parameter estimates than the ideal case (non-binned data) [153].

[4]Here, the notation means, for example: $N_{tt}^{rr} = \langle r_1 r_2 \rangle N_{\ell\ell}^{rr}$.

The probability for the number of events where each lepton is of the *tight* or *anti-tight* category, N_{tt}, $N_{t\bar{t}}$, $N_{\bar{t}t}$, and $N_{\bar{t}\bar{t}}$, is predicted by maximizing the likelihood function in equation 7.8.[5] From this, the number of fake events with (both) tight leptons is just: $N_{tt}^{\text{fake}} = N_{tt}^{fr} + N_{tt}^{rf} + N_{tt}^{ff}$. The method described here is for the simplified case of dilepton events (since that is the majority of events considered in this analysis). However, this analysis uses the extension to the LHMM for trilepton events as well. In principle, extensions to $\geq$4 leptons can be implemented, though as already addressed, this would complicate the calculations.

$$\mathcal{L} = P(N_{tt}|N_{tt}^{\text{predicted}}) \times P(N_{t\bar{t}}|N_{t\bar{t}}^{\text{predicted}}) \times P(N_{\bar{t}t}|N_{\bar{t}t}^{\text{predicted}}) \times P(N_{\bar{t}\bar{t}}|N_{\bar{t}\bar{t}}^{\text{predicted}}) \tag{7.8}$$

While the SMM was used in the Run I version of this analysis [44], the move to using the LHMM occurred during the first implementation of the 13 TeV data analysis. Several drawbacks to using the SMM were observed when implementing the algorithm with early Run II data (2015 dataset). The LHMM ameliorates these drawbacks in its implementation. The following weaknesses, especially prevalent for low statistics, as is the case in this analysis, were discovered for the SMM:

1. The resulting N_{tt}^{fake} estimate could be negative if there was a large enough negative weight in one or more events. This results in an unphysical interpretation of the resulting fakes estimate.

2. Due to the use of a standard statistical uncertainty estimation ($\sqrt{N}$) versus the true Poisson uncertainty at low statistics, a larger and unreliable statistical uncertainty is calculated in some regions with very low number of fakes.

3. If the fake efficiency calculation yields much higher efficiencies (f above about 0.5), then the result from SMM can be numerically unstable. This results in very large (positive or negative) fake weights due to the dependence $w \propto 1/(r-f)$, as shown in equation 7.7.

Additional studies for the fake and non-prompt lepton background are discussed in Appendix B.

[5] In practice, calculating the maximal likelihood probability for the fake background estimate in this analysis is done with the `TMinuit` class in ROOT [90]. This class is based on the `Minuit` FORTRAN package [154] and is designed to find the values of the parameters which give a multivariate function the minimal value. In order to maximize the likelihood function in equation 7.8, the likelihood function input to `TMinuit` is actually $-\ln(\mathcal{L})$ and then minimized [155].

7.2 Charge Mis-Identification of Electrons

The number of same charge dilepton events selected for this analysis can be exaggerated if the charge of one of the leptons is mis-measured. Typically, this happens when a process that produces a pair of opposite charge leptons, for example, $Z \to e^{\pm}e^{\mp}$, is mis-identified as containing two electrons of the same charge. Charge mis-identification is negligible for muons since the ATLAS muon system has a long lever arm and the muon charge is measured in both the ID and the Muon Spectrometer. Additionally, muons typically do not radiate via *bremsstrahlung* at the energies observed in ATLAS. Therefore, this background is focused solely on electrons and only estimated for the same-sign dilepton channels with at least one electron (SSee, SSeμ), since the trilepton regions do not have a charge requirement. The two primary ways the electron charge can be mis-measured are

1. *Photon conversion*: if an electron emits a photon through *bremsstrahlung* with sufficiently high energy, while still inside the inner tracker, the photon could produce an electron-positron pair, as depicted in figure 7.9. In this example, if the track of the positron is close to the original electron, the positron charge could be measured as the original electron's charge. Photon conversion, more generally, refers to a photon converting to an electron/positron pair. Trident electrons, such as depicted in figure 7.9 are a special case of photon conversion.

2. *High p_{T} electrons*: if an electron is produced in a hard scatter event with sufficiently high energy to have only a slightly curved track, the inner detector may not be able to accurately measure the charge due to the minimal curvature in the magnetic field.

7.2.1 Flip-rate calculation

In order to estimate the contribution of the charge mis-id background to the regions important for this analysis, the probability that an electron will have its charge mis-measured must be calculated. The probability depends on the charge flip rates, which are assumed to depend on both the transverse momentum of the electron and the location of the cluster distribution inside the detector. Therefore, the calculation of the charge flip-rates is done using a likelihood minimization, parametrized with the p_{T} and $|\eta_{\mathrm{cl}}|$ of the electron. Assuming a sample of real, opposite-sign electrons, the observed number of same-sign dilepton events,

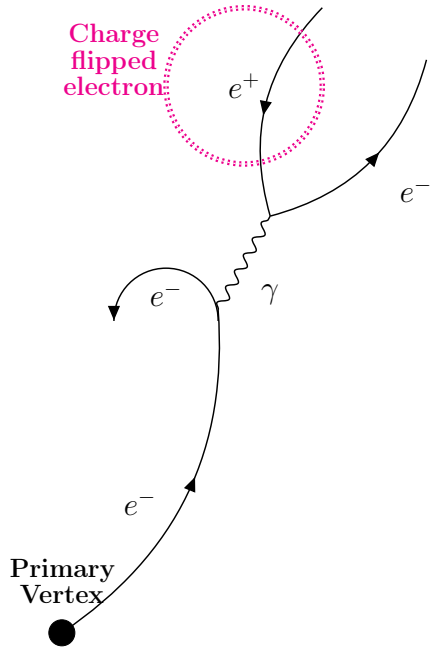

Figure 7.9: Depiction of a trident electron (a type of photon conversion). If the positron encircled is measured as the electron in the event, rather than the electron originating from the primary vertex, this is classified as a charge mis-identified electron.

N_{SS}, is represented by the following formula [156]:

$$N_{SS}^{ij} = N^{ij}(\varepsilon_i(1-\varepsilon_j) + \varepsilon_j(1-\varepsilon_i)) = N^{ij}(\varepsilon_i + \varepsilon_j - 2\varepsilon_i\varepsilon_j) \tag{7.9}$$

where i and j are indices of the bins in $(p_{\mathrm{T}}, |\eta_{\mathrm{cl}}|)$ space. The variable ε is the charge flip rate. The total number of events in the sample is represented by N. This number and N_{SS} are selected in the Z-peak region, $|m_{ee} - m_Z| < 10$ GeV, where m_{ee} is the invariant mass of the two electrons in the event and m_Z is the mass of the Z boson. Any background events not from a Z boson are removed with sideband subtraction. The sideband subtraction consists of counting the number of events in 'sidebands' of $\pm$ 10 GeV from the Z-peak region ($81 < m_{ee} < 101$ GeV) and extrapolating this number to the Z-peak region. The size of the sidebands are varied to estimate a systematic uncertainty for the background subtraction on the charge mis-id.

Using a data sample that is selected for $Z \to ee$ events without any charge requirement, the charge flip rates can be obtained by minimizing the following negative log likelihood

$$-\ln[\mathcal{L}(\varepsilon|N_{SS}, N)] = \sum_{i,j} \ln[N_{ij}(\varepsilon_i + \varepsilon_j - 2\varepsilon_i\varepsilon_j)]N_{SS}^{ij} - N^{ij}(\varepsilon_i + \varepsilon_j - 2\varepsilon_i\varepsilon_j) \tag{7.10}$$

Figure 7.10 shows the rates separated for several bins in p_{T} and binned in $|\eta_{\mathrm{cl}}|$. After the rates are obtained, the total number of same-sign events with one or both of the electrons charge-flipped in a given region (e.g. signal region) is calculated from applying the weight in equation 7.11 to each event containing opposite-sign pairs of electrons in the region. The event weight, w, can be interpreted as the probability that the *opposite-sign* dilepton event was reconstructed as a *same-sign* dilepton event:

$$w = \frac{\varepsilon_1 + \varepsilon_2 - 2\varepsilon_1\varepsilon_2}{1 - (\varepsilon_1 + \varepsilon_2 - 2\varepsilon_1\varepsilon_2)} \tag{7.11}$$

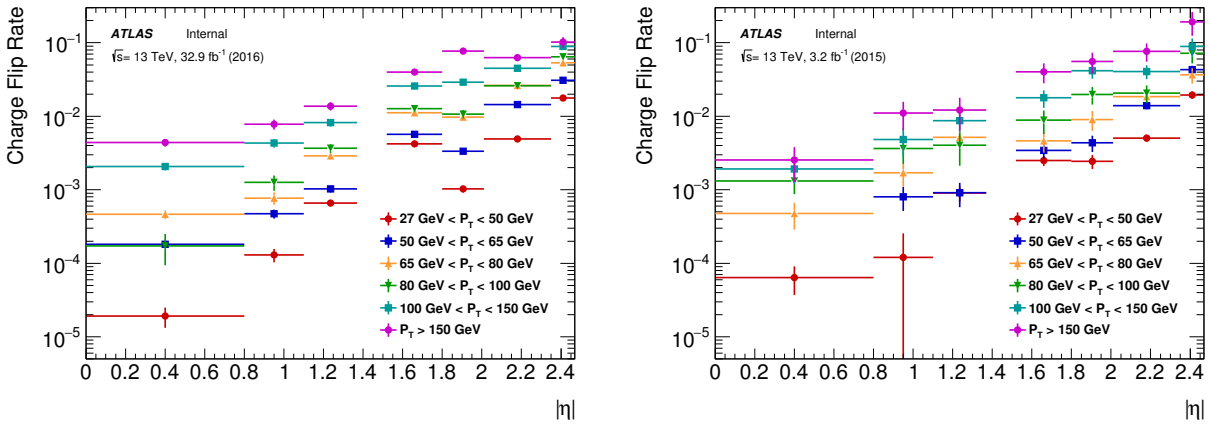

Figure 7.10: Charge flip rates calculated using 2016 (left) and 2015 (right) data events and parametrized in p_{T} and $|\eta_{\mathrm{cl}}|$. The bin between $1.37 < |\eta_{\mathrm{cl}}| < 1.52$ is empty due to the crack region. Rates are split into six p_{T} bins as shown.

7.2.2 Background Reduction

Charge mis-measured electrons can be rejected using some sophisticated techniques, such as a Boosted Decision Tree (BDT) algorithm, or not as sophisticated techniques, such as a simple cut on electrons that are more likely to be mis-identified. If charge mis-measured electrons can be rejected, the total background estimate can be reduced. This analysis applies a simple cut on the electron cluster η to reduce this background. Given the higher rates shown in figure 7.10 for $|\eta_{\mathrm{cl}}| > 1.37$, only electrons with $|\eta_{\mathrm{cl}}| < 1.37$ are used in the regions where charge mis-identified electrons are a major background. For the SS$\mu\mu$ and trilepton channels, there is no charge mis-identified background, so all muons ($|\eta| < 2.5$) and electrons ($|\eta_{\mathrm{cl}}| < 2.47$) are used. The additional cut of the $|\eta_{\mathrm{cl}}| < 1.37$ on electrons reduces the charge mis-identified background by about 87% in the SSee channel, and by about 77% in

the SSeμ channel. It was shown through early comparison studies, that the BDT algorithm was only slightly better in terms of reduction of the background compared to applying the simple $|\eta_{\text{cl}}|$ cut. Therefore, this version of the analysis employs this cut. A future version of the analysis may employ the BDT algorithm after studies with more data.

7.3 Charge Mis-identification and Fake Overlap Removal

Overlap between the charge mis-id background and the fake/non-prompt lepton background can be significant depending on the electron definition. This overlap mainly comes from the fact that the MM as described in §7.1 is not sensitive to the origin (i.e. physics process) of the leptons. Instead, it is only sensitive to the efficiency with which the *loose* lepton passes the *tight* criteria. Certain processes, such as photon converted electrons can contribute to both the charge mis-id and fake backgrounds because these electrons tend to be less isolated.

To understand the contributions from fakes and charge mis-id and remove any overlap between the two, the following mathematical formalism is used. First, let $N_{\text{bkg}}^{\text{total}}$ be the total background yield from the three primary sources of backgrounds: irreducible SM processes (N_{SM}), fake/non-prompt lepton background (N_{f}), and charge mis-id (N_{q}).

$$N_{\text{bkg}}^{\text{total}} = N_{\text{SM}} + N_{\text{MM}}^{\text{total}} + N_{\text{q}} \tag{7.12}$$

Then, the total number of fake/non-prompt leptons resulting from the Matrix Method calculation is: $N_{\text{MM}}^{\text{total}} \equiv N_{\text{f}} + \alpha \times N_{\text{q}}$, where N_{f} is the number of true fake/non-prompt lepton contributions and N_{q} is the total number of charge mis-identified leptons. The symbol α represents the fraction of the total charge mis-id leptons that is calculated in the Matrix Method. In order to reduce the overlap, $\alpha \times N_{\text{q}}$ in a given region must be accounted for and subtracted. This means equation 7.12 is shown to explicitly double count the contribution from charge mis-id by a factor of α.

$$N_{\text{bkg}}^{\text{total}} = N_{\text{SM}} + N_{\text{f}} + (1 + \alpha) \times N_{\text{q}} \tag{7.13}$$

Referencing the weight for charge mis-id events (equation 7.11), and ignoring the kinematic dependences, the weight can also be expressed as equation 7.14, assuming it will be

applied to opposite sign (OS) dilepton events (Z-peak region).

$$\begin{aligned} w_{\mathrm{OS}\to\mathrm{SS}} &\equiv \frac{N_{\mathrm{q}}^{\mathrm{SS}}}{N_{\mathrm{q}}^{\mathrm{OS}}} = \frac{N^{\mathrm{SS}} - N_{\mathrm{f}}^{\mathrm{SS}}}{N^{\mathrm{OS}} - N_{\mathrm{f}}^{\mathrm{OS}}} \\ &\approx \frac{N^{\mathrm{SS}} - N_{\mathrm{f}}^{\mathrm{SS}}}{N^{\mathrm{OS}}} \end{aligned} \tag{7.14}$$

where the contribution from fakes in the Z-peak sample with opposite-sign electrons ($N_{\mathrm{f}}^{\mathrm{OS}}$) is assumed to be negligible. Ultimately, the goal is to subtract the contribution from the MM calculation in the Z-peak region to subtract the N_{q} contribution to this region. Therefore,

$$\begin{aligned} w_{\mathrm{OS}\to\mathrm{SS}} &= \frac{N^{\mathrm{SS}} - N_{\mathrm{MM}}^{\mathrm{total}}}{N^{\mathrm{OS}}} \\ &= \frac{N^{\mathrm{SS}} - N_{\mathrm{f}}^{\mathrm{SS}} - \alpha_Z \times N_{\mathrm{q}}^{\mathrm{SS}}}{N^{\mathrm{OS}}} \\ &= \frac{(1-\alpha_Z) N_{\mathrm{q}}^{\mathrm{SS}}}{N^{\mathrm{OS}}} \end{aligned} \tag{7.15}$$

If the fraction of the charge mis-id background overlapped with the fakes due to the MM is similar to the fraction expected in the signal region,[6] then the final contribution in the signal region of the charge mis-id background can be subtracted as shown in equation 7.16.

$$N_{\mathrm{bkg}}^{\mathrm{total}} = N_{\mathrm{SM}} + N_{\mathrm{f}} + (\alpha - \alpha_Z) \times N_{\mathrm{q}} \tag{7.16}$$

[6]This should be a reasonable assumption given the fact that the charge mis-id weights are also derived in this region and applied in the signal region.

CHAPTER 8
Systematic Uncertainties

Several uncertainties must be taken into account when estimating the final yields in the signal regions and interpreting the results. There are three main classes of uncertainties that impact this analysis: (1) uncertainties that result from statistical fluctuations in the dataset, (2) uncertainties that result from detector response, reconstruction or identification inefficiencies, and background estimation methods, and (3) uncertainties from theoretical calculations.

The first class of uncertainties is purely statistical in nature and as more data are collected and available to analyze, this uncertainty decreases in proportion to one over the square root of the total integrated luminosity of the dataset. Statistical uncertainties in particle physics counting experiments are Poissonian in nature, but approach Gaussian for high average number of events. In this analysis, statistical uncertainties are calculated for each background and signal model in each region of interest (control, validation, and signal).

The second and third classes of uncertainties are systematic uncertainties, often just abbreviated as 'systematics.' The number of systematics in this analysis is extensive, though only a few provide more than about 10% uncertainty in the regions of interest. The total number of systematics is reduced by a method called *pruning*, which is discussed in Chapter 9. Typically, sample size is not a factor that can reduce most systematic uncertainties. The third class mainly comes from theoretical calculations of the cross sections of the processes important for this analysis. These theoretical uncertainties are typically included as systematic uncertainties on the MC simulation cross sections for each process. Most systematic uncertainties in this analysis are interpreted as uncertainties pertaining to the background estimate instead of the data.

Due to limited statistics in the signal regions, the statistical uncertainties are relatively large and typically both systematic and statistical uncertainties affect the final results at the same order of magnitude in most signal regions. For the more populated low-H_{T} control region, the systematic uncertainties dominate. It is not trivial to calculate the spectrum of systematic uncertainties present in this analysis. As much as possible, the systematic fluctu-

ations should be understood and minimized. This is because large systematic uncertainties will reduce the sensitivity to the signals. Every reasonable effort is made to understand the systematics associated with the background estimation in this analysis, both data-driven and MC. Systematics associated with the object and event reconstruction are taken from the ATLAS central physics analysis groups. The values for these systematics have been thoroughly studied and minimized as much as possible.

Typical systematic uncertainties in this analysis result in an upward or downward fluctuation of the nominal yield of the signals and backgrounds. In some cases, the up and down fluctuations for the uncertainties are not symmetric. Some systematics result in a unidirectional shift with respect to the nominal yield for both the positive and negative values of the systematic. In this case, the larger fluctuation is taken as the systematic uncertainty and symmetrized around the nominal value. The full systematic treatment for the signal and background events is presented as a final up and down fluctuation that incorporates all systematics by summing in quadrature. However, the systematics in the limit setting are incorporated as nuisance parameters in the likelihood distributions. Each systematic uncertainty has a corresponding nuisance parameter. A nuisance parameter must be added to the overall systematic treatment to account for any difference between simulation and data, or in the case of the data-driven backgrounds, between the nominal yield and the systematic fluctuation. Adding the nuisance parameters to the full uncertainties budget is done using the `TRexFitter` software and discussed more in §9.4.

The rest of this chapter discusses the specific systematic uncertainties in this analysis. Section 8.1 discusses the main systematics from the object definitions. The data-driven systematics are discussed in section 8.2, where the final uncertainties are derived from variations in the methods of estimation for both the charge mis-id background and the fake/non-prompt lepton background. Finally, other systematics like luminosity, cross sections, and acceptance uncertainty are discussed in section 8.3.

8.1 Object Systematics

Each object's systematic uncertainties are taken from the recommendations of the ATLAS combined performance group responsible for each object's reconstruction and identification. The systematic uncertainties for the objects used in this analysis are listed in table 8.1. Typically, the uncertainties on object characteristics are derived by calculating scale factors as the ratio of the efficiency for the object derived in data over the efficiency derived in MC. The recommended scale factors are used unless otherwise stated. When calculating

overall scale factors to apply in the full systematic treatment, individual scale factors for reconstruction, identification, trigger, etc., must be multiplied together. Scale factors are also smeared by a Gaussian to account for the $\pm 1\sigma$ uncertainty on the scale factor.

Since this analysis uses a combined dataset from 2015 and 2016, discussed in Chapter 6, the scale factors can differ between the 2015 recommendations and the 2016 recommendations. Scale factors are derived for each object based on comparisons of MC to the 2015 and 2016 datasets, as per the recommendations from the corresponding combined performance groups.

Object	**Systematic Name**	**Description**
Electrons	*EL_EFF_Reco_TOTAL_1NPCOR_PLUS_UNCOR*	Reconstruction scale factor
	EL_EFF_ID_TOTAL_1NPCOR_PLUS_UNCOR	Identification scale factor
	EL_EFF_Iso_TOTAL_1NPCOR_PLUS_UNCOR	Isolation scale factor
	EL_EFF_Trigger_TOTAL_1NPCOR_PLUS_UNCOR	Trigger scale factor
	EG_SCALE_ALL	Electron energy scale
	EG_RESOLUTION_ALL	Electron resolution scale
Muons	*MUON_EFF_SYS/STAT*	Muon identification scale factors, statistical and systematic
	MUON_ISO_SYS/STAT	Muon isolation scale factors, statistical and systematic
	MUON_EFF_TrigSystUncertainty/StatUncertainty	Muon trigger scale factors, statistical and systematic
	MUON_TTVA_SYS/STAT	TTVA scale factors, statistical and systematic
	MUON_SCALE	Muon momentum scale
	MUON_ID/MS	Muon momentum resolution (inner detector and muon spectrometer)
	MUON_SAGITTA_RESBIAS/RHO	Charge dependent muon energy scale
b-tagging	*FT_EFF_Eigen_B_**	b-jet scale factors (6 nuisance parameters)
	*FT_EFF_Eigen_C_**	c-jet scale factors (4 nuisance parameters)
	*FT_EFF_Eigen_Light_**	light-flavored jets scale factors (17 nuisance parameters)
	FT_EFF_extrapolation/extrapolation_from_charm	high p_{T} extrapolation scale factor uncertainties
Jets	*JET_EffectiveNP_1-7*	Jet energy scale (21 nuisance parameters)
	JET_EffectiveNP_8restTerm	
	JET_JvtEfficiency	
	JET_BJES_Response	
	JET_EtaIntercalibration_Modelling	
	JET_EtaIntercalibration_NonClosure	
	JET_EtaIntercalibration_TotalStat	
	JET_Flavor_Response	
	JET_Flavor_Composition	
	JET_Pileup_OffsetMu	
	JET_Pileup_OffsetNPV	
	JET_Pileup_PtTerm	
	JET_Pileup_RhoTopology	
	JET_PunchThrough_MC15	
	JET_SingleParticle_HighPt	
	JET_JER_SINGLE_NP	Jet energy resolution
$E_{\mathrm{T}}^{\mathrm{miss}}$	*MET_SoftTrk_Scale*	Jet energy scale on the soft term of $E_{\mathrm{T}}^{\mathrm{miss}}$
	MET_SoftTrk_RecoPerp/Para	Jet energy resolution on the soft term of $E_{\mathrm{T}}^{\mathrm{miss}}$

Table 8.1: Summary of object systematics name and description.

Electrons Scale factors are derived for the electron identification, reconstruction, isolation, trigger, energy scale, and energy resolution efficiencies based on the recommendations from

the *EGamma* combined performance group [114, 115]. Events from $Z \to ee$, $W \to e\nu$, and $J/\psi \to ee$ processes in data and MC are used to derive scale factors for electrons. Electrons must have $\Delta R(e, \text{jet}) > 0.4$ in order to have proper scale factors derived. Both electron energy scale and energy resolution uncertainties is derived from calibrations on the calorimeter energy measurements. Calibrations are discussed in more detail in §4.2.3. Electron energy is smeared and varied by $\pm 1\sigma$ around the nominal value, according to the recommendations.

Muons Muon scale factors are derived for muon identification, trigger, isolation, track-to-vertex association (TTVA, discussed in §4.2), momentum scale, and momentum resolution based on the recommendations from the *Muon* combined performance group [157]. Events from $Z \to \mu\mu$ and $J/\psi \to \mu\mu$ processes are used to derive the scale factors. Muon momentum scale and resolution scale factors are derived from calibrations in the inner detector and MS for a large p_{T} range of muons ($15 < p_{\text{T}} < 300$ GeV). Calibrations are discussed in more detail in §4.2.3.

Jets The calibration process for jets is discussed in §4.2.1. Systematic uncertainties arise from the uncertainties on the calibrations of MC to data for jets [105, 107]. The systematic uncertainties on the jet energy scale (JES) are derived by comparing reconstructed jets to truth jets. The calibration procedure for JES results in 21 nuisance parameters as recommended by the *JetEtMiss* combined performance group. A pruned set of nuisance parameters can be used in this analysis, but because this analysis will be included in the VLQ combination effort (as well as other signal combinations, potentially) the expanded set is required. These parameters include MC calibrations to account for pileup, calorimeter punch-through jets (when the energy of a jet reaches beyond the calorimeter), jet topology and flavor, b-jet energy scale, and *in-situ* calibrations to account for differences between data and MC. Nuisance parameters are also derived for detector versus calibrated η of the jet when using jets in the region $2.9 < |\eta| < 3.1$, the transition region between the hadronic calorimeter and the forward calorimeters. All calibrations are derived for anti-k_{T} jets with radius 0.4.

For b-tagged jets, several additional scale factors are calculated based on the uncertainties in the b, c, and *light* flavored jet contributions when deriving the b-tagging working points. The working points are discussed more in §4.2.2.

Missing Transverse Energy ($E_{\text{T}}^{\text{miss}}$) The *JetEtMiss* combined performance group is also responsible for the calibrations and uncertainty calculations for missing transverse energy ($E_{\text{T}}^{\text{miss}}$). Since the $E_{\text{T}}^{\text{miss}}$ takes into account all hard objects (electrons, muons, jets, etc) in

the event, the systematics for all objects are propagated to the calculation of $E_{\mathrm{T}}^{\mathrm{miss}}$ [121]. Jet energy scale and resolution uncertainties are applied to $E_{\mathrm{T}}^{\mathrm{miss}}$, accounting for simulation and pileup uncertainties. The soft-term $E_{\mathrm{T}}^{\mathrm{miss}}$ uncertainties also includes differences among different generator's ability to reconstruct $E_{\mathrm{T}}^{\mathrm{miss}}$ using the algorithms described in §4.2.4.

8.2 Data-Driven Systematics

The data-driven background estimation described in detail in Chapter 7 has a separate set of systematics. Variations on the charge mis-id background yields come from variations in the charge flip rate calculation, binned in p_{T} and η_{cl}. For the fake and non-prompt lepton background, the variations come from differences in the derivation of the real and fake efficiencies. Table 8.2 summarizes the different systematic uncertainties contributing to the data-driven backgrounds. All systematics for the data-driven backgrounds are incorporated into the full systematics budget for the signal regions discussed in §9.4 with a separate set of nuisance parameters for each of the backgrounds.

Background	**Systematics Description**
Charge mis-id	· Variation on the Z-peak region sideband and peak band windows · MC truth matching using $Z \to ee$ events, uncertainty is computed as difference between this MC estimate and likelihood estimate in data · Fake background systematics, variations are computed in the overlap between charge mis-id and fake/non-prompt backgrounds
Fake/non-prompt	· Alternate fake and real control regions used to calculate the efficiencies · Variation on the amount of real lepton contamination in the fake control region, estimated by implementing a 10% increase/decrease on the total MC · Control regions are sub-divided into four statistically similar subregions and the efficiencies are re-derived

Table 8.2: Description of the sources of data-driven background systematic uncertainties.

Charge Misidentification The charge mis-id systematics are computed using Δw, defined in equation 8.1, applied as an up and down variation on the weight on opposite-sign events in equation 7.11 ($w \pm \Delta w$). The charge flip rates ε_1 and ε_2 are for the first and second electron in the event, ordered in p_{T}. The variable ρ_{12} is the correlation between ε_1 and ε_2. Figure 8.1 shows the correlation between ε_1 and ε_2 for 2016 and 2015 data, binned in η_{cl} and p_{T}. The correlations are estimated using the MIGRAD algorithm in `TMinuit` [154]. In the

case of the SSeμ channel, the charge flip rate for the muon is 0 (since the charge flip rates are only calculated for electrons) and Δw is calculated accordingly.

$$\Delta w = \frac{\sqrt{(1-2\varepsilon_1)^2(\Delta\varepsilon_2)^2 + (1-2\varepsilon_2)^2(\Delta\varepsilon_1)^2 + (1-2\varepsilon_1)(1-2\varepsilon_2)\rho_{12}\Delta\varepsilon_1\Delta\varepsilon_2}}{(1-\varepsilon_1-\varepsilon_2+2\varepsilon_1\varepsilon_2)^2} \tag{8.1}$$

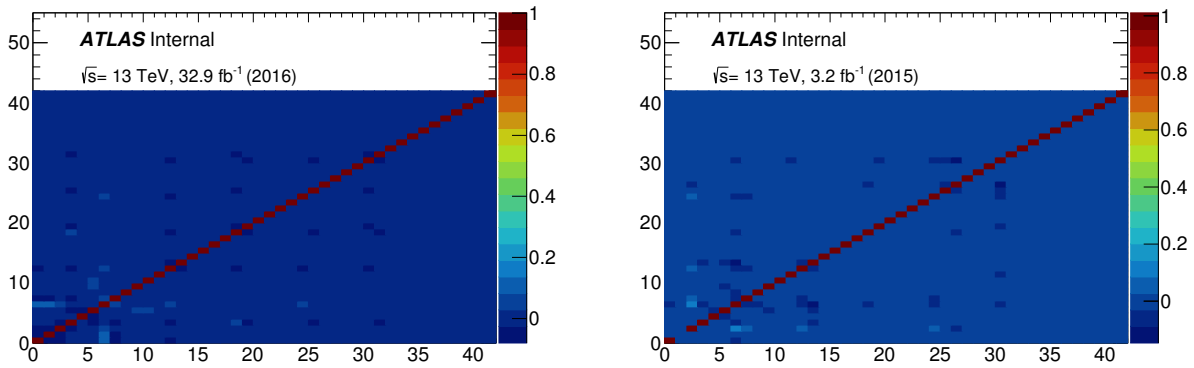

Figure 8.1: Charge flip rate correlations ρ_{12} for two electron events in 2016 (left) and 2015 (right) data. The x and y axis numbers correspond to the number of the η-p_{T} bins in the rates plot in figure 7.10.

The systematic uncertainty from the Z-peak mass window variation is calculated by shifting the upper and lower window bounds by 10 GeV and decreasing the sidebands to zero or doubling them. The largest contribution from this systematic typically comes from the variation in the Z-peak window. For the MC truth matching systematic uncertainty, the true charge flip rates calculated from the truth information stored in the MC simulations are compared with the charge flip rates measured from data. The difference between the truth flip rates (using MC) and the measured flip rates from data is taken as the systematic. Figures 8.2 through 8.5 show the charge flip rate changes from the Z-peak sideband systematics and the variations from the fakes estimations based on the fake/non-prompt background systematics. The full systematic uncertainty on the charge mis-id background is taken as all systematics combined in quadrature. The relative systematic uncertainty in the main control region (H_{T} $<$ 400 GeV) is roughly 22%. The relative charge mis-id systematic uncertainties in the signal regions are shown in figure 8.6.

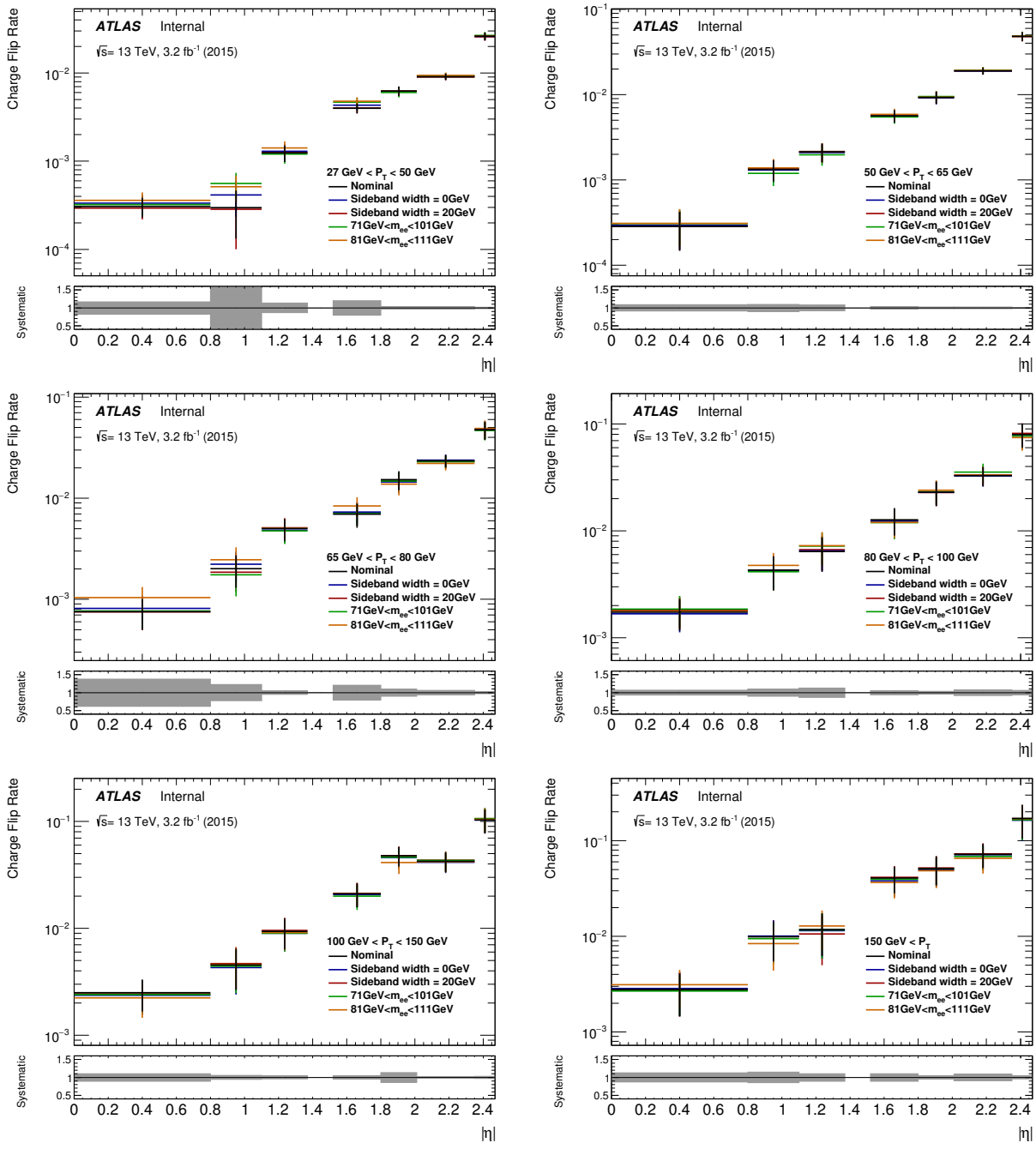

Figure 8.2: Charge mis-id rates for the 2015 dataset are shown with the up and down systematic variations in the sidebands of the Z-peak definition from Table 8.2.

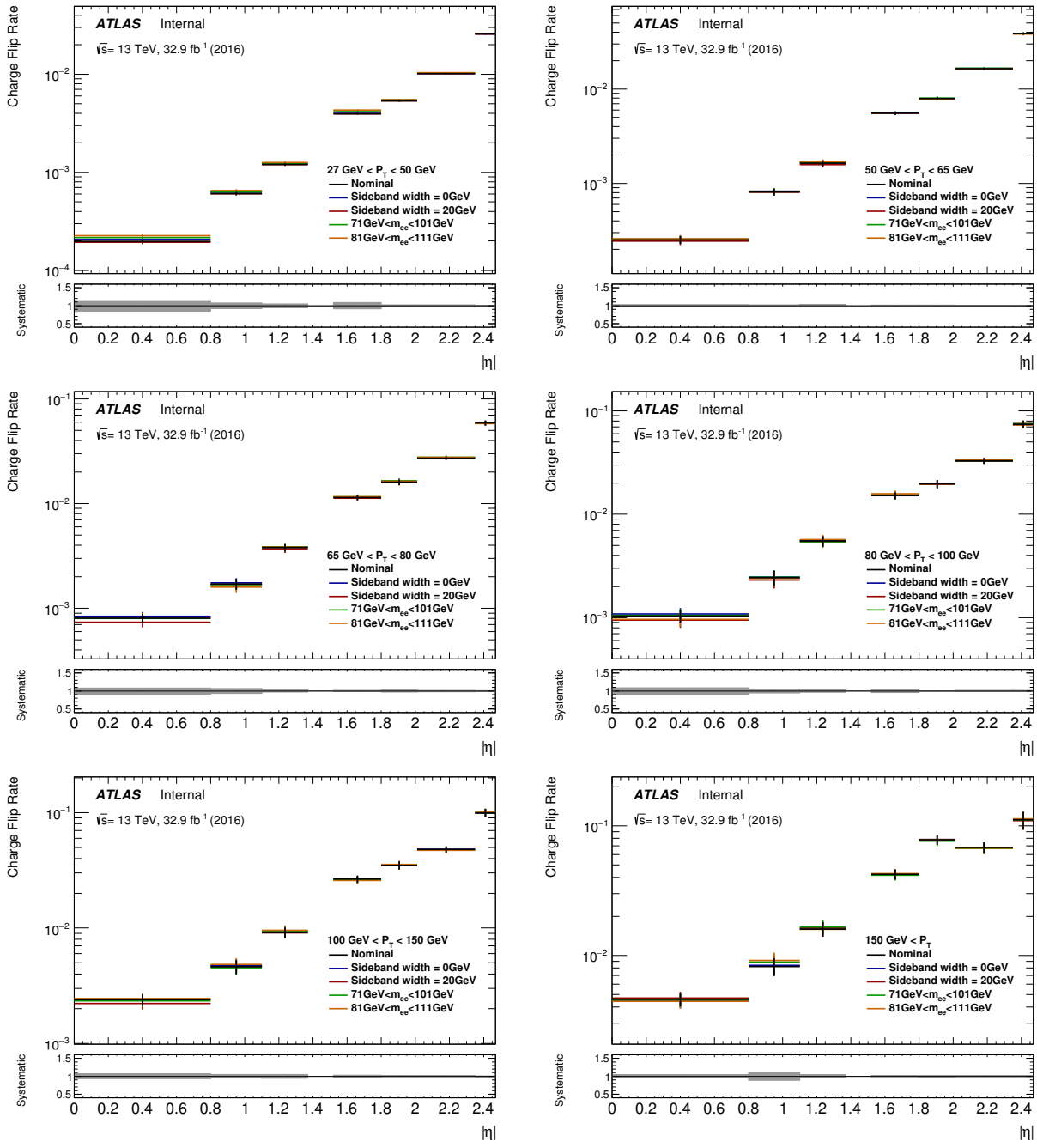

Figure 8.3: Charge mis-id rates for the 2016 dataset are shown with the up and down systematic variations in the sidebands of the Z-peak definition from Table 8.2.

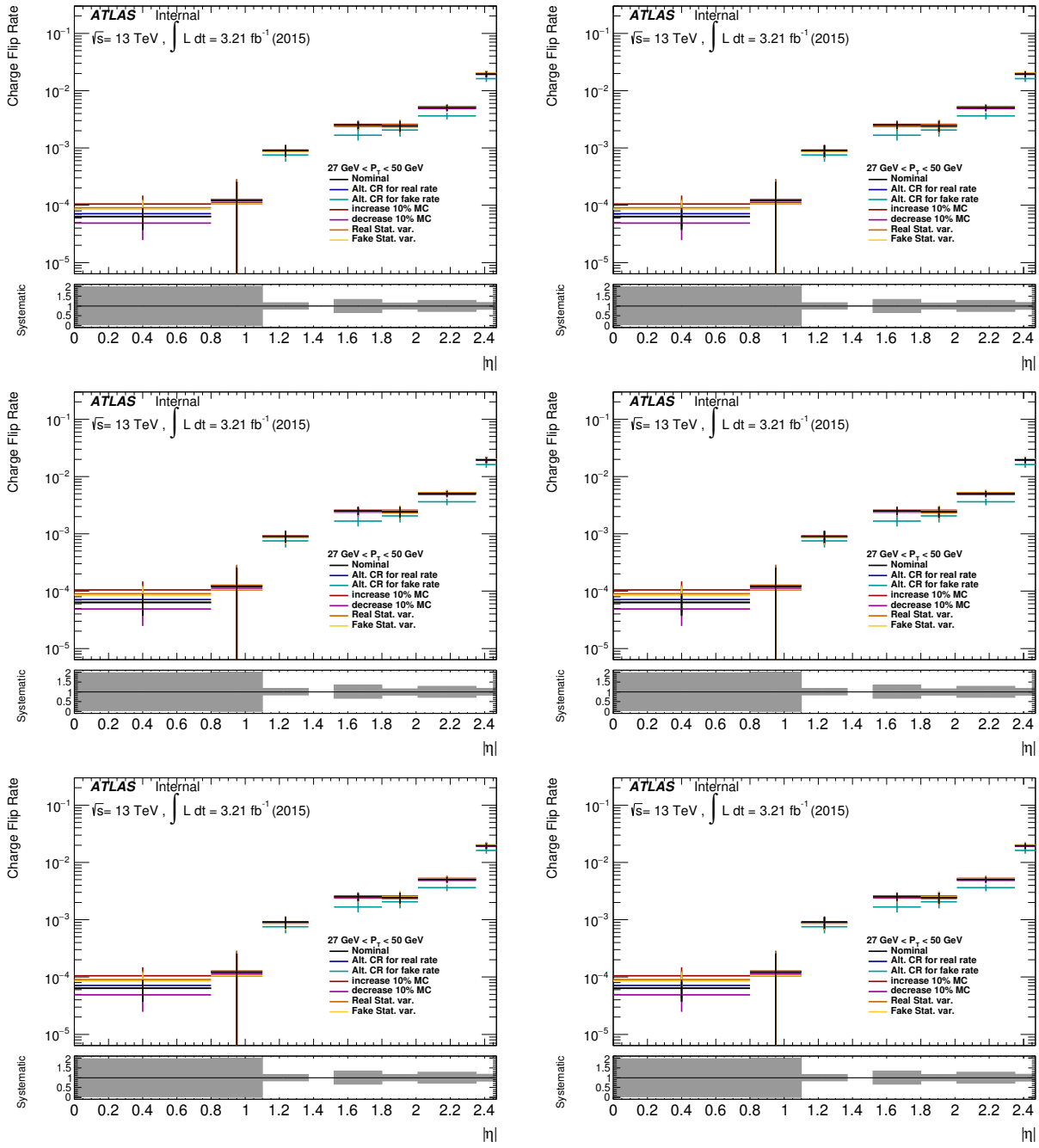

Figure 8.4: Charge mis-id rates are shown with the up and down systematic variations from the variations on the fake efficiencies, and therefore variations in the fakes subtracted from the charge mis-id estimate as described in Table 8.2. Rates are shown for 2015 dataset.

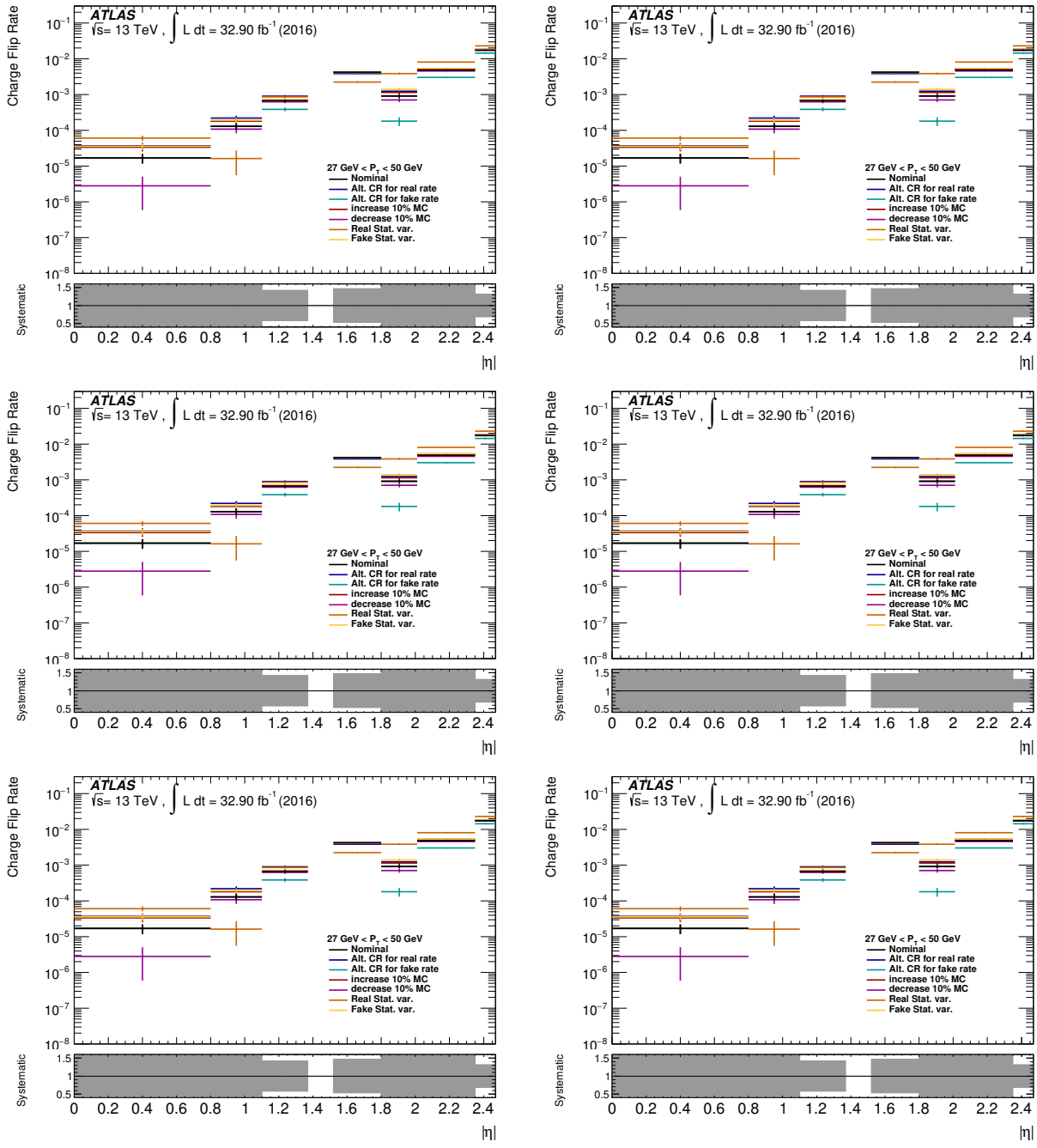

Figure 8.5: Charge mis-id rates are shown with the up and down systematic variations from the variations on the fake efficiencies, and therefore variations in the fakes subtracted from the charge mis-id estimate as described in Table 8.2. Rates are shown for 2016 dataset.

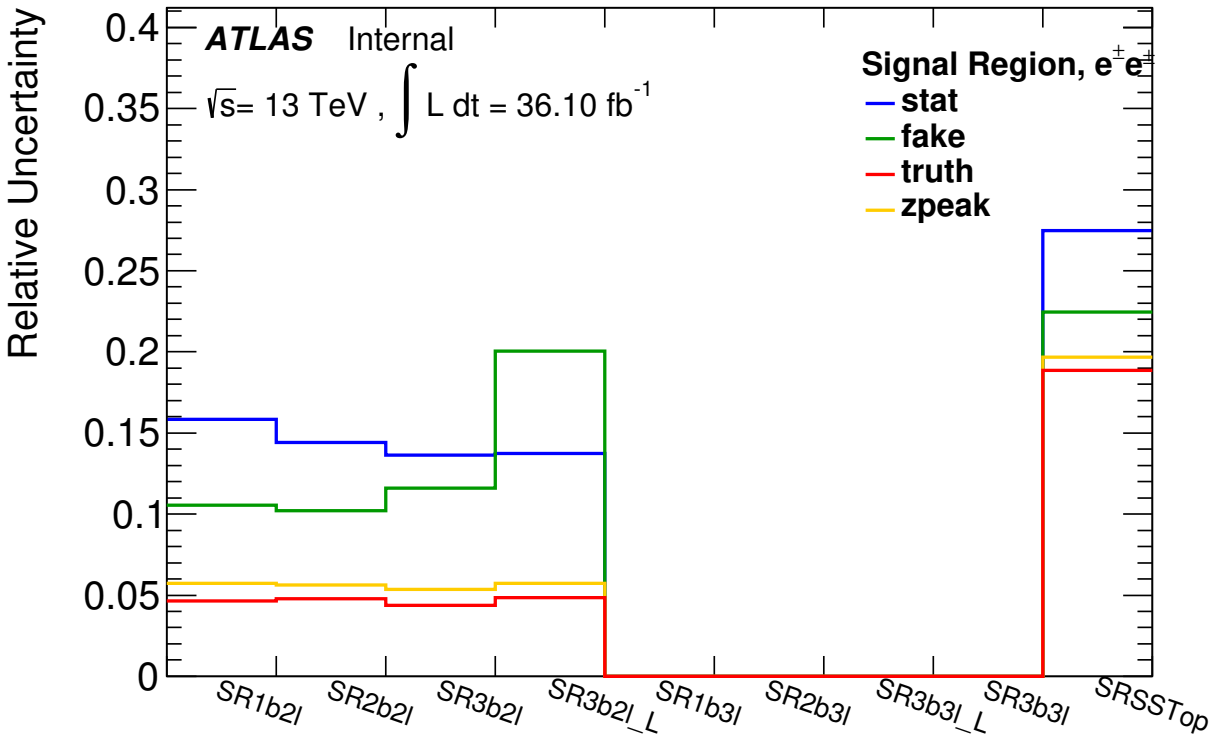

Figure 8.6: Relative systematic uncertainty on the charge mis-id in the signal regions. Note the last bin is for a non-VLQ signal model (t^+t^+). The trilepton channel signal regions do not have charge mis-id background, so the uncertainty is 0.

Fake/Non-prompt Background Of the three major sources of systematic uncertainty for the fake and non-prompt lepton background shown in table 8.2, the alternate real and fake control regions used to calculate the alternate real and fake efficiencies contribute the largest uncertainties. The alternate fake control region is typically the larger of these two uncertainties. Different levels of real lepton contamination may exist between the nominal and alternate fake control regions. The regions may also differ in the fake composition from different sources (b-flavored and c-flavored jets being the most common sources, typically). Fakes from c-jets or light-flavored jets have a higher efficiency for passing the isolation criteria in the fake control region, but b-jets, in general, comprise a larger fraction of the total number of fakes in most regions. The composition of the fakes background is studied in more detail with MC and discussed more in appendix B.3. However, MC simulations are limited and do not necessarily provide an accurate picture of the composition of the fakes. This is because the fakes may be mis-modeled in the simulations, which is why data is used to estimate this background in the first place. Also, fakes from unidentified sources (due to limitations in the MC simulation) can contribute as discussed more in appendix B.3.

Both electrons and muons have separate alternate control region definitions because different regions are prone to being enriched in fake electrons or muons, as is the case with the nominal control regions. For electrons, the alternate real control region is defined by increasing the $E_{\mathrm{T}}^{\mathrm{miss}}$ cut from 150 GeV to 175 GeV. The alternate fake control region for electrons is $E_{\mathrm{T}}^{\mathrm{miss}} < 20$ GeV. For muons, the alternate real control region is defined by increasing the $M_{\mathrm{T}}^{\mathrm{W}}$ cut from 100 GeV to 110 GeV. The alternate fake control region is defined as $M_{\mathrm{T}}^{\mathrm{W}} < 20$ GeV, $(E_{\mathrm{T}}^{\mathrm{miss}} + M_{\mathrm{T}}^{\mathrm{W}}) < 60$ GeV. The alternate fake control regions are chosen so the composition of fakes is not radically different to the lepton's nominal control region, even though variations may exist, as discussed previously. These variations are then accounted for in the alternate control region systematics. Table 7.2 shows the full description of the regions and comparisons with the nominal regions. Four nuisance parameters are derived for these systematics.

The second systematic arises from the uncertainty in the degree to which real leptons contaminate the fake enriched control region, as calculated from the MC. This contamination is subtracted during the calculation of the fake efficiencies. A $\pm 10\%$ variation is chosen to be consistent with the uncertainty on the cross sections for the major processes that contribute to the real lepton contamination. The processes that dominate come from $t\bar{t}$ and V+jets. One nuisance parameter is derived for this systematic because similar processes are expected to contribute to both fake enriched regions for electrons and muons.

Lastly, the other systematic uncertainty on the fake background arises from remeasuring the real and fake efficiencies in four subregions of the original nominal control regions. The subregions are defined by a random value assigned to each event between 0 and 1. Statistics can be limited in the nominal control regions, so this systematic is designed to account for fluctuations in the number of events in the real and fake control regions. In order to account for the total uncertainty from all the statistical subregion variations, the yields from each variation are computed separately. Then, one-half of the standard deviation of the variations in each region is taken as the up and down systematic uncertainty. This procedure takes into account correlations between the subregions and defines an overall up and down variation from the nominal fake yield. A final value for the uncertainty from the statistical subregions contributions is dependent on which analysis region the fake/non-prompt background is calculated for (i.e. control, validation, and signal region). Therefore, the likelihood MM yields from each subregion variation are calculated in each analysis region separately and combined after the calculation. The total up and down systematic uncertainty from the statistical subregions is combined in quadrature with the previous systematic uncertainties to calculate a total systematic uncertainty on the fake and non-prompt lepton background. Four separate nuisance parameters are also derived for these fluctuations to be used in the statistical analysis.

Figures 8.7 through 8.11 show the changes on the fake and real efficiencies from the different systematics for electrons. Figures 8.12 through 8.23 show the changes on the fake and real efficiencies from the different systematics for muons. Note that in some cases the fake efficiencies can be above 1. This happens only in regions where, due to low statistics, the MC subtraction results in the number of tight events greater than the number of loose events, resulting in an efficiency greater than 1. Due to the Likelihood MM using the average efficiencies in the fit, typically these events are averaged out and should not pose a problem for the final yield. However, to make sure this does not pose a problem, any efficiencies that are above 1 are set to 1 in the likelihood MM calculation.

Uncertainties that result in one-sided variations from the nominal fake/non-prompt yield are symmetrized and treated as symmetric up and down variations. Uncertainties that have asymmetric up and down fluctuations are generally kept asymmetric in the final nuisance parameter treatment. The total systematic uncertainty on the fake/non-prompt background is region dependent, in general. This means the systematic uncertainty may be different between the control region and the signal regions in the analysis. Because the total systematic uncertainty from all individual up and down variations differs by region, it is best to

treat the systematics in the final signal region fit with their nuisance parameters. Nine nuisance parameters are constructed to account for the differences between signal regions. Four parameters come from the alternate real and fake control regions for electrons and muons. These parameters are called *el_alt_real*, *el_alt_fake*, *mu_alt_real*, and *mu_alt_fake*. The MC variation by ±10% produces one nuisance parameter, called *mc_up/down*. Only one nuisance parameter is used for the MC variation due to an assumed correlation between the MC used for electrons and for muons. Lastly, four parameters come from the statistical subregions in each control region for electrons and muons. These parameters are called *stat_elReal*, *stat_elFake*, *stat_muReal*, and *stat_muFake*. In terms of a relative percentage of the nominal yield for this background, the relative systematic uncertainty in the main control region ($H_{\mathrm{T}} < 400$ GeV) is around 35%. The relative uncertainty on the fake/non-prompt background in the signal regions is shown in figure 8.24.

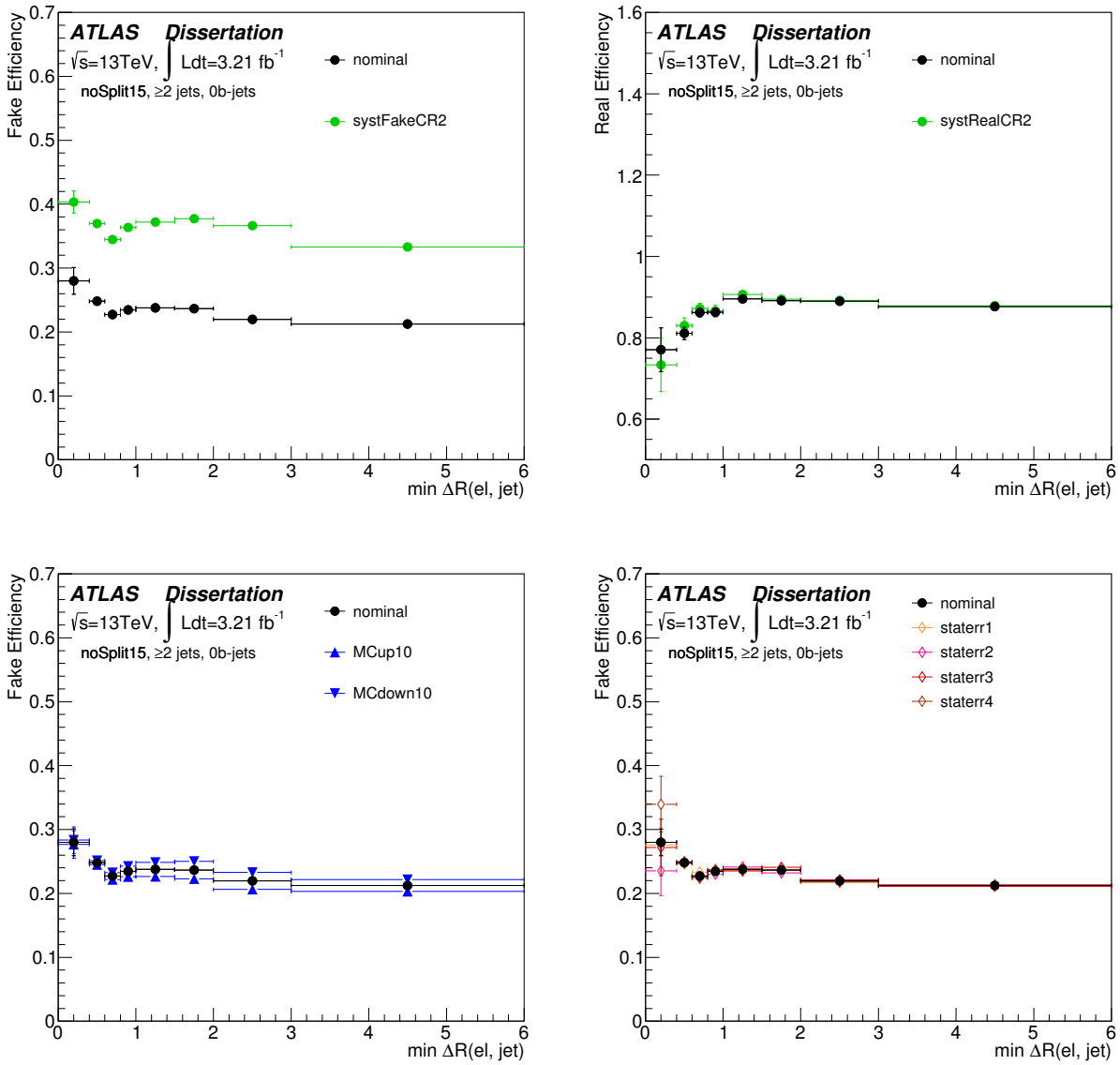

Figure 8.7: Fake and real electron efficiency variations using 2015 data with $\geq$2 jets and 0 b-tagged jets, parametrized as a function of the ΔR between the closest jet and the electron. The top left shows the nominal vs. the alternate fake CR and the top right shows the nominal vs. the alternate real CR (note the change in y-axis scale). The bottom left shows the nominal vs. the resulting fake efficiencies when the MC contamination in the fake enriched CR is varied by $\pm$10%. The bottom right plot shows the nominal vs. the statistical subregion variations in the fake enriched CR. The systematic uncertainties are described in Table 8.2.

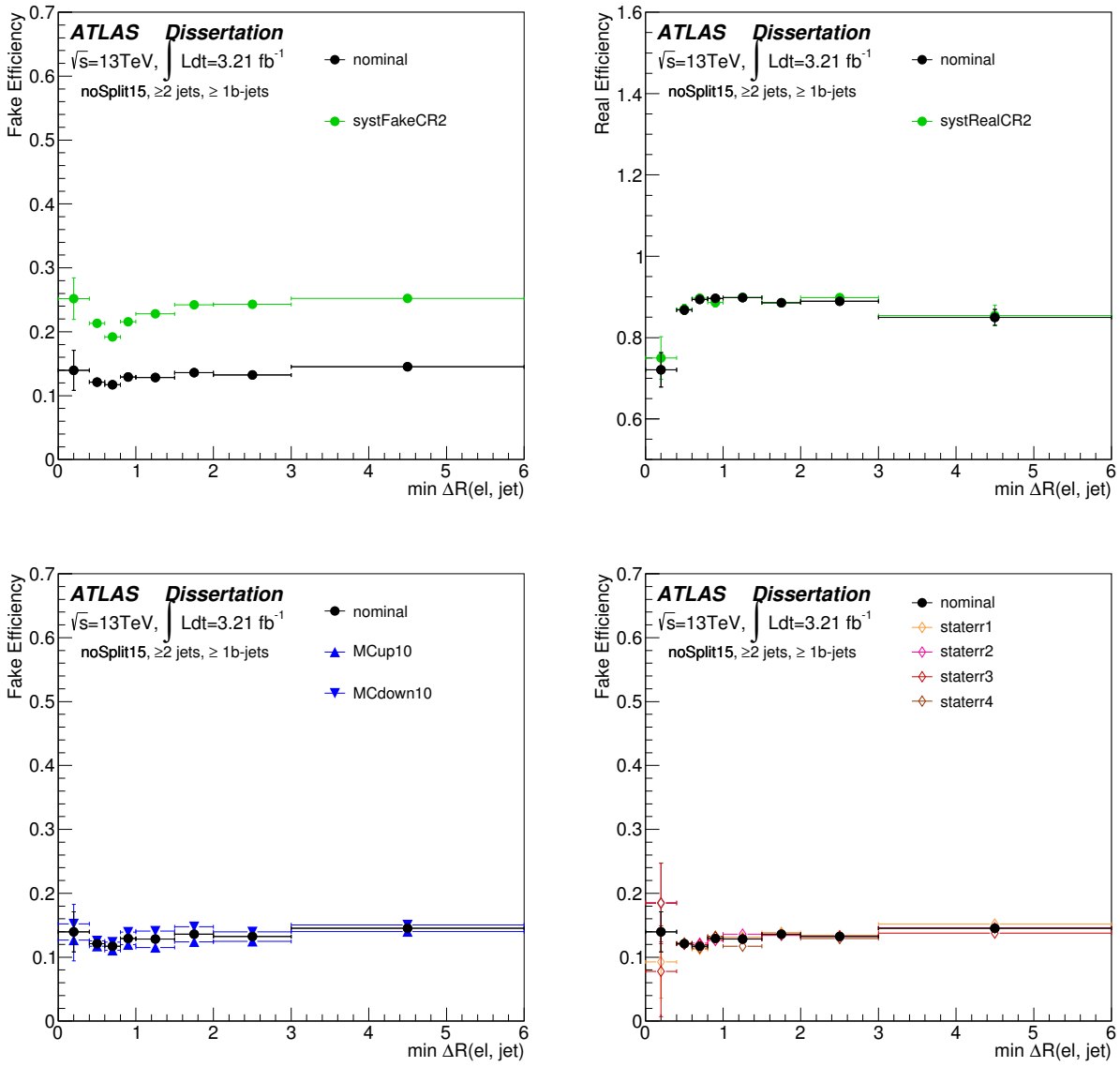

Figure 8.8: Fake and real electron efficiency variations using 2015 data with $\geq$2 jets and $\geq$1 b-tagged jets, parametrized as a function of the ΔR between the closest jet and the electron. The top left shows the nominal vs. the alternate fake CR and the top right shows the nominal vs. the alternate real CR (note the change in y-axis scale). The bottom left shows the nominal vs. the resulting fake efficiencies when the MC contamination in the fake enriched CR is varied by $\pm$10%. The bottom right plot shows the nominal vs. the statistical subregion variations in the fake enriched CR. The systematic uncertainties are described in Table 8.2.

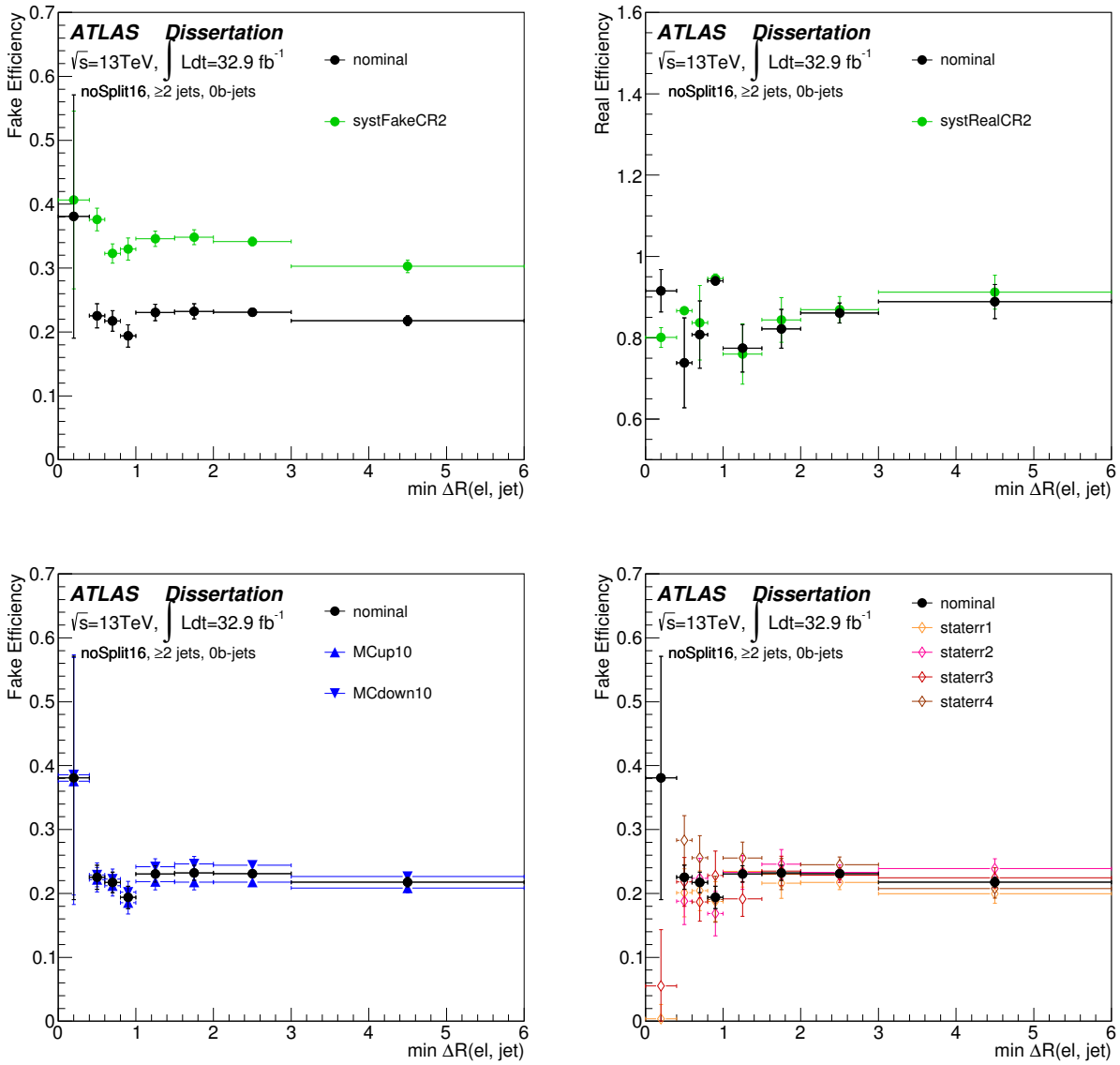

Figure 8.9: Fake and real electron efficiency variations using 2016 data with $\geq$2 jets and 0 b-tagged jets, parametrized as a function of the ΔR between the closest jet and the electron. The top left shows the nominal vs. the alternate fake CR and the top right shows the nominal vs. the alternate real CR (note the change in y-axis scale). The bottom left shows the nominal vs. the resulting fake efficiencies when the MC contamination in the fake enriched CR is varied by $\pm$10%. The bottom right plot shows the nominal vs. the statistical subregion variations in the fake enriched CR. The systematic uncertainties are described in Table 8.2.

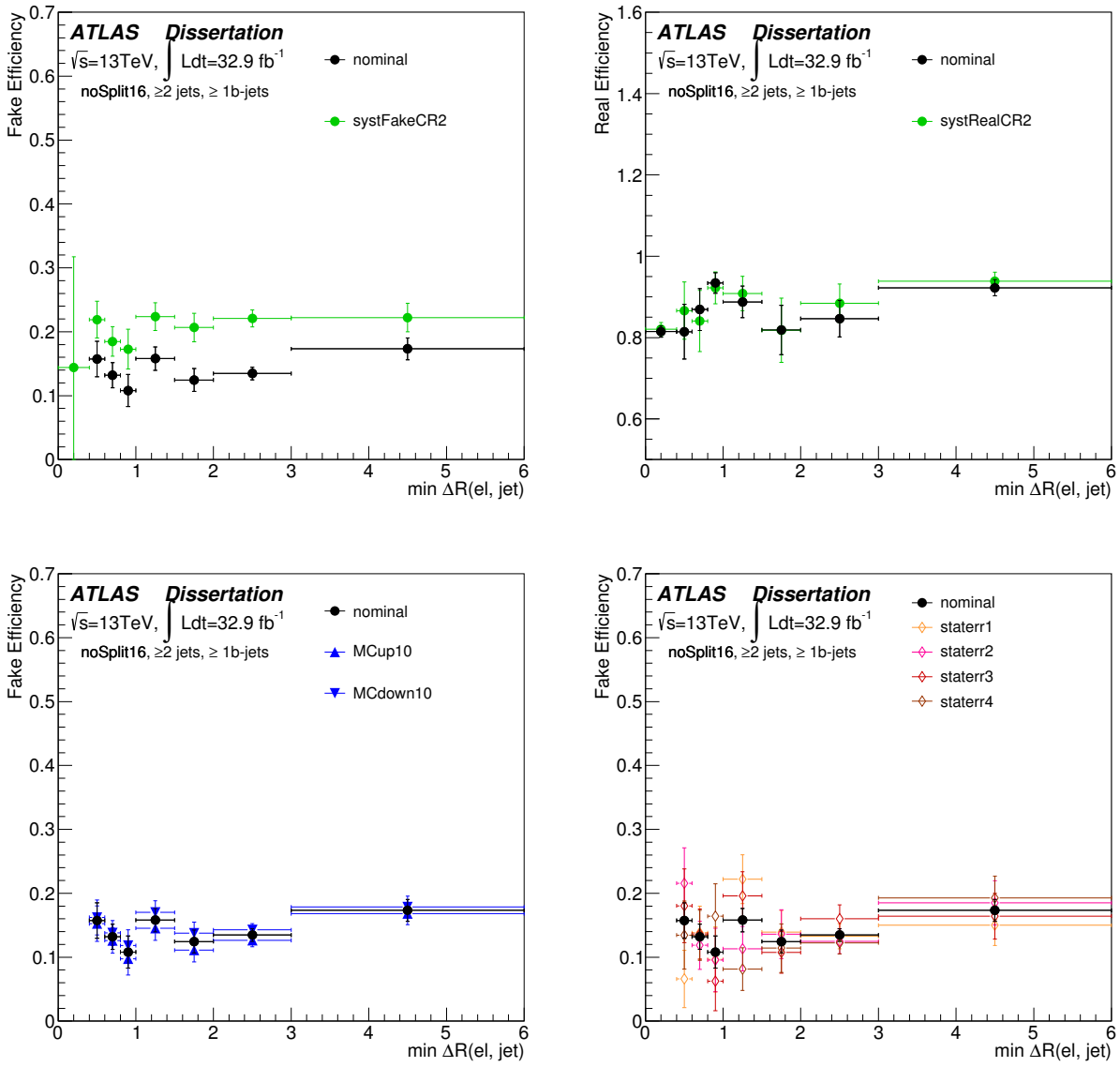

Figure 8.10: Fake and real electron efficiency variations using 2016 data with $\geq$2 jets and $\geq$1 b-tagged jets, parametrized as a function of the ΔR between the closest jet and the electron. The top left shows the nominal vs. the alternate fake CR and the top right shows the nominal vs. the alternate real CR (note the change in y-axis scale). The bottom left shows the nominal vs. the resulting fake efficiencies when the MC contamination in the fake enriched CR is varied by $\pm$10%. The bottom right plot shows the nominal vs. the statistical subregion variations in the fake enriched CR. The systematic uncertainties are described in Table 8.2.

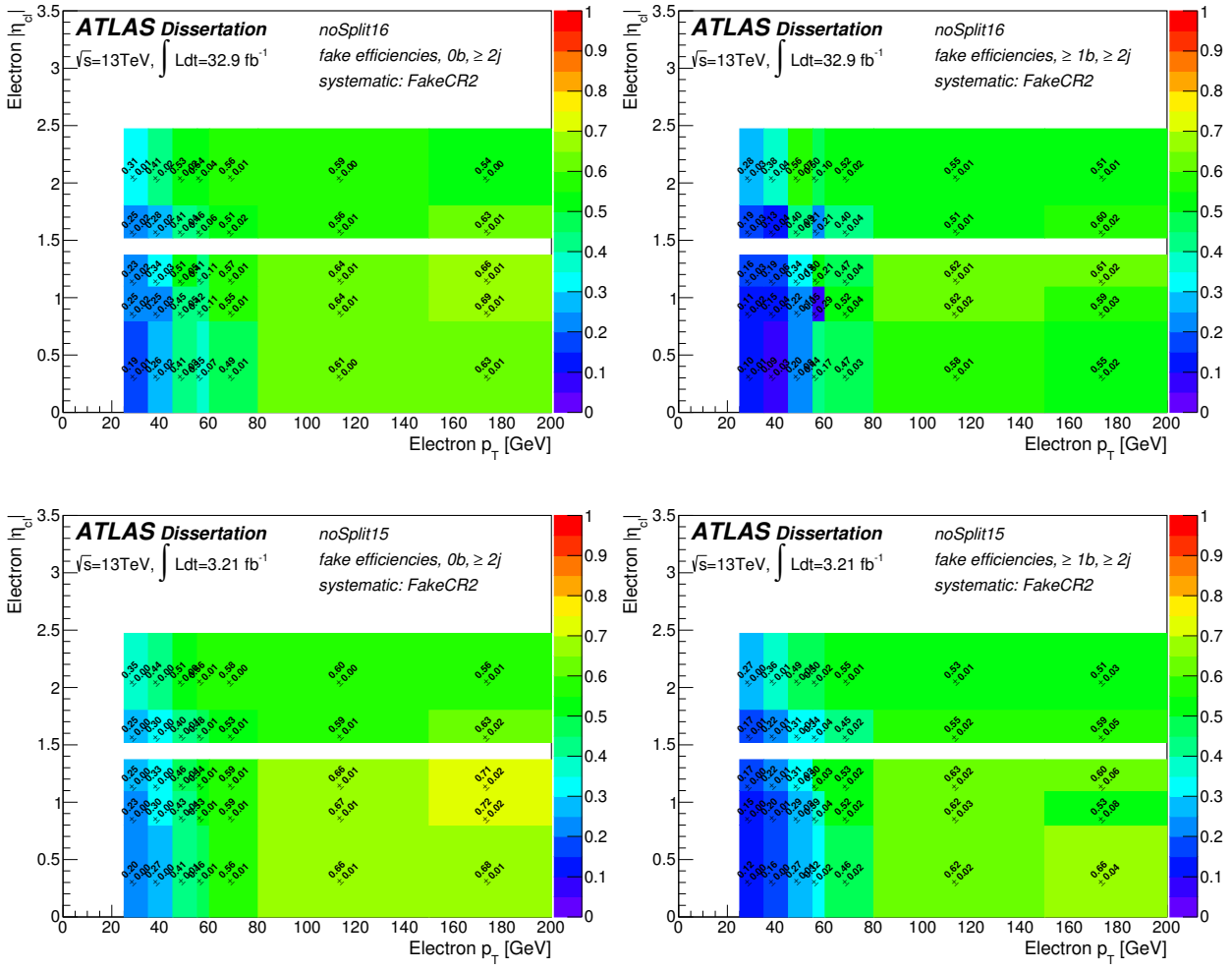

Figure 8.11: Fake efficiencies for electrons $|\eta_{\mathrm{cl}}|$ vs p_{T} from the systematic uncertainties described in Table 8.2. The top row is the alternate fake CR for electrons ($E_{\mathrm{T}}^{\mathrm{miss}} < 20$ GeV) for 2016 data with $\geq$2 jets and 0 b-tagged jets (left) and $\geq$2 jets and $\geq$1 b-tagged jets (right). The bottom row is the same but for 2015 data. Only the alternate fake CR syst is shown here because it is the largest systematic variance.

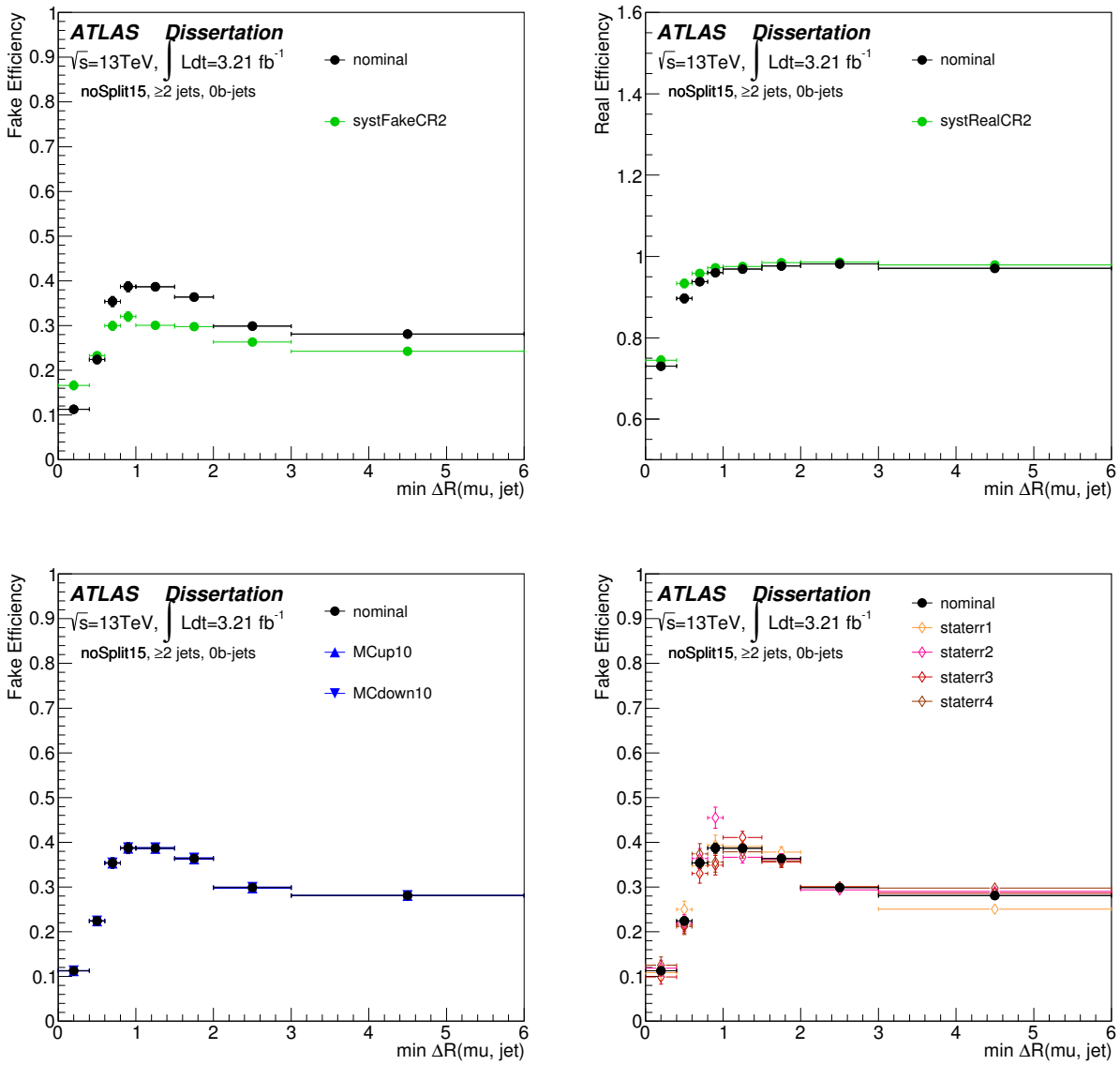

Figure 8.12: Fake and real muon efficiency variations using 2015 data with ≥2 jets and 0 b-tagged jets, parametrized as a function of the ΔR between the closest jet and the muon. The top left shows the nominal vs. the alternate fake CR and the top right shows the nominal vs. the alternate real CR (note the change in y-axis scale). The bottom left shows the nominal vs. the resulting fake efficiencies when the MC contamination in the fake enriched CR is varied by ±10%. The bottom right plot shows the nominal vs. the statistical subregion variations in the fake enriched CR. The systematic uncertainties are described in Table 8.2.

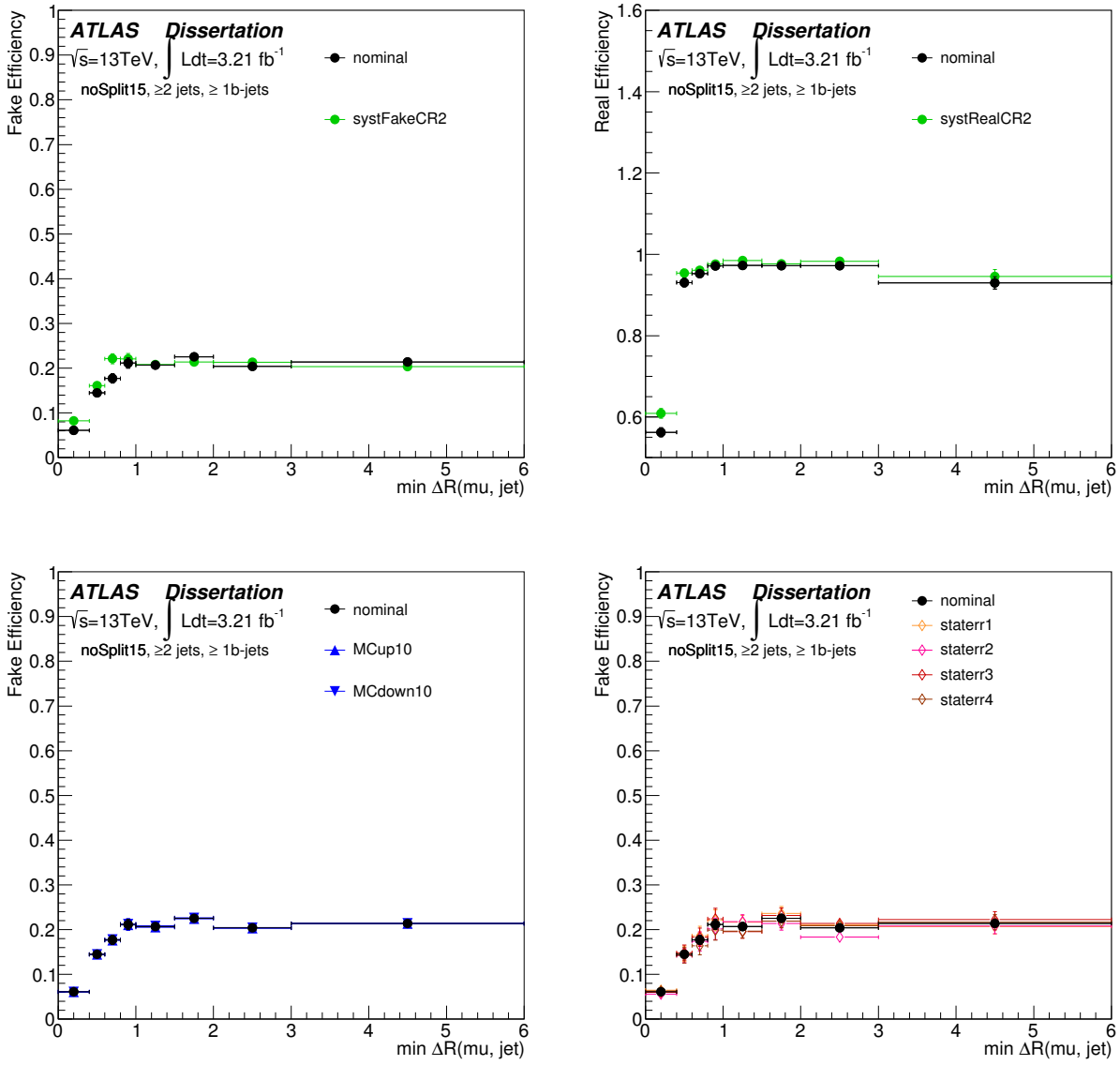

Figure 8.13: Fake and real muon efficiency variations using 2015 data with $\geq$2 jets and $\geq$1 b-tagged jets, parametrized as a function of the ΔR between the closest jet and the muon. The top left shows the nominal vs. the alternate fake CR and the top right shows the nominal vs. the alternate real CR (note the change in y-axis scale). The bottom left shows the nominal vs. the resulting fake efficiencies when the MC contamination in the fake enriched CR is varied by $\pm$10%. The bottom right plot shows the nominal vs. the statistical subregion variations in the fake enriched CR. The systematic uncertainties are described in Table 8.2.

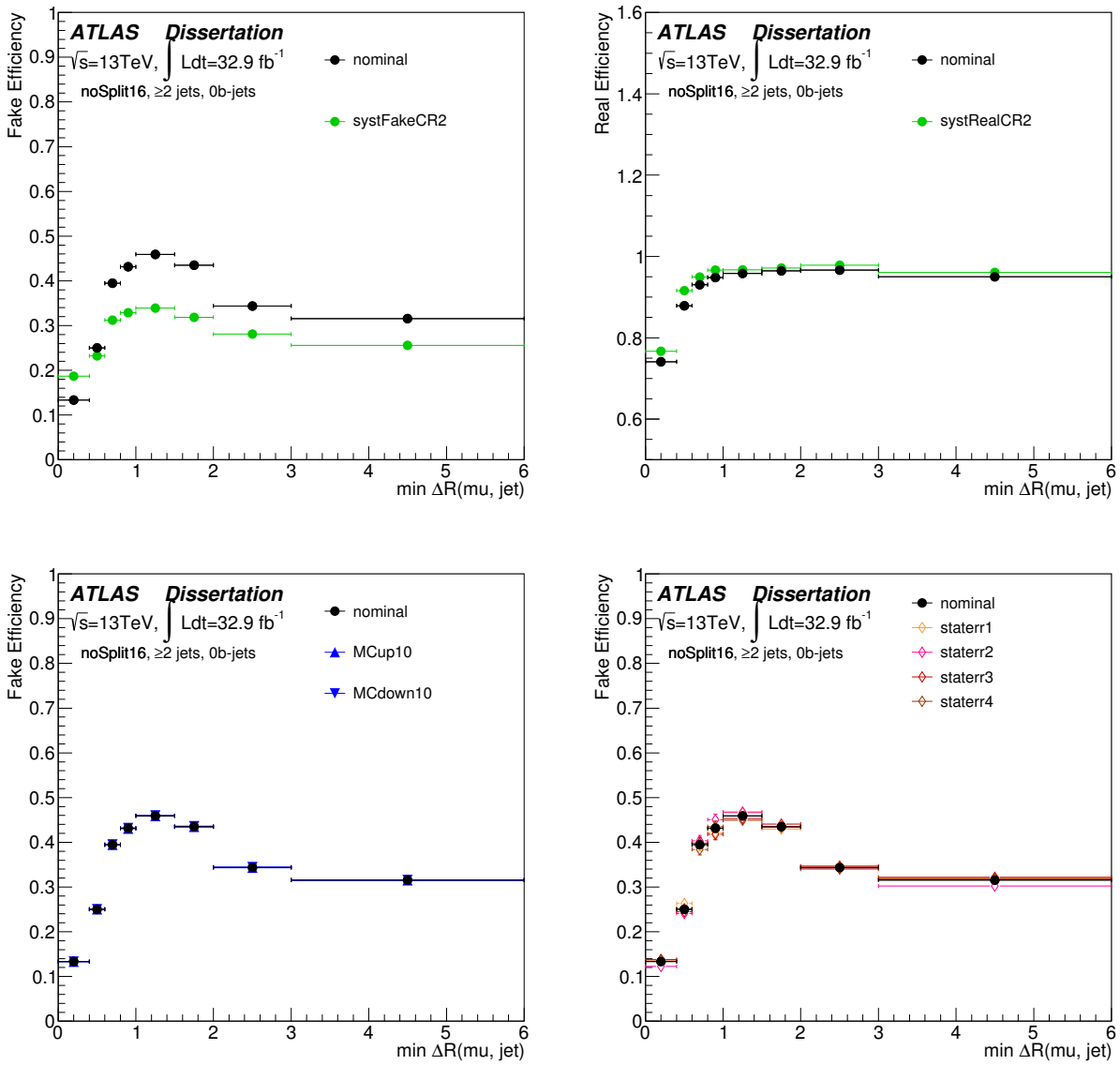

Figure 8.14: Fake and real muon efficiency variations using 2016 data with ≥2 jets and 0 b-tagged jets, parametrized as a function of the ΔR between the closest jet and the muon. The top left shows the nominal vs. the alternate fake CR and the top right shows the nominal vs. the alternate real CR (note the change in y-axis scale). The bottom left shows the nominal vs. the resulting fake efficiencies when the MC contamination in the fake enriched CR is varied by ±10%. The bottom right plot shows the nominal vs. the statistical subregion variations in the fake enriched CR. The systematic uncertainties are described in Table 8.2.

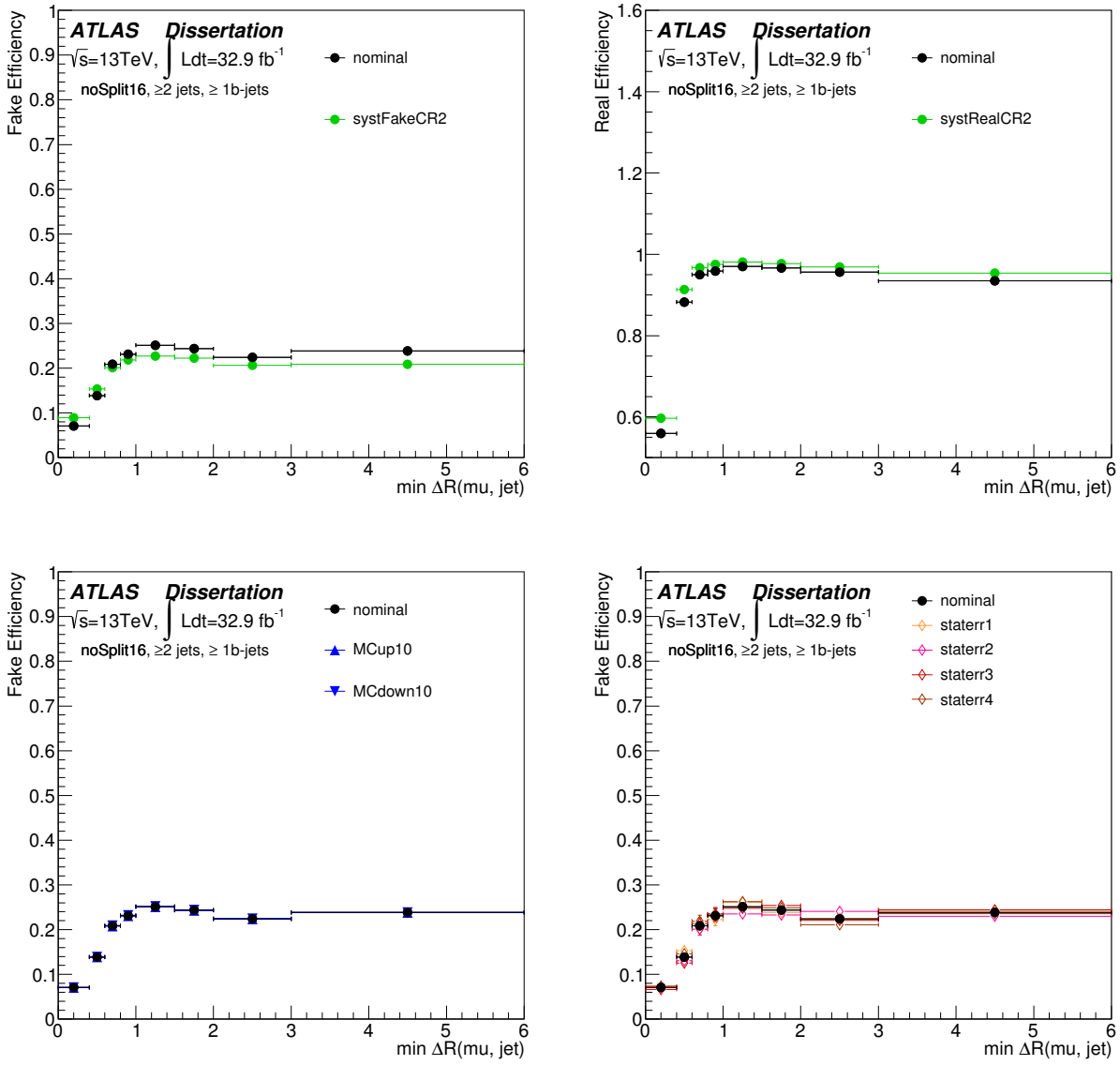

Figure 8.15: Fake and real muon efficiency variations using 2016 data with $\geq$2 jets and $\geq$1 b-tagged jets, parametrized as a function of the ΔR between the closest jet and the muon. The top left shows the nominal vs. the alternate fake CR and the top right shows the nominal vs. the alternate real CR (note the change in y-axis scale). The bottom left shows the nominal vs. the resulting fake efficiencies when the MC contamination in the fake enriched CR is varied by $\pm$10%. The bottom right plot shows the nominal vs. the statistical subregion variations in the fake enriched CR. The systematic uncertainties are described in Table 8.2.

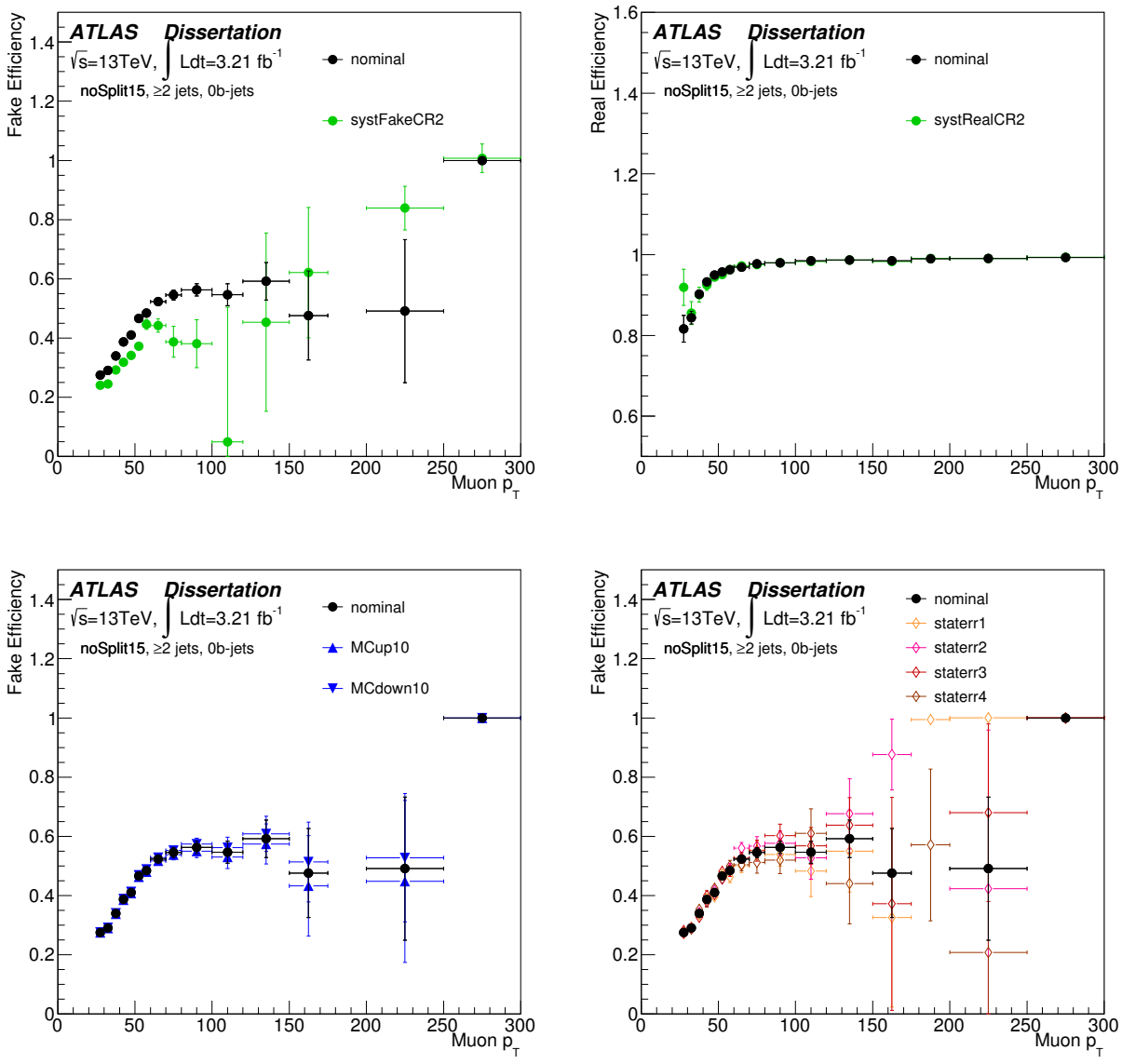

Figure 8.16: Fake and real muon efficiency variations using 2015 data with ≥2 jets and 0 b-tagged jets, parametrized as a function of the p_{T} of the muon. The top left shows the nominal vs. the alternate fake CR and the top right shows the nominal vs. the alternate real CR(note the change in y-axis scale) . The bottom left shows the nominal vs. the resulting fake efficiencies when the MC contamination in the fake enriched CR is varied by ±10%. The bottom right plot shows the nominal vs. the statistical subregion variations in the fake enriched CR. The systematic uncertainties are described in Table 8.2.

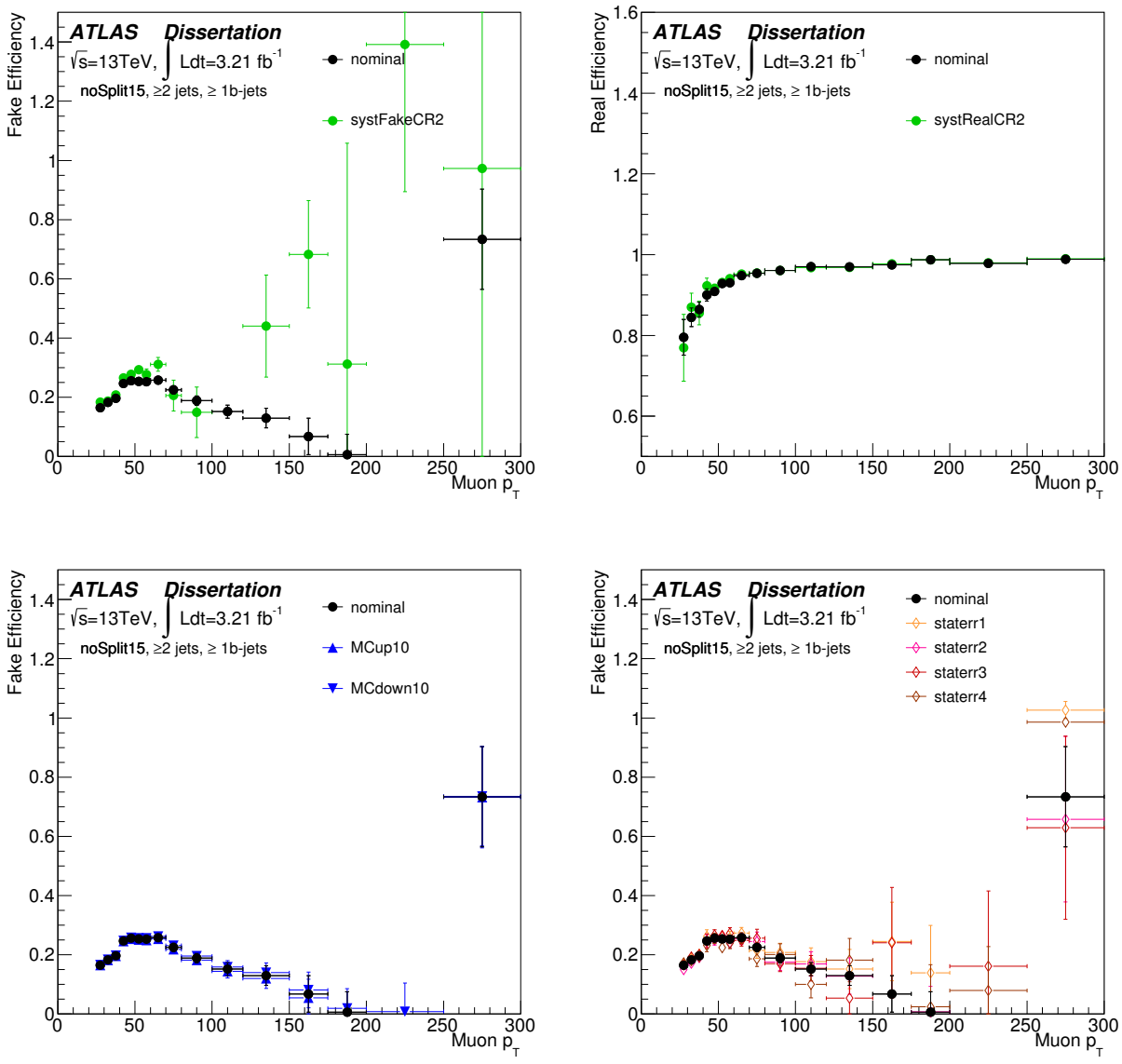

Figure 8.17: Fake and real muon efficiency variations using 2015 data with ≥2 jets and ≥1 b-tagged jets, parametrized as a function of the p_{T} of the muon. The top left shows the nominal vs. the alternate fake CR and the top right shows the nominal vs. the alternate real CR (note the change in y-axis scale). The bottom left shows the nominal vs. the resulting fake efficiencies when the MC contamination in the fake enriched CR is varied by ±10%. The bottom right plot shows the nominal vs. the statistical subregion variations in the fake enriched CR. The systematic uncertainties are described in Table 8.2.

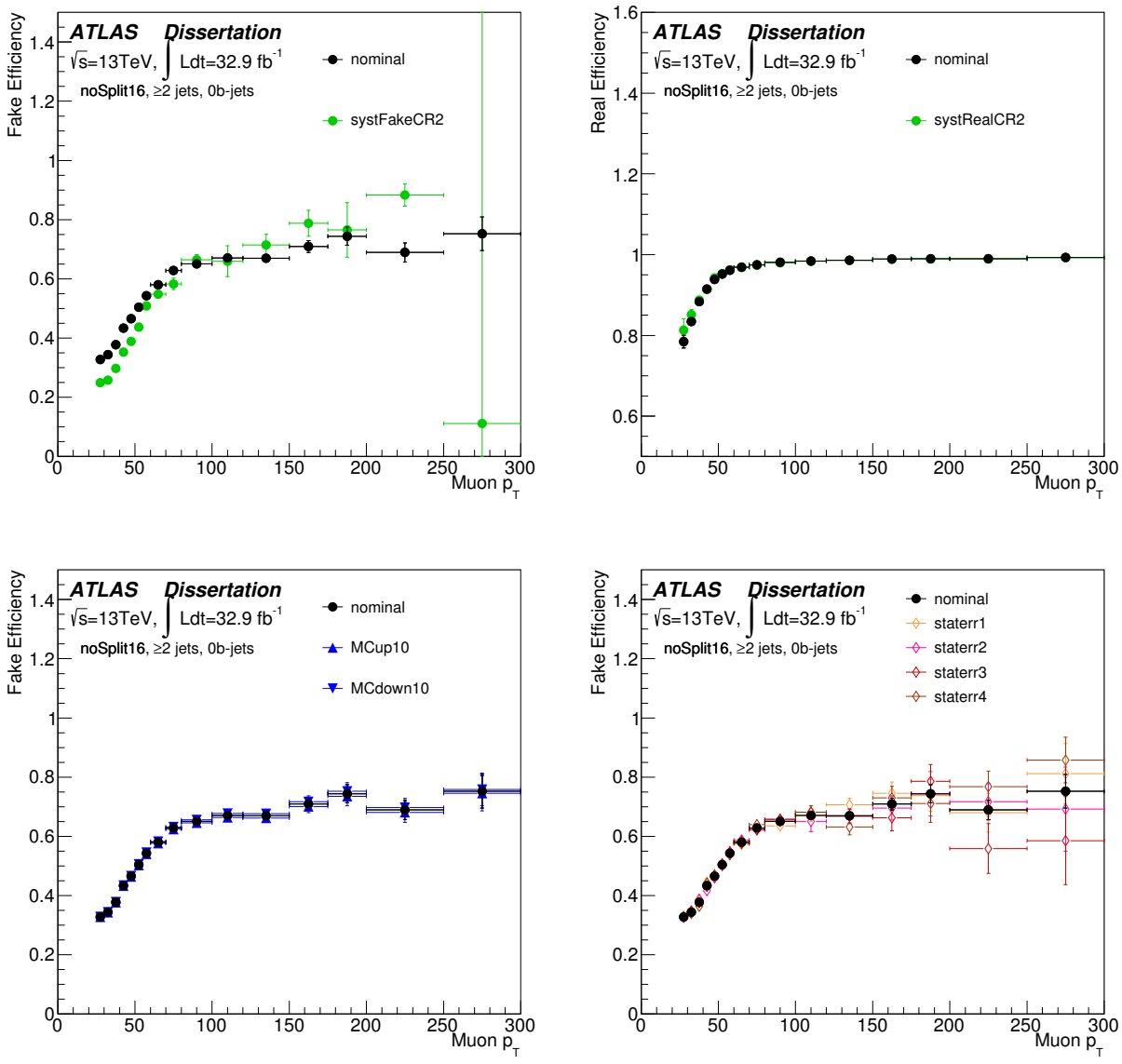

Figure 8.18: Fake and real muon efficiency variations using 2016 data with $\geq$2 jets and 0 b-tagged jets, parametrized as a function of the p_{T} of the muon. The top left shows the nominal vs. the alternate fake CR and the top right shows the nominal vs. the alternate real CR (note the change in y-axis scale). The bottom left shows the nominal vs. the resulting fake efficiencies when the MC contamination in the fake enriched CR is varied by $\pm$10%. The bottom right plot shows the nominal vs. the statistical subregion variations in the fake enriched CR. The systematic uncertainties are described in Table 8.2.

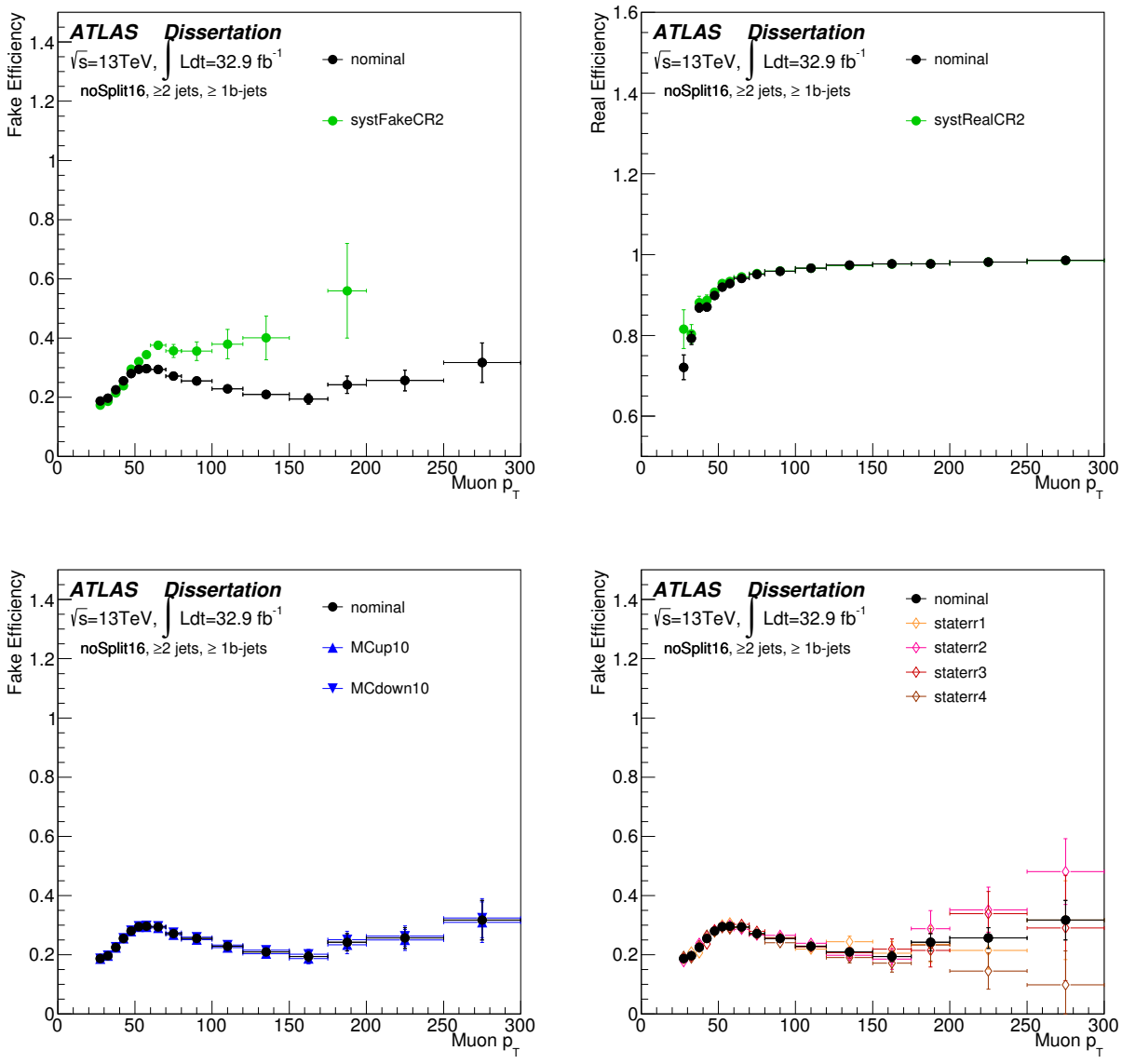

Figure 8.19: Fake and real muon efficiency variations using 2016 data with ≥2 jets and ≥1 b-tagged jets, parametrized as a function of the p_{T} of the muon. The top left shows the nominal vs. the alternate fake CR and the top right shows the nominal vs. the alternate real CR (note the change in y-axis scale). The bottom left shows the nominal vs. the resulting fake efficiencies when the MC contamination in the fake enriched CR is varied by ±10%. The bottom right plot shows the nominal vs. the statistical subregion variations in the fake enriched CR. The systematic uncertainties are described in Table 8.2.

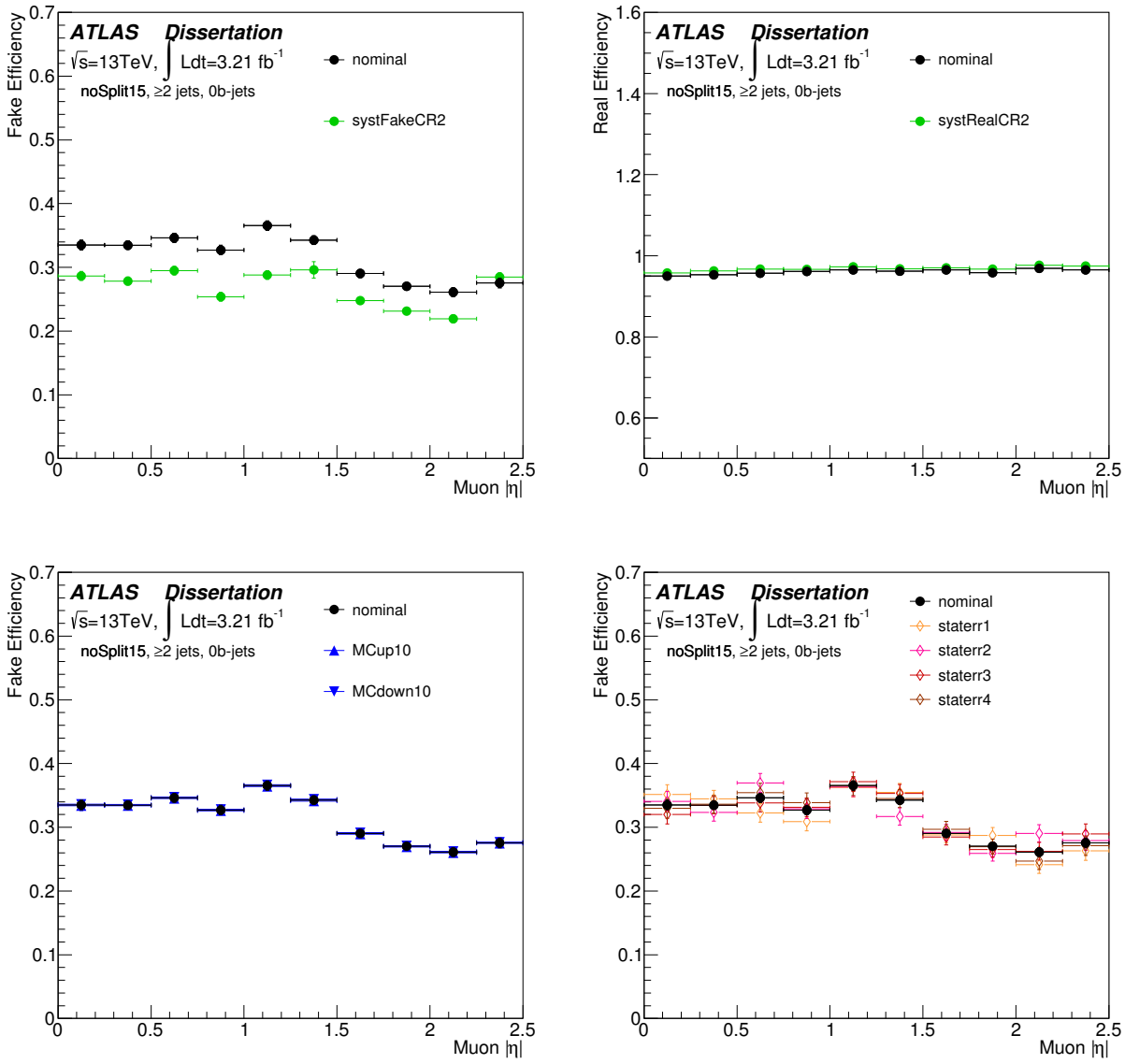

Figure 8.20: Fake and real muon efficiency variations using 2015 data with $\geq$2 jets and 0 b-tagged jets, parametrized as a function of the $|\eta|$ of the muon. The top left shows the nominal vs. the alternate fake CR and the top right shows the nominal vs. the alternate real CR (note the change in y-axis scale). The bottom left shows the nominal vs. the resulting fake efficiencies when the MC contamination in the fake enriched CR is varied by $\pm$10%. The bottom right plot shows the nominal vs. the statistical subregion variations in the fake enriched CR. The systematic uncertainties are described in Table 8.2.

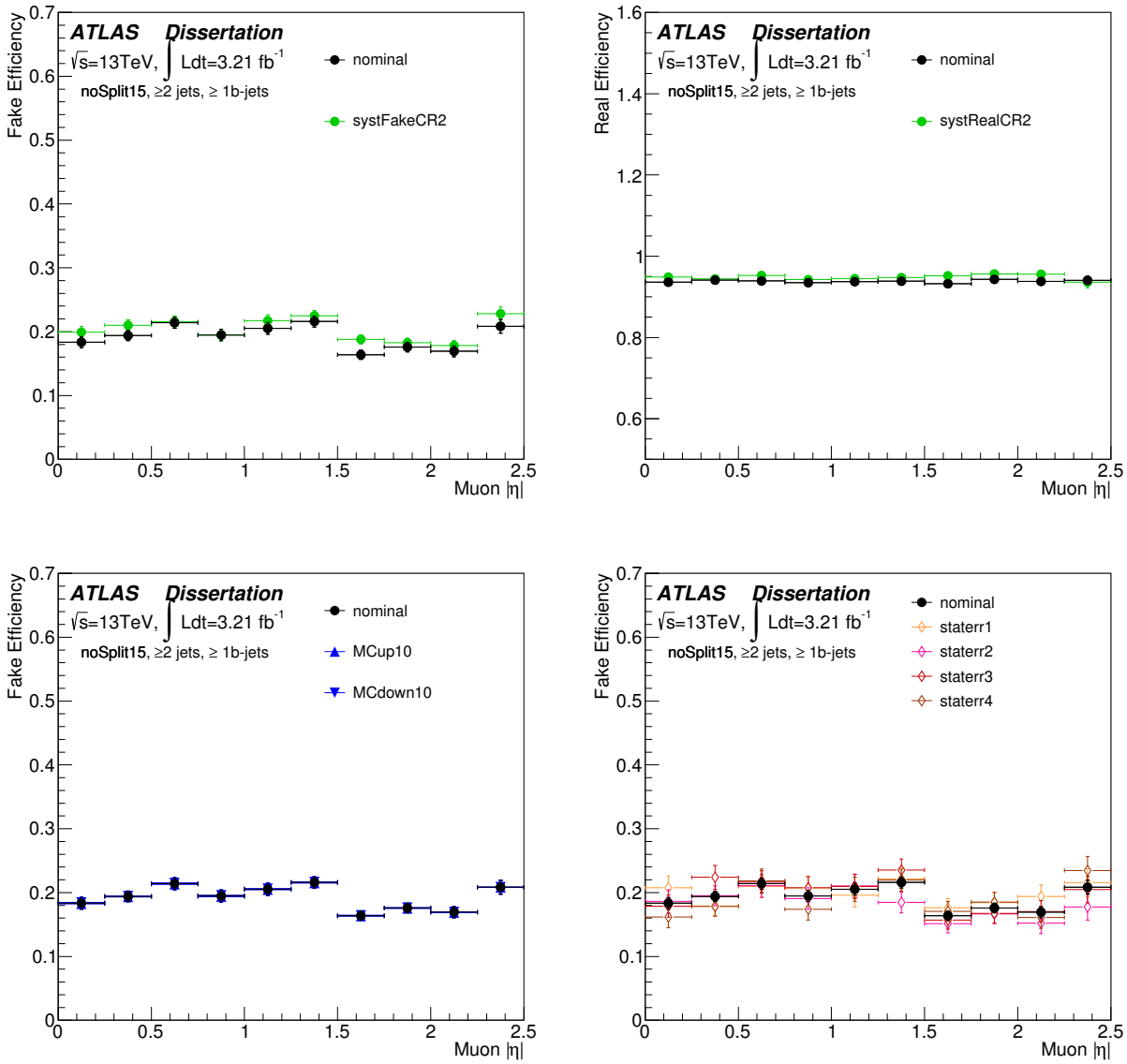

Figure 8.21: Fake and real muon efficiency variations using 2015 data with ≥2 jets and ≥1 b-tagged jets, parametrized as a function of the $|\eta|$ of the muon. The top left shows the nominal vs. the alternate fake CR and the top right shows the nominal vs. the alternate real CR (note the change in y-axis scale). The bottom left shows the nominal vs. the resulting fake efficiencies when the MC contamination in the fake enriched CR is varied by ±10%. The bottom right plot shows the nominal vs. the statistical subregion variations in the fake enriched CR. The systematic uncertainties are described in Table 8.2.

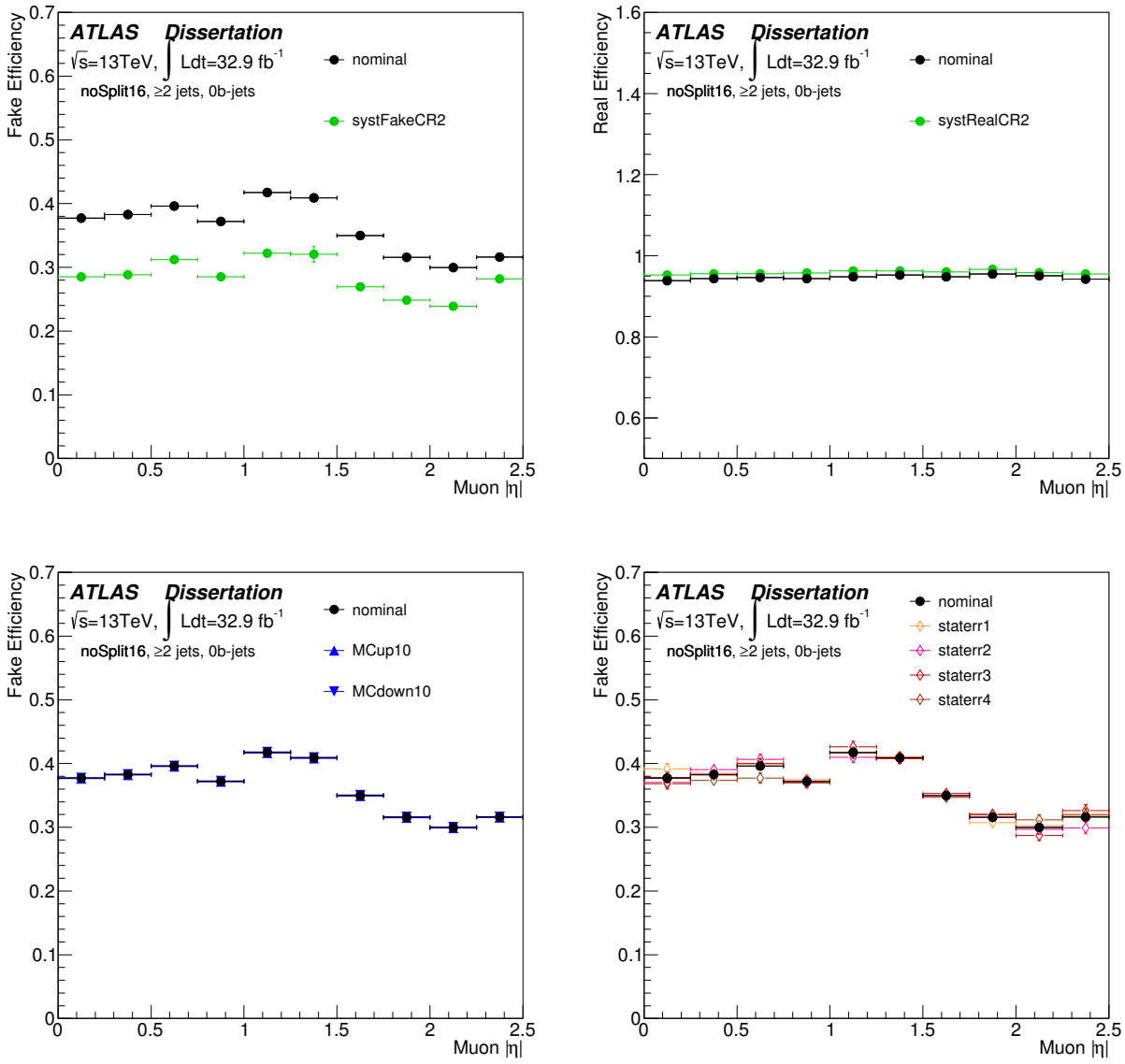

Figure 8.22: Fake and real muon efficiency variations using 2016 data with ≥2 jets and 0 b-tagged jets, parametrized as a function of the $|\eta|$ of the muon. The top left shows the nominal vs. the alternate fake CR and the top right shows the nominal vs. the alternate real CR (note the change in y-axis scale). The bottom left shows the nominal vs. the resulting fake efficiencies when the MC contamination in the fake enriched CR is varied by ±10%. The bottom right plot shows the nominal vs. the statistical subregion variations in the fake enriched CR. The systematic uncertainties are described in Table 8.2.

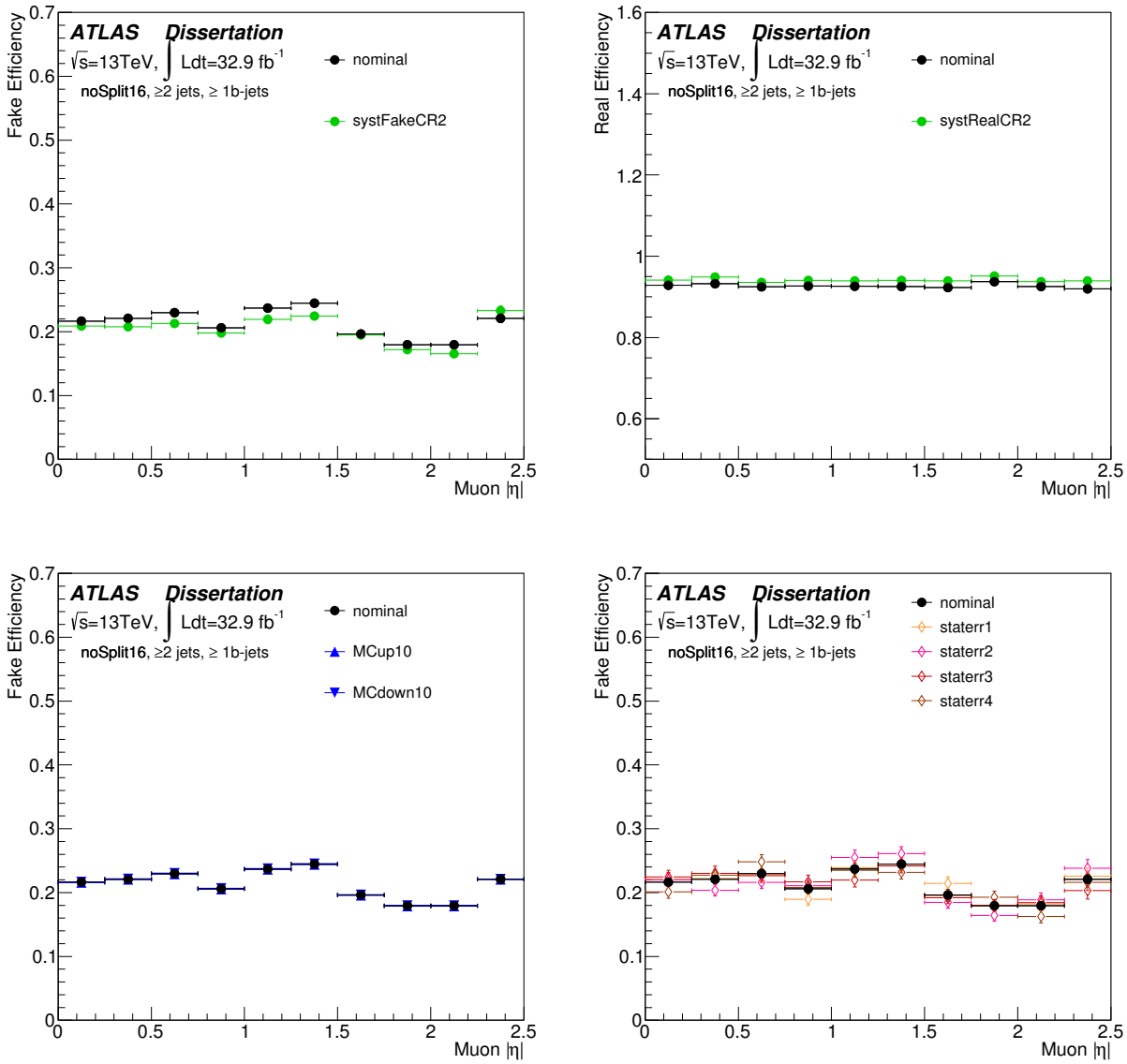

Figure 8.23: Fake and real muon efficiency variations using 2016 data with ≥2 jets and ≥1 b-tagged jets, parametrized as a function of the $|\eta|$ of the muon. The top left shows the nominal vs. the alternate fake CR and the top right shows the nominal vs. the alternate real CR (note the change in y-axis scale). The bottom left shows the nominal vs. the resulting fake efficiencies when the MC contamination in the fake enriched CR is varied by ±10%. The bottom right plot shows the nominal vs. the statistical subregion variations in the fake enriched CR. The systematic uncertainties are described in Table 8.2.

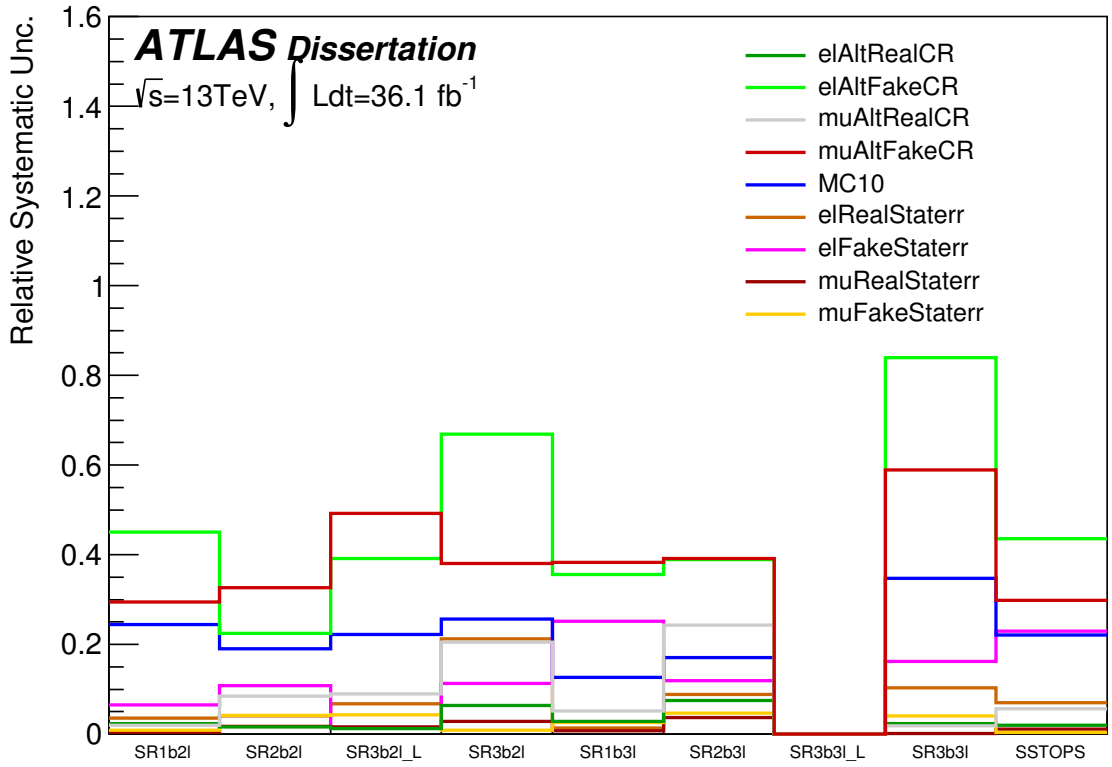

Figure 8.24: Relative systematic uncertainty on the fake and non-prompt lepton background in the signal regions. The *SR3b3l_L* bin shows an uncertainty of 0 because 0 fake events are recorded for this signal region. Note the last bin is for a signal region defined for a non-VLQ signal model (t^+t^+ – same-sign tops).

8.3 Other Major Systematics

There are several other major systematics that must be accounted for in the final systematics budget for this analysis.

Luminosity The uncertainty on the total integrated luminosity of the combined 2015 + 2016 dataset is $\delta\mathcal{L}/\mathcal{L} = \pm 2.1\%$, assuming partially correlated uncertainties between the two datasets. This value is derived from calibration measurements of van der Meer scans, which are measurements of beam separation in the x and y directions [158]. The 2015 luminosity uncertainty derivation uses a scan conducted in August 2015 and the 2016 luminosity uncertainty uses a scan conducted in May 2016.

Cross section The Monte Carlo samples used to simulate the SM backgrounds have uncertainties derived for the cross sections of their corresponding processes. The uncertainties are derived using the *Physics Modeling Group* recommendations. For the primary backgrounds $t\bar{t} + W$ and $t\bar{t} + Z$, global systematic uncertainties of 13% and 12% are applied, respectively [138]. For the diboson (VV) backgrounds, a global systematic uncertainty of 6% is applied [159]. For the rarer $t\bar{t} + H$ background, an uncertainty of $^{+6\%}_{-9\%}$ is applied [138]. For the rarer backgrounds from triboson (VVV), 3-top and 4-top production, and $t\bar{t} + WW$, a larger, conservative systematic uncertainty of 50% is applied.

Acceptance uncertainty Even though event yields are the primary observable used to interpret results in this analysis, uncertainties on the shape of certain kinematic distributions can affect the final event yields in the signal regions. A systematic uncertainty called the acceptance uncertainty is added to account for these differences and differences in the efficiency between the MC generators on the background. The acceptance uncertainty also takes into account any variations in the factorization and renormalization scales in the MC backgrounds. This uncertainty is estimated only for the largest SM background in the signal regions: the contribution from $t\bar{t} + V$ processes. For the other SM backgrounds estimated using MC, the acceptance uncertainty is assumed to be taken into account in the systematic uncertainty on the cross sections for those backgrounds.

Differences in the MC acceptance are evaluated using MC truth objects. First, the variations on the $t\bar{t} + V$ samples due to the factorization scale are calculated. If the up and down variations from the factorization and renormalization scales result in a unidirectional shift of the yield relative to the nominal, the larger shift is taken as the relative uncertainty,

and symmetrized. If the variations result in both a positive and a negative shift relative to the nominal yield, half the difference between the two is taken as the relative uncertainty.

Figure 8.25 shows the acceptance variations in the signal regions (note the last signal region designated 'SSTOPS' is defined for a non-VLQ signal model, t^+t^+). Both acceptance uncertainties are added in quadrature and combined into a single nuisance parameter for the limit fit described in Chapter 9.

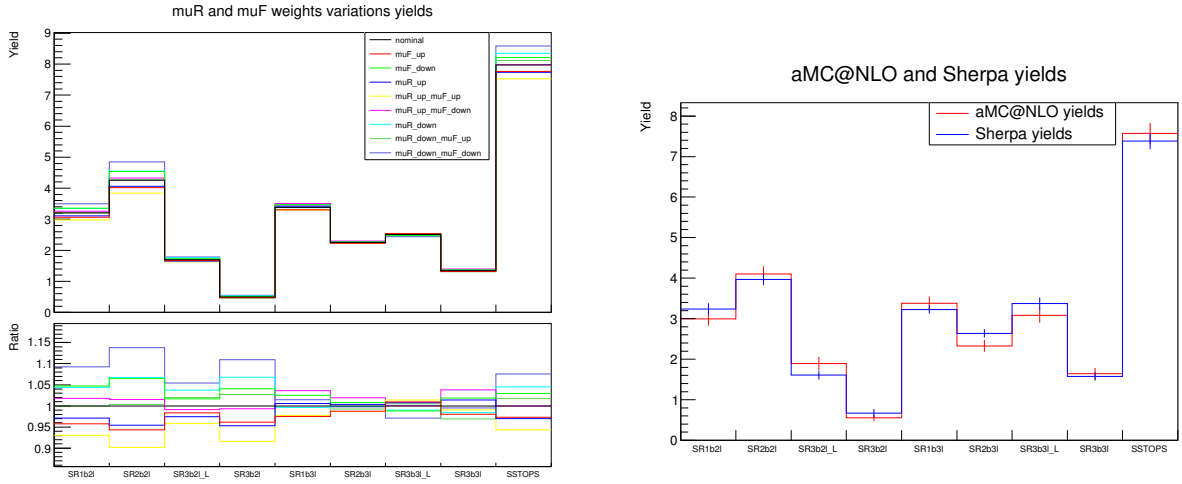

Figure 8.25: Acceptance yields from factorization and renormalization (left) and acceptance yields between MG5+aMC@NLO and Sherpa samples (right). All yields are calculated using $t\bar{t}+V$ MC. The variations in the yields is taken as the acceptance uncertainty.

CHAPTER 9
Statistical Interpretation of Results

After the event selection in the signal regions, described in Chapter 5, is applied to all 2015+2016 data as well as the data-driven and MC backgrounds, the total number of events in each region are counted. As already mentioned, this analysis is a cut-and-count analysis, where the final yields on data and total background in each signal region constitute the observables used to interpret the results. A comparison of the total background and data yields in terms of significance is used to interpret how likely any excess of signal above the background is to be consistent with a signal-plus-background hypothesis. A statistically significant excess of 5σ, probability or p-value of 3×10^{-7}, is needed to claim discovery of new physics (in this case, discovery of Vector-like Quarks). If any observed excess fails to reach 5σ or if there is no data excess, exclusion limits are set on the mass and cross section for Vector-like Quarks. Expected exclusion limits, which are calculated assuming no VLQ signals (*background-only* hypothesis), are set to compare to the observed exclusion limits, and to provide an estimate of the sensitivity of the analysis. Stronger limits are set if the data agrees well with the expected background.[1] In general, if the data show some excess consistent with the signal-plus-background hypothesis, even if not statistically significant enough to claim discovery, then weaker limits are set. There is also an intermediate case often used in particle physics: 3σ. If data is observed with a 3σ excess (p-value $= 3 \times 10^{-3}$), then it is said there is "evidence" of a signal.

The analysis is blinded until the backgrounds are understood in the validation regions. Once unblinded, the total background estimation is compared with data in the eight signal regions defined in table 5.4. The validation regions are also discussed in Chapter 5. This chapter explains the statistical interpretation of the results in the signal regions using a mostly frequentist statistical tool: the $\mathrm{CL_s}$ Method. Section 9.1 provides a brief primer on the calculation of significance and the method of combining p-values used in this analysis. Section 9.2 discusses the CL_S method of estimating limits on the Vector-Like Quark mass and

[1] *Stronger* here implies ruling out more of the mass and cross-section ranges for VLQ.

cross section. Section 9.3 discusses the final yields in the signal regions, and additional checks on some data excesses. Finally, section 9.4 discusses the limit setting package `TRExFitter`.

9.1 Significance

In order to understand how significant any deviation of data from the total expected background is, a calculation of the statistical significance is used. Because the background models are not without uncertainties, the significance of data versus total expected background must incorporate the statistical and systematics uncertainties on the backgrounds. The statistical uncertainty comes from the Poisson uncertainty associated with the number of events in a given region. The systematic uncertainties are described in Chapter 8.

Significance is a term frequently used in particle physics to describe the threshold for which a claim of discovery of new physics must meet. It is also used to describe how sensitive an analysis is to a particular new physics signal. In relation to the p-value, which is often quoted as a measure of the probability of a certain result, significance typically takes the form[2] of Z in equation 9.1.

$$Z = \Phi^{-1}(1 - p) \tag{9.1}$$

where Φ is the cumulative distribution of the probability distribution and p is the p-value. The significance is often quoted as some number of *sigma* away from the mean of a distribution and is used to assess the significance of a deviation assuming the background-only, or *null*, hypothesis. The typical threshold for discovery is 5σ ($Z = 5$), which is a statement of the probability that, if the particle in question does not exist, then the data collected is as extreme as what is observed (in other words very unlikely).[3] A significance of 5σ translates to a chance of roughly 1 in 3.5 million that the observed signal excess was produced by a random fluctuation from the background-only hypothesis in the signal-like direction. It should be obvious that this high threshold for discovery is good for making sure physicists are sure about a claim of discovery.

Since the Higgs Boson, discovered in 2012, was the last remaining piece to the Standard Model (SM), any new discovery would require a deviation of 5σ from the expected number of SM events given a particular final state signature. Thus, the background (*null* hypothesis) in this search means SM events. This, in general, goes for any other search for new physics beyond the SM as well.

[2]Sometimes in the literature this is referred to as the Z-value, so Z is used here.

[3]NB: this is not the same as saying that the particle exists or does not exist with some x% certainty.

Significance can also be determined from the expected or observed number of signal and background events. A figure of merit, equation 9.2, is used to calculate the expected significance in order to optimize the signal region selection in this analysis. This is calculated using the yields from signal MC events and background MC events.[4] This definition of significance is used to explicitly take into account the uncertainty on the background and is used early in the analysis to evaluate the optimal signal region definitions using only simulated events (because the signal regions are blinded until the backgrounds are understood).

$$Z = \frac{\mathrm{S}}{\sqrt{\mathrm{S} + \mathrm{B} + \sigma_{\mathrm{B}}^2}} \tag{9.2}$$

where S is the number of signal events, B is the number of expected background events, and σ_{B} is the total error on the expected background events. Once unblinded, the total significance of data above the background in the signal regions is calculated. In this analysis, where more than one signal region is used to evaluate the signal models, one can compute a total signal significance for a particular signal model, which includes all of the signal regions. To compute the combined significance, equation 9.3 is used, where i runs through all of the signal regions.[5] The p-value in each signal region is computed using 9.1 and 9.2 in each region. The total p-value for all signal regions is the probability of obtaining a χ^2 greater than the observed value for $2 \times N_{\mathrm{SR}}$ degrees of freedom, where N_{SR} is the number of signal regions. This overall p-value is converted to a Gaussian significance (Z-value).

$$\chi^2 = \sum_{\mathrm{i}=1}^{N_{\mathrm{SR}}} \ln(p_{\mathrm{i}}) \tag{9.3}$$

9.2 $\mathrm{CL_S}$ Method

The $\mathrm{CL_S}$ method [160, 161] is a modified frequentist method of interpreting results in terms of hypothesis testing. The *null* hypothesis in searches for new physics typically means interpreting the data under the assumption that the SM backgrounds are the only processes producing the events of interest, and the signals are non-existent. The *signal-plus-background* hypothesis interprets the data assuming the signal exists with the SM background. In this

[4] Typically the figure of merit $\frac{\mathrm{S}}{\sqrt{\mathrm{B}}}$ is used in cases with large statistics to find the expected significance of discovery. However, equation 9.2 is used here to optimize the signal regions and provide a more accurate way of assessing the sensitivity to the various signal models while also incorporating an estimate of the background uncertainties.

[5] A variation on this equation is also known as Fisher's method in statistics.

context, the signal is an extension to the SM. The CL_S method is the method of interpretation of the signal models most often used in high energy particle physics analyses. It is also especially useful for not excluding models to which an analysis may not have any sensitivity [153]. This can happen when low statistics dominate, when the background and signal-plus-background probability density functions are very close to each other, or when there is a downward fluctuation in the observed yield.

Setting limits on parameters within a signal model allows for an interpretation of the signal model given the data collected. In the event 5σ is not reached to claim discovery of new physics, then the main goal of new physics searches is to set limits on the signal-plus-background hypothesis. Since this analysis is a counting experiment, the measurements made are the number of events, S or B, in certain regions. In a region, the average number of background events for a particular signature is given by $B = \sigma_B L$, where σ_B is the cross section of the background process to decay to the particles kinematically defining the region, L is the integrated luminosity.[6] The average number of signal events is $S = \sigma_S L$, where σ_S is the cross section of the new physics process (signal). The statistical uncertainties on S and B are given by a standard Poisson distribution and both statistical and systematic uncertainties would affect the width of the distributions.

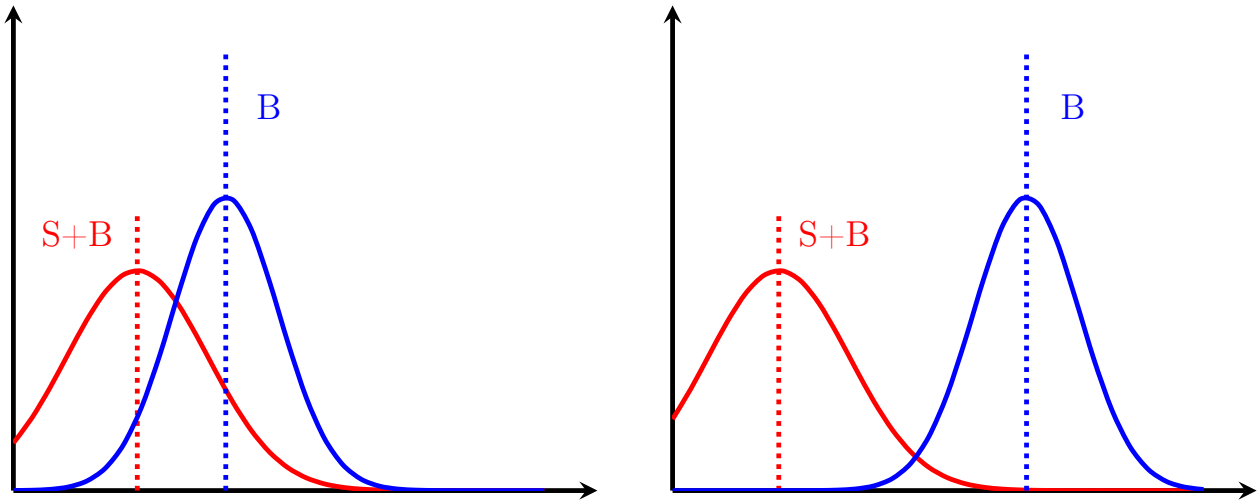

Figure 9.1: Different probability distribution functions for signal-plus-background (red) and background (blue) distributions with different levels of sensitivity. The y-axis is in arbitrary units. The x-axis is the test statistic in equation 9.6.

Figure 9.1 shows a cartoon of these two distributions with some separation. The red curve

[6] In reality, there are also acceptance and selection efficiencies that influence the total number of events, but for the purposes of this discussion, B and S are left simplified.

shows the *signal-plus-background* distribution and the blue curve shows the *background* distribution. In an analysis where these distributions are sufficiently separated from each other, the search sensitivity to the signal model increases. From these distributions, a likelihood for each hypothesis can be constructed by running a large number of pseudo-experiments under each hypothesis. The likelihood distributions are Poisson distributions, as shown in equations 9.4 and 9.5.

$$\mathcal{L}(x|\mathrm{S{+}B}) = \prod_{\mathrm{i}} \frac{(\mathrm{S_i{+}B_i})^x e^{-(\mathrm{S_i{+}B_i})}}{x!} \prod_{\mathrm{j}} \mathcal{N}_{\mathrm{j}}(\mu_{95\%}, \theta_{\mathrm{j}}) \tag{9.4}$$

$$\mathcal{L}(x|\mathrm{B}) = \prod_{\mathrm{i}} \frac{\mathrm{B_i}^x e^{-\mathrm{B_i}}}{x!} \prod_{\mathrm{j}} \mathcal{N}_{\mathrm{j}}(\theta_{\mathrm{j}}) \tag{9.5}$$

The product over i runs over all signal regions. Also, $\mu_{95\%}$ is defined as the signal strength such that $\mu_{95\%} \equiv \sigma_{95\%}/\sigma_{\mathrm{theory}}$, where $\sigma_{95\%}$ indicates the signal cross section at the 95% CL (described later) and σ_{theory} is the theoretical cross section for the signal. Included in these equations are the nuisance parameter distributions represented by $\mathcal{N}_{\mathrm{j}}(\mu, \theta_{\mathrm{j}})$ and $\mathcal{N}_{\mathrm{j}}(\theta_{\mathrm{j}})$. The product runs over all functional distributions of each parameter θ_{j}. The likelihoods are combined into a test statistic used in the $\mathrm{CL_S}$ method to assess the maximal difference between the distributions. In practice, the minimum of -2 times the log of the ratio of the likelihoods is used, which is called the *log-likelihood ratio* (q) given in equation 9.6.

$$q = -2\ln\Big(\frac{\mathcal{L}(x|\mathrm{S{+}B})}{\mathcal{L}(x|\mathrm{B})}\Big) \tag{9.6}$$

In order to determine if the observed log-likelihood ratio is more similar to the background-only hypothesis or the signal-plus-background hypothesis, the p-value is calculated. The p-values of the likelihood distributions may be obtained by equations 9.7 and 9.8 [161, 162] based on the observed q_{obs}.

$$p_{\mathrm{S+B}} = 1 - \Phi\Big(\frac{q_{\mathrm{obs}} + 1/\sigma^2_{\mathrm{S+B}}}{2/\sigma_{\mathrm{S+B}}}\Big) \tag{9.7}$$

$$p_{\mathrm{B}} = \Phi\Big(\frac{q_{\mathrm{obs}} - 1/\sigma^2_{\mathrm{B}}}{2/\sigma_{\mathrm{B}}}\Big) \tag{9.8}$$

Again, Φ is the cumulative distribution and $\sigma_{\mathrm{S+B}}$ and σ_{B} are the total uncertainties on the distributions. As shown in equations 9.4 and 9.5, the width of the distribution is parameterized with the set of nuisance parameters, which reduces the sensitivity to the signal model of interest. The functional form of the nuisance parameters can vary, in general,

but here it is typically Gaussian (but can be asymmetric due to asymmetric errors). The nuisance parameters are discussed in Chapter 8 in more detail.

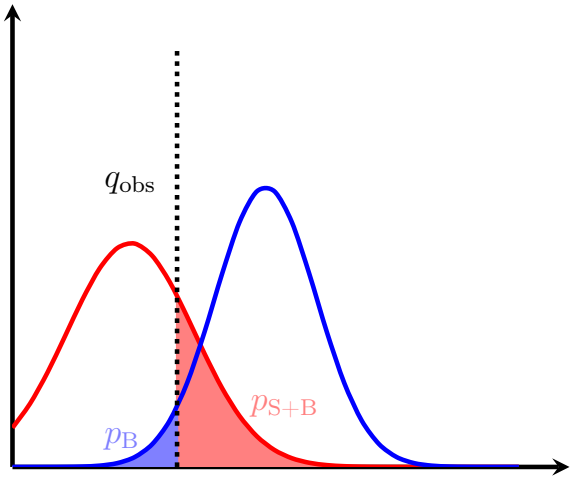

Figure 9.2: Illustration of the p-values (shaded regions) for the S+B and B-only likelihood functions. The observed value of the test statistic is shown by the dotted line (q_{obs}). The 'signal-like' direction is more to the left, while 'background-like' is more to the right.

Figure 9.2 illustrates the p-values on the set of distributions. Typically, signal models are excluded in the CL_S method by comparing the p-value for S+B and B-only to a fixed value α by: $\text{CL}_\text{S} = p_{\text{S+B}}/(1 - p_{\text{B}}) < \alpha$. In most particle physics analyses at the LHC, $\alpha = 0.05$. This means $\text{CL}_\text{S} < 0.05$ excludes the signal at the 95% confidence level.[7]

9.3 Results

Figure 9.3 shows the summary plot with the total background and data yields in each signal region. The total statistical and systematic uncertainties are included for each bin. Two signals are plotted as well for comparison: pair production of singlet T at a mass of 1 TeV and the 4-top SM production (plotted with 4.6 times the expected production cross-section). The signal yields are estimated from MC simulation samples. Table 9.1 shows the yields for the major backgrounds and the data for the signal regions containing two leptons. Table 9.2 shows the yields for the major backgrounds and the data for the signal regions containing three leptons. The nominal yield for a given region is expressed with the $\pm 1\sigma$ statistical and systematic uncertainties of the measurement separated. The values are quoted as: nominal $\pm$ stat $\pm$ syst, where the uncertainties have been symmetrized for readability.

[7]Note that although confidence level is often abbreviated CL in the literature, the CL in CL_S does not mean confidence level. CL_S is related to the p-values and is not a confidence level.

In the regions with ≥3 b-tagged jets there are observed excesses. The two highest excess regions are the ≥3 b-tagged regions with looser cuts on H_{T}. These regions were optimized specifically for the $t\bar{t}t\bar{t}$ signal (non-VLQ). The significance in these regions reaches to roughly 1.83σ (p-value $= 0.033$) for *SR3b3l_ L* and 1.89σ (p-value $= 0.029$) for *SR3b2l_ L*. Several cross-checks were made to determine if these modest excesses are legitimate in the analysis (meaning not due to an obvious error in the background estimations).

The excess in the *SR2b3l_ L* and *SR3b3l_ L* regions was determined to be concentrated in events containing mostly muons, so several checks were done to determine if anything awry with these muons happened in data. Figures 9.5 and 9.6 show some muon variables (p_{T}, $|\eta|$, $|d_0^{\mathrm{sig}}|$, etc.) for checking where the excess is most prominent. Additionally, figure 9.7 shows some event kinematic distributions for the *SR3b2l_ L* and *SR3b3l_ L* regions.

Several other checks were performed to scrutinize events in data that are in excess of what is expected from the backgrounds. Also, several checks are performed for the fake and non-prompt lepton background because this background is the hardest to estimate. Additional checks are discussed in more detail in appendices B and C.

Process	*SR1b2l*	*SR2b2l*	*SR3b2l_ L*	*SR3b2l*
Fake/Non-prompt	$4.13 \pm 1.63 \pm 2.48$	$2.48 \pm 1.02 \pm 1.14$	$1.21 \pm 0.85 \pm 0.82$	$0.20 \pm 0.47 \pm 0.18$
Charge mis-ID	$1.18 \pm 0.10 \pm 0.19$	$1.30 \pm 0.10 \pm 0.21$	$0.32 \pm 0.04 \pm 0.05$	$0.21 \pm 0.04 \pm 0.03$
$t\bar{t}Z$	$0.58 \pm 0.08 \pm 0.06$	$0.95 \pm 0.11 \pm 0.12$	$0.72 \pm 0.11 \pm 0.09$	$0.11 \pm 0.05 \pm 0.02$
$t\bar{t}H$	$0.56 \pm 0.07 \pm 0.05$	$0.57 \pm 0.10 \pm 0.05$	$0.91 \pm 0.11 \pm 0.08$	$0.19 \pm 0.05 \pm 0.02$
$t\bar{t}W$	$2.04 \pm 0.14 \pm 0.37$	$2.68 \pm 0.15 \pm 0.51$	$0.95 \pm 0.11 \pm 0.20$	$0.40 \pm 0.06 \pm 0.11$
Dibosons	$3.18 \pm 1.51 \pm 0.61$	0.00 ± 0.46	$0.13 \pm 0.45 \pm 0.04$	0.00 ± 0.46
Other bkg.	$0.62 \pm 0.08 \pm 0.14$	$1.12 \pm 0.20 \pm 0.23$	$1.93 \pm 0.15 \pm 0.16$	$0.94 \pm 0.19 \pm 0.05$
Total bkg.	$12.27 \pm 2.23 \pm 2.59$	$9.11 \pm 1.16 \pm 1.29$	$6.17 \pm 0.99 \pm 0.87$	$2.05 \pm 0.69 \pm 0.22$
Data	14	10	12	4
p-value	0.37	0.43	0.029	0.17

Table 9.1: Total yields in the signal regions defined in §5.4 for dilepton events. Only the prominent backgrounds are separated, with very rare processes combined into the 'other' category. The first uncertainty is statistical and the second is systematic. The p-values are the probability for the expected background to fluctuate to equal or exceed the observed yield in each SR.

Full MC background estimate In order to understand the backgrounds in the signal regions and estimate the expected number of events for the data driven backgrounds, the yields are calculated assuming a full MC background estimate. Tables 9.4 and 9.5 show these yields, including yields on some signals (calculated from MC samples) to compare. Note that

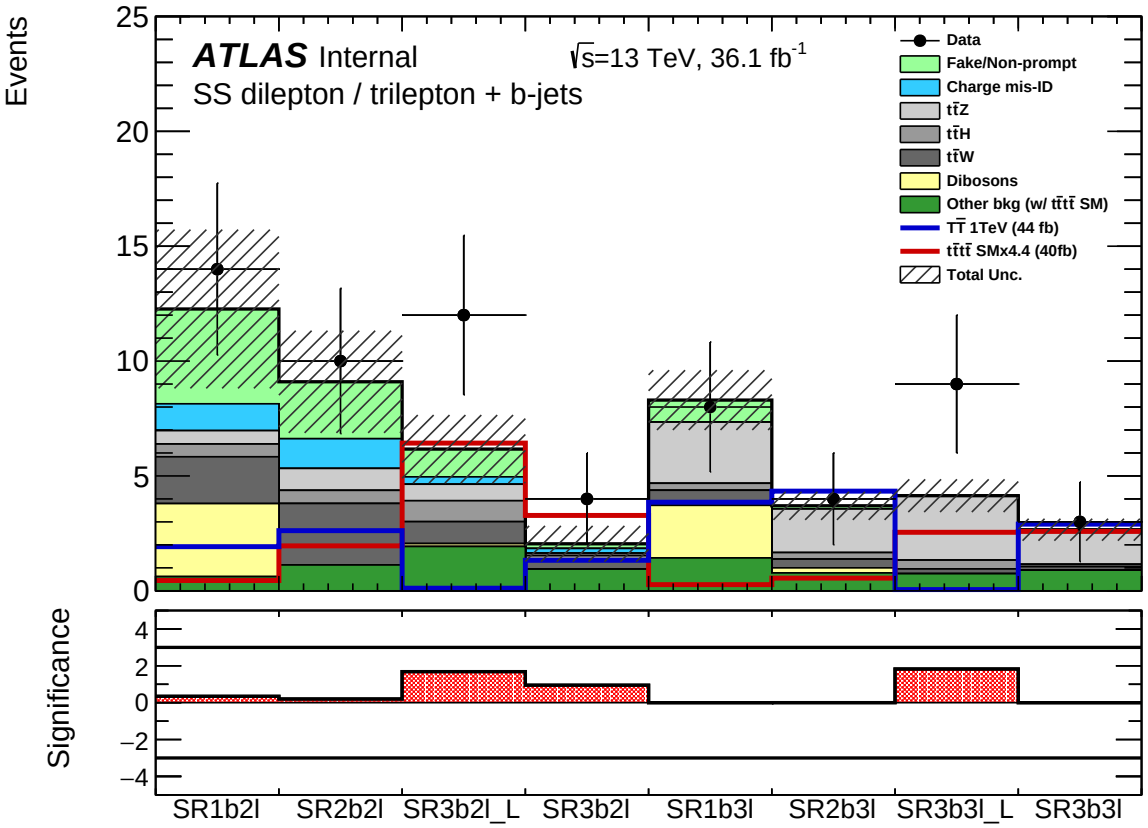

Figure 9.3: Summary plot of the total background and data events in each signal region. The x-axis is the signal region index as described in Table 5.4. The total systematic and statistical uncertainties are included for each bin.

Process	*SR1b3l*	*SR2b3l*	*SR3b3l_L*	*SR3b3l*
Dibosons	$2.29 \pm 0.66 \pm 0.37$	$0.22 \pm 0.46 \pm 0.07$	0.00 ± 0.46	0.00 ± 0.46
Fake/Non-prompt	$0.96 \pm 0.61 \pm 0.58$	$0.14 \pm 0.31 \pm 0.09$	$0.00 \pm 0.27 \pm 0.00$	$0.03 \pm 0.15 \pm 0.04$
$t\bar{t}Z$	$2.66 \pm 0.15 \pm 0.25$	$1.90 \pm 0.14 \pm 0.24$	$2.80 \pm 0.17 \pm 0.31$	$1.47 \pm 0.14 \pm 0.14$
$t\bar{t}H$	$0.30 \pm 0.04 \pm 0.02$	$0.28 \pm 0.05 \pm 0.02$	$0.38 \pm 0.06 \pm 0.03$	$0.10 \pm 0.03 \pm 0.01$
$t\bar{t}W$	$0.66 \pm 0.08 \pm 0.09$	$0.38 \pm 0.05 \pm 0.07$	$0.21 \pm 0.05 \pm 0.03$	$0.15 \pm 0.04 \pm 0.02$
Other bkg.	$1.43 \pm 0.13 \pm 0.44$	$0.78 \pm 0.10 \pm 0.24$	$0.74 \pm 0.21 \pm 0.04$	$0.90 \pm 0.20 \pm 0.10$
Total bkg.	$8.30 \pm 0.92 \pm 0.86$	$3.70 \pm 0.58 \pm 0.37$	$4.14 \pm 0.60 \pm 0.31$	$2.66 \pm 0.54 \pm 0.17$
Data	8	4	9	3
p-value	0.57	0.50	0.033	0.49

Table 9.2: Total yields in the signal regions defined in §5.4 for trilepton events. Only the prominent backgrounds are separated, with very rare processes combined into the 'other' category. The first uncertainty is statistical and the second is systematic. The p-values are the probability for the expected background to fluctuate to equal or exceed the observed yield in each SR.

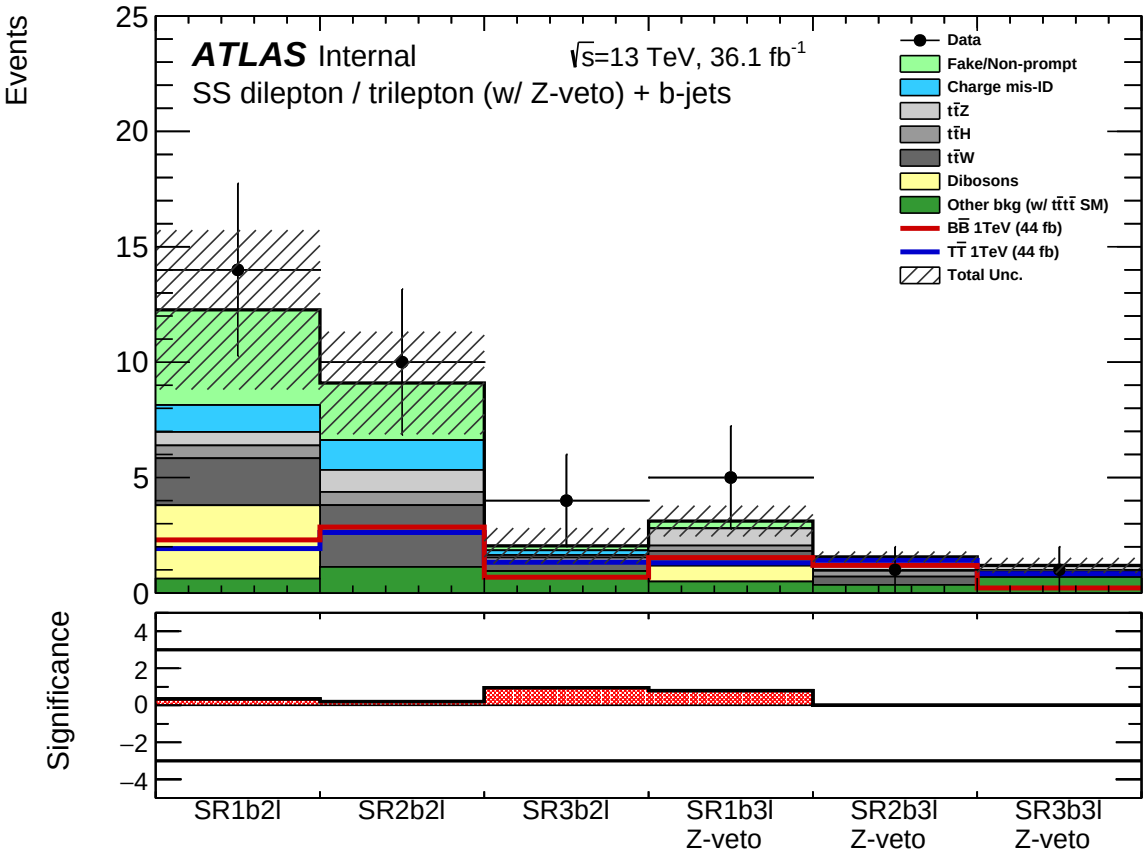

Figure 9.4: Summary plot of the total background and data events in each signal region relevant for the VLQ signal and combination effort. The x-axis is the signal region index as described in Table 5.4. The trilepton regions are the same definition as in Table 5.4, except the Z-peak region is vetoed as well. The total systematic and statistical uncertainties are included for each bin.

Process	*SR1b3l (Z-veto)*	*SR2b3l (Z-veto)*	*SR3b3l (Z-veto)*
Dibosons	$0.68 \pm 0.46 \pm 0.11$	0.00 ± 0.46	0.00 ± 0.46
Fake/Non-prompt	$0.32 \pm 0.45 \pm 0.19$	$0.08 \pm 0.11 \pm 0.05$	0.00 ± 1.14
$t\bar{t}Z$	$0.74 \pm 0.09 \pm 0.07$	$0.52 \pm 0.07 \pm 0.07$	$0.27 \pm 0.07 \pm 0.02$
$t\bar{t}H$	$0.24 \pm 0.04 \pm 0.02$	$0.25 \pm 0.04 \pm 0.02$	$0.09 \pm 0.03 \pm 0.01$
$t\bar{t}W$	$0.64 \pm 0.08 \pm 0.09$	$0.36 \pm 0.05 \pm 0.07$	$0.14 \pm 0.04 \pm 0.02$
Other bkg.	$0.49 \pm 0.09 \pm 0.12$	$0.35 \pm 0.05 \pm 0.09$	$0.69 \pm 0.19 \pm 0.28$
Total bkg.	$3.11 \pm 0.66 \pm 0.28$	$1.56 \pm 0.49 \pm 0.14$	$1.19 \pm 1.25 \pm 0.28$
Data	5	1	1
p-value	0.22	0.76	0.57

Table 9.3: Total yields in the signal regions defined for trilepton events with Z-veto applied. Only the prominent backgrounds are separated, with very rare processes combined into the 'other' category. The first uncertainty is statistical and the second is systematic. The p-values are the probability for the expected background to fluctuate to equal or exceed the observed yield in each SR.

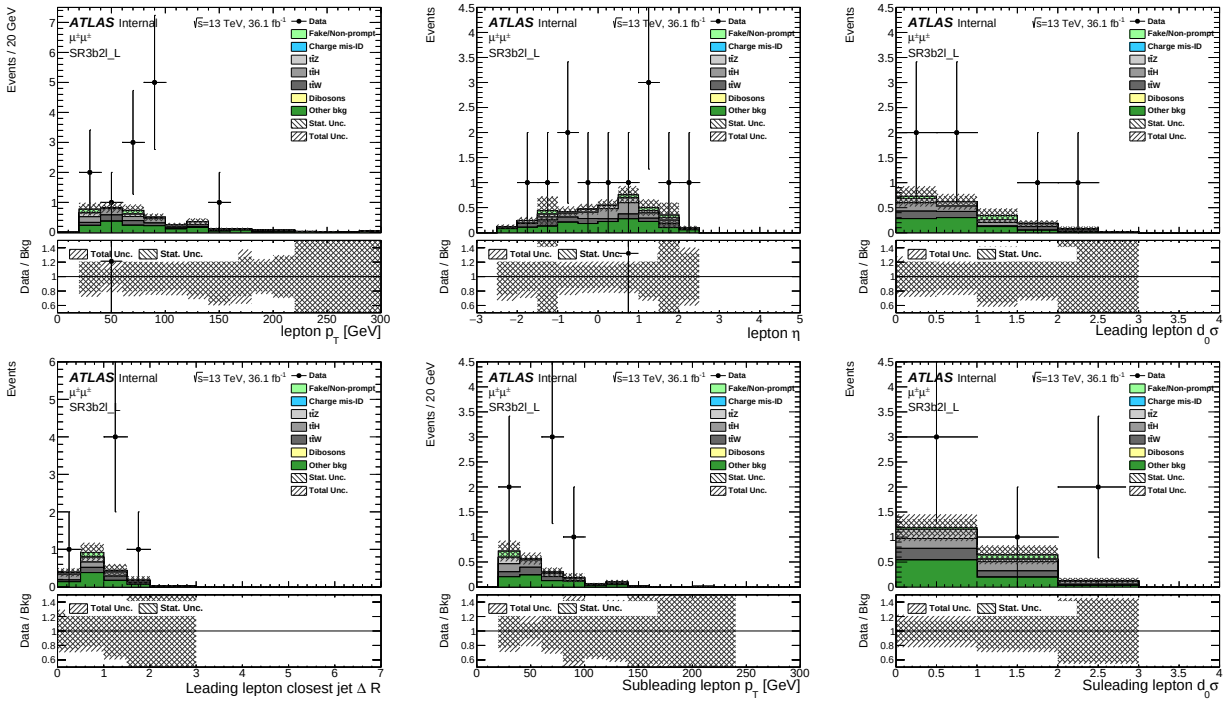

Figure 9.5: Leading and sub-leading muon quality checks for the SSμμ channel in *SR3b2l_L*.

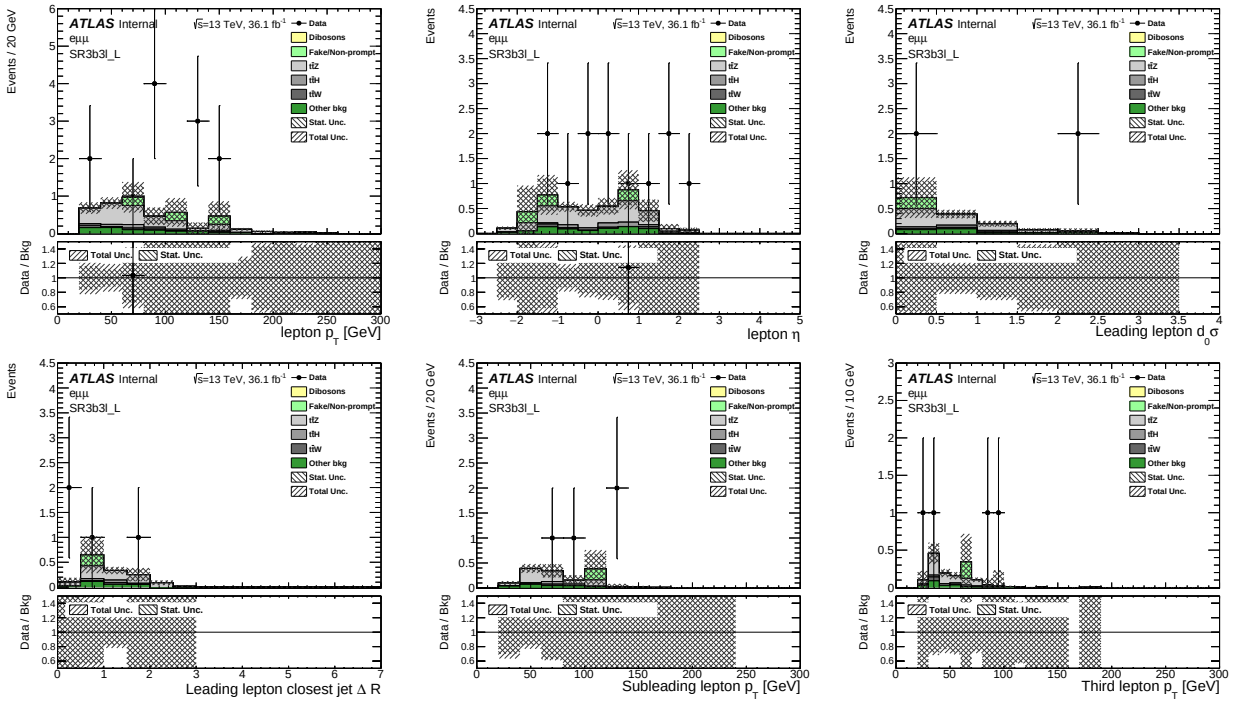

Figure 9.6: Leading and sub-leading muon quality checks for the eμμ channel in *SR3b3l_L*.

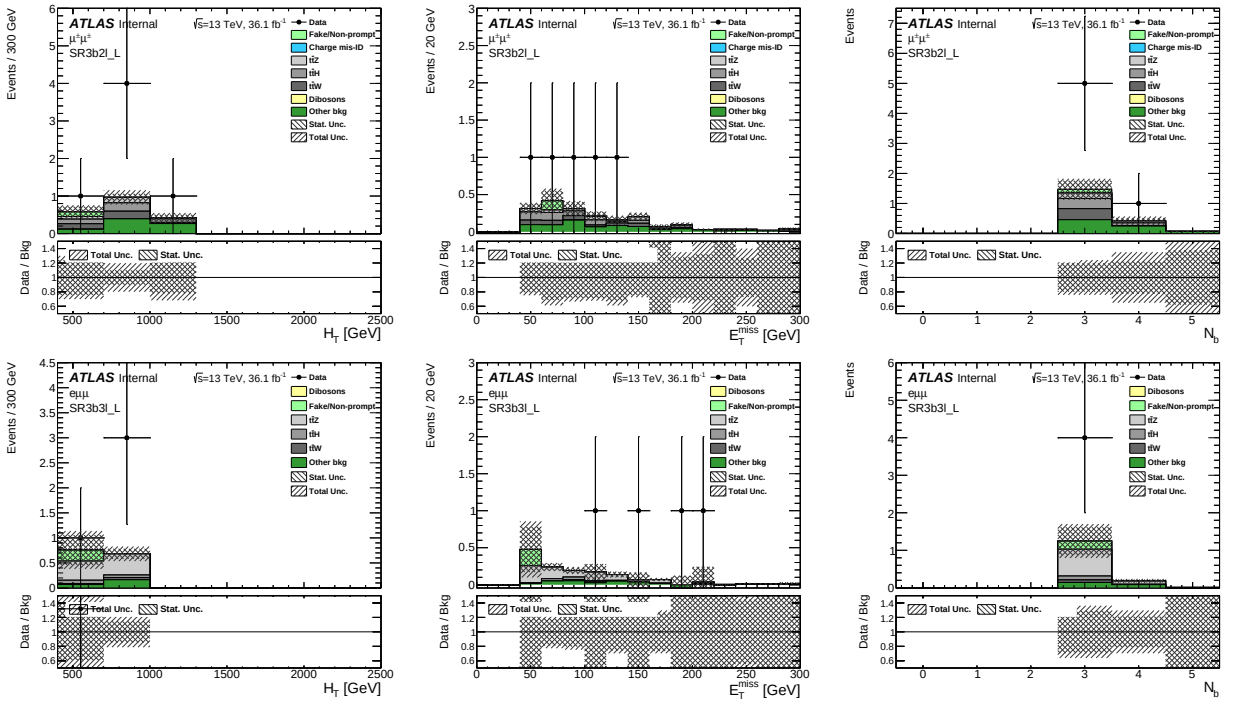

Figure 9.7: H_{T} (left), $E_{\mathrm{T}}^{\mathrm{miss}}$ (middle), and number of b-jets (right) kinematics checks for the SSμμ (top) and eμμ (bottom) channels in *SR3b2l_L* and *SR3b3l_L* signal regions.

it is expected these numbers will not agree perfectly with the data-driven background yields because a full MC estimation is limited by accuracy in the simulation to recreate fake/non-prompt and charge mis-measured leptons.

Also, table 9.3 shows the yields in the trilepton signal regions in the event a Z-veto is applied. Figure 9.4 shows the summary plot with the trilepton regions with the Z-veto cut applied. These regions are explicitly relevant for the VLQ signals (the "_L" regions were optimized for a different signal, so those regions are taken out in this plot). Table 9.6 shows the expected yields in these regions with MC simulated backgrounds. Applying the Z-veto cut significantly decreases the number of events in the trilepton regions. The reason this is applied is to see if there is a difference in behavior between these and the normal trilepton signal regions in order to prepare for using the Z-veto cut in the combination of this analysis with another analyses looking for VLQ. The background composition is expected to be different with a Z-veto, so the yields must be checked separately. As evident from this figure, there is no significant excess of data above the total background estimate. The VLQ combination effort is discussed more in Chapter 10.

Case of yield = 0 In some cases, due to the strict requirements on b-tagging and other kinematic variables in some signal regions, the loose selection may yield zero events. This would result in a yield of zero events for the data driven backgrounds since the loose selection is needed to estimate both of these backgrounds.[8] In signal regions that have this feature, the central value for the corresponding background is set to zero and the lower statistical uncertainty is also set to zero. The upper statistical uncertainty is set to the value of the estimate assuming the number of loose events satisfying the selection is 1.4 at the 68% CL. For the fake and non-prompt background, the following would be used in this case: $N^{tt} = 0$, $N^{t\bar{t}} = N^{\bar{t}t} = N^{\bar{t}\bar{t}} = 0.47$. As an example, the upper limit on the number of fakes with these criteria is then calculated to be 0.2 assuming conservative values for the real and fake efficiencies: 80% and 20%, respectively. For the charge mis-id background, the loose event yield of 1.4 is multiplied by a conservative value for the charge flip rate (on the order of 5×10^{-2}) and the resulting number would be 0.07 events, which is set as the upper statistical uncertainty on 0 charge mis-id events. For the systematic uncertainties, in cases where the background yield is zero, the typical procedure is to set the systematic uncertainty also to zero. An upper statistical uncertainty is set in these cases.

[8] In the case of charge mis-id background, the *loose* selection means opposite sign electron events. In the case of the fake background, the *loose* selection is defined by the non-isolated lepton criteria (see Table 7.3).

9.4 Limit Setting

The limit setting in this analysis uses a software package called `TRExFitter`, which is used as the primary statistical interpretation package of ATLAS exotics searches and is built from common tools used in most ATLAS analyses: `RooStats` [163] and `HistFitter` [164]. The primary methods employed by this package include calculating the significance of any excess of data above the total background yields and interpreting the data in terms of hypothesis testing given all uncertainties. In this analysis, the package takes as input the nominal yields for each signal region, statistical uncertainties on the yields, and a list of nuisance parameters for the systematics. While the `TRExFitter` package is structured to provide tools for a range of analyses, including more complicated multi-binned analyses, this analysis is simpler in that only the yields in the signal regions and uncertainties are used in the fit.

Limits are set by calculating $p_{\mathrm{S+B}}$ and p_{B} in equations 9.7 and 9.8, respectively, then calculating $\mathrm{CL_S}$. $\mathrm{CL_S}$ is calculated for different values of μ (the signal strength, as defined previously). Values of the signal model cross section (values of μ) for which $\mathrm{CL_S} \leq 0.05$ are excluded at the 95% CL. For VLQ signal models, typically the parameters of interest are the production cross section and the mass of the VLQ. Limits are set in VLQ cross-section vs. mass space, which is sometimes referred to as a '1D' exclusion limit. This just means for the VLQ signal models, the branching ratios to the three decay modes are assumed to be those of a single type, in this case the VLQ are singlets (see §2.2). Figure 9.8 shows the 1D limits on the T model and B model, both produced in pairs, assuming singlet branching ratios, respectively. As described in §2.2.1, the pair production cross section of these VLQ is known. Figure 9.9 shows the limits for pair production of $T_{5/3}$. The blue curve shows the theoretical cross-section calculated at NNLO. The expected limit is where the dashed line crosses the theoretical curve. Cross sections above this point and to the left of the theoretical curve and mass values below this point and to the left of the theoretical curve are excluded at the 95% CL. The 1σ and 2σ error bands are shown as the expected uncertainty on the expected limits. The mass limits for the VLQ models are summarized in table 9.7. Tables 9.8 and 9.9 show the expected and observed cross-section limits for each mass point individually for the singlet T and B VLQ, respectively. The observed limits are only slightly weaker than the expected due to the slight excesses in several of the signal regions. However, since the data excesses are predominantly limited to the signal regions optimized for the $t\bar{t}t\bar{t}$ signal (discussed more in Chapter 10), and not the VLQ signals, the limits for the VLQ signal models are more consistent with the background-only model.

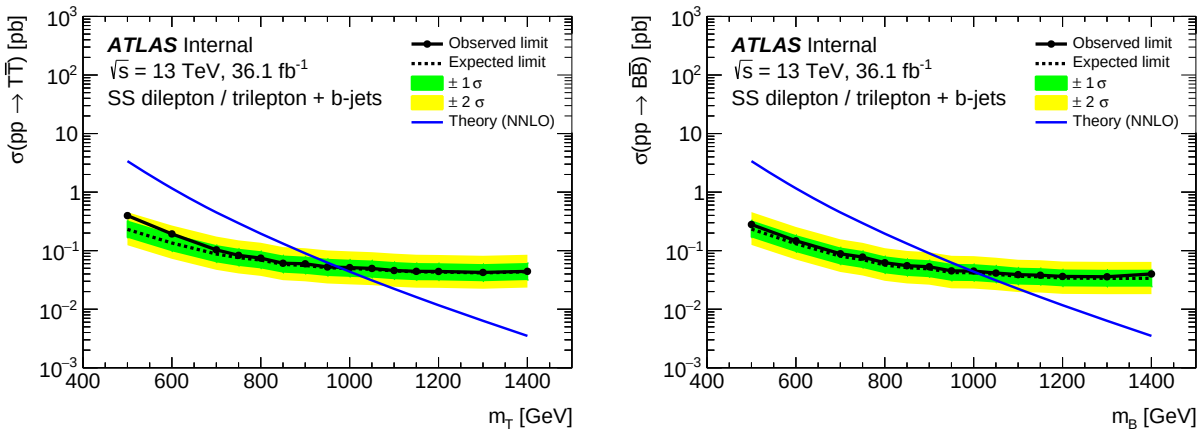

Figure 9.8: Expected (dashed) and observed (solid) limits on Vector-like Top (left) and Vector-like Bottom (right) quarks at 95% CL. The branching ratios used to determine the cross section assume the T or B is a singlet.

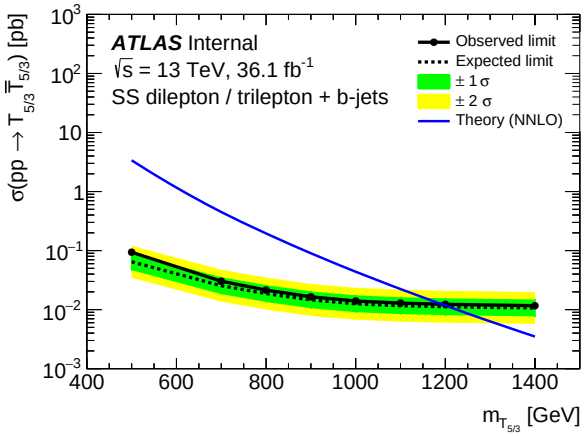

Figure 9.9: Expected (dashed) and observed (solid) limits on Vector-like Top with a charge of +5/3 at 95% CL.

Additionally, so-called 2D exclusion limits are set on the VLQ signal models, where the branching ratios are free to vary under the constraint: $\mathrm{BR}_{Wq'} + \mathrm{BR}_{Zq} + \mathrm{BR}_{Hq} = 1$, where q = t, b (q' = t, q = b for B and q' = b, q = t for T). These 2D exclusion limits are typically represented in a plane with one BR on each axis and the third BR implied by the constraint. This analysis is most sensitive to the $T \to Zt$, $T \to Ht$, and $B \to Wt$ decay modes since those modes can readily produce same-charge dilepton final states. This sensitivity practically means the limits are the strongest for branching ratios that favor these decay modes. Figures 9.10 and 9.11 show the limits assuming arbitrary branching ratios over the

full plane for the T and B models, respectively. Note, $T_{5/3}$ decays to Wt 100% of the time, so 2D exclusion limits are unnecessary. The white area in the upper right of each plot is forbidden by the constraint. Contours are shown for major mass points. The color in each bin represents the limit (expected or observed) at the 95% CL.

9.4.1 Pruning Systematics

To reduce the number of systematic uncertainties to only those that are most important for the signal regions, a pruning procedure is performed inside `TRExFitter` where only systematics contributing more than a 3% change to the nominal yields in the signal regions are kept. The uncertainties on each background in the eight signal regions defined in §5.3.3 are calculated for all systematics. If the uncertainty is below 3%, the systematic is pruned from the list of systematics. The signal regions in this analysis are dominated by statistical uncertainties in most cases.

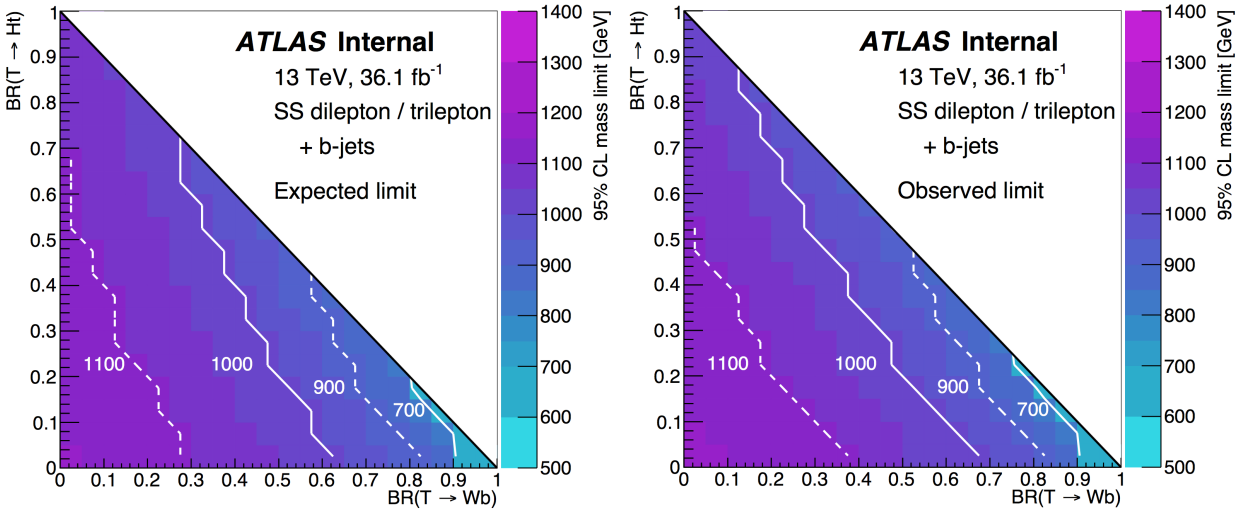

Figure 9.10: Expected (left) and observed (right) limits on Vector-like Top quark at 95% CL. The branching ratios are unfixed except with the constraint $\mathrm{BR}_{Wb} + \mathrm{BR}_{Zt} + \mathrm{BR}_{Ht} = 1$.

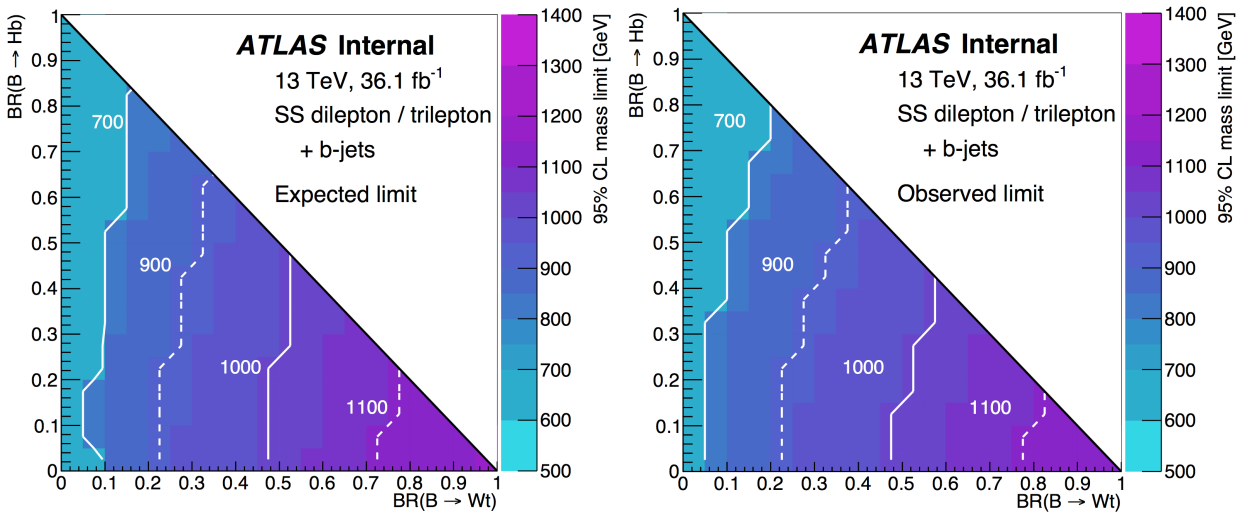

Figure 9.11: Expected (left) and observed (right) limits on Vector-like Bottom quark at 95% CL. The branching ratios are unfixed except with the constraint $\mathrm{BR}_{Wt} + \mathrm{BR}_{Zb} + \mathrm{BR}_{Hb} = 1$.

Source	*SR1b2l*	*SR2b2l*	*SR3b2l_L*	*SR3b2l*	*SR1b3l*	*SR2b3l*	*SR3b3l_L*	*SR3b3l*	*SRSStops*
$t\bar{t}W$	$2.04 \pm 0.14 \pm 0.36$	$2.68 \pm 0.15 \pm 0.49$	$0.95 \pm 0.11 \pm 0.26$	$0.40 \pm 0.06 \pm 0.12$	$0.66 \pm 0.08 \pm 0.09$	$0.38 \pm 0.05 \pm 0.07$	$0.21 \pm 0.05 \pm 0.04$	$0.15 \pm 0.04 \pm 0.02$	$5.41 \pm 0.22 \pm 0.00$
$t\bar{t}Z$	$0.58 \pm 0.08 \pm 0.10$	$0.95 \pm 0.10 \pm 0.17$	$0.72 \pm 0.10 \pm 0.20$	$0.11 \pm 0.04 \pm 0.03$	$2.66 \pm 0.15 \pm 0.36$	$1.90 \pm 0.13 \pm 0.35$	$2.80 \pm 0.17 \pm 0.51$	$1.47 \pm 0.14 \pm 0.23$	$1.73 \pm 0.12 \pm 0.00$
$t\bar{t}W^+W^-$	$0.18 \pm 0.04 \pm 0.03$	$0.44 \pm 0.07 \pm 0.08$	$0.28 \pm 0.08 \pm 0.08$	$0.07 \pm 0.03 \pm 0.02$	$0.13 \pm 0.03 \pm 0.02$	$0.10 \pm 0.03 \pm 0.02$	$0.02 \pm 0.01 \pm 0.00$	$0.08 \pm 0.04 \pm 0.01$	$0.52 \pm 0.09 \pm 0.00$
$t\bar{t}$ (fake)	$0.55 \pm 0.55 \pm 0.19$	$0.55 \pm 0.39 \pm 0.19$	$0.27 \pm 0.27 \pm 0.09$	$0.00 \pm 0.00 \pm 0.00$	$0.45 \pm 0.45 \pm 0.16$	$0.25 \pm 0.25 \pm 0.09$	$0.00 \pm 0.00 \pm 0.00$	$0.00 \pm 0.00 \pm 0.00$	$4.84 \pm 1.23 \pm 0.00$
$t\bar{t}$ (Q mis-ID)	$1.10 \pm 0.55 \pm 0.22$	$1.11 \pm 0.58 \pm 0.22$	$1.57 \pm 0.95 \pm 0.31$	$0.62 \pm 0.44 \pm 0.12$	$0.00 \pm 0.00 \pm 0.00$	$0.00 \pm 0.00 \pm 0.00$	$0.00 \pm 0.00 \pm 0.00$	$0.00 \pm 0.00 \pm 0.00$	$1.68 \pm 0.70 \pm 0.00$
$t\bar{t}t$	$0.03 \pm 0.00 \pm 0.01$	$0.06 \pm 0.00 \pm 0.03$	$0.16 \pm 0.01 \pm 0.09$	$0.07 \pm 0.01 \pm 0.04$	$0.01 \pm 0.00 \pm 0.01$	$0.02 \pm 0.00 \pm 0.01$	$0.06 \pm 0.00 \pm 0.03$	$0.05 \pm 0.01 \pm 0.03$	$0.10 \pm 0.01 \pm 0.00$
VV	$3.18 \pm 1.48 \pm 1.19$	$0.00 \pm 0.00 \pm 0.00$	$0.13 \pm 0.13 \pm 0.13$	$0.00 \pm 0.00 \pm 0.00$	$2.29 \pm 0.60 \pm 0.73$	$0.22 \pm 0.16 \pm 0.07$	$0.00 \pm 0.00 \pm 0.00$	$0.00 \pm 0.00 \pm 0.00$	$2.31 \pm 0.62 \pm 0.00$
VVV	$0.06 \pm 0.02 \pm 0.03$	$0.00 \pm 0.00 \pm 0.00$	$0.01 \pm 0.01 \pm 0.00$	$0.00 \pm 0.00 \pm 0.00$	$0.18 \pm 0.03 \pm 0.09$	$0.02 \pm 0.00 \pm 0.01$	$0.00 \pm 0.00 \pm 0.00$	$0.00 \pm 0.00 \pm 0.00$	$0.01 \pm 0.00 \pm 0.00$
$t\bar{t}H$	$0.56 \pm 0.07 \pm 0.28$	$0.57 \pm 0.10 \pm 0.29$	$0.91 \pm 0.11 \pm 0.48$	$0.19 \pm 0.05 \pm 0.10$	$0.30 \pm 0.04 \pm 0.15$	$0.28 \pm 0.05 \pm 0.15$	$0.38 \pm 0.06 \pm 0.21$	$0.10 \pm 0.03 \pm 0.05$	$1.31 \pm 0.12 \pm 0.00$
VH	$0.00 \pm 0.00 \pm 0.00$	$0.00 \pm 0.00 \pm 0.00$	$0.00 \pm 0.00 \pm 0.00$	$0.00 \pm 0.00 \pm 0.00$	$0.00 \pm 0.00 \pm 0.00$	$0.00 \pm 0.00 \pm 0.00$	$0.00 \pm 0.00 \pm 0.00$	$0.00 \pm 0.00 \pm 0.00$	$0.00 \pm 0.00 \pm 0.00$
W+jets	$0.23 \pm 0.08 \pm 0.08$	$0.05 \pm 0.03 \pm 0.02$	$0.00 \pm 0.00 \pm 0.00$	$0.00 \pm 0.00 \pm 0.00$	$0.00 \pm 0.00 \pm 0.00$	$0.00 \pm 0.00 \pm 0.00$	$0.00 \pm 0.00 \pm 0.00$	$0.00 \pm 0.00 \pm 0.00$	$0.04 \pm 0.03 \pm 0.00$
Z+jets	$0.10 \pm 0.05 \pm 0.02$	$0.06 \pm 0.03 \pm 0.01$	$0.00 \pm 0.00 \pm 0.00$	$0.00 \pm 0.00 \pm 0.00$	$0.00 \pm 0.00 \pm 0.00$	$0.00 \pm 0.00 \pm 0.00$	$0.09 \pm 0.09 \pm 0.02$	$0.00 \pm 0.00 \pm 0.00$	$-0.16 \pm 0.12 \pm 0.00$
single top	$0.55 \pm 0.32 \pm 0.28$	$0.36 \pm 0.26 \pm 0.18$	$0.00 \pm 0.00 \pm 0.00$	$0.46 \pm 0.46 \pm 0.23$	$0.00 \pm 0.00 \pm 0.00$	$0.00 \pm 0.00 \pm 0.00$	$0.00 \pm 0.00 \pm 0.00$	$0.00 \pm 0.00 \pm 0.00$	$1.75 \pm 1.15 \pm 0.00$
tZ	$0.03 \pm 0.02 \pm 0.02$	$0.07 \pm 0.02 \pm 0.04$	$0.02 \pm 0.02 \pm 0.01$	$0.01 \pm 0.01 \pm 0.01$	$0.21 \pm 0.04 \pm 0.11$	$0.05 \pm 0.03 \pm 0.03$	$0.02 \pm 0.01 \pm 0.01$	$0.01 \pm 0.01 \pm 0.00$	$0.17 \pm 0.04 \pm 0.00$
tWZ	$0.22 \pm 0.06 \pm 0.11$	$0.11 \pm 0.05 \pm 0.06$	$-0.00 \pm 0.01 \pm 0.00$	$0.05 \pm 0.02 \pm 0.02$	$0.84 \pm 0.11 \pm 0.42$	$0.47 \pm 0.09 \pm 0.24$	$0.06 \pm 0.09 \pm 0.03$	$0.18 \pm 0.06 \pm 0.09$	$0.33 \pm 0.07 \pm 0.00$
Tot. bkg.	$9.41 \pm 1.72 \pm 1.34$	$7.02 \pm 0.78 \pm 0.69$	$5.02 \pm 1.02 \pm 0.69$	$1.97 \pm 0.64 \pm 0.31$	$7.74 \pm 0.78 \pm 0.95$	$3.69 \pm 0.35 \pm 0.47$	$3.66 \pm 0.23 \pm 0.55$	$2.04 \pm 0.16 \pm 0.25$	$20.03 \pm 1.96 \pm 0.00$
BBS800	$6.52 \pm 0.38 \pm 3.26$	$9.91 \pm 0.45 \pm 5.01$	$0.31 \pm 0.08 \pm 0.16$	$2.69 \pm 0.25 \pm 1.38$	$8.98 \pm 0.41 \pm 4.51$	$8.14 \pm 0.36 \pm 4.20$	$0.11 \pm 0.04 \pm 0.06$	$2.46 \pm 0.26 \pm 1.24$	$4.74 \pm 0.28 \pm 0.00$
TTS800	$5.25 \pm 0.29 \pm 2.63$	$8.76 \pm 0.37 \pm 4.42$	$1.15 \pm 0.16 \pm 0.60$	$4.11 \pm 0.27 \pm 2.11$	$12.05 \pm 0.47 \pm 6.05$	$13.35 \pm 0.45 \pm 6.90$	$1.08 \pm 0.23 \pm 0.59$	$11.11 \pm 0.47 \pm 5.61$	$5.00 \pm 0.30 \pm 0.00$
BBS900	$4.02 \pm 0.19 \pm 2.01$	$4.97 \pm 0.20 \pm 2.51$	$0.12 \pm 0.03 \pm 0.06$	$1.30 \pm 0.13 \pm 0.67$	$5.10 \pm 0.21 \pm 2.56$	$4.43 \pm 0.19 \pm 2.29$	$0.06 \pm 0.02 \pm 0.03$	$1.12 \pm 0.11 \pm 0.57$	$2.48 \pm 0.17 \pm 0.00$
TTS900	$3.21 \pm 0.16 \pm 1.61$	$4.54 \pm 0.20 \pm 2.29$	$0.43 \pm 0.08 \pm 0.22$	$2.73 \pm 0.16 \pm 1.40$	$6.82 \pm 0.24 \pm 3.43$	$7.66 \pm 0.24 \pm 3.96$	$0.30 \pm 0.05 \pm 0.17$	$5.69 \pm 0.24 \pm 2.88$	$2.38 \pm 0.15 \pm 0.00$
BBS1000	$2.30 \pm 0.10 \pm 1.15$	$2.85 \pm 0.11 \pm 1.44$	$0.03 \pm 0.01 \pm 0.01$	$0.68 \pm 0.06 \pm 0.35$	$2.97 \pm 0.11 \pm 1.49$	$2.46 \pm 0.09 \pm 1.27$	$0.01 \pm 0.00 \pm 0.00$	$0.49 \pm 0.05 \pm 0.25$	$1.15 \pm 0.07 \pm 0.00$
TTS1000	$1.92 \pm 0.09 \pm 0.96$	$2.62 \pm 0.11 \pm 1.32$	$0.11 \pm 0.02 \pm 0.06$	$1.33 \pm 0.07 \pm 0.68$	$3.86 \pm 0.12 \pm 1.94$	$4.34 \pm 0.14 \pm 2.24$	$0.05 \pm 0.01 \pm 0.03$	$2.90 \pm 0.13 \pm 1.47$	$1.25 \pm 0.07 \pm 0.00$
BBS1100	$1.39 \pm 0.05 \pm 0.70$	$1.52 \pm 0.05 \pm 0.77$	$0.01 \pm 0.00 \pm 0.00$	$0.41 \pm 0.03 \pm 0.21$	$1.77 \pm 0.06 \pm 0.89$	$1.39 \pm 0.05 \pm 0.72$	$0.01 \pm 0.01 \pm 0.00$	$0.30 \pm 0.03 \pm 0.15$	$0.56 \pm 0.03 \pm 0.00$
TTS1100	$0.98 \pm 0.04 \pm 0.49$	$1.48 \pm 0.06 \pm 0.75$	$0.05 \pm 0.01 \pm 0.03$	$0.66 \pm 0.04 \pm 0.34$	$2.24 \pm 0.07 \pm 1.13$	$2.45 \pm 0.07 \pm 1.27$	$0.01 \pm 0.00 \pm 0.01$	$1.54 \pm 0.06 \pm 0.78$	$0.70 \pm 0.04 \pm 0.00$
BBS1200	$0.80 \pm 0.03 \pm 0.40$	$0.90 \pm 0.03 \pm 0.45$	$0.00 \pm 0.00 \pm 0.00$	$0.21 \pm 0.02 \pm 0.11$	$0.96 \pm 0.03 \pm 0.48$	$0.76 \pm 0.03 \pm 0.39$	$0.00 \pm 0.00 \pm 0.00$	$0.15 \pm 0.01 \pm 0.07$	$0.29 \pm 0.02 \pm 0.00$
TTS1200	$0.58 \pm 0.02 \pm 0.29$	$0.83 \pm 0.04 \pm 0.42$	$0.01 \pm 0.00 \pm 0.01$	$0.42 \pm 0.02 \pm 0.21$	$1.32 \pm 0.04 \pm 0.66$	$1.32 \pm 0.04 \pm 0.68$	$0.01 \pm 0.00 \pm 0.00$	$0.78 \pm 0.03 \pm 0.39$	$0.35 \pm 0.02 \pm 0.00$
4topSM	$0.10 \pm 0.01 \pm 0.05$	$0.44 \pm 0.03 \pm 0.22$	$1.46 \pm 0.05 \pm 0.77$	$0.75 \pm 0.04 \pm 0.38$	$0.06 \pm 0.01 \pm 0.03$	$0.13 \pm 0.02 \pm 0.06$	$0.58 \pm 0.04 \pm 0.32$	$0.59 \pm 0.03 \pm 0.30$	$0.64 \pm 0.04 \pm 0.00$
4topRPP1400	$1.97 \pm 0.08 \pm 0.98$	$4.57 \pm 0.13 \pm 2.31$	$0.01 \pm 0.00 \pm 0.00$	$6.56 \pm 0.15 \pm 3.37$	$1.06 \pm 0.05 \pm 0.53$	$2.03 \pm 0.07 \pm 1.05$	$0.00 \pm 0.00 \pm 0.00$	$3.31 \pm 0.10 \pm 1.67$	$1.66 \pm 0.08 \pm 0.00$
4topCI	$1.51 \pm 0.15 \pm 0.76$	$5.51 \pm 0.28 \pm 2.78$	$6.95 \pm 0.31 \pm 3.65$	$7.91 \pm 0.35 \pm 4.06$	$0.92 \pm 0.16 \pm 0.46$	$1.58 \pm 0.14 \pm 0.82$	$2.99 \pm 0.22 \pm 1.64$	$5.19 \pm 0.27 \pm 2.62$	$6.55 \pm 0.34 \pm 0.00$
Data	14	10	12	4	8	4	9	3	30

Table 9.4: Expected signal and background yields in the signal regions. The first uncertainty is statistical and the second is systematic. The systematic uncertainties reflect all the MC uncertainties, plus ad-hoc uncertainties of 35% and 20% for the fake/non-prompt leptons and charge mis-ID backgrounds, respectively.

Source	*SR1b2l*	*SR2b2l*	*SR3b2l_L*	*SR3b2l*	*SR1b3l*	*SR2b3l*	*SR3b3l_L*	*SR3b3l*	*SRSStops*
$t\bar{t}W$	$0.30 \pm 0.05 \pm 0.05$	$0.39 \pm 0.07 \pm 0.07$	$0.27 \pm 0.07 \pm 0.07$	$0.08 \pm 0.03 \pm 0.02$	$0.09 \pm 0.02 \pm 0.01$	$0.05 \pm 0.02 \pm 0.01$	$0.03 \pm 0.02 \pm 0.01$	$0.01 \pm 0.01 \pm 0.00$	$0.70 \pm 0.09 \pm 0.00$
$t\bar{t}Z$	$0.09 \pm 0.03 \pm 0.02$	$0.07 \pm 0.03 \pm 0.01$	$0.05 \pm 0.03 \pm 0.01$	$0.01 \pm 0.01 \pm 0.00$	$0.54 \pm 0.07 \pm 0.07$	$0.25 \pm 0.05 \pm 0.05$	$0.73 \pm 0.08 \pm 0.13$	$0.23 \pm 0.05 \pm 0.04$	$0.19 \pm 0.04 \pm 0.00$
$t\bar{t}W^+W^-$	$0.00 \pm 0.00 \pm 0.00$	$0.02 \pm 0.01 \pm 0.00$	$0.01 \pm 0.01 \pm 0.00$	$0.01 \pm 0.01 \pm 0.00$	$0.05 \pm 0.02 \pm 0.01$	$0.02 \pm 0.01 \pm 0.00$	$0.00 \pm 0.00 \pm 0.00$	$0.01 \pm 0.01 \pm 0.00$	$0.01 \pm 0.01 \pm 0.00$
$t\bar{t}$ (fake)	$10.42 \pm 1.88 \pm 3.65$	$11.61 \pm 2.12 \pm 4.06$	$2.40 \pm 1.04 \pm 0.84$	$1.17 \pm 0.55 \pm 0.41$	$6.34 \pm 1.41 \pm 2.22$	$1.21 \pm 0.73 \pm 0.42$	$0.69 \pm 0.50 \pm 0.24$	$0.94 \pm 0.47 \pm 0.33$	$31.80 \pm 3.14 \pm 0.00$
$t\bar{t}$ (Q mis-ID)	$0.22 \pm 0.22 \pm 0.04$	$1.23 \pm 0.62 \pm 0.25$	$0.50 \pm 0.50 \pm 0.10$	$0.00 \pm 0.00 \pm 0.00$	$0.00 \pm 0.00 \pm 0.00$	$0.00 \pm 0.00 \pm 0.00$	$0.00 \pm 0.00 \pm 0.00$	$0.00 \pm 0.00 \pm 0.00$	$2.86 \pm 1.01 \pm 0.00$
$t\bar{t}t$	$0.00 \pm 0.00 \pm 0.00$	$0.01 \pm 0.00 \pm 0.01$	$0.02 \pm 0.00 \pm 0.01$	$0.02 \pm 0.00 \pm 0.01$	$0.00 \pm 0.00 \pm 0.00$	$0.00 \pm 0.00 \pm 0.00$	$0.01 \pm 0.00 \pm 0.01$	$0.01 \pm 0.00 \pm 0.01$	$0.02 \pm 0.00 \pm 0.00$
VV	$0.00 \pm 0.00 \pm 0.00$	$0.26 \pm 0.18 \pm 0.33$	$0.00 \pm 0.00 \pm 0.00$	$0.00 \pm 0.00 \pm 0.00$	$0.92 \pm 0.43 \pm 0.29$	$0.00 \pm 0.00 \pm 0.00$	$0.00 \pm 0.00 \pm 0.00$	$0.10 \pm 0.10 \pm 0.03$	$0.00 \pm 0.00 \pm 0.00$
VVV	$0.02 \pm 0.01 \pm 0.01$	$0.00 \pm 0.00 \pm 0.00$	$0.00 \pm 0.00 \pm 0.00$	$0.00 \pm 0.00 \pm 0.00$	$0.02 \pm 0.01 \pm 0.01$	$0.00 \pm 0.00 \pm 0.00$	$0.00 \pm 0.00 \pm 0.00$	$0.00 \pm 0.00 \pm 0.00$	$0.01 \pm 0.01 \pm 0.00$
$t\bar{t}H$	$0.17 \pm 0.04 \pm 0.08$	$0.25 \pm 0.05 \pm 0.13$	$0.21 \pm 0.09 \pm 0.11$	$-0.00 \pm 0.04 \pm 0.00$	$0.05 \pm 0.02 \pm 0.02$	$0.06 \pm 0.02 \pm 0.03$	$0.13 \pm 0.03 \pm 0.07$	$0.04 \pm 0.02 \pm 0.02$	$0.11 \pm 0.08 \pm 0.00$
VH	$0.00 \pm 0.00 \pm 0.00$	$0.00 \pm 0.00 \pm 0.00$	$0.00 \pm 0.00 \pm 0.00$	$0.00 \pm 0.00 \pm 0.00$	$0.00 \pm 0.00 \pm 0.00$	$0.00 \pm 0.00 \pm 0.00$	$0.00 \pm 0.00 \pm 0.00$	$0.00 \pm 0.00 \pm 0.00$	$0.00 \pm 0.00 \pm 0.00$
W+jets	$1.67 \pm 0.37 \pm 0.58$	$0.86 \pm 0.32 \pm 0.30$	$0.16 \pm 0.11 \pm 0.06$	$0.02 \pm 0.01 \pm 0.01$	$0.00 \pm 0.00 \pm 0.00$	$0.00 \pm 0.00 \pm 0.00$	$0.00 \pm 0.00 \pm 0.00$	$0.00 \pm 0.00 \pm 0.00$	$3.85 \pm 0.78 \pm 0.00$
Z+jets	$0.14 \pm 0.04 \pm 0.03$	$0.11 \pm 0.05 \pm 0.02$	$0.04 \pm 0.03 \pm 0.01$	$0.00 \pm 0.00 \pm 0.00$	$0.41 \pm 0.10 \pm 0.08$	$0.14 \pm 0.06 \pm 0.03$	$0.06 \pm 0.03 \pm 0.01$	$0.03 \pm 0.02 \pm 0.01$	$0.24 \pm 0.08 \pm 0.00$
single top	$1.31 \pm 0.63 \pm 0.65$	$0.58 \pm 0.34 \pm 0.29$	$0.18 \pm 0.18 \pm 0.10$	$0.33 \pm 0.33 \pm 0.17$	$0.00 \pm 0.00 \pm 0.00$	$0.16 \pm 0.16 \pm 0.08$	$0.00 \pm 0.00 \pm 0.00$	$0.00 \pm 0.00 \pm 0.00$	$3.43 \pm 1.03 \pm 0.00$
tZ	$0.00 \pm 0.00 \pm 0.00$	$0.00 \pm 0.00 \pm 0.00$	$0.00 \pm 0.00 \pm 0.00$	$0.00 \pm 0.00 \pm 0.00$	$0.05 \pm 0.02 \pm 0.02$	$0.01 \pm 0.01 \pm 0.00$	$0.00 \pm 0.00 \pm 0.00$	$0.00 \pm 0.00 \pm 0.00$	$0.01 \pm 0.01 \pm 0.00$
tWZ	$0.01 \pm 0.01 \pm 0.01$	$0.02 \pm 0.01 \pm 0.01$	$0.01 \pm 0.02 \pm 0.00$	$0.03 \pm 0.02 \pm 0.01$	$0.16 \pm 0.10 \pm 0.08$	$0.07 \pm 0.03 \pm 0.04$	$-0.04 \pm 0.03 \pm 0.02$	$0.07 \pm 0.03 \pm 0.04$	$0.03 \pm 0.02 \pm 0.00$
Tot. bkg.	$14.34 \pm 2.03 \pm 3.75$	$15.41 \pm 2.27 \pm 4.11$	$3.84 \pm 1.18 \pm 0.86$	$1.67 \pm 0.65 \pm 0.45$	$8.63 \pm 1.49 \pm 2.24$	$1.98 \pm 0.75 \pm 0.44$	$1.60 \pm 0.51 \pm 0.28$	$1.43 \pm 0.49 \pm 0.34$	$43.23 \pm 3.55 \pm 0.00$
BBS800	$1.08 \pm 0.17 \pm 0.54$	$1.50 \pm 0.19 \pm 0.76$	$0.01 \pm 0.01 \pm 0.01$	$0.23 \pm 0.07 \pm 0.12$	$1.36 \pm 0.14 \pm 0.68$	$1.11 \pm 0.13 \pm 0.57$	$0.03 \pm 0.02 \pm 0.01$	$0.39 \pm 0.10 \pm 0.20$	$0.78 \pm 0.13 \pm 0.00$
TTS800	$1.01 \pm 0.12 \pm 0.51$	$1.32 \pm 0.13 \pm 0.67$	$0.46 \pm 0.14 \pm 0.24$	$0.78 \pm 0.12 \pm 0.40$	$1.94 \pm 0.20 \pm 0.98$	$2.19 \pm 0.21 \pm 1.13$	$0.26 \pm 0.07 \pm 0.14$	$2.07 \pm 0.23 \pm 1.05$	$1.39 \pm 0.19 \pm 0.00$
BBS900	$0.58 \pm 0.07 \pm 0.29$	$0.74 \pm 0.08 \pm 0.37$	$0.02 \pm 0.01 \pm 0.01$	$0.14 \pm 0.04 \pm 0.07$	$0.92 \pm 0.09 \pm 0.46$	$0.69 \pm 0.07 \pm 0.36$	$0.00 \pm 0.00 \pm 0.00$	$0.09 \pm 0.02 \pm 0.04$	$0.36 \pm 0.06 \pm 0.00$
TTS900	$0.68 \pm 0.11 \pm 0.34$	$0.91 \pm 0.10 \pm 0.46$	$0.09 \pm 0.02 \pm 0.05$	$0.51 \pm 0.09 \pm 0.26$	$1.12 \pm 0.09 \pm 0.56$	$1.25 \pm 0.09 \pm 0.64$	$0.04 \pm 0.02 \pm 0.02$	$1.10 \pm 0.13 \pm 0.56$	$0.59 \pm 0.09 \pm 0.00$
BBS1000	$0.39 \pm 0.05 \pm 0.20$	$0.41 \pm 0.05 \pm 0.20$	$0.00 \pm 0.00 \pm 0.00$	$0.10 \pm 0.02 \pm 0.05$	$0.54 \pm 0.05 \pm 0.27$	$0.42 \pm 0.05 \pm 0.22$	$0.00 \pm 0.00 \pm 0.00$	$0.10 \pm 0.02 \pm 0.05$	$0.22 \pm 0.03 \pm 0.00$
TTS1000	$0.42 \pm 0.05 \pm 0.21$	$0.55 \pm 0.05 \pm 0.28$	$0.03 \pm 0.01 \pm 0.02$	$0.33 \pm 0.04 \pm 0.17$	$0.71 \pm 0.05 \pm 0.35$	$0.78 \pm 0.05 \pm 0.40$	$0.02 \pm 0.01 \pm 0.01$	$0.52 \pm 0.04 \pm 0.26$	$0.24 \pm 0.03 \pm 0.00$
BBS1100	$0.23 \pm 0.02 \pm 0.11$	$0.26 \pm 0.03 \pm 0.13$	$0.00 \pm 0.00 \pm 0.00$	$0.03 \pm 0.01 \pm 0.02$	$0.32 \pm 0.03 \pm 0.16$	$0.27 \pm 0.03 \pm 0.14$	$0.00 \pm 0.00 \pm 0.00$	$0.08 \pm 0.02 \pm 0.04$	$0.11 \pm 0.02 \pm 0.00$
TTS1100	$0.20 \pm 0.02 \pm 0.10$	$0.36 \pm 0.03 \pm 0.18$	$0.01 \pm 0.00 \pm 0.01$	$0.14 \pm 0.02 \pm 0.07$	$0.47 \pm 0.04 \pm 0.24$	$0.51 \pm 0.04 \pm 0.26$	$0.01 \pm 0.00 \pm 0.00$	$0.28 \pm 0.03 \pm 0.14$	$0.16 \pm 0.02 \pm 0.00$
BBS1200	$0.13 \pm 0.01 \pm 0.06$	$0.12 \pm 0.01 \pm 0.06$	$0.00 \pm 0.00 \pm 0.00$	$0.04 \pm 0.01 \pm 0.02$	$0.20 \pm 0.02 \pm 0.10$	$0.14 \pm 0.01 \pm 0.07$	$0.00 \pm 0.00 \pm 0.00$	$0.03 \pm 0.01 \pm 0.02$	$0.06 \pm 0.01 \pm 0.00$
TTS1200	$0.14 \pm 0.01 \pm 0.07$	$0.18 \pm 0.01 \pm 0.09$	$0.00 \pm 0.00 \pm 0.00$	$0.09 \pm 0.01 \pm 0.05$	$0.30 \pm 0.02 \pm 0.15$	$0.31 \pm 0.02 \pm 0.16$	$0.00 \pm 0.00 \pm 0.00$	$0.19 \pm 0.02 \pm 0.10$	$0.10 \pm 0.01 \pm 0.00$
4topSM	$0.03 \pm 0.01 \pm 0.01$	$0.11 \pm 0.02 \pm 0.05$	$0.26 \pm 0.03 \pm 0.14$	$0.13 \pm 0.02 \pm 0.07$	$0.02 \pm 0.01 \pm 0.01$	$0.04 \pm 0.01 \pm 0.02$	$0.10 \pm 0.01 \pm 0.06$	$0.14 \pm 0.02 \pm 0.07$	$0.12 \pm 0.02 \pm 0.00$
4topRPP1400	$0.58 \pm 0.04 \pm 0.29$	$1.19 \pm 0.06 \pm 0.60$	$0.00 \pm 0.00 \pm 0.00$	$1.31 \pm 0.06 \pm 0.68$	$0.50 \pm 0.04 \pm 0.25$	$0.80 \pm 0.04 \pm 0.42$	$0.00 \pm 0.00 \pm 0.00$	$0.86 \pm 0.05 \pm 0.44$	$0.48 \pm 0.03 \pm 0.00$
4topCI	$0.26 \pm 0.05 \pm 0.13$	$1.03 \pm 0.12 \pm 0.52$	$0.93 \pm 0.13 \pm 0.49$	$1.16 \pm 0.12 \pm 0.60$	$0.27 \pm 0.10 \pm 0.14$	$0.39 \pm 0.08 \pm 0.20$	$0.51 \pm 0.08 \pm 0.28$	$1.02 \pm 0.17 \pm 0.51$	$1.01 \pm 0.14 \pm 0.00$

Table 9.5: Expected signal and background yields with the same selection as the signal regions, except that at least one lepton is required to fail the tight criteria. The first uncertainty is statistical and the second is systematic. The systematic uncertainties reflect all the MC uncertainties, plus ad-hoc uncertainties of 35% and 20% for the fake/non-prompt leptons and charge mis-ID backgrounds, respectively.

Source	*SR1b3l_Zveto*	*SR2b3l_Zveto*	*SR3b3l_Zveto*
$t\bar{t}W$	$0.64 \pm 0.08 \pm 0.09$	$0.36 \pm 0.05 \pm 0.07$	$0.14 \pm 0.04 \pm 0.02$
$t\bar{t}Z$	$0.74 \pm 0.08 \pm 0.10$	$0.52 \pm 0.06 \pm 0.10$	$0.27 \pm 0.06 \pm 0.04$
$t\bar{t}W^+W^-$	$0.12 \pm 0.03 \pm 0.02$	$0.09 \pm 0.03 \pm 0.02$	$0.08 \pm 0.04 \pm 0.01$
$t\bar{t}$ (fake)	$0.45 \pm 0.45 \pm 0.16$	$0.25 \pm 0.25 \pm 0.09$	$0.00 \pm 0.00 \pm 0.00$
$t\bar{t}$ (Q mis-ID)	$0.00 \pm 0.00 \pm 0.00$	$0.00 \pm 0.00 \pm 0.00$	$0.00 \pm 0.00 \pm 0.00$
$t\bar{t}t$	$0.01 \pm 0.00 \pm 0.01$	$0.02 \pm 0.00 \pm 0.01$	$0.05 \pm 0.01 \pm 0.02$
VV	$0.68 \pm 0.32 \pm 0.22$	$0.00 \pm 0.00 \pm 0.00$	$0.00 \pm 0.00 \pm 0.00$
VVV	$0.07 \pm 0.02 \pm 0.03$	$0.01 \pm 0.00 \pm 0.00$	$0.00 \pm 0.00 \pm 0.00$
$t\bar{t}H$	$0.24 \pm 0.04 \pm 0.12$	$0.25 \pm 0.04 \pm 0.13$	$0.09 \pm 0.03 \pm 0.04$
VH	$0.00 \pm 0.00 \pm 0.00$	$0.00 \pm 0.00 \pm 0.00$	$0.00 \pm 0.00 \pm 0.00$
W+jets	$0.00 \pm 0.00 \pm 0.00$	$0.00 \pm 0.00 \pm 0.00$	$0.00 \pm 0.00 \pm 0.00$
Z+jets	$0.00 \pm 0.00 \pm 0.00$	$0.00 \pm 0.00 \pm 0.00$	$0.00 \pm 0.00 \pm 0.00$
single top	$0.00 \pm 0.00 \pm 0.00$	$0.00 \pm 0.00 \pm 0.00$	$0.00 \pm 0.00 \pm 0.00$
tZ	$0.04 \pm 0.02 \pm 0.02$	$0.00 \pm 0.00 \pm 0.00$	$0.00 \pm 0.00 \pm 0.00$
tWZ	$0.19 \pm 0.07 \pm 0.10$	$0.11 \pm 0.04 \pm 0.06$	$0.02 \pm 0.02 \pm 0.01$
Tot. bkg.	$3.19 \pm 0.57 \pm 0.34$	$1.62 \pm 0.27 \pm 0.21$	$0.65 \pm 0.09 \pm 0.07$
BBS800	$4.16 \pm 0.27 \pm 2.09$	$3.48 \pm 0.24 \pm 1.80$	$1.14 \pm 0.19 \pm 0.58$
TTS800	$3.82 \pm 0.27 \pm 1.92$	$4.15 \pm 0.25 \pm 2.14$	$3.01 \pm 0.22 \pm 1.52$
BBS900	$2.52 \pm 0.15 \pm 1.26$	$1.92 \pm 0.12 \pm 0.99$	$0.49 \pm 0.06 \pm 0.25$
TTS900	$2.42 \pm 0.16 \pm 1.22$	$2.32 \pm 0.13 \pm 1.20$	$1.75 \pm 0.13 \pm 0.89$
BBS1000	$1.53 \pm 0.08 \pm 0.77$	$1.19 \pm 0.06 \pm 0.62$	$0.21 \pm 0.03 \pm 0.11$
TTS1000	$1.30 \pm 0.08 \pm 0.66$	$1.41 \pm 0.09 \pm 0.73$	$0.83 \pm 0.06 \pm 0.42$
BBS1100	$0.86 \pm 0.04 \pm 0.43$	$0.68 \pm 0.03 \pm 0.35$	$0.16 \pm 0.02 \pm 0.08$
TTS1100	$0.81 \pm 0.04 \pm 0.41$	$0.83 \pm 0.04 \pm 0.43$	$0.51 \pm 0.04 \pm 0.26$
BBS1200	$0.48 \pm 0.02 \pm 0.24$	$0.40 \pm 0.02 \pm 0.21$	$0.08 \pm 0.01 \pm 0.04$
TTS1200	$0.45 \pm 0.02 \pm 0.23$	$0.42 \pm 0.02 \pm 0.22$	$0.26 \pm 0.02 \pm 0.13$
4topSM	$0.06 \pm 0.01 \pm 0.03$	$0.12 \pm 0.02 \pm 0.06$	$0.54 \pm 0.03 \pm 0.27$
4topRPP1400	$1.05 \pm 0.05 \pm 0.53$	$2.01 \pm 0.07 \pm 1.04$	$3.25 \pm 0.10 \pm 1.64$
4topCI	$0.88 \pm 0.16 \pm 0.44$	$1.52 \pm 0.14 \pm 0.78$	$4.98 \pm 0.26 \pm 2.52$

Table 9.6: Expected signal and background yields in the three-lepton signal regions with a Z-veto applied. The first uncertainty is statistical and the second is systematic. The systematic uncertainties reflect all the MC uncertainties, plus *ad hoc* uncertainties of 35% and 20% for the fake/non-prompt leptons and charge mis-id backgrounds, respectively.

	Signal	VLQ Limits (TeV) Observed	Expected
Run II	$T\overline{T}$	0.976	0.981
	$B\overline{B}$	0.997	1.01
	$T_{5/3}\overline{T}_{5/3}$	1.20	1.21
Run I	$T\overline{T}$	0.59	0.66
	$B\overline{B}$	0.62	0.69
	$T_{5/3}\overline{T}_{5/3}$	0.74	0.81

Table 9.7: Summary of mass limits for the VLQ signal models searched for in this analysis. Limits are set at the 95% CL (see text). Run II limits come from this analysis. Run I limits comes from a similar analysis to this one using 20.3 fb^{-1} of data taken at $\sqrt{s} = 8$ TeV [44].

Mass (GeV)	Expected 1σ range	Expected median	Observed
500	0.17 – 0.33	0.23	0.4
600	0.097 – 0.19	0.14	0.19
700	0.063 – 0.12	0.088	0.1
750	0.055 – 0.11	0.076	0.083
800	0.05 – 0.098	0.069	0.075
850	0.042 – 0.083	0.058	0.061
900	0.04 – 0.079	0.056	0.06
950	0.037 – 0.073	0.051	0.053
1000	0.036 – 0.07	0.049	0.051
1050	0.035 – 0.068	0.048	0.05
1100	0.033 – 0.064	0.045	0.046
1150	0.031 – 0.061	0.043	0.044
1200	0.031 – 0.061	0.043	0.044
1300	0.03 – 0.059	0.042	0.042
1400	0.031 – 0.062	0.044	0.044

Table 9.8: Expected 95% C.L. upper limits (in pb) on vector-like T pair production, assuming the singlet model.

Mass (GeV)	Expected 1σ range	Expected median	Observed
500	0.17 – 0.33	0.23	0.28
600	0.095 – 0.18	0.13	0.15
700	0.058 – 0.11	0.081	0.089
750	0.051 – 0.099	0.07	0.078
800	0.041 – 0.08	0.057	0.062
850	0.037 – 0.072	0.051	0.055
900	0.035 – 0.069	0.049	0.053
950	0.031 – 0.06	0.042	0.045
1000	0.03 – 0.059	0.042	0.045
1050	0.028 – 0.055	0.04	0.041
1100	0.026 – 0.051	0.037	0.039
1150	0.026 – 0.05	0.036	0.038
1200	0.025 – 0.048	0.034	0.036
1300	0.024 – 0.047	0.034	0.036
1400	0.024 – 0.047	0.034	0.04

Table 9.9: Expected 95% C.L. upper limits (in pb) on vector-like B pair production, assuming the singlet model.

CHAPTER 10
Conclusion and Discussion

The LHC and its physics program at the various physics detectors, such as ATLAS, have been very successful in their first decade of operation. With the discovery of the Higgs boson using Run I data at $\sqrt{s}$ = 7 TeV + 8 TeV, and the confirmation of the Standard Model electroweak symmetry breaking mechanism, the physics program at the LHC has now turned to beyond the SM mechanisms to answer still open questions about the Universe at even higher energies. Vector-like Quarks (VLQ), Supersymmetry (SUSY), dark matter interaction models, etc. are all examples of models or mechanisms that could potentially provide answers to some of these questions.

A search is presented here for beyond the SM exotic physics in the form of VLQ using data totaling approximately 36.1 fb^{-1}of pp collisions taken at a center-of-mass energy of 13 TeV with ATLAS. The final state topology is a pair of leptons with the same charge or three leptons and associated b-jets and missing transverse energy ($E_{\mathrm{T}}^{\mathrm{miss}}$). This topology may also be used to search for other signal models, aside from VLQ, which may produce same-charge lepton pairs or three leptons in excess of what is predicted by the Standard Model. These signals are not discussed in detail in this dissertation, but are summarized briefly here.

- Production of four top quarks ($t\bar{t}t\bar{t}$) via contact interaction, universal extra dimension (RPP/UED), or Standard Model mechanisms
- Same-sign top pairs (t^+t^+) produced via weakly interacting dark matter mechanisms
- A two-Higgs Doublet Model (2HDM) extension to the Higgs sector

The VLQ and these signal models share common signal regions in this analysis because they can produce similar final states. Limits are set on the cross section for each model. In the case of the $t\bar{t}t\bar{t}$ contact interaction, limits are set on the coupling constant, which is a free parameter in the model. In the case of the RPP/UED model mass limits are set, in a similar manner to the VLQ signals, on a Kaluza-Klein particle in the model. For the same-sign top

signal, mass limits are split up by prompt t^+t^+ production, on-shell mediator, and off-shell mediator models.

The signal regions in this analysis are optimized as best as possible to search for all of these signals, while still maintaining a reasonable limit to the number of signal regions. Some signal regions are more sensitive to the non-VLQ models. In the case of the t^+t^+ signal, a separate ninth signal region is selected and combined with the other eight signal regions in the limit setting fit. As described in Chapter 9, a slight discrepancy is observed in a few of the signal regions ranging from approximately $1-2\sigma$, in the regions with the highest data excess. However, since none of the signal regions contain an excess near 5σ, upper limits on the cross section and lower limits on the mass of VLQ signal models are set. Weaker limits are set for the $t\bar{t}t\bar{t}$ and 2HDM due to the slight excess of data in some regions. The relative agreement between the observed and expected limits on each model depends on the whether the excesses observed were localized to signal regions favorable for a given model. In this analysis, the signal regions with the highest excesses (*SR3b2l_L* and *SR3b3l_L*) were regions optimized in the search for $t\bar{t}t\bar{t}$, not VLQ. Therefore, the limits for the VLQ T, B, and $T_{5/3}$ all show good agreement between observed and expected limits.

The signal models with pair production of T and B assuming singlet branching ratios show an observed (expected) limit of 0.976 (0.981) TeV and 0.997 (1.01) TeV, respectively. The pair production limits for $T_{5/3}$ show an observed (expected) limit of 1.20 (1.21) TeV. For the four top and same-sign top signal models, limits on the coupling constants are set, which translates into a limit on the production cross section. The contact interaction coupling constant shows an observed (expected) limit of 39 (21) fb. The RPP/UED model shows an observed (expected) limit of 1.44 (1.48) TeV on the mass of the Kaluza-Klein excitation. The t^+t^+ signal model has an observed (expected) limit $g_{SM} > 0.31$ (0.28) assuming a mediator mass of 3 TeV and $g_{SM} > 0.14$ (0.13) assuming a mediator mass of 1 TeV.

10.1 VLQ Combination Effort

In searching for new physics models beyond the SM, sometimes multiple searches exist for the same model but are optimized to exploit different signatures in the detector. In the search presented here, the signature is a specific decay product of pair production of T, B, or $T_{5/3}$ Vector-like Quarks. T and B single production as well as $B_{-4/3}$ are not included in this search because it is very unlikely that they would produce the final state topology of interest. However, because T (B) can decay to Zt (Zb), Ht (Hb), and Wb (Wt) they can potentially produce a variety of signatures other than pairs of same-charge leptons in the

final state. Therefore, in ATLAS (and CMS) several different searches exist to search for T and B using other final state signatures.

Ideally, in order to increase the sensitivity of the global search for Vector-like Quarks, a combination of all final state signature results must be performed. For now, the combination effort is focused on the pair production modes of T and B since those have the highest variety of final state signatures to cover by multiple analyses. The potential for improvement on the sensitivity of the search for pair production of T and B can be significant. In Run I, the improvement from combining VLQ searches was expected to be on the order of $35-50$ GeV in terms of the expected limits. The ATLAS Run I searches for VLQ were not combined in a public result, however the push for a Run II VLQ combination results is on-going and expected by the end of 2017. The limits are expected to improve significantly with the Run II dataset.

The combination effort requires similar object definitions in each analysis to minimize overlap of events in the signal regions. There are six analyses involved in the combination effort presented here. These are listed in table 10.1.

Analysis Name	Final State
Same-sign dilepton, trilepton	$\ell^{\pm}\ell^{\pm}$(or $\ell\ell\ell$) + b-jets
$Z(\ell\ell)t$+X	$\geq 2\ell$, leptons are matched to a Z boson
$Z(\nu\nu)t$+X	1ℓ, lepton matched to a Z boson + high $E_{\mathrm{T}}^{\mathrm{miss}}$
$H(b\bar{b})t$+X	0 and 1ℓ
$W(\ell\nu)t$+X	1ℓ
VLQ all-hadronic	high and low $E_{\mathrm{T}}^{\mathrm{miss}}$ search, 0 ℓ, purely hadronic final states

Table 10.1: Analyses and their final state signatures used in the combination effort for pair production of T and B.

Combining the same-sign dilepton and trilepton analysis (this analysis) with the Z-tag multi-lepton analysis with require some changes in the selection for the signal regions since there is currently some overlap in events. Therefore, the yields in table 9.6 are shown to reflect a Z-veto cut on the trilepton signal regions. This is done because the events with a Z identified are present in both this analysis and the Z-tag multi-lepton analysis. During the combination, the trilepton signal regions with the Z-veto will be used instead of the normal trilepton signal regions.

It is expected the overlap between the same-sign analysis and the other analysis is minimal and current studies show minimal changes will be needed to the analyses prior to the VLQ

combination. In addition to setting limits on the singlet multiplets for T and B, the 2D limits similar to figures 9.10 and 9.11 are set in the combination to cover as much of the phase space as possible. Current estimates show an improvement in limits of around 70 GeV after combining the $Z(\nu\nu)t$+X, $H(b\bar{b})t$+X, and $W(\ell\nu)t$+X analyses together so far.

10.2 Future Prospects

Several methods other than what has been presented here can be applied to this analysis to potentially improve the search for VLQ in the future. One is the addition of a multivariate Boosted Decision Tree (BDT) to apply the selection and final event discrimination into the signal regions. A training set would be needed to improve sensitivity in the regions of interest. A BDT was explored in the Run I version of this analysis [44, 165] and showed minor improvements, but with more data the BDT could be revisited.

Additionally, since the modest excess seen in this analysis was focused on the signal regions with the highest number of b-tagged jets (≥ 3) and relatively large H_{T} and $E_{\mathrm{T}}^{\mathrm{miss}}$, the next iteration of the analysis should focus on studying the high b-jet multiplicity regions in more detail. Specifically, for the data-driven backgrounds, studies like the one presented in appendix B.5 should be redone once more data are collected. The limiting factor for the higher b-tag efficiencies derived for the fake/non-prompt background is the lack of statistics in that region. For the rest of the analysis, the optimization process should take into account the fact that previous versions of the analysis showed some deviation of data in the higher b-jet multiplicity regions.

A number of improvements on the data-driven backgrounds can be employed in the future versions of this analysis. From Run I to Run II, the matrix method for estimating the fake and non-prompt lepton background was significantly improved as already described in §7.1.4. Care must be taken when estimating these backgrounds in relatively low statistics regions, which is the main reason why the Likelihood Matrix Method is favored. The fake and non-prompt lepton background is one of the most difficult backgrounds to estimate in this analysis. Further studies, in addition to those described in appendix B, may be needed in the next version of the analysis in order to further improve the parametrization of the efficiencies and understand the systematic uncertainties.

In terms of the charge mis-id background, a BDT algorithm was provided by the *EGamma* physics group for use in Run II analyses, inside the package called `ElectronChargeID-SelectorTool`. The algorithm is designed to essentially cut a significant portion of the charge mis-id background using a multivariate technique based on electron cluster and track

properties: the track impact parameter, the track curvature significance, the cluster width and the quality of the matching between the cluster and its associated track, both in terms of energy and position. The main reason this algorithm is not employed in this analysis is because the $|\eta_{\text{cl}}| < 1.37$ cut on electrons provides sufficient reduction in the charge mis-id background and could be implemented quickly. The improvements suggested by a simple comparison between this cut and the BDT charge mis-id 'killer' were on the order of a few percent in favor of the BDT algorithm. This should be revisited in the next iteration of the analysis.

LHC Schedule The LHC is currently operating at $\sqrt{s} = 13$ TeV and is expected to eventually upgrade to $\sqrt{s} = 14$ TeV with collisions at $2-3$ times the current nominal luminosity (10^{34} cm^{-2} s^{-1}). The dataset used here totals 36.1 fb^{-1}, but ATLAS is expected to at least double that from the data collected in 2017 and 2018 (the remaining years of running for Run II). The LHC and the experiments are scheduled to undergo a long shutdown from 2019−2020 for important upgrades and maintenance. The LHC will undergo upgrades to its injector chain during this period. ATLAS will undergo upgrades to its Muon Spectrometer, liquid argon calorimeter, and tracker systems. The Micromegas front-end electronics described in appendix A is part of the effort to upgrade the ATLAS Muon Spectrometer system for successful operation over the next 10−20 years. It is expected that ATLAS and CMS will collect around 300 fb^{-1} in the next run (Run III), which would provide a major increase in statistics for analyses such as the one presented here. Beyond about 2026, the LHC is expected to undertake another upgrade to prepare for collisions at ≥ 5 times the current nominal luminosity. Beyond this, a new generation of accelerators is being proposed (likely only one of the proposals with be built) for post-2050 particle physics searches, operating at $\sqrt{s} = 100$ TeV.

APPENDIX A
MicroMegas Front-end Electronics

A.1 Introduction

The LHC is currently collecting collision data at $\sqrt{s} = 13\,\text{TeV}$ and a luminosity of $\mathcal{L} = 1 - 1.5 \times 10^{34}\text{cm}^{-2}\,\text{s}^{-1}$. The current run is its second proton-proton physics run (Run II) since initiation in 2008. In 2019, ATLAS will cease taking data for the Long Shutdown 2 (LS2) for two years to initiate the Phase-1 upgrade. This upgrade will enhance physics performance at higher luminosities starting at about $\mathcal{L} = 2 - 3 \times 10^{34}\text{cm}^{-2}\,\text{s}^{-1}$ in the next run and into the high luminosity LHC (HL-LHC), where $\mathcal{L} \geq 5 \times 10^{34}\text{cm}^{-2}\,\text{s}^{-1}$. Several improvements to the tracking and triggering in the Muon System will be implemented during this shutdown in order to handle the increase in luminosity.

The New Small Wheel (NSW) upgrade [166] is one of the priorities for the LS2 aimed at replacing the current Small Wheels (SW) in order to improve the muon spectrometer end-cap system [167, 168] of ATLAS. Specifically, adding Level-1 (L1) trigger capability to the SW will reduce the high trigger rate of fakes in the end-cap regions as the LHC continues to operate at higher luminosities. Currently, the muon trigger rate in the end-cap regions is dominated by fake triggers originating from sources other than the main impact event. Replacing the existing detector systems and readout electronics will serve to reduce the rates and improve muon reconstruction in the end-cap region. Particle hit rates in the SW region are expected to exceed the current detectors' design capabilities, rising to $\sim$15 kHz/cm^2 at $\mathcal{L} = 5 \times 10^{34}\text{cm}^{-2}\,\text{s}^{-1}$.

Importantly, as the luminosity is increased, the low p_T threshold for single lepton triggers and the overall trigger rate must be maintained at similar levels while simultaneously rejecting fakes due to the higher background rates. In Figure A.1, a cross section of one end of the ATLAS detector is shown with three tracks through the muon spectrometer's end-cap detectors. Tracks B and C are rejected with the addition of the L1 trigger in the NSW because the hits in the Big Wheel do not match track vectors in the NSW directing back to

the interaction point (track A is accepted).

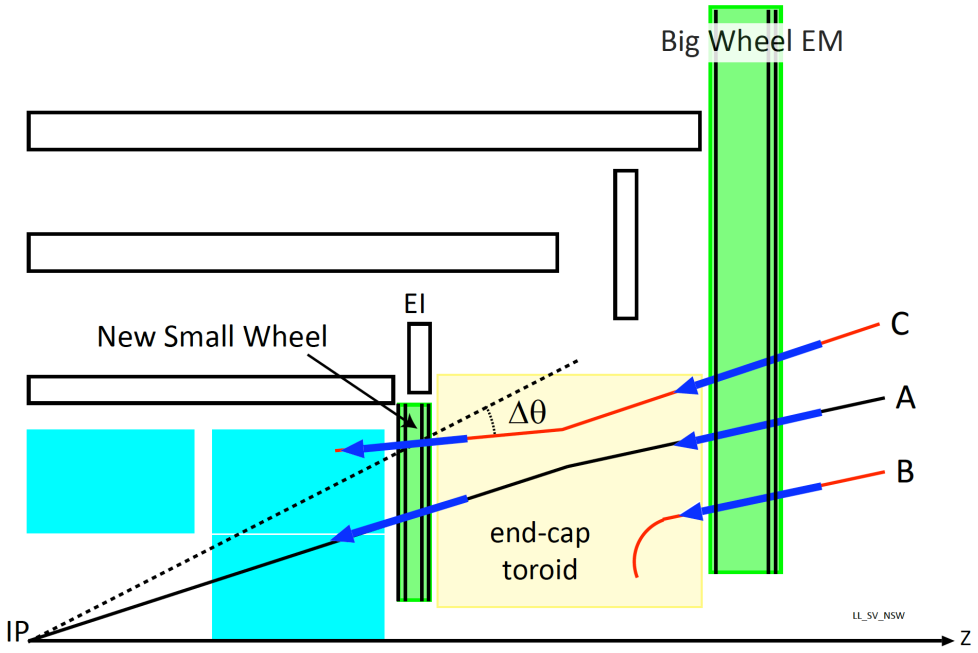

Figure A.1: Schematic showing the trigger scheme in the muon spectrometer end-cap region of ATLAS [166]. Tracks B and C are rejected because they do not originate from muons coming from the interaction point. Track C is triggered in the NSW, but does not meet the requirement of $\Delta\theta < \pm 7$ mrad to be counted as a desired muon.

Several requirements must be met for the NSW and the detector readout electronics. For the L1 trigger, the detectors must provide trigger angular resolution of <1 mrad. For tracking, the muon track resolution must be 15% of the transverse momentum, p_T, for 1 TeV muons. Due to the higher background rates, the electronics and chambers must be able to withstand increased radiation while maintaining precision tracking of muons, and do so for 10+ years. The NSW must also have redundancies to reduce the likelihood of failures in tracking or triggering on the part of the detectors. Additionally, full coverage of what is currently covered by the Small Wheels must be provided without introducing holes in either the trigger or tracking acceptance capabilities. Finally, due to the timeframe of this upgrade, the systems must also operate efficiently during Phase-2 of the LHC, which means being compatible with the Phase-2 requirements for latency, trigger rates, and withstanding around 3000 fb^{-1} integrated luminosity.

The NSW final design will have a pseudorapidity coverage range of $1.3 < |\eta| < 2.7$. It will consist of 16 layers of two detector technologies 'sandwiched' back to back in multiplets, with a total of eight small sectors and eight large sectors per wheel [169]. The two tech-

nologies are called the small-strip Thin Gap Chambers (sTGC) and the Micromegas (MM). Primarily, the sTGC systems will be commissioned to provide the Level-1 triggering in the NSW [170], while the MM systems will focus on precision tracking due to their superior resolution and higher hit rate capabilities. Each detector system will have the secondary function of providing redundancy to each other's primary functions. The NSW configuration of these detectors in each multiplet module is sTGC−MM−MM−sTGC to optimize on the redundancy. Together, the two detector technologies will consist of about 2.5 million channels in the readout electronics for both end-cap NSW.

The front-end electronics are responsible for reading out the hit information from particles going through the detectors and feeding it through a readout chain to a host PC. The focus of this paper with be on the readout electronics for the MM detectors.

Section A.2 will cover the details of the MM chambers and the full readout chain for the front-end electronics being designed and tested at the University of Arizona. The 'demonstrator' version of the front-end boards is covered in section A.3, with a description of the updates to the design of the first prototype version for early 2017. Finally, section A.4 covers the various chamber tests performed at University of Arizona and at CERN, using the demonstrator version of the board. Section A.5 provides a summary and remarks on the future board designs.

A.2 Detectors and Electronics Overview

A.2.1 Micromegas Detectors

MM are micro-pattern gaseous drift chambers [171] with a thin stainless steel mesh separating the gaseous region into a drift region with moderate electric field (typically on the order of hundreds of V/cm) and an amplification region with an electric field 50−100 times stronger than the field in the drift region. The mesh is set to ground and lies just 100−150 µm above a layer of resistive strips. The resistive strips are embedded in a thin insulator and cover the conductive readout strips to protect the chamber from sparking [172]. The resistive strips are capacitively coupled to the conductive readout strips, which are connected to the front-end electronics for signal processing. The planar drift electrode is set to negative high voltage (HV) and the resistive strips are set to positive HV.

When a high energy particle enters the chamber, the gas (Ar:CO_2 93:7% in the NSW configuration) surrounding the particle's track becomes ionized and electrons from the ionization process drift towards the mesh. Approximately 95% of the electrons move through

the mesh without hinderance and enter the high electric field amplification region. There they gain enough energy to further ionize the gas and a large 'avalanche' of charge forms and creates a signal on the readout strips. Typically, the gas gain for this configuration of MM is on the order of 10^4.

Figure A.2 shows the important aspects of the MM technology. In the NSW, the MM will operate with the parameters shown in Table A.1.

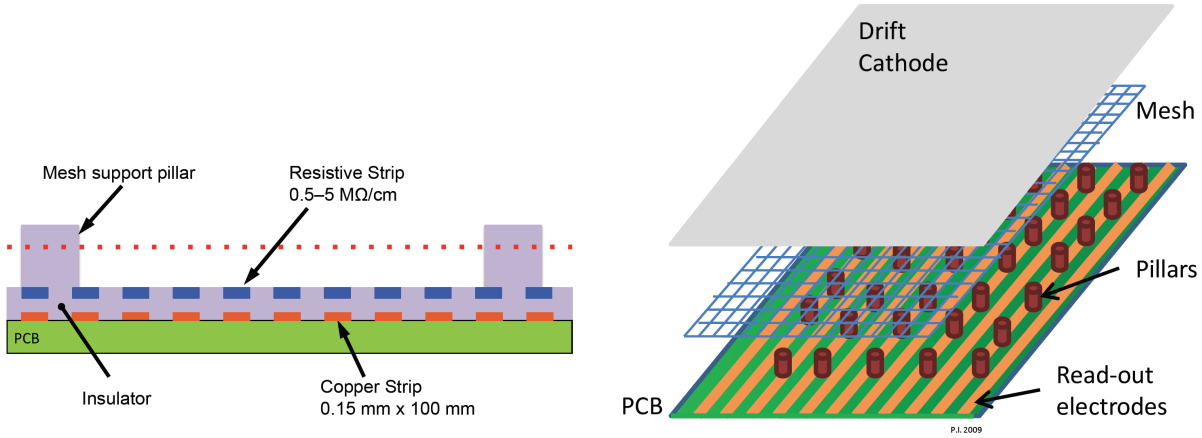

(a) (b)

Figure A.2: Drawings of the MM chamber design [166]. (a) The resistive strips are embedded in the insulating layer over the conductive readout strips. (b) The main components of the MM design are shown with the mesh separating the gaseous region. Typically the mesh sits just 100−150 µm from the readout strips.

Parameter	**Value**
Mesh	325 lines/inch
Amplification region	128 µm
Drift region	5 mm
Gas	Ar:CO_2, 93:7
Gas Gain	10^4
HV on resistive strips	+550V
HV on drift cathode	-300V
Amplification field	40 kV cm^{-1}
Drift field	600 V cm^{-1}

Table A.1: Micromegas chamber operating parameters.

Of the 2.5 million channels in the NSW electronics, about 2.1 million belong to the

MM detector system. The strip pitch in a MM detector is 400 µm. This is part of the advantage of MM over the current detector technologies in the ATLAS SW: a higher number of channels with small pitch improves the spatial resolution of reconstructed muon tracks. The requirements for the MM chambers to improve tracking resolution include track accuracy of 30 µm in η and 80 µm in the z direction. Spatial resolution must be around 100 µm, while the readout granularity for track separation should be around 400 µm.

For precision hit information, the MM will be layered into multiplets in the final design and two directions of strips will be used. The first direction has strips in each layer oriented in the horizontal direction and every other detector layer is offset by a stereo angle of $\pm 1.5^\circ$ with respect to the horizontal layer. Table A.2 gives further details on the strip properties of the MM detectors as they will be implemented in the NSW upgrade.

A.2.2 VMM ASIC and Readout Chain

Both NSW detector technologies will have front-end PCB boards mounted to the sides of the chambers in order to efficiently read out the hit information from the channels. The PCB boards are equipped with several custom designed Application Specific Integrated Circuits (ASIC), called VMM [173], to digitize and read out the data. The VMM is designed specifically for the NSW upgrade detectors, though it can potentially be utilized with other micro-pattern detectors.

The third generation of the VMM is called VMM3, which is presented in this paper and is undergoing several tests before installation on the production front-end boards. The VMM3 is fabricated with 130 nm 1.2 V 8-metal CMOS technology from IBM. Each VMM must provide charge and timing measurements of a pulse, and other readout logic to accommodate

Property	**Value**
Strip width (large/small chamber)	300/300 µm
Strip pitch (large/small chamber)	450/425 µm
Resistivity of strips	10−20 $\mathrm{M\Omega\,cm^{-1}}$
Stereo angle	$\pm 1.5^\circ$
Strips/Layer	8,192
Strips/Octant	131,072
Total no. of strips (both end caps)	2,097,152
VMM chips/octant	2,048
MM trigger elements	32,768

Table A.2: Micromegas strips characteristics for New Small Wheel.

the complex nature of the detectors. The MMFE consists of 8 VMM3 chips, each capable of delivering pulse information for 64 channels.[1] The channel capabilities in the VMM include charge peak and time detection, charge amplification, shaping of the signal, baseline and threshold information with threshold trimmer, analog monitoring, digital output for time-over-threshold (ToT) and time-to-peak (TtP). In nominal operating mode, the VMM detects hits from the detector once a signal charge reaches a configurable threshold. Signal peak amplitude and times are digitized by 10-bit and 8-bit ADCs, respectively. The discriminated signal also provides an address-in-real-time (ART) that can be as part of the MM trigger system.

The readout chain for the MMFE-8 boards consists of a chamber, the VMM channels, one on-board Artix-7 Xilinx FPGA [174], Gb-Ethernet, and a host PC with software to gather data. Digitized data from the VMM chips are buffered and read out using a two-bit serial output.

A.3 Micromegas Front-End Electronics

To evaluate the functionality of the VMM as well as power consumption, layout considerations, and readout capabilities, the MMFE-8 demonstrator board was constructed with several components intended to be phased out for the final production boards. The MMFE-8 demonstrator was originally constructed in 2015 and has undergone several revisions that mitigated power distribution and noise issues, and installed improved versions of the VMM ASIC. In general, the board consists of 2,698 components, with total board dimensions: 215 mm $\times$ 62.5 mm, and an approximate thickness of 2.34 mm. There are 16 electrical layers separated by 370HR. Figure A.3 shows the front (VMM-side) and back sides of the board with important features labeled.

Connections to the channels on a Micromegas detector are provided via two Zebra elastomeric connectors [175]. The pads for these connections are located on the VMM side of the boards. The Zebra connectors are held in place by a custom machined clamping mechanism, which has undergone design improvements as well. The channel traces from the Zebra connector pads to the VMM chips are as short as possible to efficiently use the tight space requirements while minimizing capacitance.

The final production boards have a height limitation due to spacing requirements between two MM chambers in the NSW. The demonstrator MMFE-8 version consists of components

[1] Collectively, the MMFE board with 8 VMM chips installed is referred to in the rest of this document as 'MMFE-8'.

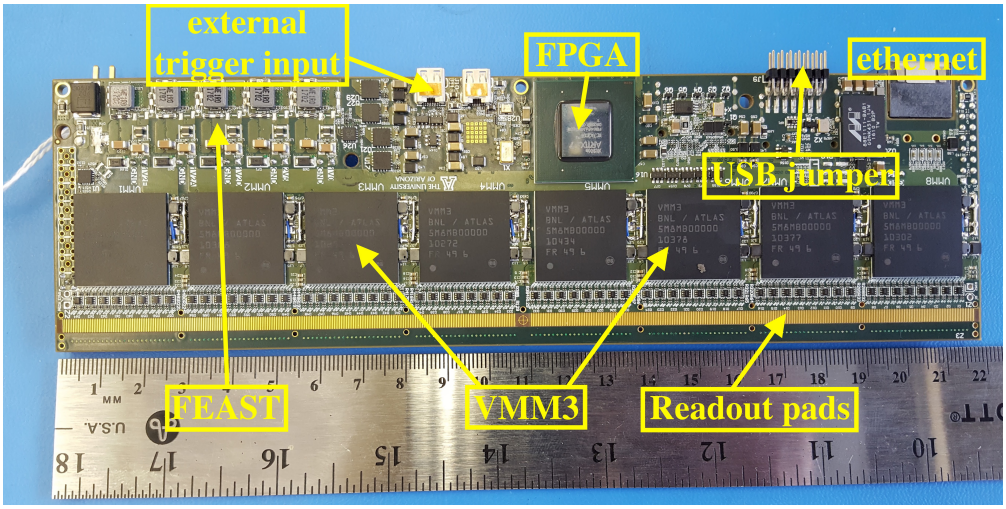

(a) VMM side (front)

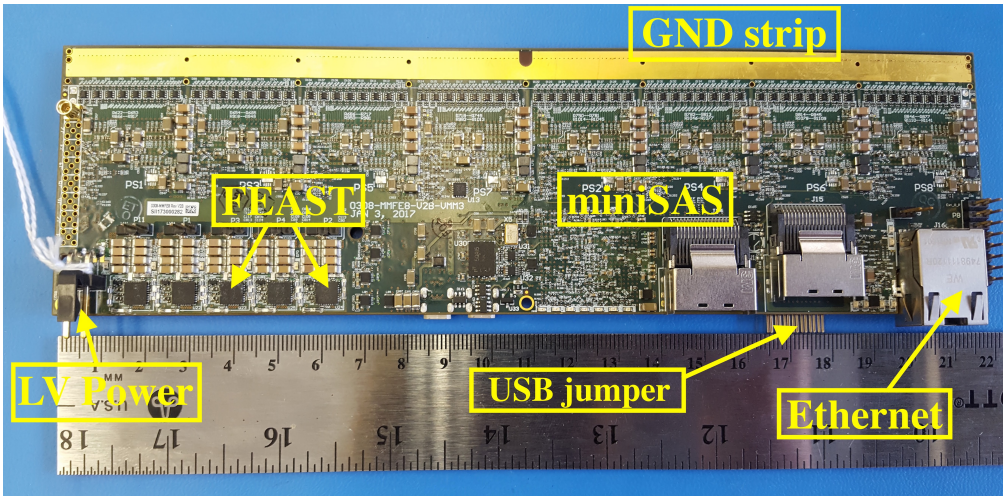

(b) Back of board

Figure A.3: Picture of MMFE-8 demonstrator board with 8 VMM ASICs and important features labeled.

that violate this height requirement, such as the ethernet connection, but will be phased out in the production board design. The major components and dimensions for the MMFE-8 boards are summarized in Table A.3. In addition, the version of the board discussed here has a custom-machined slot, roughly 2mm × 4mm, located in the middle of the board between the two sets of Zebra connection pads. This slot is important for precision positioning when mounted to the full Micromegas chambers, but is not utilized in the testing of the MMFE-8 discussed in § A.4. Figure A.3b shows the slot location (before machining).

The board is designed to place all components which require cooling, such as the VMM

chips, on one side. The cooling components are beyond the scope of this paper. In the bench testing discussed in § A.4, a fan is used for cooling the VMM chips.

Property	**Value**
Dimensions	$215 \times 62.5 \times 2.34$ mm^3
Electrical Layers	16
Number of components	2698
Material	370HR
Power Distribution	5 FEAST DC-DC
Low Voltage DC Supply	8 V
Number of ASIC / board	8
Number of channels / board	512
Connection to chamber	2 elastomeric connectors / board

Table A.3: Summary of front-end demonstrator (MMFE-8) properties for the version of the board tested in this paper. Some changes will be made due to stricter operating and environmental conditions for the final production boards.

A.3.1 FPGA Scheme

An on-board Xilinx Artix-7 XC7A200T-2FBG484I FPGA is used to handle the readout of the 8 VMM chips and to test firmware for configuration and readout schemes of the chips. Each VMM requires 64 pins for the channels plus X LVDS pins for the differential signals for configuration and readout. Approximately 67% of all I/O pins on the FPGA are used by the VMM chips. Other pins are used for the ethernet, miniSAS, and other connectors on the board. The FPGA will eventually be phased out and replaced by two ASICs, a Readout Controller (ROC) and a Slow Control Adapter (SCA), in the final design of the MMFE boards.

Firmware is loaded onto the FPGA using Xilinx Vivado Design Suite 2016.2 [176]. The board is also equipped with flash memory, which can be programmed for immediate use on power-up.

A.3.2 Input Protection

The 64 input channels for each VMM are equipped with a 15 Ω resistor for current limitation and an SP3004-04XTG input protection device to protect against electrostatic discharge. Each device has 4 channels with ultra low capacitance rail-to-rail diodes and an additional Zener diode on the Vcc and GND pins. The version of the MMFE-8 used in

the results presented here have these ESD protection diodes, however, an updated design will include additional SEMTECH UCLAMP3321ZATFT back to back Zener diodes to be placed between the signal lines and GND because repeated exposure to discharges damaged the SP3004 parts.

A.3.3 Environmental Constraints

The primary environmental challenges for the final MMFE-8 design are the high magnetic fields and high radiation environment in the NSW region of ATLAS. Simulations of the magnetic fields and radiation tolerance levels for the NSW region were performed assuming 10 years operating at $\mathcal{L} = 5 \times 10^{34}\text{cm}^{-2}\,\text{s}^{-1}$ [177]. The range in magnetic fields the electronics must withstand is about $1 - 5$ kG. The radiation tolerance is measured in three ways: Total Ionizing Dose (TID), Non-Ionizing Energy Loss (NIEL) measured with respect to the equivalent fluence of 1 MeV neutrons, and Single-Event inducing particles (SEE) measured with respect to the fluence of hadrons above 20 MeV. The radiation dose depends heavily on the radial distance from the center of the NSW, but generally, the TID is 1740 Gy in the inner rim around 1 meter from the center of the NSW and 84 Gy in the outer rim around 5 meters from the center of the NSW. The inner (outer) radius NIEL is 2.3×10^{13} neutrons/cm^2 (7.3×10^{11} neutrons/cm^2); the SEE is 4.2×10^{12} protons/cm^2 (1.3×10^{11} protons/cm^2).

A.3.4 Power Considerations

Several revisions to the power supply design and noise issues of the MMFE-8 prompted the newest version of the demonstrator board, which is called revision 2B. In previous versions of the board, when operating at maximum power output, the supply rails failed to provide the necessary output with all eight VMM chips programmed and all 512 channels pulsing. Several solutions were implemented to fix this problem (e.g. soldering on fixes to the outside of the board), but ultimately a redistribution of the power layout of the board was necessary. The initial power supply design was done with little *a priori* knowledge concerning the VMM requirements, board space limitations, voltage requirements for the FPGA, radiation hardness requirements, and the high-voltage, low-current, high-efficiency input supply requirements. This led to an approach that used on-board DC-DC converters, with Low Drop Out (LDO) regulators in the distribution. Four LTM4612 DC-DC converters were used in conjunction with twelve ADP1755ACPZ-R7 LDO regulators, eight to filter the analog supplies to each VMM and four to provide specific FPGA bank voltages. This DC-DC design was implemented in order to make the board as small as possible instead of as quiet

as possible. However, further radiation studies revealed they were limited in Single-Event Effects (SEE) tests.

The new design for revision 2B implements FEAST DC-DC converters, which are radiation hard and reduce noise [178]. The DC-DC design and in-lab testing was provided by University of Michigan. University of Arizona produced the power distribution system. Two FEAST DC-DC are used for the VMM analog signals at 1.2 V; one FEAST is used for the VMM digital and FPGA at 1.2 V; one FEAST at 2.5 V is used for the FPGA and ethernet as well as 1.0 volt for the FPGA and ethernet. An additional requirement banning the use of inductors was shown to be unnecessary if shielded inductors were used. For the current iteration of the board, only shielded and tested inductors are used. The final boards are to be tested in a high magnetic field to validate this. Noise tests are proceeding with the FEAST power design using the revision 2B boards. For the production boards, the power distribution system will consist of three FEAST DC-DC converters: two for VMM analog at 1.2 V and one at 1.2 V for VMM digital and the SCA and ROC chips that will replace the FPGA.

A.4 Measurements with the MMFE-8 Demonstrator

The data collection chain and the VMM capabilities on the demonstrator boards have undergone several validation tests. A small-scale $10 \times 10\,\mathrm{cm}^2$ MM chamber, built at CERN, is used to take data from cosmic ray muons and an ^{55}Fe X-ray source in order for the full readout scheme to be tested. One board at a time is mounted on the chamber via the readout pads, which are connected to two Zebra connectors, each spanning half the length of the board. The chamber pads have a pitch of 400 µm and a width of 300 µm. The strip resistivity is about 25 $\mathrm{M\Omega\,cm^{-1}}$. Figure A.4 depicts a small-scale chamber with a single MMFE-8 board fixed to it via two elastomeric Zebra connectors. This chamber design is equipped to read out only the middle four of the 8 VMM chips on a MMFE-8 board.

The Zebra connectors work by compression and must be aligned to high precision in order for all 512 channels per board to be connected properly. Each Zebra is housed inside a G10 custom-machined holder to provide support during compression. The Zebras connect the input traces on the MMFE boards directly to the strips on the MM chamber. The connectors are 110 mm × 6.30 mm × 2.50 mm and have 6 parallel rows of gold wires oriented vertically through a silicone core. The width of the connector wires is 30 µm and the pitch is 50 µm, guaranteeing at least 18 wires contact each pad to secure a reliable connection. Each connector mates with 256 channels from the chamber, and four additional

channels per Zebra are reserved for identification of the MMFE-8 board. Thorough testing of the Zebras is underway, including ESD issues, force of compression, longevity, and reliability testing.

The compression apparatus shown in Figure A.4 was designed and machined at the University of Arizona specifically for the bench testing of the MMFE-8 boards and is not the final design of the compression apparatus for the NSW due to space limitations. The apparatus serves both to align the board and to provide full compression of both Zebra connectors, with adjustable screws for customizing pressure along the back length of the board.

For bench testing and data taking (more on this in § A.4.2), the board is affixed to the chamber by compressing the Zebras and is powered with a low voltage supply providing 12V. HV is supplied to the chamber strips and drift planes from a standard CAEN 2-channel power supply [179]. The FPGA is then programmed from a JTAG Digilent mini-USB connection. A Python GUI is used to configure and control the readout of the VMM chips. Each board is assigned a unique IP address on the LAN from the GUI, and the data are read out using UDP ethernet packet protocol.

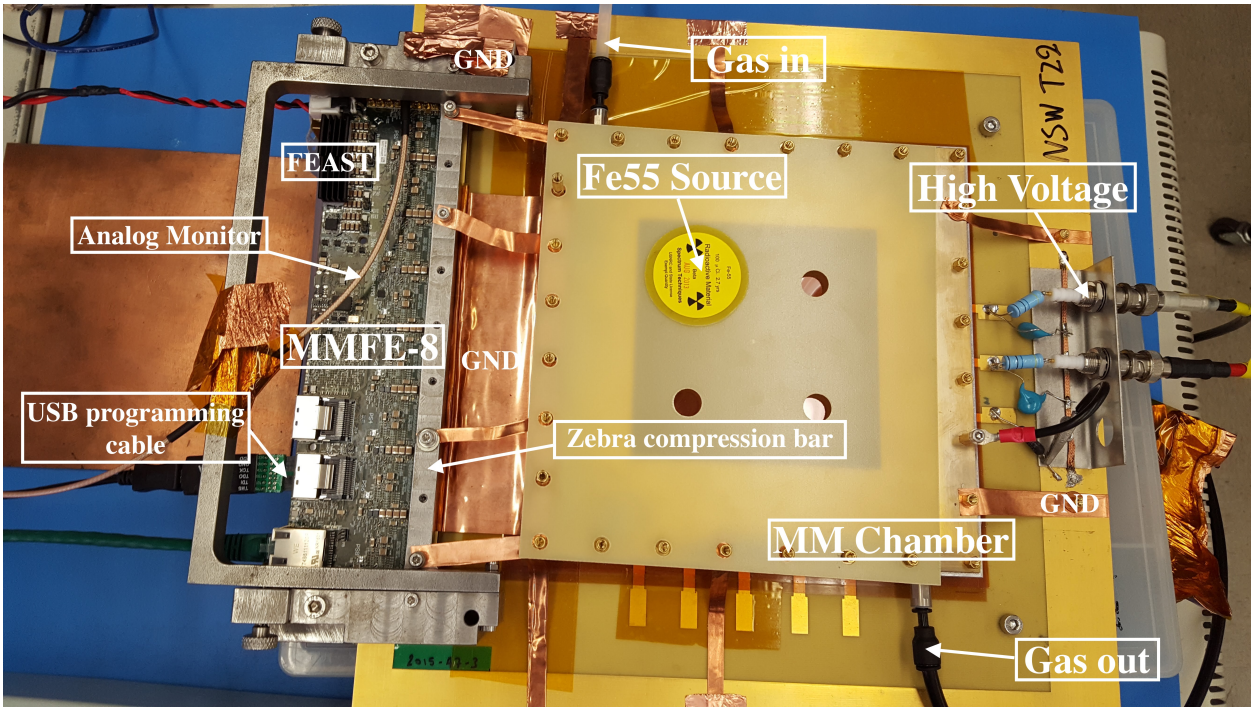

Figure A.4: Setup of an MMFE board mounted to a small-scale MM chamber at University of Arizona. The ^{55}Fe X-ray source shown is placed over the relevant channels when taking data with specific VMM chips since the X-ray are minimally penetrating.

A.4.1 Noise

Assuming a chamber gas gain of 10^4 the expected signal from a minimum ionizing particle (MIP) yields approximately 240 thousand electrons (38.5 fC) [180]. Of course, typically the MIP signal is spread over several chamber strips (on average, about $3-7$ strips) and depends on the incoming angle of the MIP. Therefore, the signal per strip yields approximately 48 thousand electrons (7.7 fC). The design goal of the MM chambers is that the noise is expected to be less than about 4000 electrons (0.64 fC) for an input capacitance of 200 pF.

A major concern for the MMFE-8 board is noise on the readout channels, especially when the board is attached to a MM chamber. In the previous design of the MMFE-8 board, the DC-DC converters were seen to output a large amount of noise, on the order of 100 mV and at the switching frequency of 1.2 MHz. In order to reduce this noise several modifications to the boards were made. Initially, a small Faraday cage was used to shield the DC-DC converter noise from the VMM chips. After some experimentation, however, the converters themselves were modified from their noisiest (but most efficient) settings, the power inductors were under-sized for noise, and the recommended output filter capacitors were replaced. The noise levels were further improved once the supply frequencies were spread out by modifying the corresponding resistors to slightly offset each frequency from the others. These improvements brought the noise level to about 20 mV when attached to a small chamber. Further tests with the newer version of the MMFE-8 on MM chambers built at CERN showed radiation from the DC-DC converters was being injected into the inputs to the VMM. After the revision 2B was constructed, several tests were performed to identify noise from the FEAST DC-DC converters. It was determined that several magnetic fields were causing internal noise and if the board was powered by another MMFE-8 board's FEAST, the noise was greatly reduced. This suggests the FEAST layout is important for the noise performance of the boards. Although the external power setup shows improvement for the noise tests on the chamber, on the bench, this design is not favorable for the final boards and will require another revision of the boards.

When a board is being tested on a chamber, the chamber must be grounded properly to reduce noise levels. Grounding the chamber and board correctly required separating AGND (analog ground) from EGND (earth ground). Mostly, this resulted in using similar metals wherever possible to increase connection quality and isolating the HV ground as well.

Noise measurements are made using the analog monitor output of the VMM amplifier-shaper. This measurement calculates the RMS noise from the baseline of each channel, individually. Each channel is unmasked, one at a time, without being pulsed and the baseline

level and spread for the channel are measured. The noise is derived from the RMS of the baseline and is converted to the noise in number of electrons using the global gain configuration. For the VMM3 tests performed here, the nominal gain is set to 6 mV/fC.[2] The amount of noise seen on the channels was tested for differences when the board was unmounted or mounted to the chamber in figure A.4 and for when the MMFE-8 was powered with its own FEAST supply or form an external MMFE-8 FEAST. The externally powered boards showed an improvement (decrease) in noise by about 20−40% on average. The noise is converted from mV to equivalent noise charge (ENC) in number of electrons by using the configurable gain setting.

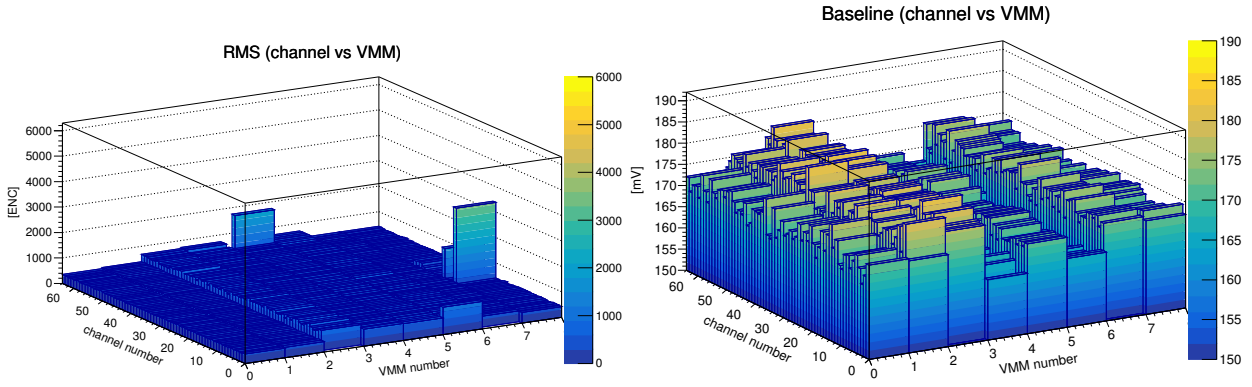

Figure A.5: Noise (a.) and baseline (b.) measurements from analog monitor output of the VMM amplifier-shaper for one MMFE-8 board powered externally by another MMFE-8 board FEAST. In this test, the board is also attached to the chamber via the Zebra connectors. The gain configuration for the VMM chips is 6 mV/fC and the peaking time is 200 ns.

Figure A.5 shows the noise levels when mounted to the chamber and when powered by an external MMFE-8 FEAST. Figure A.6 shows the noise and channel baseline levels for one MMFE-8 board when mounted to the chamber and when powered directly with its on-board FEAST. Channels with very low or very high baselines are tested with the internal pulser to determine if they are dead. Note some VMM chips tend to have higher baselines on average that others. The four middle VMM chips are the ones whose channels are connected to the chamber via the Zebra connectors, so those show a noticeable increase in noise levels, by about a factor of 2. Of course, noise depends on other factors as well, such as the power conditions. The baseline of each channel stays relatively the same when on the chamber

[2]The available options for the VMM gain configuration are controlled in the GUI and include 0.5, 1, 3, 4.5, 6, 9, 12, 16 mV/fC

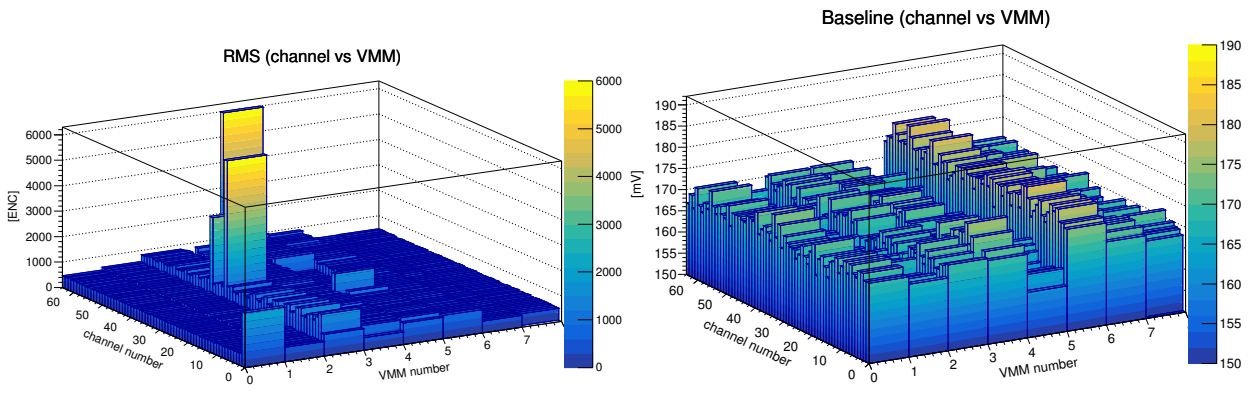

Figure A.6: Noise (a.) and baseline (b.) measurements from analog monitor output of the VMM amplifier-shaper for one MMFE-8 board powered by its on-board FEAST DC-DC converters. In this test, the board is also attached to the chamber via the Zebra connectors. The gain configuration for the VMM chips is 6 mV/fC and the peaking time is 200 ns.

versus off the chamber. This is a good indication of stability for the channels when taking measurements with the chamber. Note however, that figures A.5 and A.6 show different baseline values because they are separate boards and there is some variation in the channel baselines from board to board.

The noise level when the board is unmounted or mounted to the chamber is different due to noise induced on the channels from the chamber. The noise depends on the capacitance of the chamber strips. Both intrinsic noise of the VMM and noise external to the VMM contributes to the noise measured from the analog output. Both values are also dependent on the configurable gain and peaking time settings. The intrinsic noise for the VMM shows this dependence on gain and peaking time in Figure A.7. At a default gain of 6 mV/fC and 200 ns peaking time, the charge resolution is shown in the cyan curve. The noise is converted to equivalent noise charge (ENC) in number of electrons by dividing the output RMS noise level from the analog output data by the configurable gain in mV/fC.

A.4.2 ^{55}Fe Data Testing

An ^{55}Fe X-ray source is used to study the response of the chamber and board setup. Ar:CO_2 gas (93:7%) is input into the chamber and allowed to flow through for 30 minutes before the flow rate stabilizes. HV is then applied to the chamber using the CAEN 2-channel HV supply, where -300 V is applied to the drift electrode and around +515 V is applied to

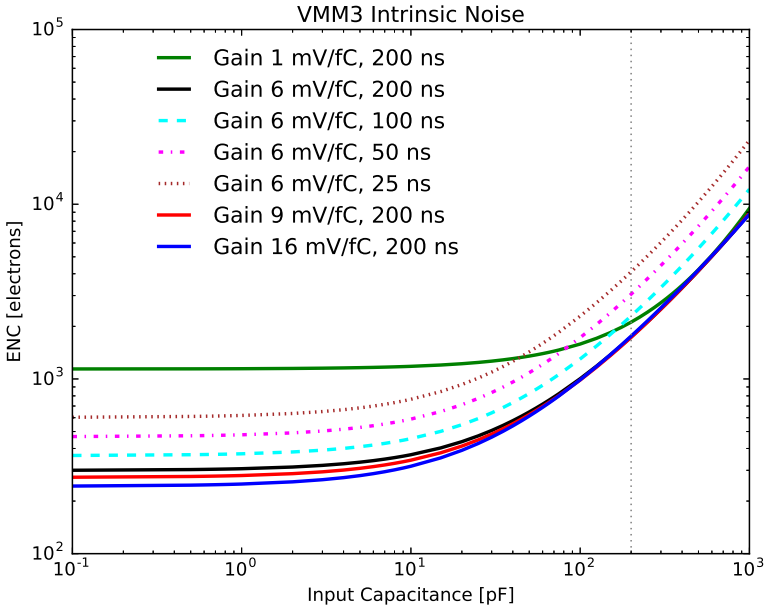

Figure A.7: Intrinsic charge resolution for the VMM3 [181]. Measurements are made at each gain for four different values of the peaking time in ns and fit to a function. Gains 1, 6, 9, and 16 mV/fC are plotted at 200 ns and at gain 9 mV/fC for 25, 50, 100, and 200 ns. The vertical dotted gray line represents the input capacitance for the MM chambers (200 pF).

the strips.[3] The mesh is held to ground as in the final Micromegas design for the NSW. The gas gain in this chamber configuration is typically on the order of 10^4.

When taking ^{55}Fe data, all channels are unmasked except the first five on each VMM. The VMM chips are then configured for continuous readout and set for acquisition mode, which primes the ASICs for data collection by looking for a pulse above the user-set threshold. The nominal global configurations are the following: the gain is set to 6 mV/fC, peaking time is 200 ns, and threshold DAC[4] is 300.

Data are read out from the FIFOs as two hex words per channel hit. The words are stored in an output data file and translated into decimal using another Python script, which extracts the channel number, amplitude, timing, BCID, VMM number, and turn number.[5] ROOT [182] scripts are then used to convert the data file into ROOT ntuples for offline analysis. The ntuple event number is defined for adjacent (or within two) channel hits which fall into a small BCID window, typically about ±10.

[3]Sometimes channel saturation can occur, so the voltage on the strips can be decreased to reduce the number of saturated channels.

[4]10-bit Digital to Analog Converter adjustable as a global configuration.

[5]The turn number is not used at this time, so is always 0.

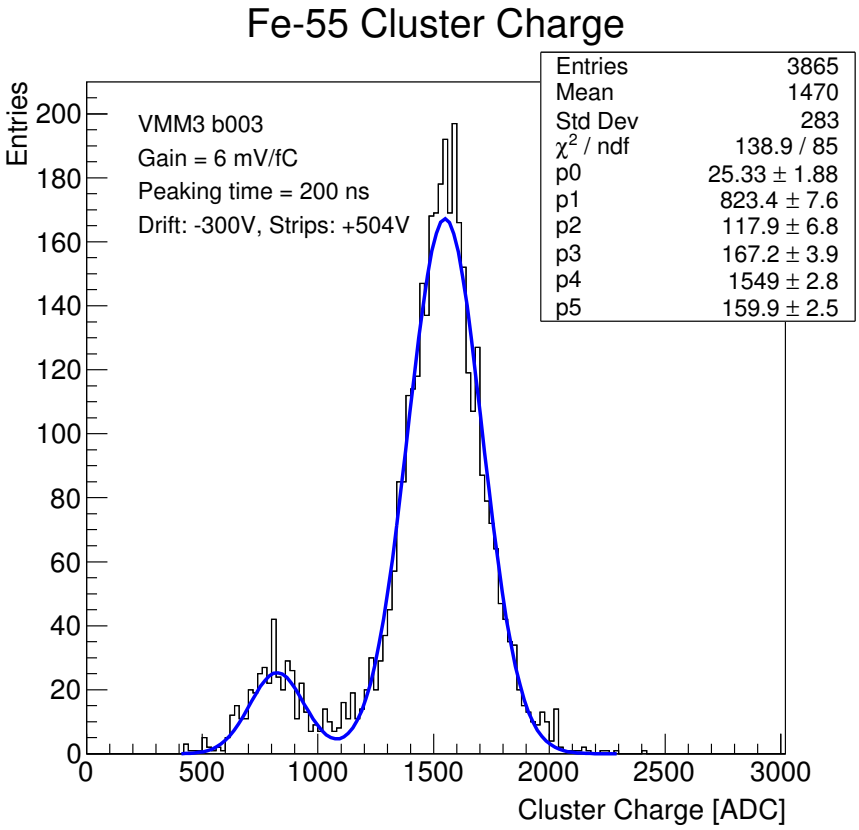

Figure A.8: ^{55}Fe cluster charge for events with 1 cluster and 3 or 4 strip hits per cluster. The primary photopeak at 5.9 keV is shown as the peak on the right. The characteristic Argon escape peak is shown as the small peak on the left.

Figure A.8 shows the cluster charge spectrum of the ^{55}Fe source taken over a period of 15 minutes for a single MMFE-8 attached to the chamber (as shown in figure A.4). Clusters are formed by identifying events with 3 or 4 adjacent strips with hits. The total cluster charge is summed from the charge on each strip in the cluster. Events included in the final spectrum have only one cluster per event. The primary peak is the characteristic 5.9 keV photopeak in the ^{55}Fe energy spectrum. The energy resolution for the MM chamber is calculated from using the σ on the photopeak Gaussian fit divided by the mean of the photopeak, and is around 10.3 $\pm$ 1.6 %. The smaller peak on the left of the primary is the Argon escape peak.

A.5 Conclusions

The phase of testing for the MMFE-8 demonstrator boards with measurements taken in 2017 is presented. These tests use the MMFE-8 version with VMM3 ASIC, FEAST power

supply design, and on-board FPGA for control and configuration. Testing and modification of the boards is on-going. There will be one more iteration of the MMFE-8 with FPGA as well as a first prototype of the MMFE-8 with ROC and SCA controller ASICs produced by the end of 2017. Several test beams are scheduled for 2018 in order to assess the capabilities of the boards on large scale MM chambers. Final production of all 4096 front-end boards is expected in late spring 2018. The Micromegas chamber production is finishing this year and preliminary tests with the prototype MMFE-8 boards are scheduled for mid-2018.

Acknowledgments

The authors would like to thank George Iakovidis, Theodoros Alexopoulos, Venetios Polychronakos, asnd the rest of the Omega Group at BNL (Brookhaven National Lab, NTU Athens) for their invaluable knowledge on the MM chamber and electronics as well as feedback on the ^{55}Fe measurements. We thank Gianluigi De Geronimo and his colleagues at Brookhaven National Lab for information on the VMM as well as the VMM intrinsic noise measurements. We thank Ryan Edgar and the team at the University of Michigan for the radiation and magnetic field measurements. We also thank the entire ATLAS Muon Collaboration for their on-going hard work on the NSW Upgrade project. This work is funded by the US Department of Energy grant number DE-SC0009913.

APPENDIX B
Further Studies with the Fakes Background

B.1 Closure Test

A closure test to validate the matrix method using the Likelihood Matrix Method and the efficiencies discussed in §7.1.3 is performed using the single lepton data and MC samples. The closure test uses both the real and fake efficiencies measured in separate control regions and applies the matrix method to one region. Therefore, this is more of a pseudo-closure test, since the real efficiencies are measured in a separate region. For the single lepton fakes estimate, the 2×2 matrix in equation 7.5 is used and the fakes are calculated on a bin-by-bin basis in the fake control region. The same parametrization variables are used for the single lepton fakes estimate as for the main analysis fakes estimate except the efficiencies are calculated for the low p_{T} trigger, which is prescaled, and the high p_{T} trigger separately. This is because in the main analysis, the prescaled trigger is not used (the dilepton triggers are used in the low p_{T} region and they are not prescaled).

Further studies into the parametrization variables for muons are discussed in §B.2.

Figures B.1 and B.2 show the single lepton p_{T}, $|\eta_{cl}|$ or $|\eta|$ for muons, and $\Delta R(\ell, \mathrm{jet})$ as well as the number of jets in the region. In general, the total background, including the fakes calculated from the single lepton likelihood Matrix Method, agrees well with the data. Some variables exhibit a slight discrepancy, such as for $M_{\mathrm{T}}^{\mathrm{W}}$ at higher values. However, this could be due to not using those variables as a parametrization in the Matrix Method. Due to the differences between these variables in single lepton and dilepton events, though, this should not pose a problem in the main analysis fake and non-prompt background estimation. Other discrepancies could be due to poor modeling of the MC samples, which in low statistics regions can affect the level of contamination from real leptons in the fake enriched control region. This issue should be accounted for in the *MC10* systematics described more in Chapter 8.

Systematic uncertainties are calculated for the fake control region for electrons and muons

to give an idea of the uncertainty on the fake/non-prompt yield in this closure test. For electrons, the systematic uncertainty on the fake yield is roughly 77%. For muons, the systematic uncertainty on the fake yield is roughly 66%. The total uncertainty would also include the MC uncertainties as well as the statistical uncertainty.

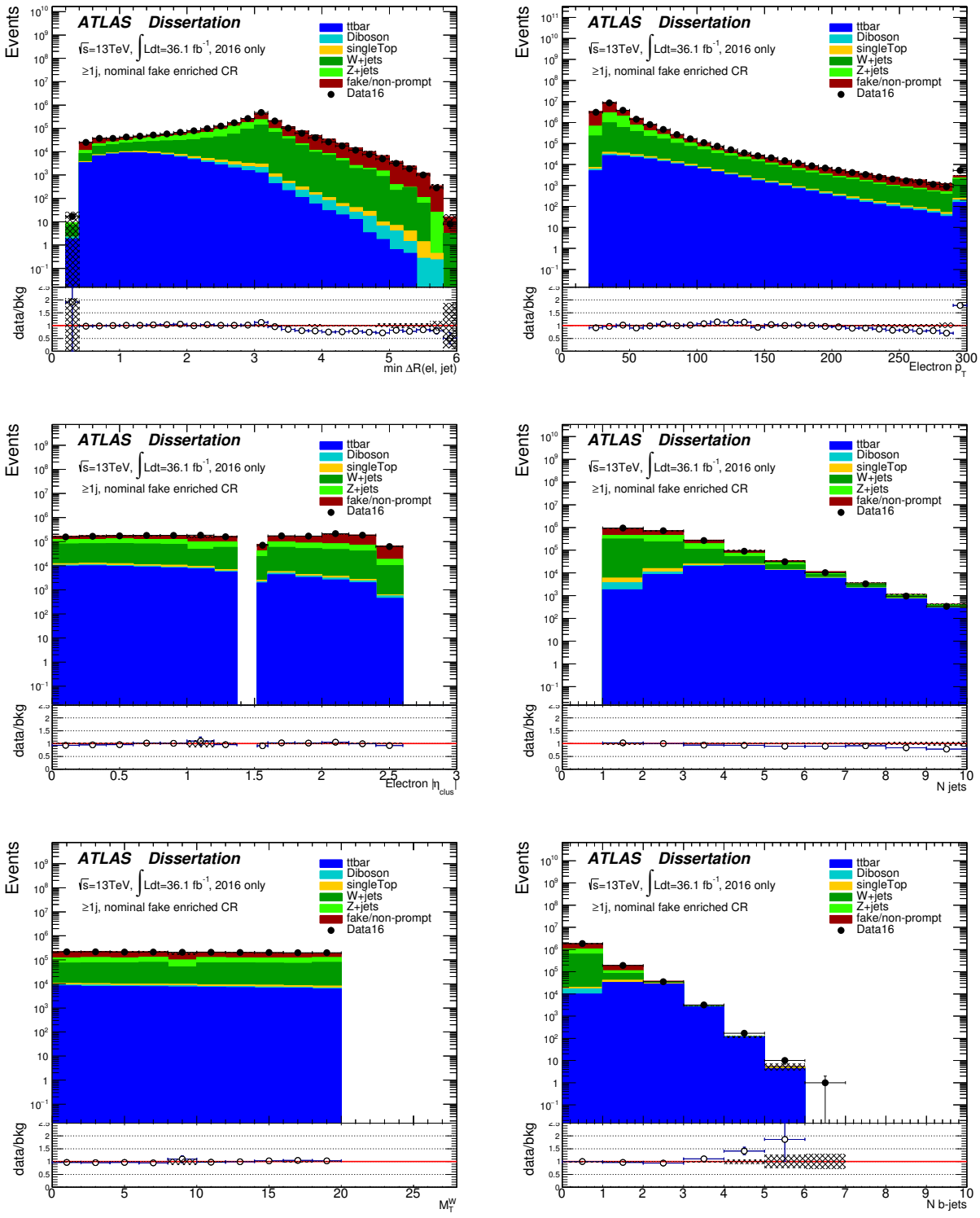

Figure B.1: Electron closure tests for the nominal fake control region ($M_{\mathrm{T}}^{\mathrm{W}} < 20$ GeV, $(E_{\mathrm{T}}^{\mathrm{miss}} + M_{\mathrm{T}}^{\mathrm{W}}) < 60$ GeV). The region includes $\geq$2 jets and inclusive b-tagged jets. From top to bottom and left to right, the first three plots are the parametrization variables used for electrons in the LHMM. The other three plots are N_{jet}, $M_{\mathrm{T}}^{\mathrm{W}}$, and $E_{\mathrm{T}}^{\mathrm{miss}}$.

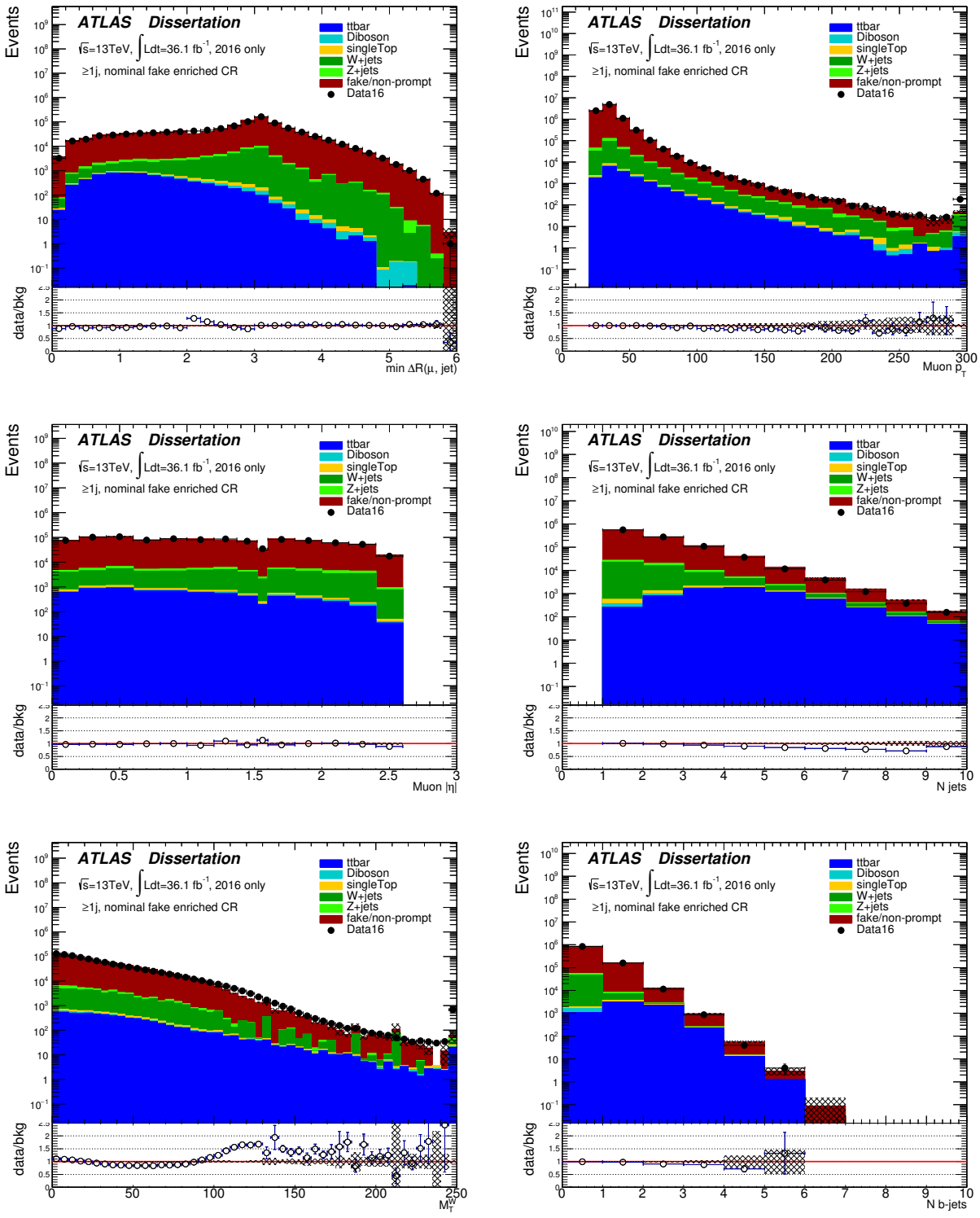

Figure B.2: Muon closure tests for the nominal fake control region ($|d_0^{\text{sig}}| > 5$). The region includes $\geq$2 jets and inclusive b-tagged jets. From top to bottom and left to right, the first three plots are the parametrization variables used for muons in the LHMM. The other three plots are N_{jet}, M_{T}^{W}, and $E_{\text{T}}^{\text{miss}}$.

B.2 Parametrization Variables

Parametrization of the real and fake efficiencies is done using the lepton properties p_{T}, η, and the ΔR between the lepton and the closest jet in the event. Other variables like $E_{\mathrm{T}}^{\mathrm{miss}}$ and $M_{\mathrm{T}}^{\mathrm{W}}$ are not used in the parametrization because those properties do not translate well between single lepton events and dilepton events (i.e. for the main analysis). For example, $E_{\mathrm{T}}^{\mathrm{miss}}$ is inherently different between events with one lepton and events with two or more leptons.

Some studies are performed on the parametrization variables used to determine if there are any correlations and to investigate the best parametrization for the leptons in the fakes background. If significant correlations between variables are found, then a 2D estimate of the real and fake efficiencies is calculated and could be used in the LHMM estimate. In the early version of this analysis with 3.2 fb^{-1} of data taken in 2015, it was determined that electron fake efficiencies had a correlation between the electron p_{T} and η_{cl}, as discussed in §7.1.3. For muons, there was a slight correlation found between the p_{T} and the ΔR variable. No significant correlation was found between muon p_{T} and η. A more thorough investigation of these parametrizations and their impact on the background estimate in the main analysis could be added for the next iteration of the analysis. Even small correlations could vary the estimate in some regions and could be added as a systematic.

Figure B.3 shows the 2D parametrization for muon p_{T} and η. Figure B.4 shows the 2D correlation between muon p_{T} and ΔR.

Jet and Muon Overlap Removal Another variable was defined for muons to investigate a small change in the definition of muons, which originated from a change in the overlap removal procedure during reconstruction. This affected muons that had a neighboring jet in the event, in close proximity to the muon's position, but the jet was removed during reconstruction due to not meeting the energy threshold or the track number requirements of the jet. The muons with this feature had to be tagged early in the reconstruction process to identify this, so a variable called `remOVRflag` was defined. The variable is true if the muon had a jet removed from its vicinity during reconstruction, meaning the muon is not as isolated as it appears in the final reconstructed definition. If `remOVRflag` is false, the muon is more isolated and did not have a neighboring jet removed.

This variable was studied in detail for this analysis, but it was decided that the estimation for the fake and non-prompt background did not require an extra parametrization of this variable because the control and validation regions showed a good level of agreement

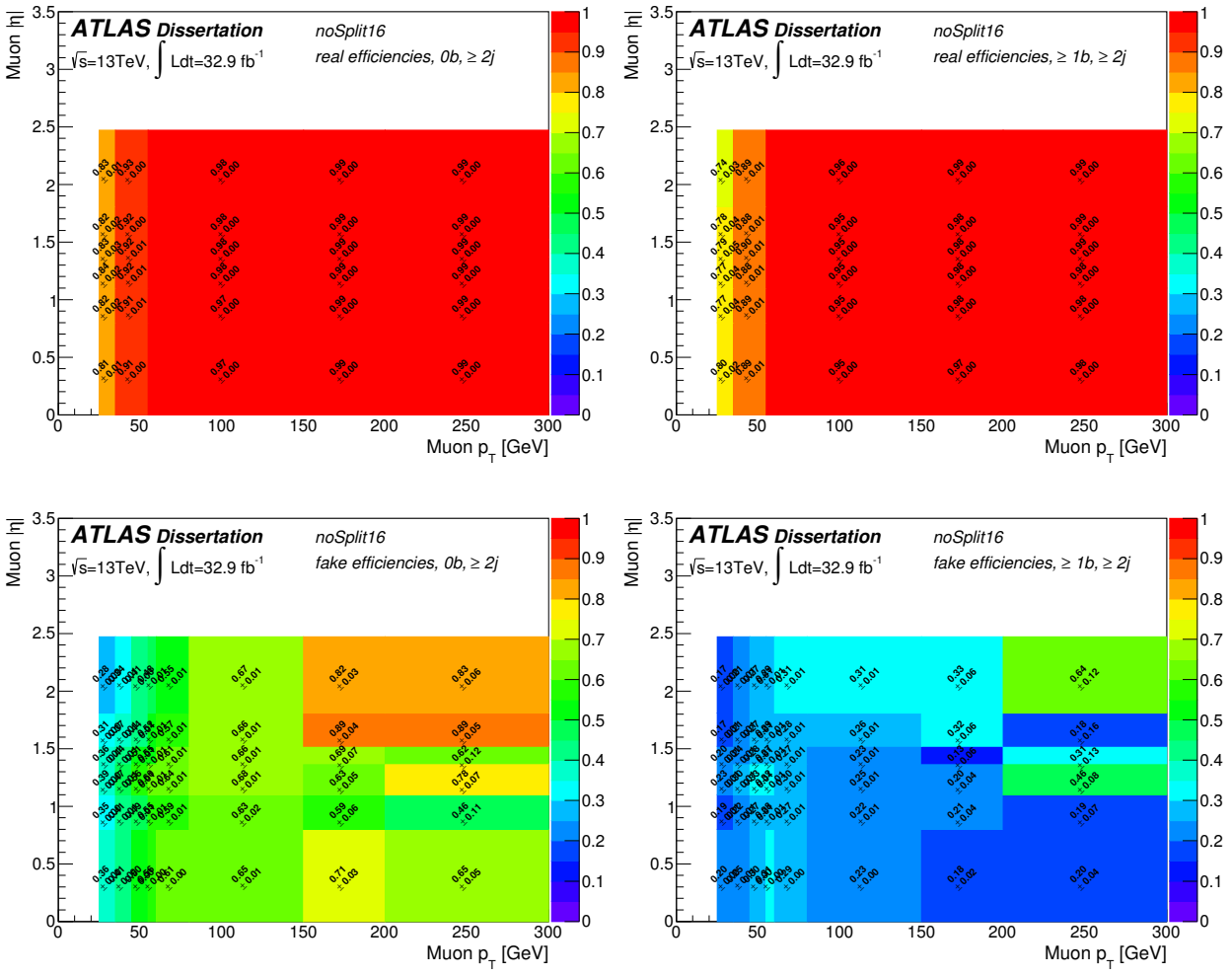

Figure B.3: Efficiencies for 2D parametrization between muon p_{T} and $|\eta|$. Only ≥ 2 jet efficiencies are shown, with 0 b-tagged jets (left) and ≥ 1 b-tagged jets (right). The top row shows the real efficiencies and the bottom row shows the fake efficiencies.

without distinguishing separate efficiencies based on this variable. However, if the same overlap removal procedure is used in the future, the next version of this analysis could investigate `remOVRflag` incorporated into the parametrization for the fakes. The muons where `remOVRflag` is true seem to account for the majority of the small correlations observed between the p_{T} and ΔR variables in figure B.4. Figure B.5 shows the `remOVRflag` variable for the normal criteria. Although the efficiencies between true and false appear very different, it should be noted that the muons where `remOVRflag` is true only constitute a small portion of the overall muons in the datasets used for the main analysis, on the order of $5-6\%$ (this is another reason why this was not included in the nominal parameterization

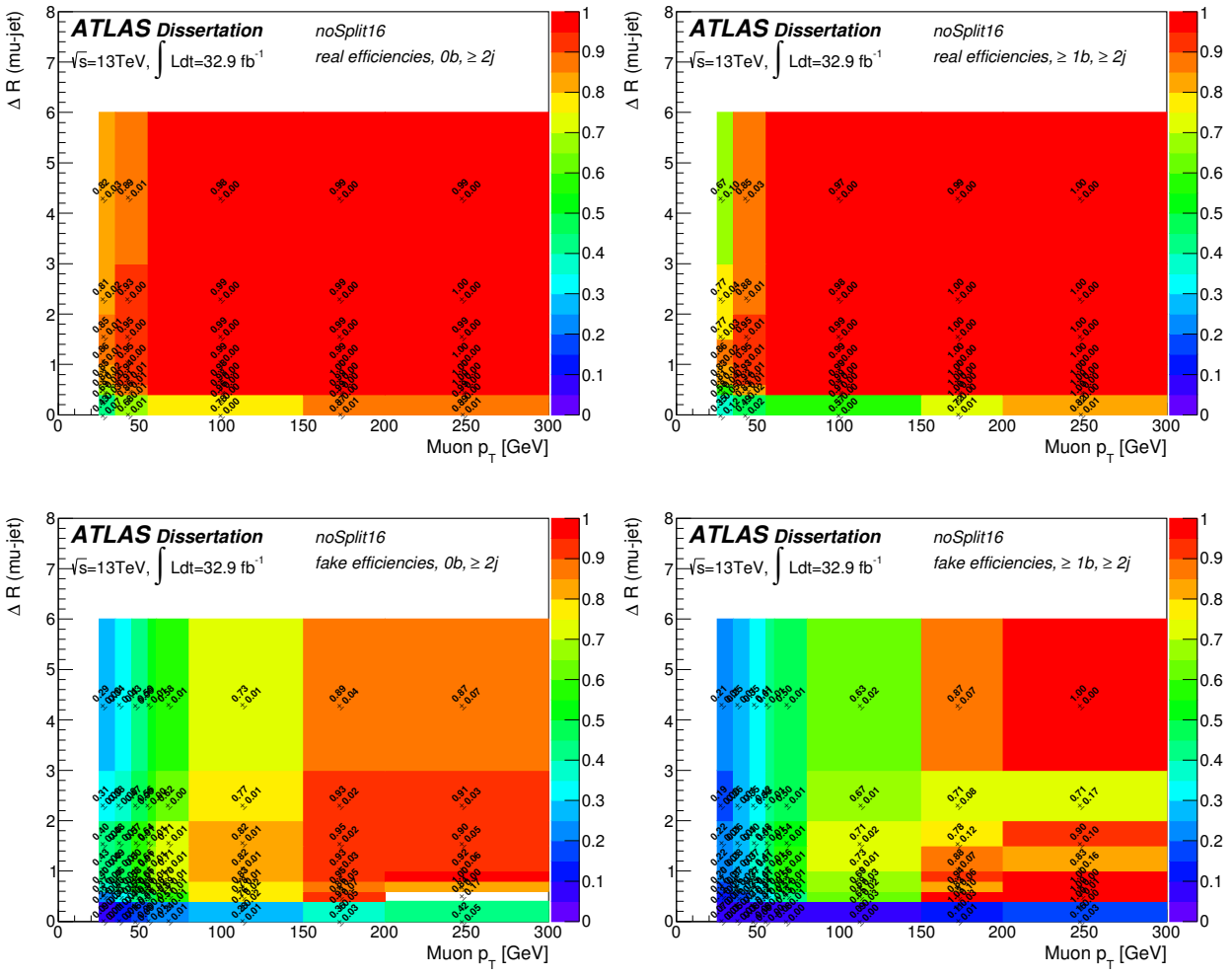

Figure B.4: Efficiencies for 2D parametrization between muon p_{T} and $\Delta R(\mu, \mathrm{jet})$. Only ≥ 2 jet efficiencies are shown, with 0 b-tagged jets (left) and ≥ 1 b-tagged jets (right). The top row shows the real efficiencies and the bottom row shows the fake efficiencies.

for fake muons).

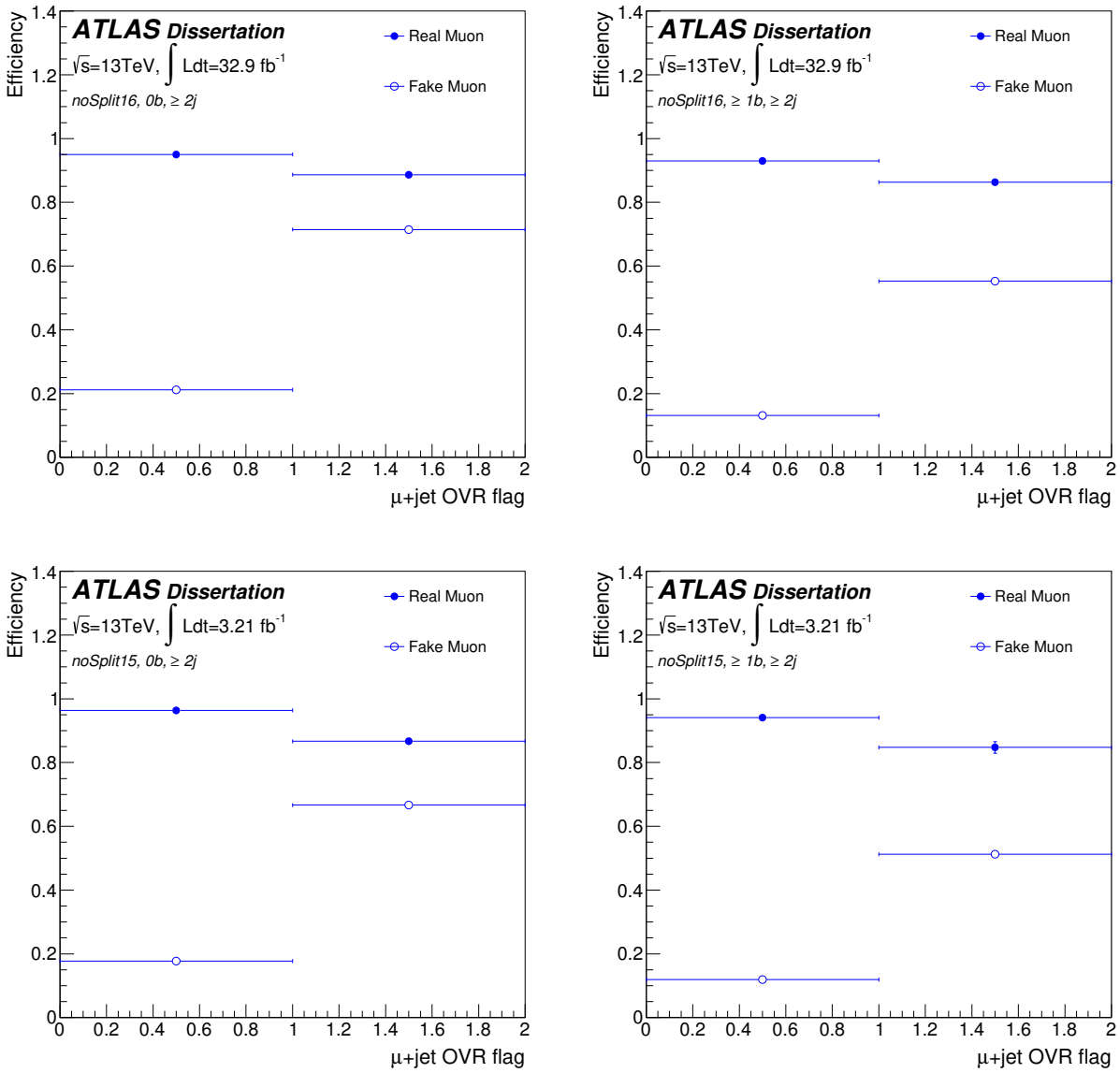

Figure B.5: Efficiencies using 2016 dataset (top row) and 2015 dataset (bottom row) for the variable `remOVRflag`. Efficiencies are separated by 0 b-tagged jets (left) and ≥ 1 b-tagged jets (right) like normal. Note the significant difference in efficiencies between false (first bin) and true (second bin) efficiencies. The change in real efficiency is because the muons with `remOVRflag` = true are less isolated than muons with `remOVRflag` = false. The significant change in the fake efficiencies could be due to the *appearance* of the fake muon passing the isolated criteria in the fake control region, but because these muons had a jet in close proximity during reconstruction, they pass the tight criteria with a greater efficiency.

B.3 Monte Carlo Studies

For the data-driven fake and non-prompt background, an estimation of the composition of fakes and the efficiencies calculated purely from MC was employed to understand the data-driven estimate in more detail. The simulation by itself does not provide a perfectly reliable estimate of this background, which is why the full background estimation used in the analysis is data-driven. However, the MC studies described here can provide some useful information on the composition of the fakes and the reliability of the calculated efficiencies used in the Likelihood Matrix Method.

MC truth is used to study the composition of the fakes and the efficiency calculation. Typically, $t\bar{t}$ or V+jets (where V is W or Z) samples are used because those constitute the majority of the real contamination in the fake enriched control regions. In the following, a $t\bar{t}$ sample (DSID: 410501) is used to study the truth information in order to compare expected efficiencies and study the fake control region in more detail.

Figures B.6 and B.7 show the composition of the fake and non-prompt sources for electrons and muons, respectively. These numbers are measured in the fake enriched control regions defined for electrons and muons (see definitions in tables 7.2).

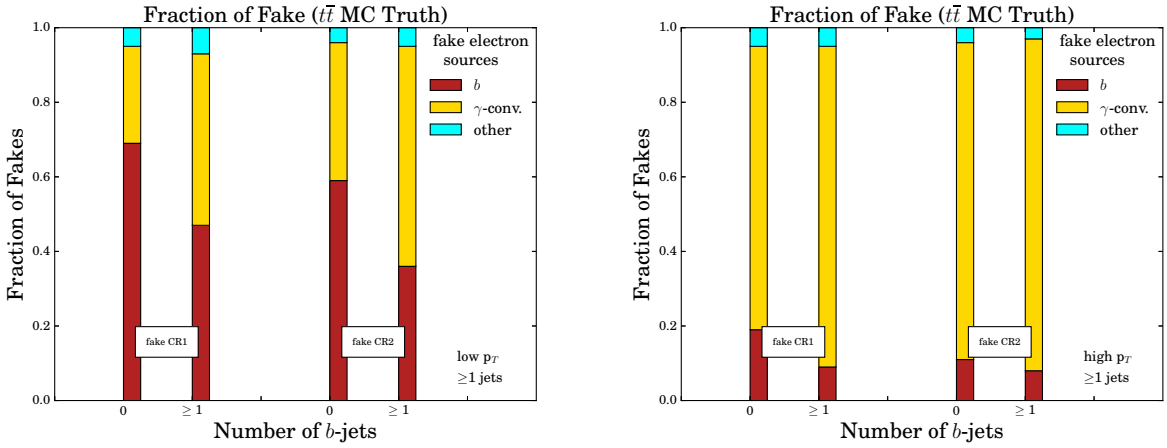

Figure B.6: Approximate fraction of electron fakes sources in the fake CR1 $(M_{\mathrm{T}}^{\mathrm{W}} < 20$ GeV) && $(E_{\mathrm{T}}^{\mathrm{miss}} + M_{\mathrm{T}}^{\mathrm{W}} < 60$ GeV) and CR2 $E_{\mathrm{T}}^{\mathrm{miss}} < 20$ GeV. Events passing the low p_{T} trigger are shown on the left, while events passing the high p_{T} trigger are shown on the right. Selection in fake CRs has additional veto on leptons originating from W, Z, τ, top, Higgs origins. The sample used to measure truth origins for the electrons is ttbar PowPy8 (410501).

Figures B.8 and B.9 show the fake efficiencies calculated from different sources by measuring the leptons that are identified as fake by the `MCTruthClassifier`, which then pass

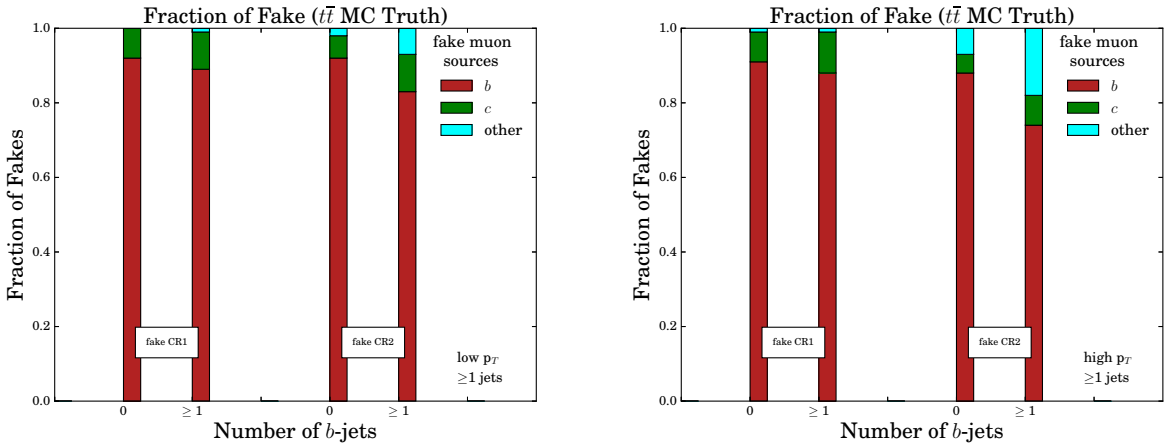

Figure B.7: Approximate fraction of muon fakes sources in the fake CR1 $|d_0^{sig}| > 5$ and CR2 $(M_{\mathrm{T}}^{\mathrm{W}} < 20)\&\&(E_{\mathrm{T}}^{\mathrm{miss}} + M_{\mathrm{T}}^{\mathrm{W}} < 60$ GeV). Events passing the low p_{T} trigger are shown on the left, while events passing the high p_{T} trigger are shown on the right. Selection in fake CRs has additional veto on leptons originating from W, Z, τ, top, Higgs origins. The sample used to measure truth origins for the electrons is ttbar PowPy8 (410501).

the normal tight criteria. Fake leptons in `MCTruthClassifier` are identified if their *truth origin* does not emanate from W, Z, τ, t, or Higgs sources, which are all sources that produce real leptons, or additionally in the case of electrons only, from photon conversion. Note that for electrons, photon conversion is separated in this study because electrons from photon conversion are *real* electrons, but they are classified as non-prompt so this truth study does not account for that fraction of the fake and non-prompt background.

The fake leptons are separated by their truth origin by all sources of fakes, which includes b-tagged jets, c-tagged jets, light-flavored jets, and other sources. Both electron and muon fake origins are, in general, dominated by b and c sources, which includes b-mesons and b-flavored baryons and c-mesons and c-flavored baryons. Other identifiable sources of fake leptons include light flavored mesons, pion and kaon decays, and initial or final state radiation. A significant portion of the other sources is dominated by the truth identification *unknown* sources, which poses a limit on the usefulness of the MC samples in investigating the sources of fake leptons. Figures B.10 through B.13 show the electron and muon composition of fakes, as a function of different variables, identified in the same $t\bar{t}$ sample using the `MCTruthClassifier`. The composition plots are separated by *loose* and *tight* criteria to show the difference in composition as the *tight* selection is applied to the lepton. A significant drawback to this study is the fact that the *unknown* sources from the `MCTruthClassifier` dominate the tight criteria in some regions.

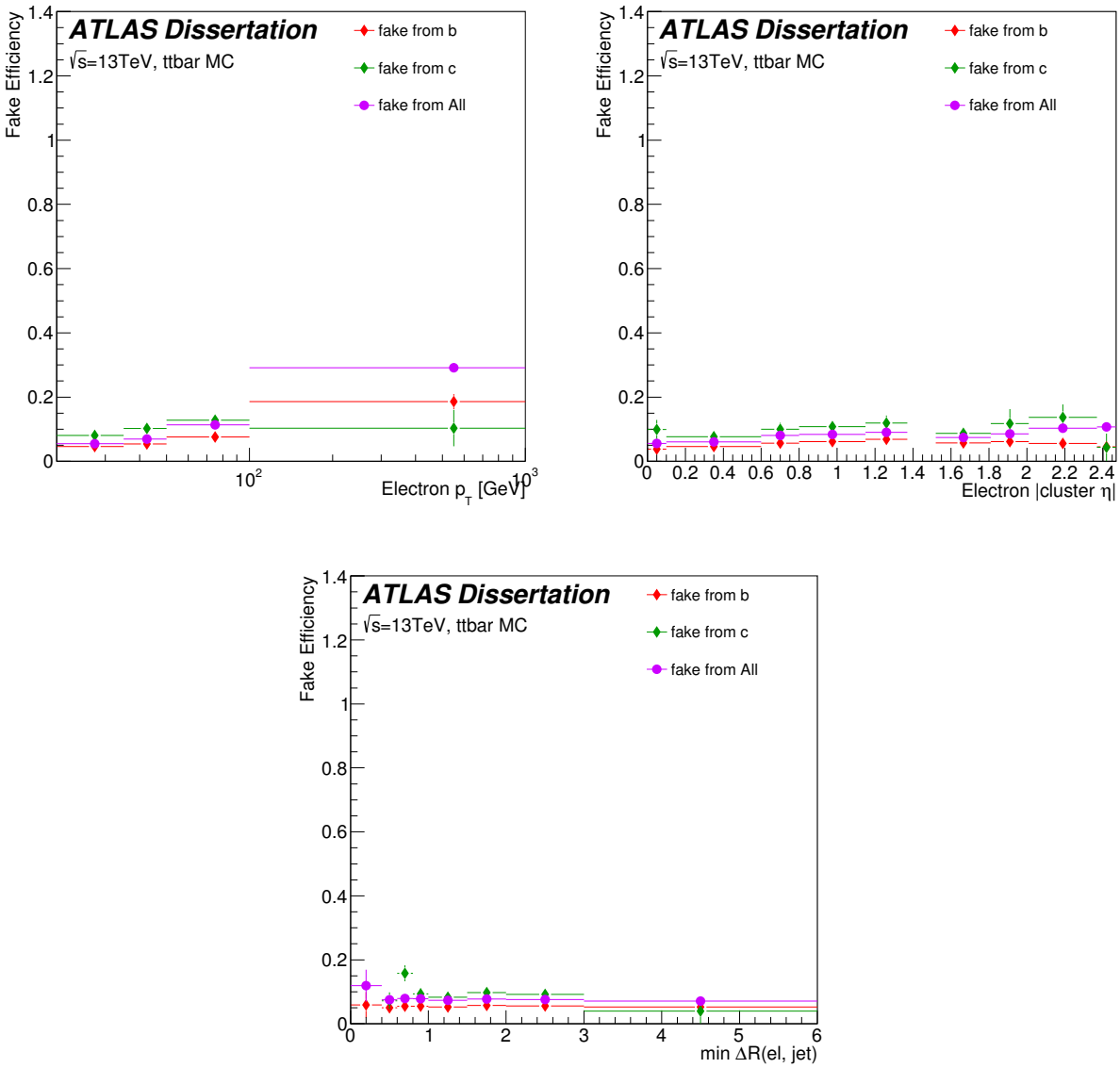

Figure B.8: Efficiencies for electrons using MC truth information in a $t\bar{t}$ sample (DSID: 410501). The efficiencies are calculated in the normal manner (N_{tight}/N_{loose}, see §7.1) except that the number of electrons is selected from MC truth information, not measured in a fake enriched control region.

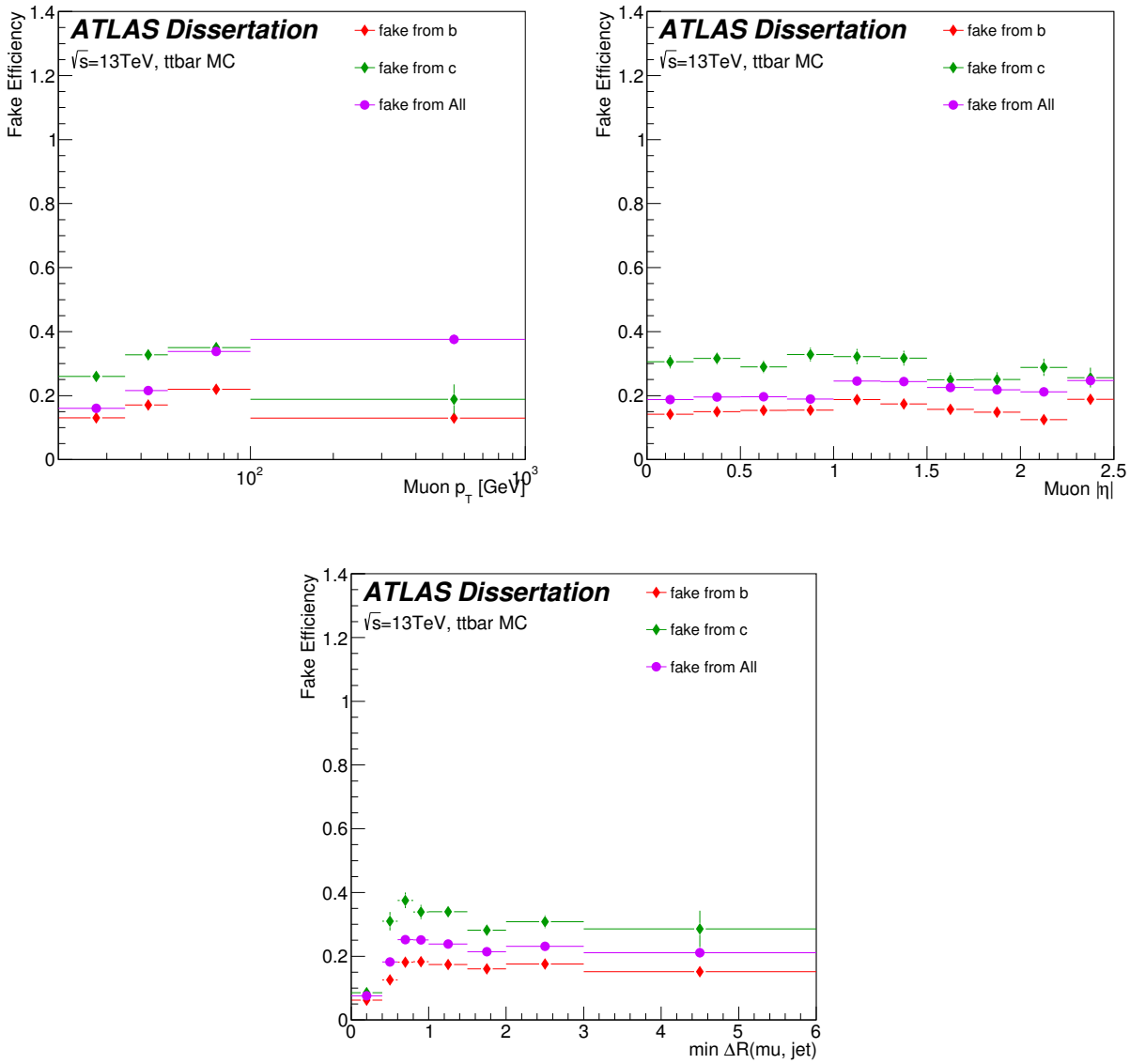

Figure B.9: Efficiencies for muons using MC truth information in a $t\bar{t}$ sample (DSID: 410501). The efficiencies are calculated in the normal manner (N_{tight}/N_{loose}, see §7.1) except that the number of muons is selected from MC truth information, not measured in a fake enriched control region.

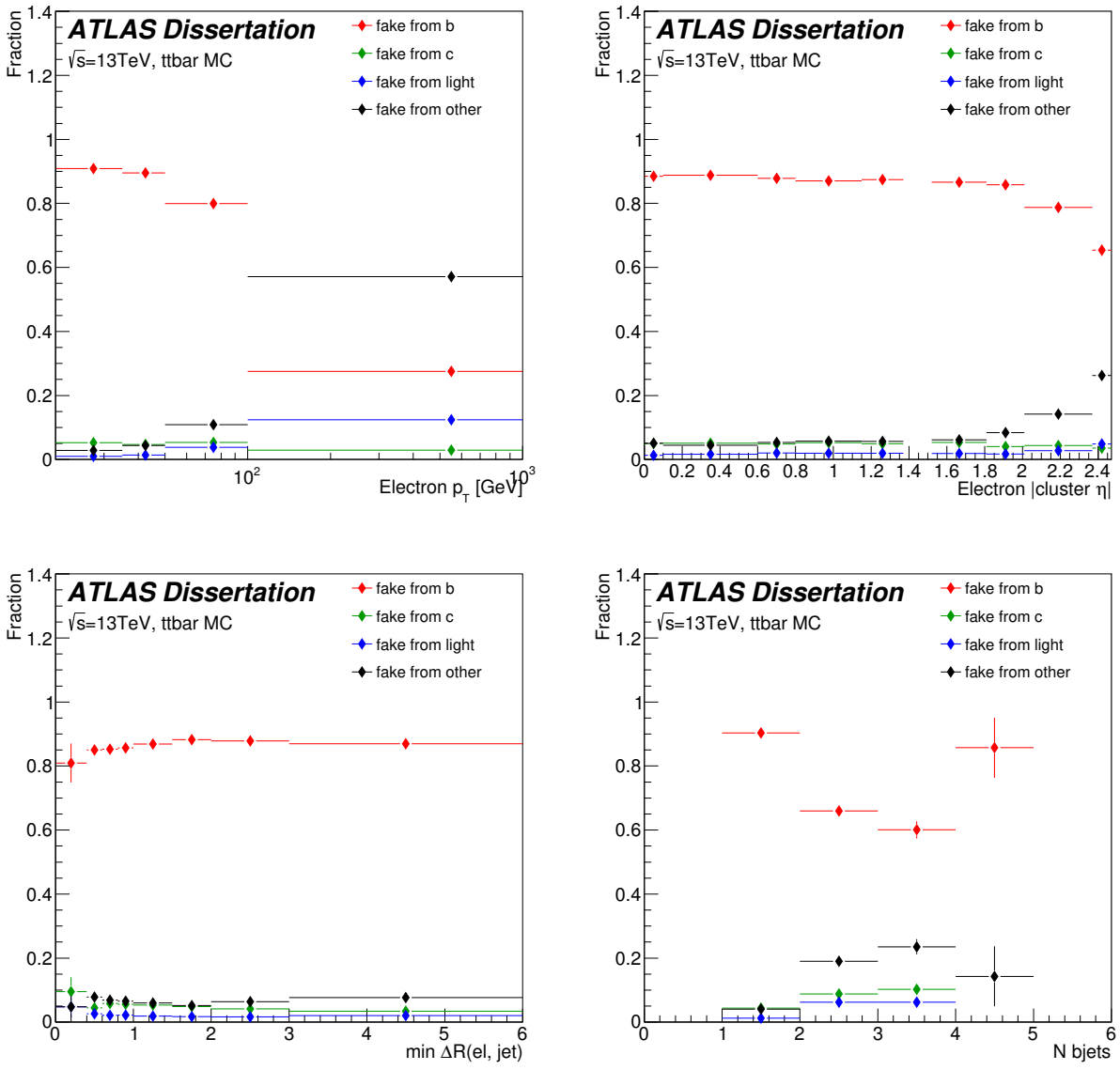

Figure B.10: Fraction of fake electron composition in the loose selection using MC truth information in a $t\bar{t}$ sample (DSID: 410501). Composition is determined by calculating the total number of fakes in the loose sample (from the truth criteria) and then dividing the number in each source category: b, c, light-flavored, and other.

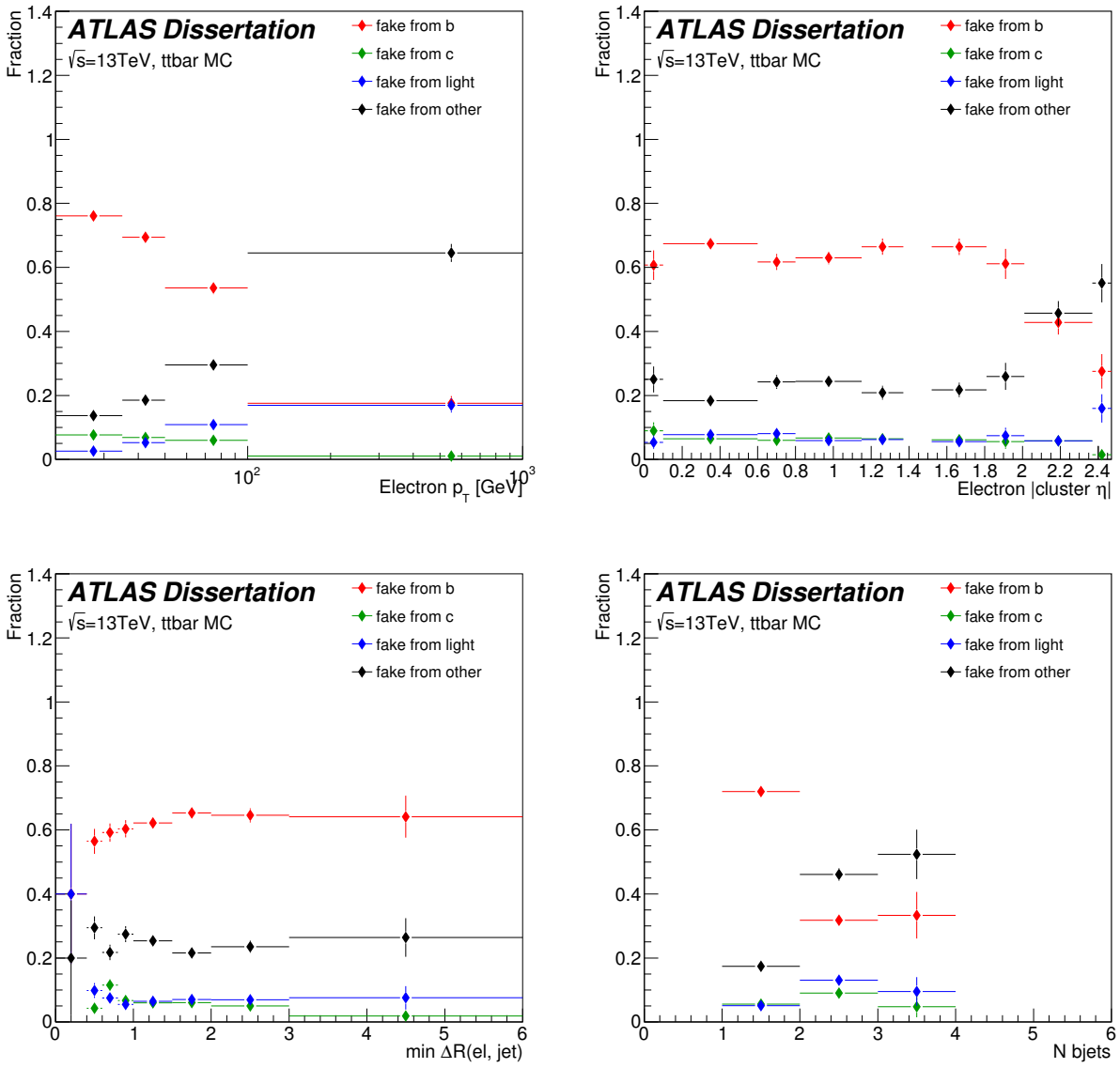

Figure B.11: Fraction of fake electron composition in the tight selection using MC truth information in a $t\bar{t}$ sample (DSID: 410501). Composition is determined by calculating the total number of fakes in the tight sample (from the truth criteria) and then dividing the number in each source category: b, c, light-flavored, and other.

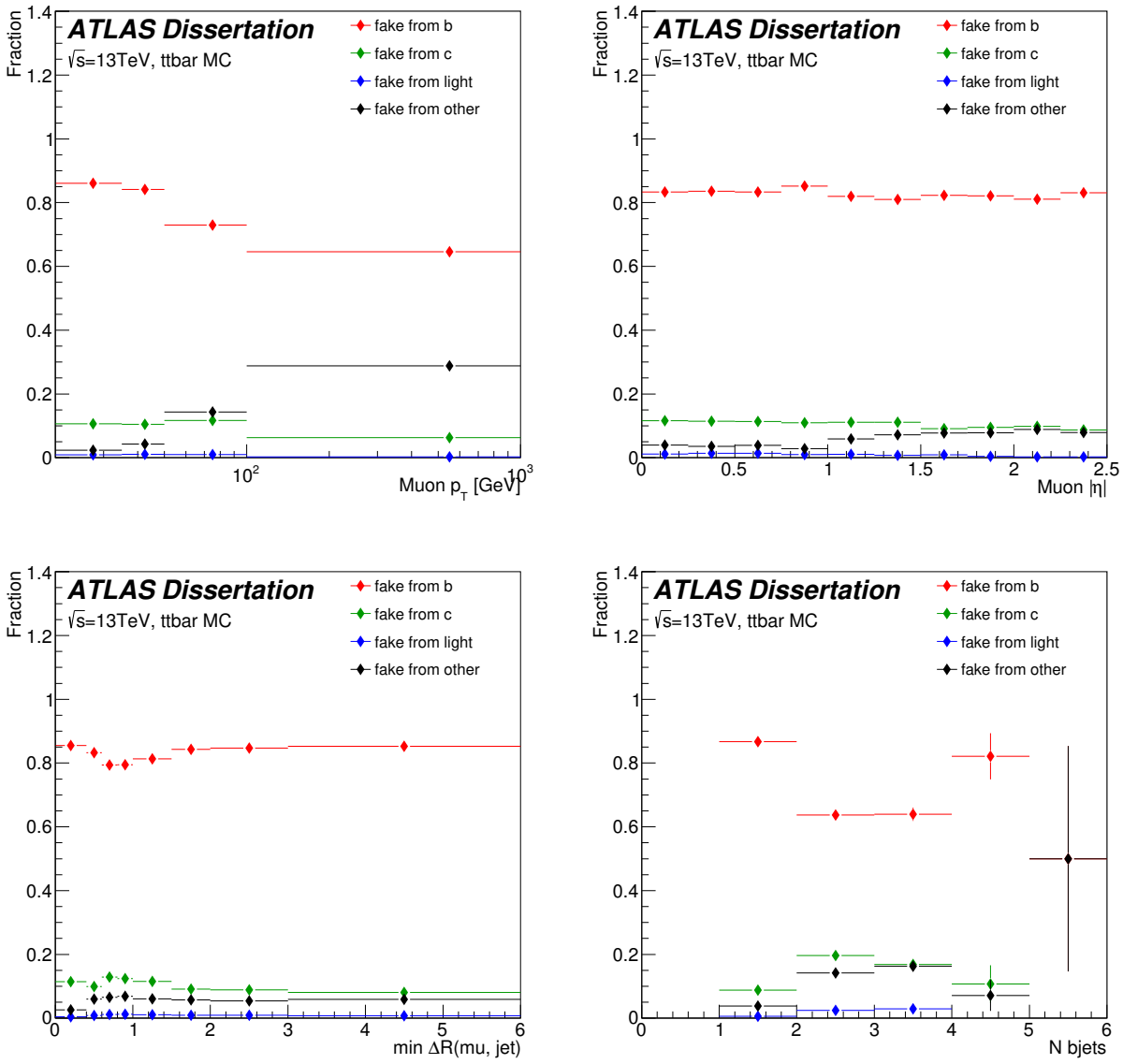

Figure B.12: Fraction of fake muon composition in the loose selection using MC truth information in a $t\bar{t}$ sample (DSID: 410501). Composition is determined by calculating the total number of fakes in the loose sample (from the truth criteria) and then dividing the number in each source category: b, c, light-flavored, and other.

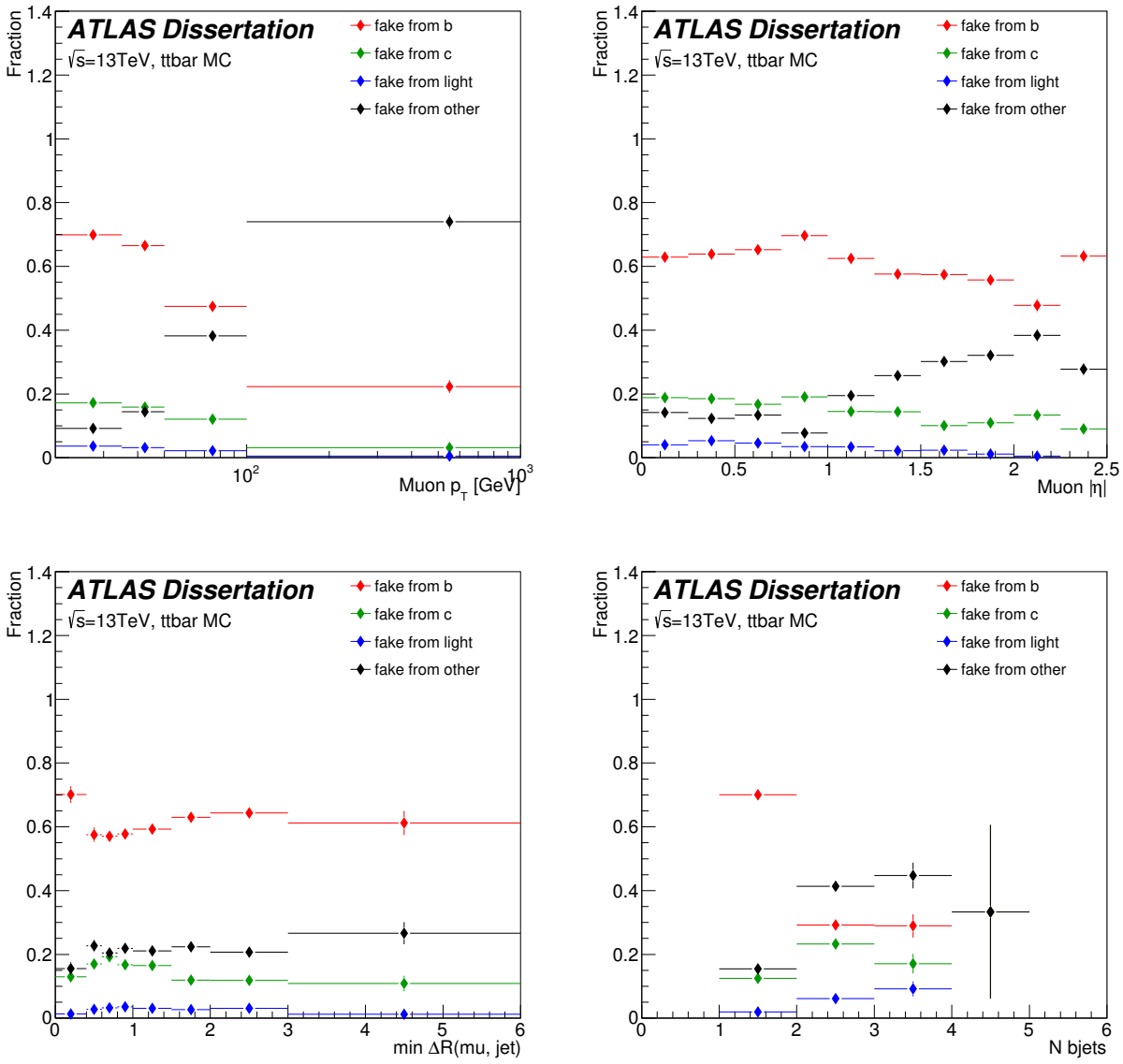

Figure B.13: Fraction of fake muon composition in the tight selection using MC truth information in a $t\bar{t}$ sample (DSID: 410501). Composition is determined by calculating the total number of fakes in the tight sample (from the truth criteria) and then dividing the number in each source category: b, c, light-flavored, and other.

B.4 Trigger Strategies

In earlier versions of this analysis, a trigger strategy that took advantage of isolated triggers was employed. The advantage of this strategy is the use of isolated triggers, which in this case require isolation at the High Level Trigger (HLT) level on the lepton firing the trigger. Isolation increases the trigger efficiency and serves to improve the quality of the efficiencies calculated for the matrix method. This appendix describes how the trigger strategy was employed using these triggers in the Matrix Method for the fake and non-prompt lepton background.

Efficiencies are calculated separately for the isolated trigger and the non-isolated trigger(s). The reason they cannot be combined into one set of efficiencies is because the isolated trigger biases the events due to lepton quality. The use of isolated triggers makes the application of the Matrix Method efficiencies more complex. It is not always appropriate to apply the isolated trigger to a lepton that fired the `HLT_e26_lhtight_nod0_ivarloose`, or `HLT_mu26_ivarmedium`, trigger since there could be more than one lepton in the event that fired the trigger. If that is the case, applying the associated biased efficiencies to multiple leptons in the same event would introduce an isolation-based overestimation of fakes resulting from the larger fake efficiencies. Therefore, separate efficiencies are calculated for the isolated triggers and for the low p_{T} prescaled triggers (unbiased by isolation). In events where multiple leptons fire the low p_{T} isolated trigger, only one lepton is assigned the associated efficiencies. The other lepton(s) is assigned the prescaled trigger efficiencies, as per the lowest ϕ determination, as shown in the decision flowchart in Figure B.14. The use of the ϕ variable is just to randomly assign the unbiased trigger to one of the leptons that fired the isolated trigger.

The decision was made in the Run II analysis with 36.1 $\mathrm{fb}^{-1}$to move to non-isolated triggers only in the main analysis, making the isolated efficiencies unnecessary. This greatly simplifies the application of the efficiencies during the Matrix Method, as described in §7.1, and allows for a single set of efficiencies to be applied by combining the low p_{T} and high p_{T} trigger efficiencies since neither are biased by isolation.

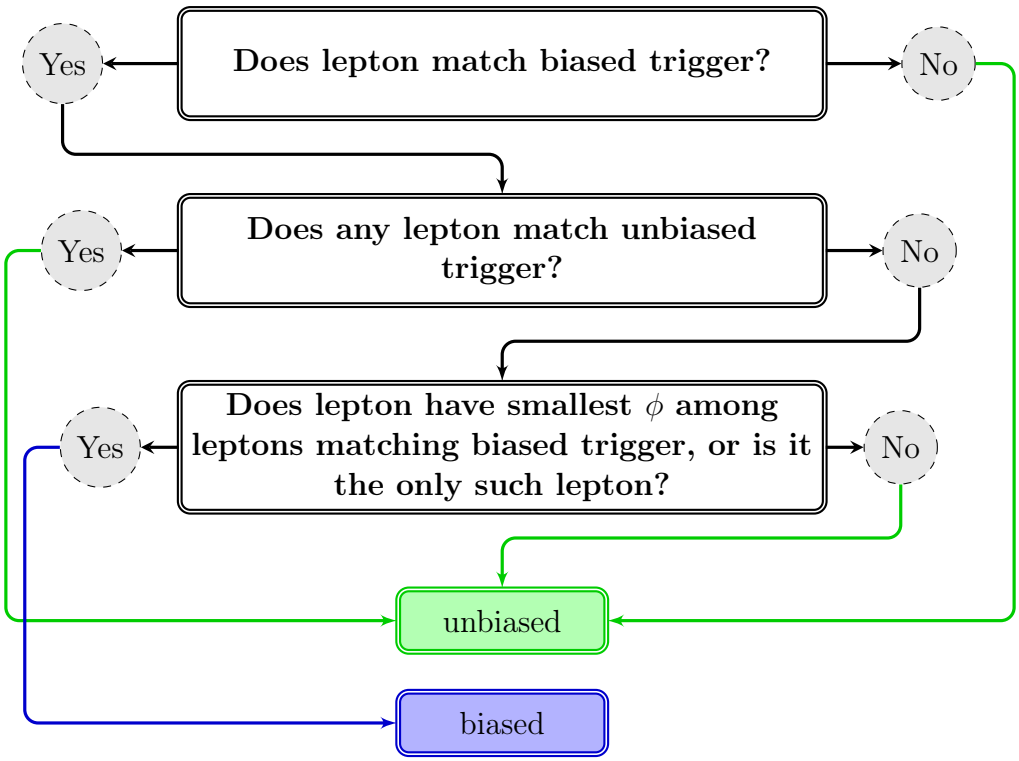

Figure B.14: Trigger decision flowchart for fake/non-prompt lepton background. The green arrows lead to applying the unbiased trigger to the lepton, while the blue leads to applying the biased trigger. The trigger decision is made for each lepton in the event such that only one lepton is applied the biased trigger if there is at least one lepton in the event that fired that trigger.

B.5 Studies with b-tagged jets

Given the modest excess in the signal regions that require at least 3 b-tagged jets, the possibility of parametrization the fakes with a more precise dependance on b-tagged jets was explored. This was actually studied before unblinding because some minor discrepancies were observed in regions with higher number of b-tagged jets. Due to the relatively limited statistics in the fake enriched control regions for both electrons and muons, the resulting efficiencies were not trusted to accurately predict the fakes in this region, however. Therefore, the normal delineation of efficiencies into 0 b-jets and ≥ 1 b-jets was employed.

Figures B.15 and B.16 show the fake efficiencies broken up by b-tagged jet multiplicity for electrons and muons, respectively. The statistics are very limited in the fake enriched control region with 3 b-tagged jets or more, as can be seen by the large statistical errors and the fluctuations. For electrons especially, this means that the fake efficiencies appear higher than they would otherwise be due to large subtraction of the real contamination from MC. The high fake efficiency in this case would lead to a higher estimation of the fake/non-prompt background in regions with ≥ 3 b-jets. This was tested early on (pre-unblinding) in the control region and led to agreement in the 3 b-jet bin. However, because the statistics are so low, the fake efficiencies for this case are unreliable and therefore the 'agreement' in the 3 b-jet bin is probably artificial. Hence, the normal parametrization of efficiencies with 0 b-jets and ≥ 1 b-jets is used. Further studies should be performed in the future to explore this b-jet multiplicity dependance in more detail once more data are collected.

B.5.1 Fakes Estimation with 0 b-tag Efficiencies

Given the obvious differences between the 0 b-tag efficiencies and the efficiencies calculated from events with ≥ 1 b-tag, there may be some concern that the fakes estimate in the signal regions is biased low. To investigate this, a test was performed where the fakes in the signal regions were calculated with the normal likelihood Matrix Method, except applying the 0 b-tag efficiencies only, instead of applying the normal efficiencies, which due to the b-tag requirements in the signal regions effectively means the ≥ 1 b-tag efficiencies. Then, we applied the 0 b-tag efficiencies to just the SS$\mu\mu$ events in the dilepton signal regions. The latter is done because the majority of the excess was observed to come from the SS$\mu\mu$ channel, and the 0 b-tag efficiencies for muons show a larger difference (especially in p_{T}).

Table B.1 shows the fakes yields from applying the 0 b-tag efficiencies. For easy comparison, the fakes yields from each signal region using the normal efficiencies is shown as

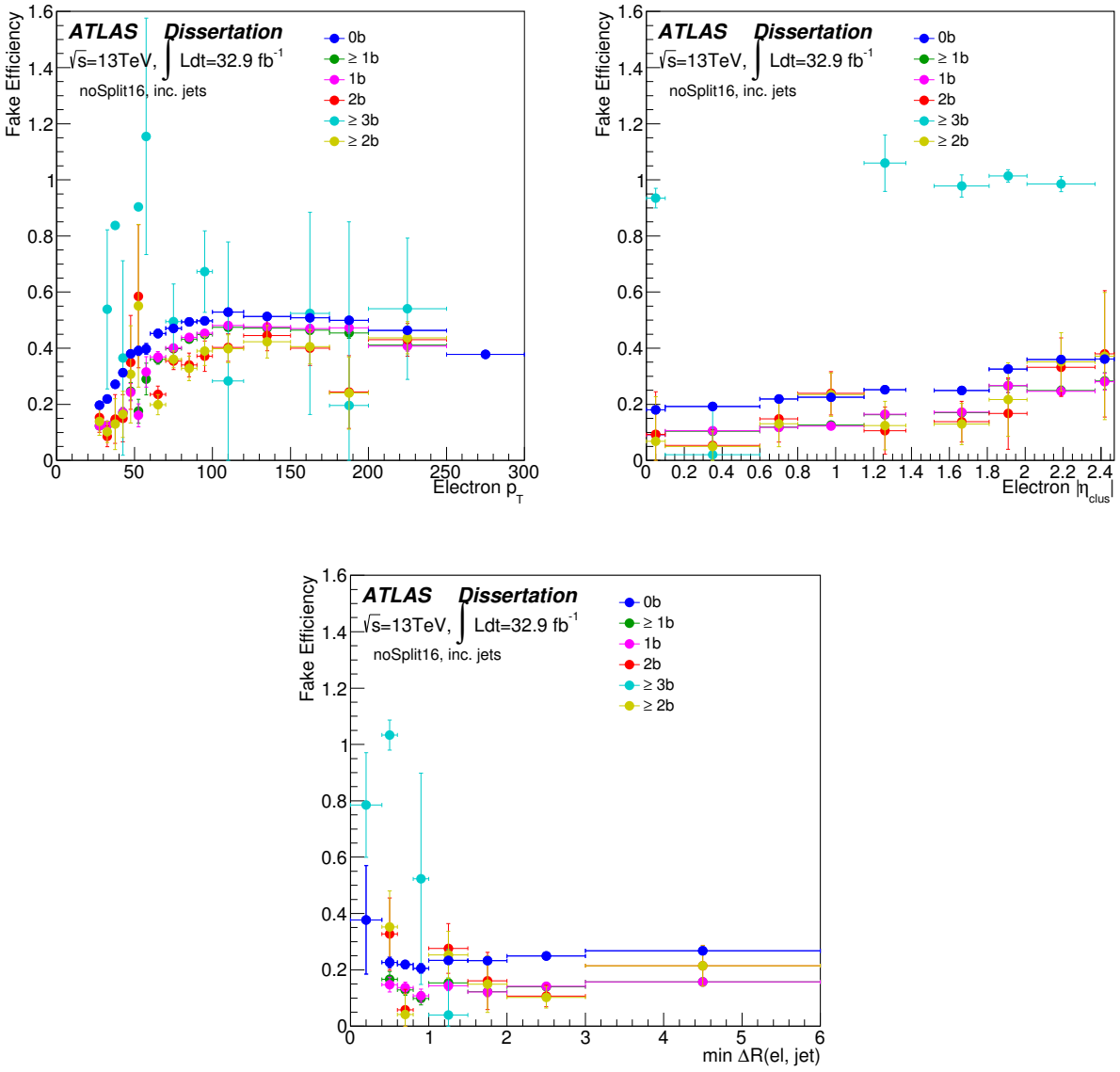

Figure B.15: Fake efficiencies for electrons separated by b-tagged jet multiplicity. Note that only 1D parametrizations are shown here and p_{T} and $|\eta_{\mathrm{cl}}|$ are separated. The largest difference is clearly between the 0 b-jet and ≥ 1 b-jet efficiencies, which is the normal separation of efficiencies in this analysis with respect to b-jets. Here the number of jets in the events is inclusive, so the full spectrum of b-tagged jets can be explored without setting constraints on the total number of jets.

well. From this information, it is observed that the fake yields are very close and within statistical uncertainties. This suggests the fakes estimate is stable and there doesn't appear to be a deficit of fakes anywhere, especially for the loose H_{T} regions where the excess is most prominent.

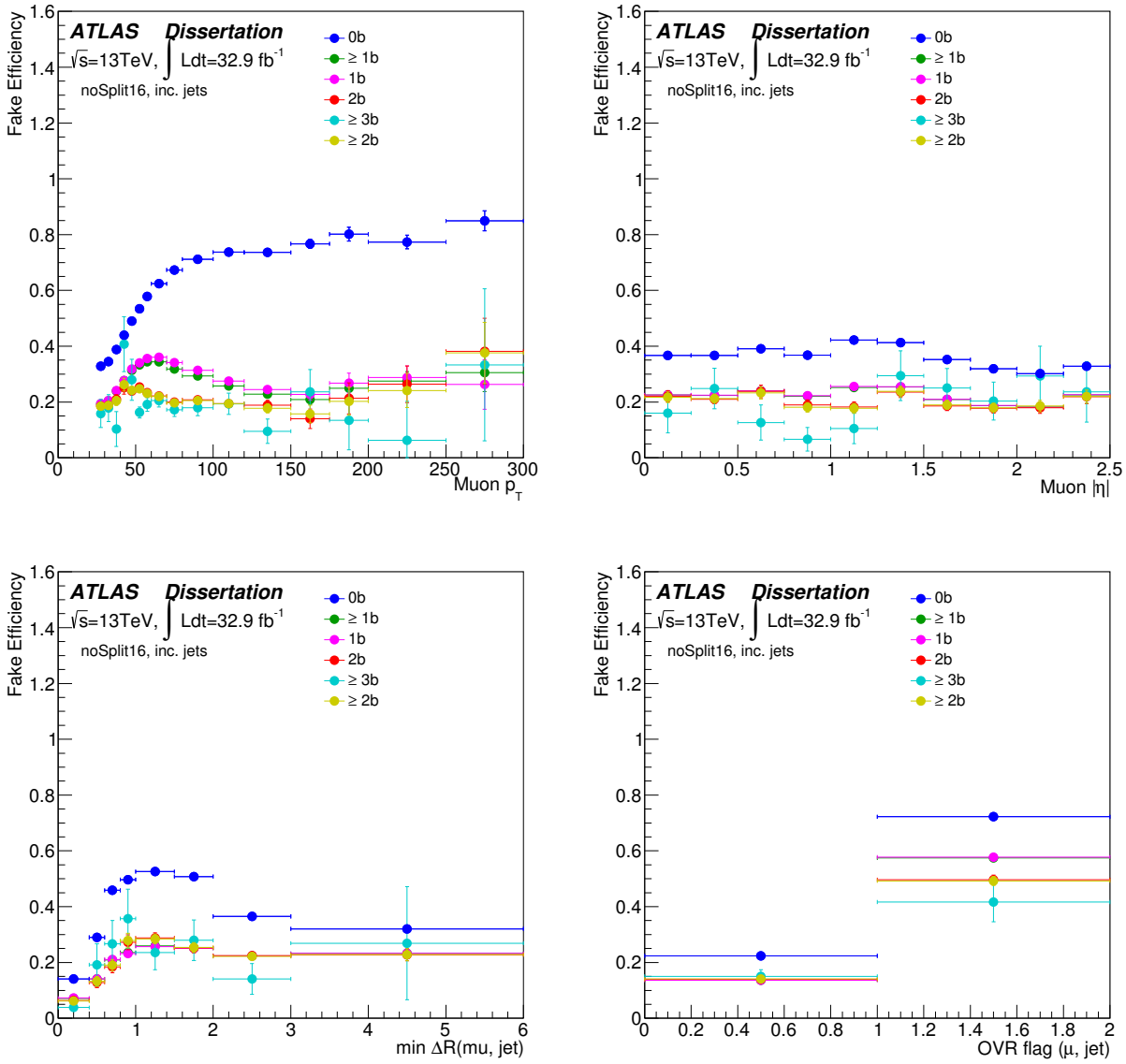

Figure B.16: Fake efficiencies for muons separated by b-tagged jet multiplicity. The largest difference is clearly between the 0 b-jet and ≥ 1 b-jet efficiencies, which is the normal separation of efficiencies in this analysis with respect to b-jets. Here the number of jets in the events is inclusive, so the full spectrum of b-tagged jets can be explored without setting constraints on the total number of jets.

However, without an obvious reason for why the 0 b-tag efficiencies are much higher than the ≥ 1 b-tag efficiencies, they may not be trustworthy. It is therefore probably not prudent to use these efficiencies for a more 'conservative' estimate of the fakes in the signal regions. To prove this, the fakes estimate in the validation regions using the 0 b-tag efficiencies was also tested. Table B.3 shows a comparison of the normal fakes yields using the normal (≥ 1

b-tag) efficiencies and the 0 b-tag only efficiencies. The results in these regions show a gross overestimation of the fakes yields in all regions, which would yield an overestimation of the total background in these regions.

Signal region	≥ 1 b-tag efficiencies	0 b-tag efficiencies
SR1b2l	4.1 ± 3.0	$8.14^{+3.29}_{-3.24}$
SR2b2l	2.5 ± 1.5	$6.26^{+2.49}_{-2.36}$
SR3b2l_L	1.2 ± 1.2	$2.47^{+2.25}_{-1.64}$
SR3b2l	0.2 ± 0.5	$0.09^{+1.02}_{-0.09}$
SR1b3l	1.0 ± 0.8	$2.03^{+1.52}_{-1.08}$
SR2b3l	0.1 ± 0.3	$0.2^{+0.63}_{-0.2}$
SR3b3l_L	0.0 ± 0.3	$0.0^{+0.74}_{-0.0}$
SR3b3l	0.03 ± 0.02	$0.13^{+0.45}_{-0.1}$
SRSStops	6.4 ± 1.7	$10.23^{+3.59}_{-3.77}$

Table B.1: Fakes estimate in the signal regions using the likelihood Matrix Method where only 0 b-tag efficiencies (right column) are applied and for ≥ 1 b-tag efficiencies, which are the normal ones used in these regions (left column). For the normal fake yields, the total uncertainty is shown. For the 0 b-tag efficiencies, only statistical uncertainties are shown. The statistical uncertainties are asymmetric and result from the likelihood MM fit.

Signal region	≥ 1 b-tag efficiencies	0 b-tag efficiencies
SR1b2l	$0.25^{+0.32}_{-0.22}$	$0.9^{+0.88}_{-0.66}$
SR2b2l	$0.28^{+0.31}_{-0.23}$	$1.3^{+1.42}_{-0.88}$
SR3b2l_L	$0.13^{+0.32}_{-0.13}$	$0.42^{+0.88}_{-0.42}$
SR3b2l	$0.09^{+0.16}_{-0.09}$	$0.51^{+0.68}_{-0.46}$
SRSStops	$0.2^{+0.24}_{-0.2}$	$0.93^{+0.65}_{-0.52}$

Table B.2: Fakes estimate, in the SSmm channel only, using the likelihood Matrix Method where only 0 b-tag efficiencies (right column) are applied and for ≥ 1 b-tag efficiencies, which are the normal ones used in these regions (left column). Note: for this test, only asymmetric statistical uncertainties from the likelihood MM fit are shown.

Signal region	≥ 1 b-tag efficiencies	0 b-tag efficiencies
VR1b2l	$169.63^{+7.85}_{-7.7}$	$321.8^{+14.95}_{-14.64}$
VR2b2l	$53.35^{+4.53}_{-4.4}$	$89.16^{+10.16}_{-9.81}$
VR3b2l	$7.76^{+1.55}_{-1.43}$	$17.01^{+3.79}_{-3.5}$
VR1b3l	$21.86^{+3.91}_{-3.37}$	$35.92^{+7.17}_{-7.44}$
VR2b3l	$2.7^{+1.48}_{-1.29}$	$1.0^{+4.97}_{-0.61}$
VR3b3l	$0.21^{+0.31}_{-0.18}$	$0.32^{+1.0}_{-0.29}$

Table B.3: Fakes estimate in the validation regions using the likelihood Matrix Method where only 0 b-tag efficiencies (right column) are applied and for ≥ 1 b-tag efficiencies, which are the normal ones used in these regions (left column). Note: for this test, only asymmetric statistical uncertainties from the likelihood MM fit are shown.

APPENDIX C
Further Checks for Excess in Signal Regions

C.1 Monte Carlo Studies with $t\bar{t}b\bar{b}$

A MC $t\bar{t}b\bar{b}$ sample (DSID: 410051, `Sherpa`) was used to study the fake background in more detail, especially with respect to the number of b-jets. Table C.1 shows the number of events in the loose and tight samples for different number of b-jets in the events. The additional selection applied is the MC truth for identifying the origin of the muons (using `MCTruthClassifier`). Muons from b sources must have origin classifier 26, 29, or 33. Muons from c sources must have origin classifier 25, 27, or 32. All sources of fake muons would be any muon that does not originate from top (origin classifier 10), τ-leptons (origin classifier 9), W/Z bosons (origin classifier 12/13), or Higgs (origin classifier 14). Figure C.1 shows the efficiencies derived from all, b, and c fakes sources. Since b dominates the samples, the b source efficiencies are very close to the efficiencies from all sources. Figure C.2 shows the fraction of fakes from b, c, or other sources (which means all fake sources other than b or c) in each b-jet category.

N b-tags	fakes from b		fakes from c		all sources	
	loose	tight	loose	tight	loose	tight
0	196	24	5	1	201	25
1	454	47	30	3	485	50
2	282	27	14	0	296	27
≥ 2	352	30	18	0	372	31
≥ 3	70	3	4	0	76	4

Table C.1: Fake muons in the loose and tight samples passing preselection, number of b-jets listed, and relevant truth-matching (see text).

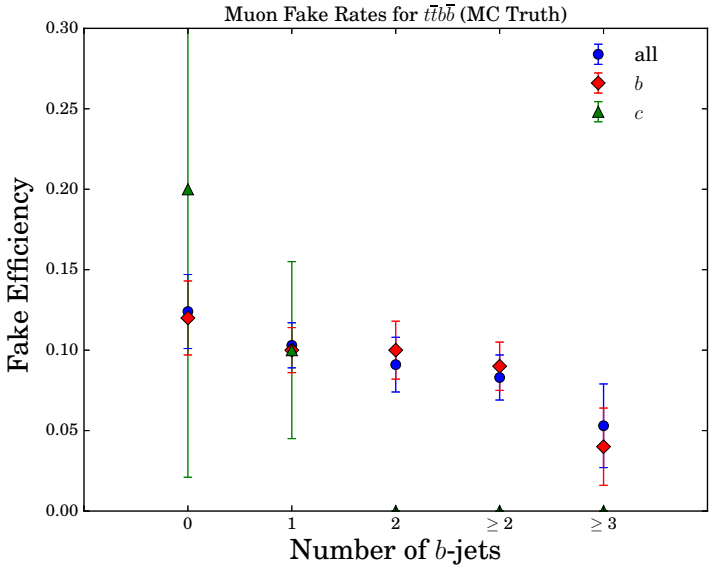

Figure C.1: Fake efficiencies (N_{tight}/N_{loose}) plotted for all muons in the $t\bar{t}b\bar{b}$ sample. All sources of fakes are shown in cyan, along with just the fakes from b sources and c sources.

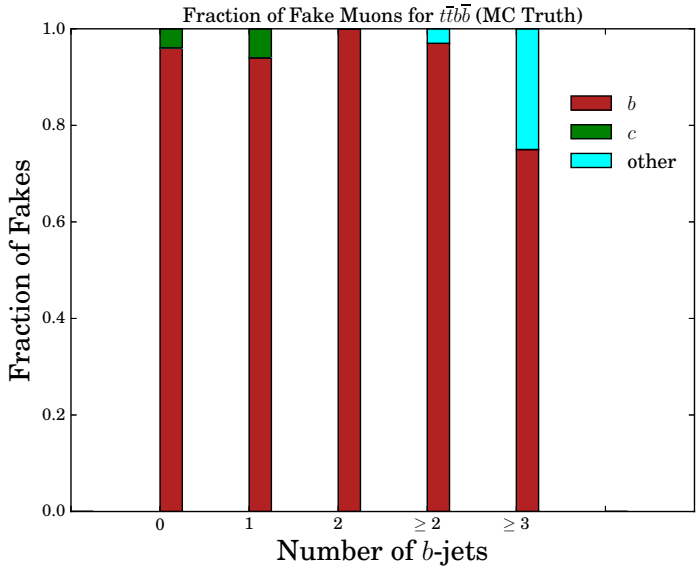

Figure C.2: Fraction of fakes from $t\bar{t}b\bar{b}$ sample, plotted for all *tight* muons. Obviously, fakes come mostly from b sources. Note: the stats in the ≥ 3 b-jet region shows roughly 25% from other sources, but keep in mind from table C.1 there are only 4 events in this sample so only 1 event comes from other sources.

C.2 Fake Efficiencies in SSμμ Events

One can compare the nominal fake efficiencies used for the fake/non-prompt lepton background estimation in this analysis with a completely different method of measuring fakes to determine if the fake efficiencies used are biased. In this study, a tag & probe method is used to measure the fake efficiency using SSμμ events.[1] The basic principle requires one muon in the event to act as the tag, which is matched to the single lepton high-p_{T} trigger (used in the main analysis trigger matching), and the other muon in the event is the probe, which is used to measure *loose*-to-*tight* efficiency. The *loose* and *tight* definitions used here are the same as in the main analysis.

Figure C.3 shows the efficiencies of the probe muon before and after MC subtraction of prompt sources in data. The MC simulations used to estimate the prompt contamination are primarily sourced from $t\bar{t}+V$, diboson (VV), and $t\bar{t}+H$ events. Efficiencies are also broken up by number of b-tagged jets in the events, 0 b-jets or ≥ 1 b-jets. The conclusion here is that the efficiencies are comparable to the efficiencies from the main analysis, especially after re-binning the p_{T} fake efficiencies for muons from figures 7.5 and 7.6 to those shown in figure C.4. However, the SSμμ efficiencies are higher in the higher p_{T} range. This could be due to a number of factors, the most prominent being: less statistics in the high p_{T} region and the probe muon is allowed to be both the leading and sub-leading p_{T} muon (this is done because the fake efficiencies are heavily dependent on p_{T}). The results can be thought of as conservative upper limits on the fake efficiencies used in the main analysis.

[1] SSμμ events are used because the main excess of data in the signal regions is prominent in μμ events and this study is simpler if one does not have to deal with the charge mis-id background in the estimation of the efficiency.

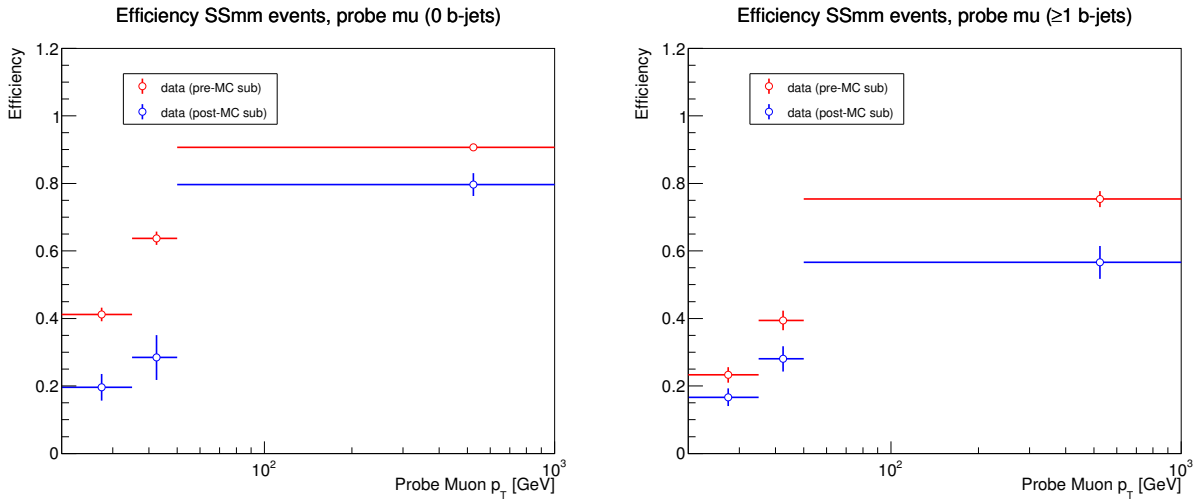

Figure C.3: Fake efficiencies measured for the probe muon in SS$\mu\mu$ events for 0 b-jet events (left) and ≥ 1 b-jet events (right). Binning for high p_{T} is limited due to statistics so all muons above 50 GeV have a single bin.

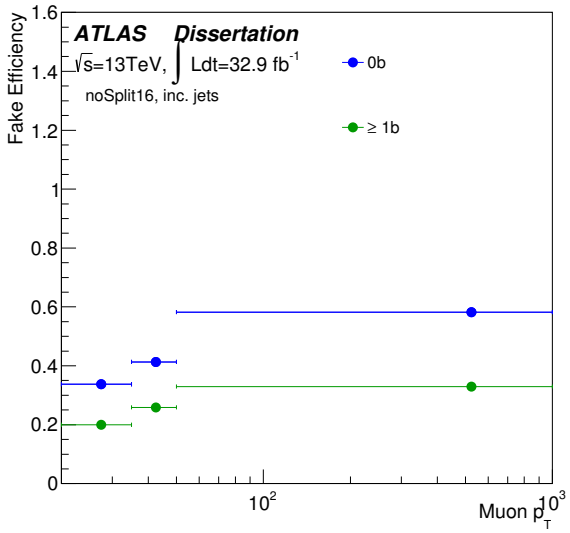

Figure C.4: Fake efficiencies from figures 7.5 and 7.6 re-binned to match p_{T} binning in figure C.3 for direct comparison. Inclusive jet selection is also included in these efficiencies (as opposed to $\{1j, \geq 2j\}$). Note this plot shows the resulting fake efficiencies for 0 b-jet and ≥ 1 b-jet after prompt MC subtraction on the same plot. These efficiencies should be compared with the efficiencies from figure C.3 *after* MC subtraction.

C.3 Event Displays

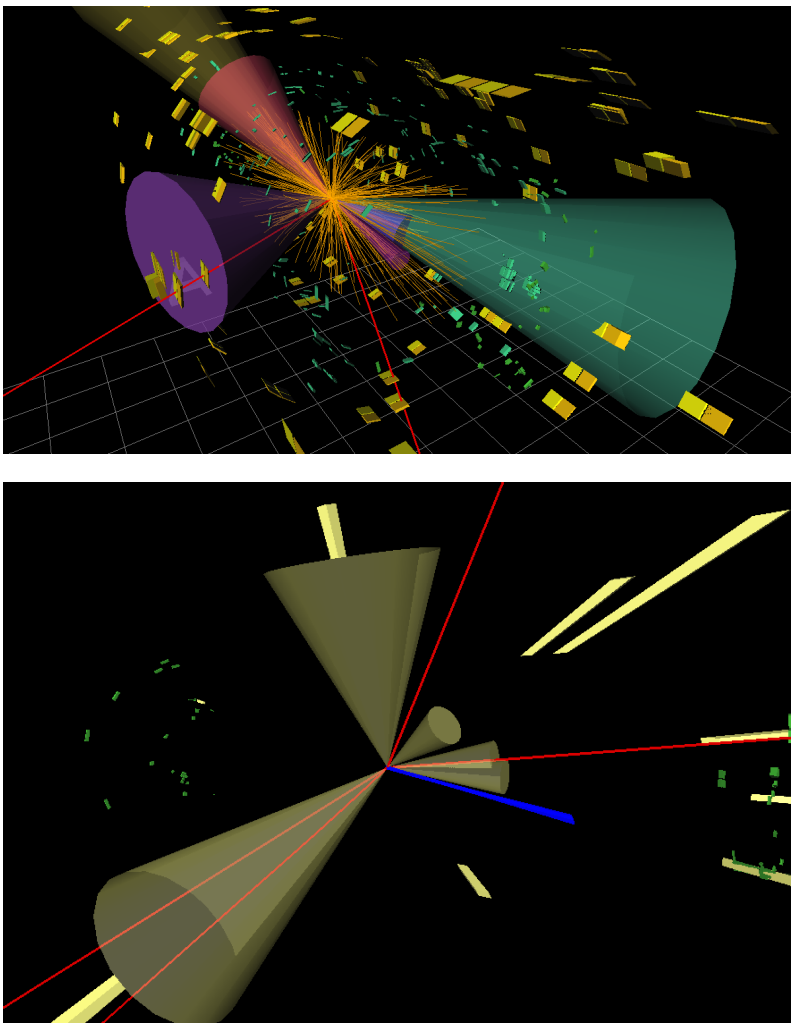

Figure C.5: Event displays of same-sign $\mu\mu$ event passing SR3b2l_L selection (top) and $e\mu\mu$ event passing SR3b3ll_L selection (bottom). Muons are shown as red lines, electron in blue and jets are colored cones.

Shown in figure C.5 is an event from run number 322481 (top), which is an event in the *SR3b2l_L* signal region and an event from run number 305618 (bottom), which is an event in the *SR3b3l_L* signal region. These events were checked specifically to see if any anomalies or other issues were present for the objects. They seem to be normal.

REFERENCES

[1]M. Peskin, and D. Schroeder, *An Introduction to Quantum Field Theory*, Advanced book classics (Avalon Publishing, 1995).

[2]M. Riordan, *The discovery of quarks*, Apr. 1992 (cit. on p. 33).

[3] ATLAS Collaboration, "Observation of a new particle in the search for the Standard Model Higgs boson with the ATLAS detector at the LHC", Physics Letters B **716**, 1–29 (2012) (cit. on pp. 33, 40, 60).

[4]"Observation of a new boson at a mass of 125 GeV with the CMS experiment at the LHC", Physics Letters B **716**, 30–61 (2012) (cit. on pp. 33, 40).

[5]S. Abachi, et al., "Search for High Mass Top Quark Production in $\overline{p}p$ Collisions at $\sqrt{s} =$ 1.8 TeV", Phys. Rev. Lett. **74**, 2422–2426 (1995) (cit. on p. 34).

[6]F. Abe, et al., "Observation of Top Quark Production in $\overline{p}p$ Collisions with the Collider Detector at Fermilab", Phys. Rev. Lett. **74**, 2626–2631 (1995) (cit. on p. 34).

[7]J. A. Aguilar-Saavedra, D. E. López-Fogliani, and C. Muñoz, "Novel signatures for vector-like quarks", (2017) (cit. on pp. 37, 51).

[8]M. Chala, "Direct Bounds on Heavy Top-Like Quarks With Standard and Exotic Decays", (2017) (cit. on pp. 37, 54).

[9]A. F., et al., "Observation of Top Quark Production in $\overline{p}p$ collisions with the Collider Detector at Fermilab", Phys. Rev. Lett **74**, 2626–2631 (1995) (cit. on p. 40).

[10]S. Abachi, et al., "Observation of the Top Quark", Phys. Rev. Lett. **74**, 2632–2637 (1995) (cit. on p. 40).

[11]C. Patrignani, et al., *Review of particle physics*, Vol. 40, 10 (2016), p. 100001 (cit. on p. 42).

[12]*Measurements of the Higgs boson production and decay rates and constraints on its couplings from a combined ATLAS and CMS analysis of the LHC pp collision data at* $\sqrt{s}$ *= 7 and 8 TeV*, tech. rep. ATLAS-CONF-2015-044 (CERN, Geneva, Sept. 2015) (cit. on p. 42).

[13]P. S. Cooper, "The masses of the neutrinos", (2016) (cit. on pp. 42, 46).

[14]E. Noether, "Invariant Variation Problems", [translated from German, *Invariante Variationsprobleme*, Nachr. d. K'onig. Gesellsch. d. Wiss. zu G'ottingen, Math-phys. Klasse, 235?257 (1918)] (1971) (cit. on p. 43).

[15]P. W. Higgs, "Broken Symmetries and the Masses of Gauge Bosons", Phys. Rev. Lett. **13**, 508–509 (1964) (cit. on p. 45).

[16]F. Englert, and R. Brout, "Broken Symmetry and the Mass of Gauge Vector Mesons", Phys. Rev. Lett. **13**, 321–323 (1964) (cit. on p. 45).

[17]K. Nakamura, and S. Petcov, in C. Patrignani, et al., *Review of particle physics*, Vol. 40, 10 (2016) Chap. 14. Neutrino Mixing, p. 100001 (cit. on p. 46).

[18]R. Aaij, et al., "Observation of $J/\psi p$ Resonances Consistent with Pentaquark States in $\Lambda_b^0 \to J/\psi K^- p$ Decays", Phys. Rev. Lett. **115**, 072001 (2015) (cit. on p. 47).

[19]M. Peskin, and D. Schroeder, in, *An Introduction to Quantum Field Theory*, Advanced book classics (Avalon Publishing, 1995) Chap. 22. Quantum Field Theory at the Frontier (cit. on pp. 47, 50).

[20]S. H́oche, "Introduction to parton-shower event generators", in Theoretical Advanced Study Institute in Elementary Particle Physics: Journeys Through the Precision Frontier: Amplitudes for Colliders (TASI 2014) Boulder, Colorado, June 2-27, 2014 (2014) (cit. on p. 48).

[21]R. Placakyte, "Parton Distribution Functions", in Proceedings, 31st International Conference on Physics in collisions (PIC 2011): Vancouver, Canada, August 28-September 1, 2011 (2011) (cit. on p. 48).

[22]M. Peskin, and D. Schroeder, in, *An Introduction to Quantum Field Theory*, Advanced book classics (Avalon Publishing, 1995) Chap. 14. Invitation: The Parton Model of Hadron Structure (cit. on p. 49).

[23]B. Foster, A. Martin, R. Thorne, and M. Vincter, in C. Patrignani, et al., *Review of particle physics*, Vol. 40, 10 (2016) Chap. 19. Structure Functions, p. 100001 (cit. on pp. 49, 50).

[24]K. G. Wilson, "Renormalization Group and Strong Interactions", Phys. Rev. D **3**, 1818–1846 (1971) (cit. on p. 51).

[25]G. Giudice, "Naturalness after LHC8", in *Proceedings of the european physical society conference on high energy physics* (Proceedings of Science, Stockholm, Sweden, 2013), p. 163 (cit. on p. 51).

[26]S. P. Martin, "Extra vectorlike matter and the lightest Higgs scalar boson mass in low-energy supersymmetry", Phys. Rev. D **81**, 035004 (2010) (cit. on p. 51).

[27]K. S. Babu, I. Gogoladze, M. U. Rehman, and Q. Shafi, "Higgs boson mass, sparticle spectrum, and the little hierarchy problem in an extended MSSM", Phys. Rev. D **78**, 055017 (2008) (cit. on p. 51).

[28]T. Moroi, and Y. Okada, "Upper bound of the lightest neutral Higgs mass in extended supersymmetric Standard Models", Phys. Lett. **B295**, 73–78 (1992) (cit. on p. 51).

[29]M. Schmaltz, and D. Tucker-Smith, "Little higgs theories", Annual Review of Nuclear and Particle Science **55**, 229–270 (2005) (cit. on p. 51).

[30]N. Arkani-Hamed, A. G. Cohen, E. Katz, and A. E. Nelson, "The littlest higgs", Journal of High Energy Physics **2002**, 034 (2002) (cit. on p. 51).

[31]K. Agashe, R. Contino, and A. Pomarol, "The minimal composite higgs model", Nuclear Physics B **719**, 165–187 (2005) (cit. on p. 51).

[32]D. B. Kaplan, H. Georgi, and S. Dimopoulos, "Composite higgs scalars", Physics Letters B **136**, 187–190 (1984) (cit. on p. 51).

[33]C. T. Hill, and E. H. Simmons, "Strong dynamics and electroweak symmetry breaking", Physics Reports **381**, 235–402 (2003) (cit. on p. 51).

[34]J. A. Aguilar-Saavedra, R. Benbrik, S. Heinemeyer, and M. Pérez-Victoria, "Handbook of vectorlike quarks: mixing and single production", Phys. Rev. D **88**, 094010 (2013) (cit. on pp. 51, 52, 57).

[35]M. Peskin, and D. Schroeder, in, *An Introduction to Quantum Field Theory*, Advanced book classics (Avalon Publishing, 1995) Chap. 3. The Dirac Field (cit. on p. 52).

[36]A. Angelescu, A. Djouadi, and G. Moreau, "Vector-like top/bottom-quark partners and Higgs physics at the LHC", The European Physical Journal C **76**, 99 (2016) (cit. on p. 52).

[37]F. del Aguila, J. Santiago, and M. Pérez-Victoria, "Observable contributions of new exotic quarks to quark mixing", Journal of High Energy Physics **2000**, 011 (2000) (cit. on p. 53).

[38]J. Aguilar-Saavedra, "Effects of mixing with quark singlets", Phys.Rev. **D67**, 035003 (2003) (cit. on p. 53).

[39]A. L. Kagan, "Radiative Quark Mass and Mixing Hierarchies From Supersymmetric Models With a Fourth Mirror Family", Phys. Rev. **D40**, 173 (1989) (cit. on p. 53).

[40]J. Aguilar-Saavedra, "Identifying top partners at LHC", Journal of High Energy Physics **2009**, 030 (2009) (cit. on pp. 54, 55).

[41] ATLAS Collaboration, *Search for new physics using events with b-jets and a pair of same-charge leptons in 3.2 fb^{-1} of pp collisions at $\sqrt{s}$ = 13 TeV with the ATLAS detector*, ATLAS-CONF-2016-032 (cit. on pp. 57, 58, 89).

[42]G. Aad, et al., "Search for pair-produced heavy quarks decaying to Wq in the two-lepton channel at $\sqrt{s} = 7$ TeV with the ATLAS detector", Phys. Rev. D **86**, 012007 (2012) (cit. on p. 58).

[43]G. Aad, et al., "Search for pair production of heavy top-like quarks decaying to a high-w boson and a b quark in the lepton plus jets final state at with the {atlas} detector", Physics Letters B **718**, 1284–1302 (2013) (cit. on p. 58).

[44]G. Aad, et al., "Analysis of events with b-jets and a pair of leptons of the same charge in pp collisions at $\sqrt{s} = 8$ TeV with the ATLAS detector", Journal of High Energy Physics **2015**, 150 (2015) (cit. on pp. 58, 101, 108, 153, 212, 217).

[45]G. Aad, et al., "Search for pair and single production of new heavy quarks that decay to a Z boson and a third-generation quark in pp collisions at $\sqrt{s} = 8$ TeV with the ATLAS detector", Journal of High Energy Physics **2014**, 104 (2014) (cit. on p. 58).

[46]*Search for production of vector-like top quark pairs and of four top quarks in the lepton-plus-jets final state in pp collisions at $\sqrt{s} = 13$ TeV with the ATLAS detector*, tech. rep. ATLAS-CONF-2016-013 (CERN, Geneva, Mar. 2016) (cit. on p. 58).

[47]M. Aaboud, et al., "Search for pair production of heavy vector-like quarks decaying to high-p_{T} W bosons and b quarks in the lepton-plus-jets final state in pp collisions at $\sqrt{s}$=13 TeV with the ATLAS detector", (2017) (cit. on p. 58).

[48]M. Aaboud, et al., "Search for pair production of vector-like top quarks in events with one lepton, jets, and missing transverse momentum in $\sqrt{s} = 13$ TeV pp collisions with the ATLAS detector", Journal of High Energy Physics **2017**, 52 (2017) (cit. on p. 58).

[49]S. Chatrchyan, et al., "Search for heavy, top-like quark pair production in the dilepton final state in pp collisions at $\sqrt{s} = 7$ TeV", Physics Letters B **716**, 103–121 (2012) (cit. on p. 58).

[50]S. Chatrchyan, et al., "Search for heavy quarks decaying into a top quark and a W or Z boson using lepton + jets events in pp collisions at $\sqrt{s} = 7$ TeV", Journal of High Energy Physics **2013**, 154 (2013) (cit. on p. 58).

[51]S. Chatrchyan, et al., "Combined search for the quarks of a sequential fourth generation", Phys. Rev. D **86**, 112003 (2012) (cit. on p. 58).

[52]S. Chatrchyan, et al., "Inclusive search for a vector-like T quark with charge 2/3 in pp collisions at $\sqrt{s} = 8$ TeV", Physics Letters B **729**, 149–171 (2014) (cit. on p. 58).

[53]S. Chatrchyan, et al., "Search for vector-like T quarks decaying to top quarks and Higgs bosons in the all-hadronic channel using jet substructure", Journal of High Energy Physics **2015**, 80 (2015) (cit. on p. 58).

[54]S. Chatrchyan, et al., "Search for pair production of vector-like T quarks in the lepton plus jets final state", (2016) (cit. on p. 58).

[55]A. M. Sirunyan, et al., "Search for electroweak production of a vector-like quark decaying to a top quark and a Higgs boson using boosted topologies in fully hadronic final states", Journal of High Energy Physics **2017**, 136 (2017) (cit. on p. 58).

[56]"Search for single production of vector-like quarks decaying into a b quark and a W boson in pp collisions at $\sqrt{s} = 13$ TeV", Physics Letters B **772**, 634–656 (2017) (cit. on p. 58).

[57]A. M. Sirunyan, et al., "Search for pair production of vector-like T and B quarks in single-lepton final states using boosted jet substructure techniques at $\sqrt{s} = 13$ TeV", (2017) (cit. on p. 58).

[58]*LHC Images*, http://atlasexperiment.org/photos/,http://www.stfc.ac.uk/stfc/includes/themes/MuraSTFC/assets/legacy/LHCinteractive/LHC_default.jpg (cit. on pp. 61, 64, 67, 72).

[59] ALICE Collaboration, *ALICE : Technical proposal for a Large Ion collider Experiment at the CERN LHC*, tech. rep. CERN-LHCC-95-71 (CERN, Geneva, 1995) (cit. on p. 61).

[60] LHCb Collaboration, *LHCb: Technical Proposal*, tech. rep. CERN-LHCC-98-004 (CERN, Geneva, 1998) (cit. on p. 61).

[61] TOTEM Collaboration, *Total Cross Section, Elastic Scattering and Diffraction Dissociation at the LHC at CERN*, tech. rep. CERN-LHCC-2004-002 (CERN, Geneva, Jan. 2004) (cit. on p. 61).

[62] LHCf Collaboration, *Measurement of Photons and Neutral Pions in the Very Forward Region of LHC*, tech. rep. CERN-LHCC-2006-004 (CERN, Geneva, Feb. 2006) (cit. on p. 61).

[63] MoEDAL Collaboration, *Technical Design Report of the MoEDAL Experiment*, tech. rep. CERN-LHCC-2009-006 (CERN, Geneva, June 2009) (cit. on p. 62).

[64] K. Schindl, *The Injector Chain for the LHC*, tech. rep. CERN-OPEN-99-052 (CERN, Geneva, Jan. 1999) (cit. on p. 63).

[65] ATLAS Collaboration, *ATLAS Detector and Physics Design Performance, Technical Design Report, Volume 1*, tech. rep. CERN-LHCC-99-014 (CERN, Geneva, 1999) (cit. on p. 63).

[66] ATLAS Collaboration, *ATLAS Detector and Physics Design Performance, Technical Design Report, Volume 2*, tech. rep. CERN-LHCC-99-015 (CERN, Geneva, 1999) (cit. on p. 63).

[67] G. Aad, et al., "The ATLAS Experiment at the CERN Large Hadron Collider", JINST **3**, S08003 (2008) (cit. on p. 63).

[68] Miele, P. and ten Kate, H.H.J., *The Superconducting Magnet System for the ATLAS Detector at CERN*, tech. rep. CERN-OPEN-2001-064 (CERN, Geneva, June 2001) (cit. on p. 66).

[69] G. Aad, et al., "ATLAS Pixel Detector Electronics and Sensors", JINST **03**, P07007 (2008) (cit. on p. 66).

[70] ATLAS Collaboration, *Insertable B-Layer Technical Design Report*, tech. rep. CERN-LHCC-2010-013 (CERN, Geneva, Sept. 2010) (cit. on p. 66).

[71] G. Aad, et al., "Operation and performance of the ATLAS semiconductor tracker", JINST **09**, P08009 (2014) (cit. on p. 67).

[72] J. R. Pater, "The ATLAS SemiConductor Tracker operation and performance", JINST **7**, C04001 (2012) (cit. on p. 68).

[73] G. Aad, et al., "The ATLAS Transitional Radiation Tracker (TRT) proportional drift tube: design and performance", JINST **03**, P02013 (2008) (cit. on p. 68).

[74] A. Vogel, *ATLAS Transition Radiation Tracker (TRT): Straw Tube Gaseous Detectors at High Rates*, ATL-INDET-PROC-2013-005 (cit. on p. 68).

[75] A. Yamamoto, T. Kondo, Y. Doi, Y. Makida, K. Tanaka, T. Haruyama, H. Yamaoka, H. H. J. ten Kate, L. Bjorset, K. Wada, S. Meguro, J. S. H. Ross, and K. D. Smith, "Design and development of the ATLAS central solenoid magnet", IEEE Trans. Appl. Supercond. **9**, 852–855. 6 p (1998) (cit. on p. 68).

[76] A. Artamonov, D. Bailey, G. Belanger, M. Cadabeschi, T. Y. Chen, V. Epshteyn, P. Gorbounov, K. K. Joo, M. Khakzad, V. Khovanskiy, P. Krieger, P. Loch, J. Mayer, E. Neuheimer, F. G. Oakham, M. O'Neill, R. S. Orr, M. Qi, J. Rutherfoord, A. Savine, M. Schram, P. Shatalov, L. Shaver, M. Shupe, G. Stairs, V. Strickland, D. Tompkins, I. Tsukerman, and K. Vincent, "The ATLAS Forward Calorimeter", J. of Instrum. **3**, P02010 (2008) (cit. on p. 70).

[77] ATLAS Collaboration, *ATLAS Liquid Argon Calorimeters: Technical Design Report*, tech. rep. CERN-LHCC-96-41 (CERN, Geneva, 1996) (cit. on p. 71).

[78] ATLAS Collaboration, *ATLAS Liquid Argon Calorimeter Phase-I Upgrade Technical Design Report*, tech. rep. CERN-LHCC-2013-017 (CERN, Geneva, 2013) (cit. on p. 71).

[79] ATLAS Collaboration, *ATLAS Tile Calorimeters: Technical Design Report*, tech. rep. CERN-LHCC-96-042 (CERN, Geneva, 1996) (cit. on p. 71).

[80] ATLAS TileCal Collaboration, *Design, Construction and Installation of the ATLAS Hadronic Barrel Scintillator-Tile Calorimeter*, tech. rep. ATL-COM-TILECAL-2007-019 (CERN, Geneva, 2008) (cit. on p. 71).

[81] ATLAS Collaboration, *ATLAS Muon Spectrometer: Technical Design Report*, tech. rep. CERN-LHCC-97-022 (CERN, Geneva, 1997) (cit. on p. 72).

[82] T. Kawamoto, et al., *New Small Wheel Technical Design Report*, tech. rep. CERN-LHCC-2013-006 (CERN, Geneva, June 2013) (cit. on p. 74).

[83] J. Glatzer, "Operation of the Upgraded ATLAS Level-1 Central Trigger System", Journal of Physics: Conference Series **664**, 082013 (2015) (cit. on p. 75).

[84] Y. Nakahama, "The ATLAS Trigger System: Ready for Run-2", Journal of Physics: Conference Series **664**, 082037 (2015) (cit. on pp. 75, 76).

[85] A. Buckley, T. Eifert, M. Elsing, D. Gillberg, K. Koeneke, A. Krasznahorkay, E. Moyse, M. Nowak, S. Snyder, and P. van Gemmeren, "Implementation of the ATLAS Run 2 event data model", Journal of Physics: Conference Series **664**, 072045 (2015) (cit. on p. 79).

[86] R. Seuster and M. Elsing and G. A. Stewart and V. Tsulaia, *Status and Future Evolution of the ATLAS Offline Software*, tech. rep. ATL-SOFT-PROC-2015-034 (CERN, Geneva, May 2015) (cit. on p. 79).

[87] *AnalysisTop Twiki*, https://twiki.cern.ch/twiki/bin/view/AtlasProtected/TopxAODStartGuide (cit. on p. 79).

[88] ATLAS Collaboration, *ATLAS Computing Technical Design Report*, http://atlas-proj-computing-tdr.web.cern.ch/atlas-proj-computing-tdr/Html/Computing-TDR-4.htm, 2005 (cit. on p. 79).

[89] E. Moyse, and F. Akesson, *Event Data Model in ATLAS CHEP '06 PROCEEDINGS*, https://indico.cern.ch/event/408139/contributions/979862/attachments/815826/1117898/105EdwardMoyse.pdf, 2006 (cit. on p. 79).

[90] R. Brun and F. Rademakers, "ROOT - An Object Oriented Data Analysis Framework", Nucl. Instrum. Meth. in Phys. Rev. A **389**, 81–86 (1997) (cit. on pp. 79, 153).

[91] *TopDerivation Twiki*, https://twiki.cern.ch/twiki/bin/view/AtlasProtected/TopDerivations (cit. on p. 80).

[92] ATLAS Collaboration, *Performance of the ATLAS Inner Detector Track and Vertex Reconstruction in the High Pile-up LHC Environment*, ATLAS-CONF-2012-042 (cit. on p. 81).

[93] V. Lacuesta, "Track and Vertex Reconstruction in the ATLAS experiment", JINST **8**, C02035 (2013) (cit. on p. 81).

[94]"Performance of pile-up mitigation techniques for jets in *pp* collisions at $\sqrt{s}$ 8 TeV using the ATLAS detector", The European Physical Journal C **76**, 581 (2016) (cit. on p. 81).

[95]O. S. Brüning, et al., *The LHC Design Report Vol 1*, tech. rep. CERN-2004-003-V-1 (CERN, Geneva, 2004) (cit. on p. 82).

[96] ATLAS Collaboration, *Analysis of events with b jets and a pair of same charge leptons in pp collisions at $\sqrt{s}$ = 13 TeV with the ATLAS detector*, ATL-COM-PHYS-2015-389 (cit. on p. 82).

[97] The ATLAS Collaboration, *Topological cell clustering in the ATLAS calorimeters and its performance in LHC Run 1*, tech. rep. CERN-PH-EP-2015-304 (CERN, Geneva, 2016) (cit. on pp. 82, 91).

[98] ATLAS Collaboration, *Jet energy scale and its systematic uncertainty in proton-proton collisions at $\sqrt{s}$ =7 TeV with ATLAS 2011 data*, tech. rep. ATLAS-CONF-2013-004 (CERN, Geneva, 2013) (cit. on p. 82).

[99]B. R. Webber, "Fragmentation and hadronization", International Journal of Modern Physics A **15**, 577–606 (2000) (cit. on p. 82).

[100]M. Cacciari, G. P. Salam, and G. Soyez, "The anti-k$_t$ jet clustering algorithm", Journal of High Energy Physics **2008**, 063 (2008) (cit. on pp. 83, 84).

[101]M. Cacciari, G. P. Salam, and G. Soyez, "FastJet user manual", The European Physical Journal C **72**, 1896 (2012) (cit. on p. 83).

[102]S. Catani, Y. L. Dokshitzer, M. H. Seymour, and B. R. Webber, "Longitudinally-invariant k$_T$-clustering algorithms for hadron-hadron collisions", Nuclear Physics B **406**, 187–224 (1993) (cit. on p. 83).

[103]Y. L. Dokshitzer, G. D. Leder, S. Moretti, and B. R. Webber, "Better jet clustering algorithms", Journal of High Energy Physics **1997**, 001 (1997) (cit. on p. 83).

[104] ATLAS Collaboration, *Selection of jets produced in 13TeV proton-proton collisions with the ATLAS detector*, tech. rep. ATLAS-CONF-2015-029 (CERN, Geneva, 2015) (cit. on pp. 85, 86).

[105] ATLAS Collaboration, *Jet Calibration and Systematic Uncertainties for Jets Reconstructed in the ATLAS Detector at $\sqrt{s}$ =13 TeV*, tech. rep. ATL-PHYS-PUB-2015-015 (CERN, Geneva, 2015) (cit. on pp. 85, 162).

[106] ATLAS Collaboration, *Tagging and suppression of pileup jets with the ATLAS detector*, tech. rep. ATLAS-CONF-2014-018 (CERN, Geneva, 2015) (cit. on p. 87).

[107]*JetEtMiss Recommendations Twiki*, `https://twiki.cern.ch/twiki/bin/view/AtlasProtected/JetEtmissRecommendations2016` (cit. on pp. 87, 162).

[108] The ATLAS Collaboration, "Performance of b -jet identification in the ATLAS experiment", Journal of Instrumentation **11**, P04008 (2016) (cit. on p. 88).

[109] ATLAS Collaboration, *The ATLAS b-Jet Trigger*, tech. rep. ATL-DAQ-PROC-2011-035 (CERN, Geneva, 2011) (cit. on p. 88).

[110] ATLAS Collaboration, *Expected performance of the ATLAS b-tagging algorithms in Run-2*, tech. rep. ATL-PHYS-PUB-2015-022 (CERN, Geneva, 2015) (cit. on p. 88).

[111] *b-Tagging MV2 Twiki*, https://twiki.cern.ch/twiki/bin/view/AtlasProtected/BTaggingMV2 (cit. on p. 89).

[112] *b-Tagging Calibrations Twiki*, https://twiki.cern.ch/twiki/bin/view/AtlasProtected/BTagCalib2015 (cit. on p. 89).

[113] ATLAS Collaboration, *Optimisation of the ATLAS b-tagging performance for the 2016 LHC Run*, tech. rep. ATL-PHYS-PUB-2016-012 (CERN, Geneva, 2016) (cit. on p. 89).

[114] ATLAS Collaboration, *Electron and photon energy calibration with the ATLAS Detector using data collected in 2015 at* $\sqrt{s}$ *=13 TeV*, tech. rep. ATL-PHYS-PUB-2016-015 (CERN, Geneva, 2016) (cit. on pp. 90, 162).

[115] *EGamma Recommendations Twiki*, https://twiki.cern.ch/twiki/bin/view/AtlasProtected/EGammaRecommendations (cit. on pp. 90, 162).

[116] *EGamma ID for Run 2 Twiki*, https://twiki.cern.ch/twiki/bin/view/AtlasProtected/EGammaIdentificationRun2 (cit. on p. 90).

[117] The ATLAS Collaboration, "Electron and photon energy calibration with the ATLAS detector using LHC Run 1 data", The European Physical Journal C **74**, 3071 (2014) (cit. on p. 90).

[118] ATLAS Collaboration, *Electron efficiency measurements with the ATLAS detector using the 2015 LHC proton-proton collision data*, tech. rep. ATLAS-CONF-2016-024 (CERN, Geneva, 2016) (cit. on pp. 91, 92, 94).

[119] *Isolation WP Run 2 Twiki*, https://twiki.cern.ch/twiki/bin/view/AtlasProtected/IsolationSelectionTool (cit. on p. 93).

[120] The ATLAS Collaboration, "Muon Reconstruction Performance of the ATLAS detector in proton-proton collisions at $\sqrt{s}$ = 13 TeV", The European Physical Journal C **76**, 292 (2016) (cit. on pp. 93, 96).

[121] ATLAS Collaboration, *Expected performance of missing transverse momentum reconstruction for the ATLAS detector at* $\sqrt{s}$ *= 13 TeV*, tech. rep. ATL-PHYS-PUB-2015-023 (CERN, Geneva, 2015) (cit. on pp. 98, 163).

[122] *Combination of the Searches for vector-like partners of the third generation quarks at* $\sqrt{s}$ *= 13 TeV with the ATLAS detector*, tech. rep. ATLAS-COM-PHYS-2017-687 (CERN, Geneva, 2017) (cit. on p. 102).

[123] M. Aaboud, et al., "Performance of the ATLAS Trigger System in 2015", Eur. Phys. J. **C77**, 317 (2017) (cit. on p. 105).

[124] ATLAS Collaboration, *Search for new phenomena using events with b jets and a pair of same-charge leptons in 3.2* fb^{-1} *of pp collisions at* $\sqrt{s}$ *= 13 TeV with the ATLAS detector*, ATLAS-CONF-2016-036 (cit. on p. 108).

[125] "Luminosity determination in pp collisions at $\sqrt{s}$ = 8 TeV using the ATLAS detector at the LHC", The European Physical Journal C **76**, 653 (2016) (cit. on p. 124).

[126] *Public Luminosity Group Results, Run 2*, https://twiki.cern.ch/twiki/bin/view/AtlasPublic/LuminosityPublicResultsRun2 (cit. on p. 124).

[127]T. Golling, H. S. Hayward, P. U. E. Onyisi, H. J. Stelzer, and P. Waller, "The ATLAS data quality defect database system", The European Physical Journal C **72**, 1960 (2012) (cit. on pp. 124, 125).

[128]"The ATLAS Simulation Infrastructure", The European Physical Journal C **70**, 823–874 (2010) (cit. on pp. 127, 130).

[129]A. Buckley, J. Butterworth, S. Gieseke, D. Grellscheid, S. Höche, H. Hoeth, F. Krauss, L. Lönnblad, E. Nurse, P. Richardson, S. Schumann, M. H. Seymour, T. Sjöstrand, P. Skands, and B. Webber, "General-purpose event generators for LHC physics", Physics Reports **504**, 145–233 (2011) (cit. on pp. 130, 131).

[130]P. Nason, and P. Skands, in C. Patrignani, et al., *Review of particle physics*, Vol. 40, 10 (2016) Chap. 41. Monte Carlo Event Generators, p. 100001 (cit. on p. 130).

[131]M. R. Whalley, D. Bourilkov, and R. C. Group, "The Les Houches accord PDFs (LHAPDF) and LHAGLUE", in HERA and the LHC: A Workshop on the implications of HERA for LHC physics. Proceedings, Part B (2005), pp. 575–581 (cit. on p. 130).

[132]*LHAPDF C++ Interpolator*, `http://lhapdf.hepforge.org` (cit. on p. 130).

[133]H.-L. Lai, M. Guzzi, J. Huston, Z. Li, P. M. Nadolsky, J. Pumplin, and C. Yuan, "New parton distributions for collider physics", Phys. Rev. **D82**, 074024 (2010) (cit. on p. 130).

[134]CTEQ, *ct10 pdfs*, `http://www.physics.smu.edu/scalise/cteq/` (cit. on p. 130).

[135]S. Carrazza, S. Forte, and J. Rojo, "Parton Distributions and Event Generators", in Proceedings, 43rd international symposium on multiparticle dynamics (ismd 13) (2013), pp. 89–96 (cit. on p. 130).

[136]R. D. Ball, V. Bertone, S. Carrazza, C. S. Deans, L. D. Debbio, S. Forte, A. Guffanti, N. P. Hartland, J. I. Latorre, J. Rojo, and M. Ubiali, "Parton distributions with {LHC} data", Nuclear Physics B **867**, 244–289 (2013) (cit. on p. 130).

[137]*ATLAS Run 1 Pythia8 tunes*, tech. rep. ATL-PHYS-PUB-2014-021 (CERN, Geneva, Nov. 2014) (cit. on p. 130).

[138]J. Alwall, R. Frederix, S. Frixione, V. Hirschi, F. Maltoni, O. Mattelaer, H.-S. Shao, T. Stelzer, P. Torrielli, and M. Zaro, "The automated computation of tree-level and next-to-leading order differential cross sections, and their matching to parton shower simulations", Journal of High Energy Physics **2014**, 79 (2014) (cit. on pp. 131, 191).

[139]T. Sjöstrand, S. Mrenna, and P. Skands, "PYTHIA 6.4 physics and manual", Journal of High Energy Physics **2006**, 026 (2006) (cit. on p. 131).

[140]T. Sjöstrand, S. Mrenna, and P. Skands, "A brief introduction to PYTHIA 8.1", Computer Physics Communications **178**, 852–867 (2008) (cit. on p. 131).

[141]S. Frixione, P. Nason, and C. Oleari, "Matching NLO QCD computations with Parton Shower simulations: the POWHEG method", JHEP **11**, 070 (2007) (cit. on p. 131).

[142]J. Aguilar-Saveedra, PROTOS *version 2.2*, `http://jaguilar.web.cern.ch/jaguilar/protos/` (cit. on p. 131).

[143]D. J. Lange, "The EvtGen particle decay simulation package", Nuclear Instruments and Methods in Physics Research Section A: Accelerators, Spectrometers, Detectors and Associated Equipment **462**, BEAUTY2000, Proceedings of the 7th Int. Conf. on B-Physics at Hadron Machines, 152–155 (2001) (cit. on p. 132).

[144]S. Agostinelli, et al., "Geant4 simulation toolkit", Nuclear Instruments and Methods in Physics Research Section A: Accelerators, Spectrometers, Detectors and Associated Equipment **506**, 250–303 (2003) (cit. on p. 132).

[145]J. Ferrando, and D. Wendland, *Reference $t\bar{t}$ production cross sections for use in ATLAS analyses*, tech. rep. ATL-COM-PHYS-2014-112 (CERN, Geneva, Feb. 2014) (cit. on p. 133).

[146]*Central MC15 Production*, https://twiki.cern.ch/twiki/bin/viewauth/AtlasProtected/CentralMC15ProductionList (cit. on p. 136).

[147]B. Abbott, et al., "Extraction of the width of the W boson from measurements of $\sigma(p\bar{p}\to W + X) \times B(\vec{W}e\nu)$ and $\sigma(p\bar{p}\to Z + X) \times B(\vec{Z}ee)$ and their ratio", Phys. Rev. D **61**, 072001 (2000) (cit. on p. 137).

[148]G. Aad, et al., "Estimation of non-prompt and fake lepton backgrounds in final states with top quarks produced in proton-proton collisions at $\sqrt{s}$ =8 TeV with the ATLAS detector", (2014) (cit. on pp. 137, 151).

[149]"Measurement of the top quark pair production cross section with ATLAS in *pp* collisions at $\sqrt{s}$ = 7 TeV", The European Physical Journal C **71**, 1577 (2011) (cit. on p. 137).

[150]F. Derue, *Estimation of fake lepton background for top analyses using the Matrix Method with the 2015 dataset at $\sqrt{s}$ =13 TeV with AnalysisTop-2.3.41*, tech. rep. ATL-COM-PHYS-2016-198 (CERN, Geneva, Feb. 2016) (cit. on p. 151).

[151]M. Aaboud, et al., "Measurement of the $t\bar{t}$ production cross-section using eμevents with *b*-tagged jets in *pp* collisions at $\sqrt{s}$ = 13 TeV with the ATLAS detector", Physics Letters B **761**, 136–157 (2016) (cit. on p. 151).

[152]E. Varnes, *A Poisson likelihood approach to fake lepton estimation with the matrix method*, private communication, tech. rep., Geneva, Mar. 2016 (cit. on pp. 151, 152).

[153]G. Cowan, in C. Patrignani, et al., *Review of particle physics*, Vol. 40, 10 (2016) Chap. 39. Statistics, p. 100001 (cit. on pp. 152, 196).

[154]F. James, and M. Roos, "Minuit - a system for function minimization and analysis of the parameter errors and correlations", Computer Physics Communications **10**, 343–367 (1975) (cit. on pp. 153, 163).

[155]E. Varnes, private communication, Apr. 12, 2017 (cit. on p. 153).

[156]D. Paredes, and D. Calvet, *Estimation of the mis-identification rates of the electron charge at 8 TeV*, tech. rep. ATL-COM-PHYS-2013-1622 (CERN, Geneva, Dec. 2013) (cit. on p. 155).

[157]*Muon Recommendations Twiki*, https://twiki.cern.ch/twiki/bin/view/AtlasProtected/MCPAnalysisGuidelinesMC15 (cit. on p. 162).

[158]"Luminosity determination in pp collisions at $\sqrt{s} = 8$ TeV using the ATLAS detector at the LHC", The European Physical Journal C **76**, 653 (2016) (cit. on p. 191).

[159]J. Butterworth, E. Dobson, U. Klein, B. Mellado Garcia, T. Nunnemann, J. Qian, D. Rebuzzi, and R. Tanaka, *Single Boson and Diboson Production Cross Sections in pp Collisions at sqrts=7 TeV*, tech. rep. ATL-COM-PHYS-2010-695 (CERN, Geneva, Aug. 2010) (cit. on p. 191).

[160]A. L. Read, "Modified frequentist analysis of search results (the CL_s method)", (2000) (cit. on p. 195).

[161]A. L. Read, "Presentation of search results: the CL_s technique", Journal of Physics G: Nuclear and Particle Physics **28**, 2693 (2002) (cit. on pp. 195, 197).

[162]G. Cowan, K. Cranmer, E. Gross, and O. Vitells, "Asymptotic formulae for likelihood-based tests of new physics", The European Physical Journal C **71**, 1554 (2011) (cit. on p. 197).

[163]*RooStats Twiki*, https://twiki.cern.ch/twiki/bin/view/RooStats/WebHome (cit. on p. 205).

[164]M. Baak, G. J. Besjes, D. Côté, A. Koutsman, J. Lorenz, and D. Short, "HistFitter software framework for statistical data analysis", The European Physical Journal C **75**, 153 (2015) (cit. on p. 205).

[165]F. O'Grady, "Search for Vector-like Quarks using trilepton and same-sign dilepton events in 20.3 fb^{-1} of proton-proton collisions at $\sqrt{s} = 8$ TeV with the ATLAS detector", Presented 07 Jul 2015 (2015) (cit. on p. 217).

[166]T. Kawamoto, et al., *New Small Wheel Technical Design Report*, tech. rep. CERN-LHCC-2013-006 (CERN, Geneva, June 2013) (cit. on pp. 219, 220, 222).

[167] ATLAS Collaboration, *ATLAS Muon Spectrometer: Technical Design Report*, tech. rep. CERN-LHCC-97-022 (CERN, Geneva, 1997) (cit. on p. 219).

[168]A. Zibell, "*Micromegas Detectors for the Upgrade of the ATLAS Muon Spectrometer*", JINST **9**, C0813 (2014) (cit. on p. 219).

[169]M. Iodice, "*Micromegas Detectors for the Muon Spectrometer Upgrade of the ATLAS Experiment*", JINST **10**, C02026 (2015) (cit. on p. 220).

[170]D. Gerbaudo, "*ATLAS L1 Muon Trigger Upgrade with sTGC: Design and Performance*", PoS **EPS-HEP2013**, 094 (2013) (cit. on p. 221).

[171]J. R. Y. Giomataris, P. Rebourgeard and G. Charpak, "*Micromegas: A High granularity position sensitive gaseous detector for high particle flux environments*", Nucl. Instrum. Meth. **A376**, 29 (1996) (cit. on p. 221).

[172]T. Alexopoulos, et al., "*A spark-resistant bulk-Micromegas chamber for high-rate applications*", Nucl. Instrum. Meth. **A640**, 110–118 (2011) (cit. on p. 221).

[173]G. D. Geronimo, et al., "*VMM1 - An ASIC for Micropattern Detectors*", IEEE Trans. Nucl. Sci. **60**, 2314 (2013) (cit. on p. 223).

[174]*Xilinx Artix-7 FPGA*, http://www.xilinx.com/products/silicon-devices/fpga/artix-7.html (cit. on p. 224).

[175] *Zebra Elastomeric Connectors*, http://www.fujipoly.com/usa/products/zebra-elastomeric-connectors.html,http://www.zaxisconnector.com/index.htm (cit. on p. 224).

[176] Xilinx, *Vivado Design Suite*, https://www.xilinx.com/products/design-tools/vivado.html, Mar. 2017 (cit. on p. 226).

[177] R. Edgar, J. Ameel, D. Amidei, K. S. Edgar, and L. Guan, *New Small Wheel Radiation and Magnetic Field Environment*, Private Communication (cit. on p. 227).

[178] CERN, *Radiation Tolerant 10W Synchronous Step-down Buck DC-DC Converter*, http://project-dcdc.web.cern.ch/project-dcdc/public/Documents/FEAST%20datasheet.pdf (cit. on p. 228).

[179] *CAEN*, http://www.caen.it/ (cit. on p. 229).

[180] G. Iakovidis, Private Communication, Feb. 7, 2017 (cit. on p. 230).

[181] G. De Geronimo, Private Communication, Jan. 18, 2017 (cit. on p. 233).

[182] *ROOT Data Analysis Framework*, https://root.cern.ch/ (cit. on p. 233).